Inaugural dissertation

for

obtaining the doctoral degree

of the

Combined Faculty of Mathematics, Engineering and Natural Sciences

of the

Ruprecht - Karls - University

Heidelberg

Presented by

M.Sc. Kaisa Pakari

born in: Houston, Texas, USA

Oral examination: 06.10.2025

Modeling human PMM2-CDG in medaka to understand systemic effects of hypoglycosylation on development

Referees: Prof. Dr. Joachim Wittbrodt

Prof. Dr. Sabine Strahl

Abstract

Congenital disorders of glycosylation (CDG) are a group of rare metabolic diseases caused by mutations in the enzymes involved in glycosylation. To date, no conclusive pathogenic mechanism is linked to the disease and there are only limited therapeutic options available. The most common form of CDG is caused by compound heterozygous hypomorphic alleles of the cytosolic enzyme Phosphomannomutase 2 (PMM2), leading to global protein hypoglycosylation and a multiorgan phenotype in patients. Complete loss-of-function mutations in the essential protein are incompatible with life. Patients that survive carry mutations that lead to reduced enzyme activity of PMM2.

PMM2 plays a crucial role at the basis of the glycosylation cascade in the endoplasmic reticulum by providing the essential mannose precursor required for the three glycosylation routes *N*-glycosylation, *O*- and *C*-mannosylation. The entire glycosylation machinery is evolutionarily highly conserved which allows generating translational models in other organisms. The small teleost medaka (*Oryzias latipes*) offers a great advantage as model organism to investigate the early embryogenesis through the extrauterine and transparent developing embryos. To understand acute effects of Pmm2 loss on development and disease progression, I have created translational models that mimic the reduced residual enzyme activity of PMM2-CDG patients. I followed two routes to investigate the role of PMM2 on development: establish a conditional knockdown system for acute Pmm2 interference at the protein level and patient-based genetic models by precision genome editing in medaka.

For the conditional knockdown in medaka, I applied an inducible degron system to selectively degrade Pmm2-GFP, mimicking reduced enzyme activity.

To generate patient-based *pmm2* alleles, I used canonical base editing to generate the p.C139R mutation and a deletion variant. Further, I developed and carefully examined a novel two step one-shot base editing approach termed “inception”. Inception introduces a new binding site for a second base editing event that subsequently leads to the anticipated edit. With inception I created one of the common patient mutations p.F119L. Depending on the generated alleles, different *pmm2* variants resulted in varying enzymatic activity in medaka, phenocopied the patient symptoms and caused hypoglycosylation of proteins. Bottom-up proteomics revealed molecular changes already present before the onset of multisystemic phenotypes, affecting particularly mRNA processing and eye development.

Zusammenfassung

Angeborene Stoffwechselkrankheiten, die Proteinglykosylierung betreffen, werden als „Congenital Disorder of Glycosylation“ (CDG) bezeichnet. Dies ist eine Gruppe seltener Erkrankungen, die durch Mutationen in den Enzymen des Glykosylierungsprozesses verursacht werden. Bisher ist kein Mechanismus bekannt, der die Pathogenese der Krankheit erklären kann und therapeutische Optionen sind nur begrenzt verfügbar. Die häufigste Form der CDG wird durch heterozygote hypomorphe Allele des zytosolischen Enzyms Phosphomannomutase 2 (PMM2) verursacht, die bei den Patienten zu einer globalen Hypoglykosylierung der Proteine und einem multisystemischen Phänotyp führen. Mutationen des PMM2 Genes, die zu einem vollständigen Funktionsverlust führen, sind embryonal lethal. Daher liegt nahe, dass überlebende Patienten Mutationen tragen, die zu einer reduzierten Funktionalität von PMM2 führen.

PMM2 spielt eine entscheidende Rolle am Anfang der Glykosylierungskaskade im endoplasmatischen Retikulum, indem es den essenziellen Mannose-Vorläufer für die drei Glykosylierungsprozesse *N*-Glykosylierung, *O*- und *C*-Mannosylierung bereitstellt. Der gesamte Glykosylierungsprozess ist evolutionär hoch konserviert und ermöglicht daher dessen Erforschung in Modellorganismen. Der kleine Teleost Medaka (*Oryzias latipes*) bietet einen großen Vorteil als Modellorganismus, da die frühe Embryogenese durch die extrauterine Entwicklung der Embryonen in transparenten Eischalen untersucht werden kann. Um die akuten Auswirkungen des Pmm2-Verlusts auf die Entwicklung und das Fortschreiten der Krankheit zu verstehen, habe ich translationale Tiermodelle geschaffen, die die reduzierte Restaktivität des Enzyms von PMM2-CDG-Patienten nachahmen. Um die Rolle von PMM2 auf die Entwicklung zu untersuchen, habe ich zwei Ansätze verfolgt: die Etablierung eines induzierbaren Degron-Systems für einen akuten Abbau des Pmm2 Proteins und patientenbasierte genetische Modelle durch präzise Genome-Editierung in Medaka.

Für den gezielten Abbau des Pmm2 Proteins habe ich ein induzierbares System für den akuten Proteinabbau in Medaka angewandt. Dieses erkennt gezielt GFP-markierte Pmm2 Proteine und führt zum Proteinabbau, um die reduzierte Enzymaktivität nachzuahmen.

Zur Erzeugung patientenbasierter *pmm2* Allele verwendete ich etablierte Basen-Editoren, um die Mutation p.C139R und eine Deletionsvariante des Gens zu erzeugen. Darüber hinaus habe ich ein neuartiges zweiteiliges Edit-Verfahren entwickelt und untersucht: den so genannten „Inception“ Ansatz. Bei der Inception wird eine neue Bindungsstelle für ein zweites Editierungsereignis eingeführt, das anschließend zu der erwarteten Veränderung führt. Mit Inception habe ich eine der häufigen Patientenmutationen p.F119L erzeugt. Abhängig von den erzeugten Allelen führten verschiedene *pmm2* Varianten zu unterschiedlicher Enzymaktivität in Medaka, was eine generelle Hypoglykosylierung von Proteinen verursachte und zu den von

Pmm2-CDG Patienten bekannten Symptomen im Fischmodell führte. Bottom-up-Proteomik-Untersuchungen zeigten molekulare Veränderungen, die bereits vor dem Auftreten der multisystemischen Phänotypen vorhanden waren und insbesondere die mRNA-Prozessierung und Augenentwicklung betrafen.

Abbreviations

A	adenine
ABE	adenine base editor
ACEofBASEs	a careful evaluation of base edits
acsl5	*Long-chain-fatty-acid—CoA ligase 5*
AID	auxin-induced degron
Ala	alanine
ALG	Asn linked glycosylation
Asn	asparahine
bact	beta actin
bp	basepair
C	cytosine
Cas9	CRISPR-associated system 9
CBE	cytosine base editor
CDG	Congenital Disorders of Glycosylation
cDNA	complementary DNA
ConA	Concanavalin A
COS	Centre for Organismal Studies
crispant	CRISPR/Cas9 edited embryos
CRISPR	clustered regularly interspaced short palindromic repeats
crk	*Adapter molecule crk*
crRNA	CRSIPR RNA
CUL1	cullin 1
DAPI	4’,6-diamidino-2-phenyindole
DMSO	dimethyl sulfoxide
DNA	deoxyribunuleic acid
dNTP	deoxynucleoside triphosphate
Dol	dolichol
Dol-P	dolichol phosphate
DPAGT1	UDP-N-acetylglucosamine--dolichyl-phosphate N-acetylglucosaminephosphotransferase
dpf	days post fertilization
dph	days post hatch
dpi	days post induction
dpi	days post injection
DSB	double-strand break

E. coli	*Escherichia coli*
E3	ubiquitin ligase
editant	base edited embryos
emc10	*ER Membrane Protein Complex Subunit 10*
ER	endoplasmic reticulum
ERAD	ER-associated protein degradation
ERM	embryo rearing media
EtBr	ethidium bromide
F	generation
F0	injected generation
F1	first generation
F2	second generation
fwd	forward
G	Guanine
GalNac	N-Acetylgalactosamine
gDNA	genomic DNA
GDP	guanosindiphosphat
GFP	green fluorescent protein
GlcA	glucuronic acid
GlcNAc	*N-acetylglucosamine*
Glu	glutamine
GO	Gene Ontology
GOBP	Gene Ontology Biological Processes
GPI	glycosylphosphatidylinositol
h	hours
HDR	homology-directed repair
Het	heterozygous
HF	homology flank
Hom	homozygous
hpf	hours post fertilization
hpi	hours post injection or induction
HRP	horse radish peroxidase
hs	*Homo sapiens (human)*
IAA	Indole-3-acetic acid
IEF	isoelectric focusing
immt	*Inner Membrane Mitochondrial Protein*

Indel	insertion/deletion
INL	inner nuclear layer
IPL	inner plexiform layer
KO	knockout
LC-MS	Liquid Chromatography-Mass Spectrometry
LLO	lipid-linked oligosaccharide
Lys	lysine
mAID	mini auxin-induced degron
Man	mannose
mCherry	monomeric Cherry
mean	mean value
min	minutes
ml	milliliter
mM	millimolar
MPI	mannose phosphate isomerase
mRNA	messenger RNA
MS	mass spectrometry
mucin	mucus glycoprotein
n	Sample number
NAA	naphthaleneacetic acid
ng	nanogram
NHEJ	non-homologous end joining
NTP	nucleotide triphosphate
O/N	overnight
oca2	*Oculocutaneous albinism II*
ol	*Oryzias latipes*
ONL	outher nuclear layer
OST	oligosaccharyltransferase
P	phosphate
PAM	protospacer adjacent motif
PCR	polymerase chain reaction
pegRNA	prime editing guide RNA
PMM2	Phosphomannomutase 2
PNGase F	peptide-N-glycosidase F
PTC	premature termination codon
PTM	post-translational modification

Rbx	ring box 1
rev	reverse
rfc4	*Replication Factor Complex 4*
RFT1	oligosaccharid-Translocationsprotein RFT1 Homolog
RNA	ribonucleic acid
rp2	*Retinitis pigmentose 2*
RPE	retinal pigmented epithelium
rpm	rounds per minute
SCF	SKP1-CUL1-F-Box
sd	standard deviation
SDS-PAGE	sodium dodecyl sulfate polyacrylamide gel electrophoresis
Ser	serine
sgRNA	single guide RNA
SKP1	S-phase kinase associated protein 1
srsf2a	*Serine And Arginine Rich Splicing Factor 2a*
st	developmental stage
T	thymine
TALEN	transcription activator-like effector nuclease
TB	terrific broth
TF	transferrin
Thr	threonine
Tir1	transport inhibitor response 1
tracrRNA	transactivating CRISPR RNA
UPR	unfolded protein response
UTR	untranslated region
WGA	Wheat germ agglutinin
WT	wild-type
x	any amino acid
xCGE-LIF	multiplexed capillary gel electrophoresis with laser-induced fluorescence detection
ZFIN	Zebrafish Information Network
µl	microliter
µM	micromolar
µm	micrometer

Table of contents

1. Introduction

Our lives depend on sugar, not only as a source of energy but as a fundamental building block of glycans. Glycans are composed of multiple monosaccharides and, covalently linked to proteins via glycosylation, they ensure key biological functions in development, growth and survival (Kobata, 1992; Varki, 1993). Any disturbance in the process of glycosylation has severe effects and is caused by genetic mutations that lead to congenital disorders of glycosylation (CDGs). The most common type is PMM2-CDG, caused by mutations in the phosphomannomutase 2 (PMM2) enzyme. The disorder is characterized by a multisystemic phenotype of which the onset and progression are not yet elucidated and currently no cure is available. Patient models which resemble the patients' symptoms are thus required to investigate how glycosylation disorders affect development in vertebrate systems.

1.1 Glycosylation: a key post-translational modification

The glycome is the complete set of all glycans in an organism and is considered more complex than the proteome, transcriptome or genome. This complexity results from the template-free mode of glycan biosynthesis which is not encoded in the genome like DNA or protein sequences (Pothukuchi et al., 2019). The development of techniques to analyze the glycome have shown the dynamics and heterogeneity of glycosylation and have extensively contributed to the growing field of glycobiology (Rudd et al., 2022).

A protein's functionality is connected to its structure. Proteins vary in their size and structure as encoded in the DNA but their essential function is determined by post-translation modifications (PTMs). Over 400 different types of PTMs are known and 200 types are associated with protein function like phosphorylation, acetylation, ubiquitination, methylation or glycosylation (Aebersold, et al. 2018; Deribe, et al. 2010).
Glycosylation is a fundamental co- and post-translational modification (Moremen et al., 2012). It is estimated that 1 to 2 % of the genome encode for enzymes involved in glycosylation (Schachter & Freeze, 2009) and 50 to 70 % of human proteins are predicted to be glycosylated (An et al., 2009a). The enzymatic addition of glycans to proteins is essential in almost every biological process. Glycans affect protein folding, quality control, facilitate trafficking through the secretory pathway to the cell surface and extracellular matrix (ECM), play an important role in biological recognition events and immune regulation (He et al., 2024; Moremen et al., 2012).

The most common form of glycosylation occurs on the cytosolic and luminal side the endoplasmic reticulum (ER) and in the Golgi apparatus (Golgi) (Spiro, 2002). There are three types of glycosylation which differ by the glycosidic linkage of the glycan to the amino acids: *N*-glycosylation, *O*-glycosylation (*O*-linked *N*-Acetylgalactosamine (GalNac) or *O*-mannosylation) and *C*-mannosylation (Schjoldager et al., 2020).

1.2 *N*-Glycosylation pathway

N-glycosylation the most common type and highly conserved across all eukaryotes (Aebi, 2013). During *N*-glycosylation the glycans are covalently transferred to the nitrogen (N) of the amino group of asparagine (Asn) (Varki et al., 2022). Asn has to be present within an *N*-glycan motif called sequon which is Asn-X-Ser/Thr, X being any amino acid expect for proline and Ser/Thr being serine and threonine (Bause & Hettkamp, 1979; Zielinska et al., 2010). Not every sequon present will be glycosylated but studies have shown that *N*-glycosylation sites are conserved across species likely due to their essential function (Park & Zhang, 2011).

The process of *N*-linked glycosylation is initiated on the cytoplasmic side of the ER by the assembly of a lipid-linked oligosaccharide (LLO) and stepwise addition of single sugars catalyzed by individual asparagine linked glycosylation (ALG) enzymes (Breitling & Aebi, 2013) (Figure 1). In the first step dolichol phosphate (Dol-P) receives *N*-acetylglucosamine-1-phosphate (GlcNAc-1-P) by the glycosyltransferase DAPGT1 and consecutively ALG13/14 transfers one more GlcNAc. ALG1, ALG2 and ALG11 elongate Dol-P-P-GlcNAc2 further by transfer of five mannoses to obtain Dol-P-P-GlcNAc2Man5. This intermediate LLO is translocated by the flippase RFT1 into the ER lumen where it is extended with four mannoses via ALG3, ALG9 and ALG12. The last steps consist the attachment of three glucoses catalyzed by ALG6, ALG8 and ALG10 to generate Dol-P-P-GlcNAc2Man9Glc3 (Helenius & Aebi, 2004). This glycan is transferred to the *N*-glycan sequon of nascent proteins by the oligosaccharyltransferase complex (OST) (Schwarz & Aebi, 2011). The chaperones calnexin and calreticulin assist in protein folding while glucosidases and mannosidases remove three glucoses and one mannose, respectively, before maturation of the glycoproteins continue in the Golgi (Kozlov & Gehring, 2020). Some glycoproteins “escape” Golgi processing and make up the class of high-mannose *N*-glycoproteins (Stanley, 2011). Before leaving the ER to the Golgi, the glycoproteins undergo quality control to prevent misfolded proteins from accumulating inside the ER. Misfolded proteins are identified and two mannoses are cleaved off to enable recognition for export to get ubiquitinated and targeted for degradation by the proteasome (Helenius & Aebi, 2004).

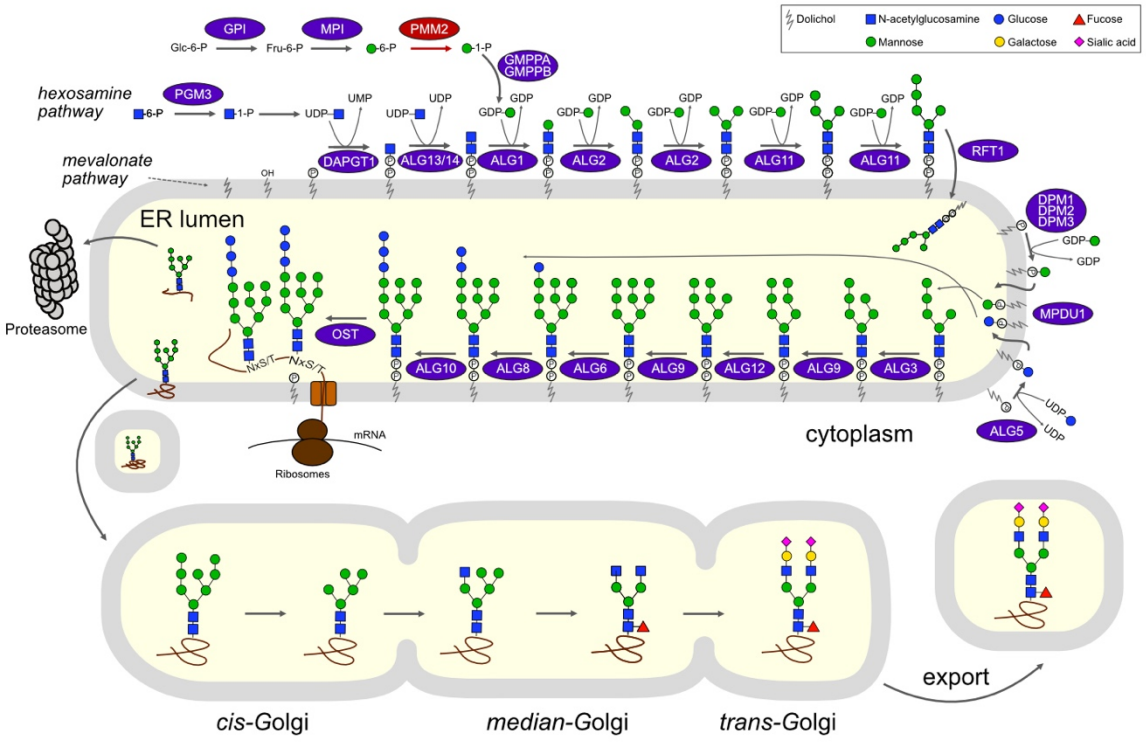

Figure 1: Schematic representation of *N*-Glycosylation in the endoplasmic reticulum and Golgi apparatus. In the ER Dol-P-P-GlcNAc2Man9Glc3 is generated via the sequential attachment of *N*-acetylglycosamines and mannoses to dolichol-phosphate to form a lipid-linked oligosaccharide (LLO). The LLO is translocated into the endoplasmic reticulum (ER) lumen via a flippase where additional mannoses and glucoses are attached. Oligosaccharyltransferases (OSTs) catalyze the transfer of the glycan to asparagine residues of nascent proteins within the motif NxS/T. The glycan undergoes trimming and addition of further nucleotide sugars in the Golgi apparatus giving rise to hybrid and complex *N*-glycans. Figure adapted from Varki et al., 2022 (Essentials in Biology Figure 9.3 and 9.4.) N, asparagine; S, serine; T, threonine; X, any amino acid except Proline

N-glycans play an essential role during folding of the proteins by changing the physical properties and making the protein soluble (Suzuki et al., 2022). Processed glycans undergo several steps of mannose removal in the *cis*-Golgi and GlcNAc addition on the *medial*-Golgi to create the precursor for complex and hybrid *N*-glycans (Stanley, 2011). Hybrid *N*-glycans contain five mannoses and one arm with GlcNAc will be further extended with the sugars galactose and sialic acid in the *trans*-Golgi. Complex *N*-glycans are further trimmed by two mannoses and receive additional sugars on both GlcNAc arms in the *trans*-Golgi. These sugars can consist of galactose, GlcNAc, GalNAc, fucose and/or sialic acid. The three types of *N*-glycans, high-mannose, complex and hybrid, and the numerous varieties of complex types during the maturation in the *trans*-Golgi create a multifaceted diversity of *N*-glycoproteins (Stanley et al., 2022).

For the synthesis of the mature *N*-glycan in the ER, multiple sugar donors act as a substrate for the enzymes involved in glycosylation. The hexosamine biosynthesis

pathway plays a central role in synthesizing the activated sugars UDP-GlcNAc, GDP-Man and UDP-Glc. UDP-GlcNAc is needed in the cytosol as substrate for DPAGT1 and ALG13/ALG14. GDP-Man is a substrate for ALGs assembling Man1-Man5 structures on the cytosolic side. Moreover, GDP-Man and UDP-Glc are transferred to Dol-P before flipping into the ER to provide mannose and glucose for the ALGs in the ER lumen.

Due to the non-template driven synthesis of glycans and its complex structures, glycosylation is less well understood than other forms of PTMs. In recent years more studies have been performed to understand the microheterogeneity of glycosylation, for example how distinct *N*-glycan sites can contain different types of glycans (Kellman et al., 2024). In sum, multiple sequons containing different glycans account for thousands of possible proteins which explains the challenge to analyze them compared to proteomics (An et al., 2009b).

1.3 Congenital Disorders of Glycosylation (CDGs)

Glycosylation is a precisely coordinated and regulated process involving over hundreds of enzymes. It plays a vital role in organismal development and if affected, the consequences can be fatal (Haltiwanger and Lowe 2004; Reily, et al. 2019). Enzymes involved in glycosylation can harbor mutations causing CDGs, autoimmune diseases, inflammatory diseases as well as cancer (Reily et al., 2019). CDG is a metabolic disorder first described by Jaak Jaeken in 1980 (Jaeken, 2013). Since then, CDGs are a rapidly growing group of rare and complex genetic diseases with over 160 subtypes identified up to date (Weixel et al., 2024). The different CDG types are named after the affected gene and the suffix “-CDG” (Jaeken et al., 2009). Due to the large number of different subtypes of CDGs, the phenotypic variability among patients represents a broad spectrum. Patients mostly suffer from a multisystemic disease with clinical features including neurological manifestations (Freeze et al., 2015), liver involvement (Marques-da-Silva et al., 2017), heart diseases (Footitt et al., 2009), eye abnormalities and aberrant skeletal phenotypes (Francisco et al., 2019).

The phenotypic spectrum and sum of different genetic types of CDGs makes patient diagnosis challenging. The gold standard is to test the isoelectric focusing (IEF) of transferrin (Jaeken et al., 1984). Transferrin is a known glycoprotein containing two biantennary sialylated complex types of glycans which can vary in their composition leading to forms of different charge in the natural condition. IEF can point towards defects in the ER and Golgi due to changes in the charge of the transferrin glycans upon complete absence or truncations. For faster processing and quantification of the different forms,

techniques like capillary zone electrophoreses (CZE) and high performance liquid chromatography (HPLC) have been developed (Carchon et al., 2004). These days, mass spectrometry-based diagnostics are used to analyze glycan structures from plasma of patients (van Scherpenzeel et al., 2015). Upon abnormalities, further diagnostic tools include enzyme assays for specific subtypes and whole exome sequencing, where only the protein-coding regions of the genome are analyzed.

There are specific CDG syndromes which benefit from supplementation with sugars (Quelhas & Jaeken, 2024). Patients with MPI-CDG benefit from supplementation with Mannose (Niehues et al., 1998) while GFUS-CDG patients respond to Fucose supplementation (Feichtinger et al., 2021) and patients with SLC35A2-CDG together with PGM1-CDG receive Galactose supplementation (Wong et al., 2017).

1.4 Phosphomannomutase 2 and PMM2-CDG

The most common type of CDG is caused by mutations in the *Phosphomannomutase 2* (*PMM2*) gene (Ng et al., 2024). PMM2-CDG patients suffer from a multiorgan phenotype which is most prominent in neural and musculoskeletal tissues and associated with mental retardation. The symptoms include, among others: hypotonia, seizure, ataxia, uneven fat distribution, underdeveloped cerebellum, strabismus, hepatomegaly, cardiomyopathy and fluid around the heart as well as blood clotting disorders (Sparks and Krasnewich 2005).

The age of diagnosis of patients in a French population ranged from neonatal to 31 years (Piedade et al., 2022). In studies examining multiple cohorts, the calculated age at diagnosis was different for patients born before and after 1995. Patients born before 1995 were diagnosed at age of 13.4 ± 4.3 years (range of 6-21 years) and patients born after 1995 at the age of 2.3 ± 2.4 years (range of 0.08-10 years) (Pérez-Cerdá et al., 2017). Nowadays, PMM2-CDG patients are diagnosed within the first years of life following a healthy pregnancy and birth without complications (Pérez-Cerdá et al., 2017; M. Vals et al., 2017).

Approximately 2447 patients have been reported to carry PMM2, but the calculated prevalence of 1:63.694 predicts the number of unreported and undiagnosed cases to be much higher than the observed prevalence (Edmondson, Honzík, et al., 2025).

PMM2 is ubiquitously expressed across all tissues. It is a cytosolic enzyme and acts at the basis of ER-glycosylation by converting mannose-6-phosphate (Man-6-P) to mannose-1-phosphate (Man-1-P) which is the precursor of the activated sugar donor GDP-mannose. GDP-mannose is needed for *N*-glycosylation, *C*- and *O*-mannosylation and GPI anchor biosynthesis (Sharma et al., 2014) (Figure 1).

Mutations in PMM2 result in reduced enzyme activities and primarily cause global protein hypo-*N*-glycosylation (Pajusalu et al., 2024) due to reduced GDP-mannose levels (Rush et al., 2000). To date, there are 183 different *Pmm2* alleles identified as disease-causing (Edmondson, Honzík, et al., 2025). Patients mostly carry compound heterozygous mutations with the most common variants being PMM2 p.R141H, p.P113L and p.F119L (Jaeken & Matthijs, 2001; Pajusalu et al., 2024). Usually, one allele completely lacks enzyme activity, like seen with the well characterized R141H null allele, and the second allele often retains residual activity (Kjaergaard et al., 1999). Complete loss of function mutations are considered not compatible with life as knockout mice showed embryonic lethality (Thiel et al., 2006) and homozygous PMM2 p.R141H patients have never been reported (Matthijs et al., 1998). Severe PMM2 variants showed activity levels below 10 %, whereas in milder forms higher activity levels were measured (Westphal et al., 2001a). The heterozygous parents are healthy suggesting a crucial threshold level of 50 % enzyme activity for PMM2 to not develop any symptoms (Giurgea et al., 2005; Iyer et al., 2019).
The structure of PMM2 consists of 28 kDa monomers that form homodimers through interaction via a hydrophobic core (Silvaggi et al., 2006). Each subunit contains two domains, the core and the cap domain, connected through a linker. The dimerization is essential for proper enzymatic activity and pathogenic mutations disrupt this interaction (Quental et al., 2010; Yuste-Checa et al., 2015). Upon binding to its ligand glucose-1,6-bisphosphate the conformation changes and the core and cap domain are brought in closer proximity for catalytic activation (Andreotti et al., 2014). Structural predictions described a functional impact of missense variants on ligand binding, catalysis, dimerization, domain folding (cap and core), and linker flexibility (Briso-Montiano et al., 2022).

1.5 Therapeutical options for PMM2-CDG patients

Finding therapeutical options for PMM2-CDG patients has been a major focus of research as it is the most prevalent type of CDG with no specific treatments available. To improve the glycosylation defects resulting from reduced enzyme activity of PMM2 one of the first proposed supplementations to treat PMM2-CDG was oral mannose ingestion (Körner et al., 1998). Patient-derived fibroblasts are obtained from skin biopsy samples and commonly used as disease PMM2-CDG models. Biochemical validation showed improvements in patient-derived fibroblasts treated with mannose (Rush et al., 2000).
Supplementation of mannose in pregnant mice rescued early lethality reported from *Pmm2* mutants (Schneider et al., 2012). However, benefits of mannose supplementation in patients are debated due to reported spontaneous improvements in transferrin

glycosylation state in PMM2-CDG patients without mannose supplementation as well (Taday et al., 2020; Witters et al., 2021).

As PMM2 mutations affect protein stability, pharmacological chaperones were suggested to improve mutant PMM2 stability by preventing its degradation and improving folding (Yuste-Checa et al., 2017). Instead of screening for potential pharmacological compounds the natural ligand glucose-1,6-bisphosphate of PMM2 was proposed as an alternative to stabilize mutant PMM2 variants (Monticelli et al., 2019). Moreover, proteostasis regulators were shown to increase PMM2 activity and stability (Vilas et al., 2020).

Other therapeutical options mainly focus on treating symptoms of patients. Acetazolamide was tested as a potential treatment for neurological symptoms like ataxia and stroke-like episodes (Martínez-Monseny et al., 2019). Furthermore, elevated sorbitol levels were found in urine samples of patients (Ligezka et al., 2021). Sorbitol is converted from glucose by the enzyme aldose reductase. Epalrestat, an aldose reductase inhibitor, was repurposed as a drug and confirmed potential as an activator of enzyme activity of frequent PMM2 variants (Iyer et al., 2019). Inhibition of the aldose reductase with Epalrestat showed improvements measured by increased GDP-mannose levels in patient fibroblasts and a *pmm2* zebrafish model, and biochemical improvements of common biomarkers in patients (Radenkovic et al., 2023). Currently Epalrestat is involved in a clinical trial (Maggie's Pearl, 2022).

The most promising therapeutic approach to date is to provide Mannose-1-Phosphate directly in liposome-encapsulated cargos (GLM101). Studies in patient derived fibroblasts have shown improvements in glycosylation as an increase in high mannose and complex/hybrid glycan structures was measured (Budhraja et al., 2024; Shirakura et al., 2024). Clinical trials in Phase 2 are ongoing for GLM101 as a targeted therapy for patients (Glycomine, 2022).

1.6 Challenges in PMM2-CDG research and current animal models

Disease models are crucial to investigate the pathophysiology of glycosylation disorders since there is no conclusive pathogenic mechanism linked to PMM2-CDG. The observed developmental defects in patients are caused by reduced PMM2 enzyme activity that results in hypoglycosylation of proteins (Freeze, 2009). Various studies on models established using cell lines and patient derived fibroblasts have already provided the basis for understanding the consequences of a reduced PMM2 activity (Budhraja et al., 2024; Gallego et al., 2024; Himmelreich et al., 2023; Radenkovic et al., 2023; Thiesler et al., 2016; Vilas et al., 2024). Despite these advances in PMM2-CDG research our understanding of the pathophysiology of this rare genetic disorder remains limited.

The entire *N*-glycosylation machinery and PMM2 are evolutionarily highly conserved across eukaryotes which allows generation of translational model organisms to study the human disease (Aebi, 2013; Peng et al., 2020). Importantly, as the patients suffer from a multisystemic phenotype, it is desirable to have animal models which displays all features of the diseases from internal organ involvement to behavioral and neurological disorders. Multiple efforts have been made to generate PMM2-CDG vertebrate animal models but establishing them has proven challenging. Knockout of *Pmm2* in mice and a compound heterozygous *Pmm2* mouse model resulted in embryonic lethality (Schneider et al., 2012; Thiel et al., 2006). A third mouse model carrying the equivalent alleles of PMM2 p.R141H/p.F119L mutations showed only 50 % survival (Chan et al., 2016). Recently two new mouse models were generated with a brain specific conditional knockout of *Pmm2* and ubiquitously inducible knockout of *Pmm2* to model the neurological manifestation of the disease (Edmondson et al., 2025; Zhong & Lai, 2025). Besides mice, morpholino-based models have been generated in zebrafish (Cline et al., 2012) and frog (Himmelreich et al., 2015). Morpholinos sterically block translation by binding to target mRNAs but these approaches lack the specificity of knockdown effects and provide only a transient loss of Pmm2 activity. Genetic zebrafish models carrying the same splice site mutation exhibited craniofacial and motility defects in one study while in another study no morphological defects were noted (Klaver et al., 2021; Mukaigasa et al., 2018).

Taken together, a genetic compound heterozygous viable vertebrate animal model showing all features of the disease is not available. Additionally, none of the existing models allow to study the early effects of loss of PMM2 nor assessing the onset of disease.

1.7 Medaka as potential model organism for PMM2-CDG

PMM2-CDG is primarily a physiological disorder with developmental consequences which highlights the importance of early interventions. To develop therapeutic strategies, studying effects of acute loss of PMM2 during early development and understanding how hypoglycosylation contributes to disease progression is essential. A major limitation is the lack of viable vertebrate animal models carrying compound heterozygous mutations and fully recapitulating the human disease phenotype.

The teleost medaka (*Oryzias latipes*) serves as a well-established small vertebrate model organism to study human diseases and gene functions in a vertebrate system (Doering et al., 2023; Hammouda et al., 2021). A specific feature of medaka is the extrauterine development and transparency of the embryos which allows to study the embryonic development (Wittbrodt et al., 2002). Previously, a model for Alg2-CDG was established in medaka which resembled patient phenotypes caused by hypo-*N*-glycosylation (Gücüm

et al., 2021). Compared to zebrafish, medaka benefit from a smaller genome with less duplicated gene duplications and the embryos and adults tolerate a wider temperature range from 4°C to 40°C (Furutani-Seiki & Wittbrodt, 2004). Moreover, isogeneity in medaka is higher as they are tolerant to inbreeding (Kirchmaier et al., 2015) which makes it suitable for modeling genetic diseases. Zebrafish are less isogenic and it was seen that the splice acceptor *pmm2* mutants showed different phenotypic outcomes possibly due to the genetic background.

Overall, medaka offers great benefits as a vertebrate animal model to study the effects of Pmm2 deficiencies with reduced enzyme activities to model the human disease.

1.8 Genetic tools to study gene and protein function *in vivo*

To investigate the function of a gene or protein of interest on biological processes, multiple tools inducing loss-of-function are available for animal models. Commonly used methods include manipulations on DNA and RNA level by mutagenesis, Clustered regularly interspaced short palindromic repeats (CRISPR) / CRISPR-associated protein (Cas9)-based editing, RNA interference or morpholinos. Moreover, pharmacological inhibitors and protein depletion systems (degrons) can be used to disrupt protein levels (Housden, et al. 2017). In the case of *Pmm2,* genetic modifications of *Pmm2* most closely resemble the patient situation but lowering the protein levels could be an alternative approach in reducing net enzyme activity regardless of genetic mutations. The latter could constitute a model system which covers the general outcome of multiple variants in patients.

1.8.1 Targeted protein degradation systems

Due to the possibility to manipulate endogenous protein levels conditionally via nanobody-based degron systems, targeted degradation of proteins *in vivo* using degron systems is suitable for manipulation of protein levels at specific stages during development.

Degron-based systems allow to degrade proteins in a precise and inducible manner via the ubiquitin proteasome pathway. Auxin-inducible degron (AID) systems are able to target tagged proteins for degradation by recruiting an E3 ubiquitin ligase complex. The exogenously expressed plant F-box protein TIR1 (transport inhibitor response 1) interacts with AID-tagged proteins upon addition of the plant hormone auxin (Nishimura et al., 2009). Tir1 forms a complex with the tagged protein and is recruited to the endogenous Skp1–Cul1–F-box (SCF) E3 ligase complex. This results in ubiquitination and proteasomal degradation of the target protein (Figure 2 A).

As the canonical TIR1 protein harbors basal degradation activity even without auxin induction (Natsume et al., 2016), TIR1 F-box variants have been created to overcome the leakiness (Nishimura et al., 2020; Yesbolatova et al., 2020). Another drawback is the requirement to fuse the AID-tag endogenously to the protein-of-interest. To gain flexibility, already available proteins tagged with GFP can be degraded by using a specific GFP-nanobody (vhhGFP4) (Caussinus et al., 2011; Caussinus & Affolter, 2016) which is fused to the minimized mAID-tag (Daniel et al., 2018). Successful degradation is additionally visible due to the loss of fluorescence by degradation of the GFP-tagged protein-of-interest upon induction. Notably, this system was found to show strong basal activity without induction in medaka (Pakari et al., 2025), but the improved AID2-based degron system with a Tir1F74G variant has been reported to efficiently degrade mAID tagged proteins in medaka (Kiyomitsu et al., 2024).

A transgenic medaka line in which the endogenous *pmm2* is tagged with a C-terminal *GFP* was previously generated and validated (Gücüm, 2021; Pakari, 2021; Pakari et al., 2025) (Figure 2 B, C). To study the acute effects of Pmm2 loss in the early stages of development, the deGradFP system in combination with Tir1 variants without basal activity renders suitable to reduce Pmm2 abundance in the established Pmm2-GFP medaka line.

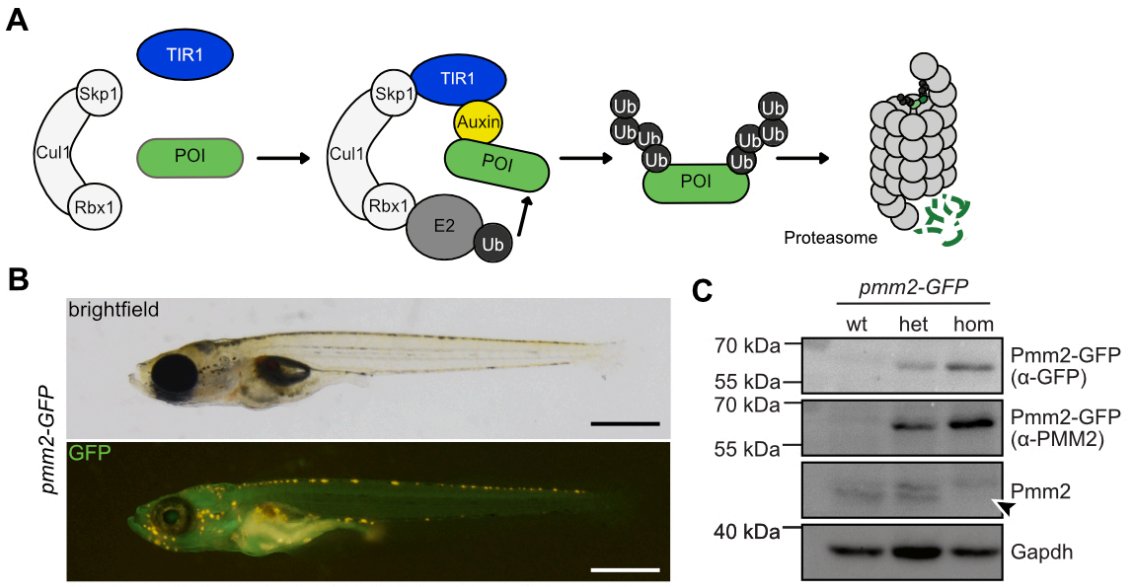

Figure 2: Inducible degron system for the use in Pmm2-GFP tagged medaka line. A) Illustration of auxin-inducible degron systems. Upon induction with auxin, the Fbox protein Tir1 and mAID tagged protein-of-interest (POI) dimerize and recruit the E3 ubiquitin ligase complex SCF (Skp1, Cul1, Rbx1 and F-box protein) which binds E2 and transfers ubiquitin and degrades the POI by the proteasome. B) Brightfield and fluorescent images of a homozygous *pmm2-GFP* tagged medaka line. Scale bar 500 µm. C) Western blot analysis reveals full tagging of homozygous *pmm2-GFP* line using antibodies against PMM2, GFP and GAPDH as loading control. Arrow indicates absence of endogenous Pmm2 band in homozygous versus wild-type (wt) and heterozygous (het) hatchlings. Figure adapted from (Pakari et al., 2025)

1.8.2 CRISPR/Cas9 based systems in medaka

To generate genetic animal models which precisely reconstitute the allele variants of the human PMM2-CDG cases, precise genome editing tools are necessary.

CRISPR/Cas9 systems revolutionized the gene editing field by allowing to edit the genome in a cheap and flexible manner (Cho et al., 2013; Cong et al., 2013; Jinek et al., 2013; Mali et al., 2013; Pacesa et al., 2024). The systems consist of a Cas9 endonuclease from *Streptococcus pyogenes* (SpyCas9) and a guide RNA that guides the complex to a genomic target site sequence next to a protospacer adjacent motif (PAM) which comprises the three nucleotides NGG for the commonly used SpyCas9. The guide RNA consists of a CRISPR RNA (crRNA) and transactivating RNA (tracrRNA) which pair and form a complex with Cas9 (Jinek et al., 2012). The complex searches for its target site, binds to the PAM motif, unwinds the double stranded DNA and after successful base-matching, Cas9 cuts 3 base pairs upstream of the PAM. The induced double-strand breaks (DSBs) are repaired by endogenous DNA repair pathways like non-homologous end (NHEJ) and cause unpredictable mutations due to small insertions or deletions (indels) during the repair process (Xue & Greene, 2021). Alternatively, the DSB is repaired by homology-directed repair (HDR) which creates precise but low efficiency editing by providing a repair donor DNA template (Xue & Greene, 2021) (Figure 3 A).

In recent years the need for efficiently generating precise point mutations led to the development of more refined tools, such as base editors and prime editors. Base editors consist of modified Cas variants that install single-nucleotide conversions at target sites without generating DSBs or requiring donor templates and only by nicking the DNA (Gaudelli et al., 2017; Komor et al., 2016). A Cas9 D10A nickase is attached to a deaminase which can introduce precise changes in a specific distance from the PAM motif, minimizing off-target and indels outcomes. The changes occur in a base editing window typically 13-17 nucleotides upstream of the PAM. Available base editors are cytosine base editors (CBE) that convert C-to-T (cytosine to thymine) and adenine base editors (ABE) converting A-to-G (adenosine to guanine) (Gaudelli et al., 2017; Komor et al., 2016). Highly efficient variants have been developed (Richter et al., 2020) and established for the use in medaka (Cornean et al., 2022) (Figure 3 B).

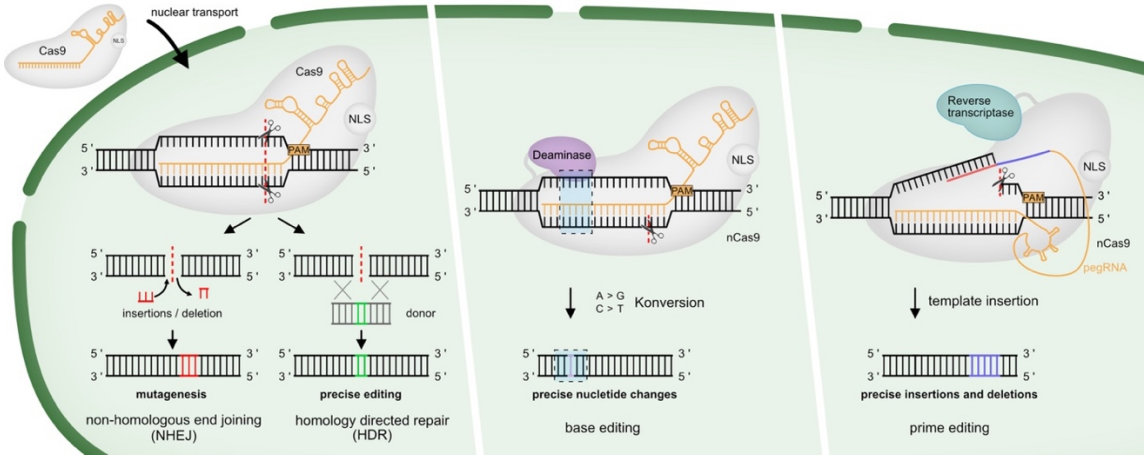

Figure 3: CRISPR/Cas9 based genome editing tools to create precise point mutations. A) After nuclear localization, the Cas9 enzyme is guided to a specific target site by a guide RNA (sgRNA). Cas9 introduces a double strand break upstream of a protospacer adjacent motif (PAM). Endogenous cell repair mechanisms non-homologous end joining (NHEJ) or homology directed repair (HDR) repair the breaks. B) Base editors only nick double stranded DNA and use a deaminase to convert specific nucleotides from A-to-G or C-to-T. C) Prime editors also contain a Cas9 nickase fused to a reverse transcriptase (RT). The prime editing guide RNA (pegRNA) contains the single-guide RNA (sgRNA) that directs the complex to the target site, but also a primer binding site and a template sequence. This template allows the RT to synthesize the desired DNA sequence directly at the target location. PAM, protospacer adjacent motif Adapted from (Pakari et al., 2023a)

Prime editing (PE) combines a Cas9 nickase with a reverse transcriptase and a prime editing guide RNA (pegRNA) to install a wide variety of genetic changes, including insertions and deletions (P. J. Chen & Liu, 2023) (Figure 3 C). At the timepoint of conducting this thesis, the understanding of the delicate design of pegRNAs and their properties for targeted modifications in medaka is limited. The to date low editing efficiencies are the main the bottleneck (personal communication, Thomas Thumberger). These advancements with CRISPR/Cas9 based approaches have expanded the toolkit by development of versatile tools for functional genomics and disease modeling, offering increasingly precise and programmable methods for generation of specific point mutations.

However, not all patient-specific mutations can be introduced into model organisms as either the conversion of the available to the desired nucleotide is not possible or because the position of the specific nucleotide cannot be reached if no PAM motif is available in proper distance.

Aims and objectives

PMM2-CDGs are rare physiological disorders caused by disrupted *N*-glycosylation due to reduced PMM2 enzyme activity and manifest with multisystemic developmental consequences after birth. To date, no conclusive pathogenic mechanisms have been described and no curative treatments are available since compensating for physiological effects after birth can only treat the symptoms. Given the essential role of PMM2 in development, *in vivo* models allowing to study early and acute loss of PMM2 activity and effects of hypomorphic genetic mutations during development are crucial to understand the onset of the disease. Given the high conservation of the glycosylation machinery, I hypothesize that reduced Pmm2 levels as well as genetic mutations in medaka *pmm2* will lead to phenotypes reminiscent of PMM2-CDG patients. These models will serve to dissect the onset and progression of the disease in a developing vertebrate context. I aim to mimic the reduced enzyme activity of PMM2-CDG patients in medaka fish using two approaches: directly reducing Pmm2 protein abundance and modifying the enzyme activity genetically.

(1) Generation of a hypo-glycosylation PMM2-CDG medaka model by ubiquitous conditional knockdown of Pmm2

To study the acute effects of Pmm2 knockdown during the early stages of development, I aim to establish a conditional and ubiquitous knockdown approach in medaka. By reducing Pmm2 protein abundance, I aim to mimic decreased enzyme activity to induce hypoglycosylation for investigating its acute effects on early embryonic development.

(2) Generation and characterization of a hypomorphic Pmm2-CDG medaka model by genetically modified enzymes which reduce Pmm2 enzyme activity using the CRISPR/Cas9 toolbox

Using CRISPR/Cas9-based genetic approaches, I aim to introduce patient-based *pmm2* mutations in medaka to characterize emerging phenotypes. To gain insights into the pathophysiology of PMM2-CDG, I focus on defects in *N*-glycosylation to explore how Pmm2 mutations affect glycan synthesis and assess rescue approaches by supplements or providing *Pmm2* mRNA. I am to investigate the early onset and progression of disease on a molecular level using proteomics analysis.

2. Results

In this thesis, I aim to model human PMM2-CDG in medaka fish. The first part introduces a technical approach to reduce Pmm2 enzyme activity using a degron system for manipulation of Pmm2 protein levels. The second part focusses on a genetic approach to circumvent local constraints of base editing to establish patient specific mutations in genomic regions which are inaccessible for base editing. In the final part, I demonstrate the generation and characterization of a patient-based genetic model to investigate the onset of Pmm2-CDG disease progression.
Contributors to parts of the thesis are directly named in the text (detailed list, see Contributions).

2.1 An inducible degron system for the use in medaka to reduce Pmm2 abundance during early embryogenesis

To induce acute protein knockdown of Pmm2 with degron systems, I established a non-leaky degron system in medaka to degrade GFP-tagged fusion proteins during early embryogenesis. The goal was to mimic the reduced Pmm2 enzyme activity reported from PMM2-CDG patients via acute, inducible degradation of the Pmm2 protein in a previously generated Pmm2-GFP line.
Parts of the text and selected figures have been adapted from the submitted preprint Pakari et al., 2025. This publication is based on the initial work conducted during Sevinc Gücüms PhD thesis (Gücüm, 2021), my Master's thesis (Pakari, 2021) and was completed with work conducted in this PhD thesis.

2.1.1 Improved TIR1(F74G)/mAID-GFP nanobody degron system offers efficient inducible Pmm2-GFP knockdown

Former studies revealed strong basal activity (degradation addition of auxin) of the auxin inducible mAID-nanobody degradation in medaka (Pakari, 2021; Pakari et al., 2025).
To overcome this issue, I turned to an improved degron system in which a point mutation was introduced into the TIR1 sequence to enhance the binding affinity to the inducer ligand and decreases leaky degradation (Yesbolatova et al., 2020). The combination of the F-box protein variant TIR1(F74G) with the mAID/GFP-nanobody could be used to target Pmm2-GFP for ubiquitination and proteasomal degradation. TIR1(F74G) interacts with the mAID/GFP-nanobody upon addition of the inducer 5-Ph-IAA, and recruits Pmm2-GFP to the endogenous Skp1–Cul1–F-box (SCF) E3 ligase complex and results in ubiquitination

and degradation of the tagged protein by the proteasome (Figure 4 A). This modified system could potentially alleviate leaky degradation enable inducible acute knockdown of Pmm2.

To test the applicability of this system in medaka, I first tested for potential toxic effects of the auxin analog 5-Ph-IAA. For the analysis, wild-type embryos were incubated in different 5-Ph-IAA concentrations and their phenotypes were assessed 4 days post fertilization (dpf) and at hatch to evaluate potential toxic effects (Supplementary Figure 1 A, B). The auxin analog can be used at very low concentrations (1–5 µM) for induction according to literature (Yesbolatova et al., 2020). At these concentrations no toxic effect of the auxin analog exposure was visible. Therefore, I selected 5 µM as standard concentration for subsequent experiments.

Next, to assess functionality of the improved degron system in medaka to degrade transiently expressed cytosolic GFP, I injected the mRNA of *GFP* and the degron components (*TIR1(F74G)* and *mAID-GFP-nanobody*) as well as the injection tracer *mCherry* into 1-cell stage wild-type medaka embryos (Figure 4 B). The injected embryos were screened for GFP and mCherry fluorescence, which represents the presence and translation of the degron components. The double-positive embryos were divided into two groups: control (kept in ERM) and experimental (induced with 5 µM 5-Ph-IAA 8 hours post fertilization (hpf)). In cell culture, degradation occurs within minutes but in a mouse model degradation took up to 24 hours (Yesbolatova et al., 2020). Hence, GFP and mCherry fluorescence was acquired before induction and 1 day after induction with 5-Ph-IAA. A clear reduction in GFP fluorescence was observed in the experimental group and no loss of GFP signal was visible in the control group (Figure 4 C).
These results show, that the improved degron system in combination with the GFP-nanobody is functional in medaka. It is capable of degrading transiently expressed cytosolic GFP upon transient degron system expression and after induction with the auxin analog 5-Ph-IAA. This serves as proof of principle for the effective use of the system in medaka.

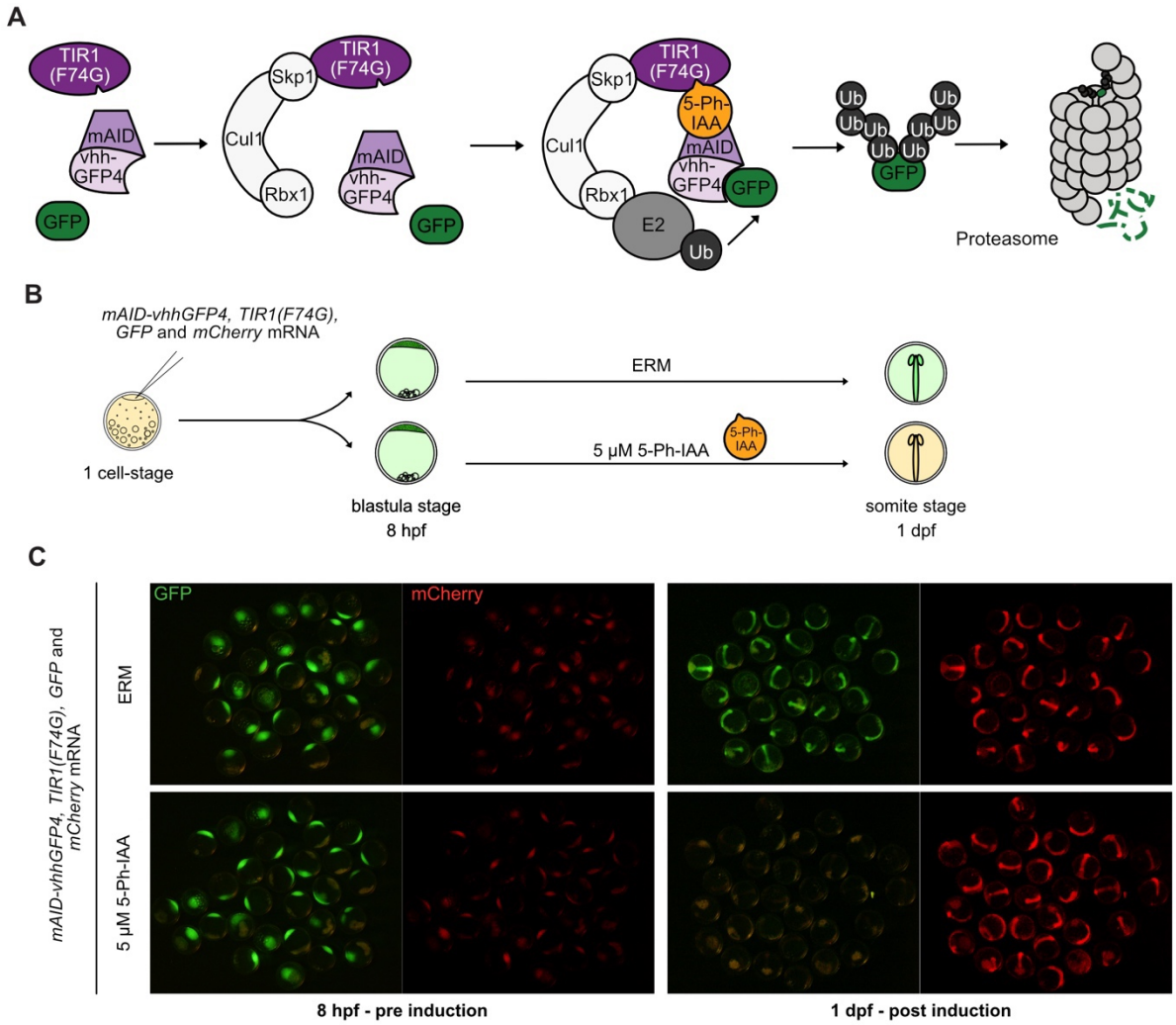

Figure 4: Transient expression of TIR1(F74G) together with the mAID/GFP nanobody as degron system allows to degrade cytosolic GFP. A) Graphical illustration of TIR1(F74G) and mAID/GFP-nanobody (vhhGFP4) based degron system (Daniel et al., 2018; Yesbolatova et al., 2020) to degrade GFP in an auxin-analog (5-Ph-IAA) inducible manner. Transiently expressed F-Box protein TIR1(F74G) and mAID-vhhGFP4 nanobody recruit endogenously expressed SCF complex (Skp1, Cul1, Rbx1) upon addition of auxin, causing ubiquitination and degradation of GFP by the proteasome. B) Workflow of injection to test functionality of improved degron system in medaka to degrade transiently expressed cytosolic GFP. 1-cell stage wild-type embryos were injected with *GFP*, *mCherry* and degron components (*TIR1(F74G)* and *mAID-vhhGFP4*) mRNA. 8 hpf embryos were screened for green fluorescence and induced with 5 µM 5-Ph-IAA or kept in ERM. 1 dpf embryos were screened for GFP fluorescence again. C) Fluorescence images of wild-type Cab embryos injected with *GFP*, *mCherry* and degron components (*TIR1(F74G)* and *mAID-vhhGFP4*) mRNA before and after induction with 5 µM 5-Ph-IAA at 8 hpf or kept in ERM as a control. dpf, days post fertilization; ERM, embryo rearing media; hpf, hour post fertilization; 5-Ph-IAA, auxin analog. Panel A adjusted from Pakari et al., 2025.

To assess the applicability of the degron system to degrade stably and endogenously expressed GFP fusion proteins (Figure 5 A), I injected the degron components (*TIR1(F74G)* and *mAID-GFP-nanobody)* as mRNA together with *mCherry* as injection tracer into homozygous *pmm2-GFP* 1-cell stage embryos. The injected embryos were induced with 5 µM 5-Ph-IAA and incubated with vehicle (ERM with 0.007 % DMSO). As

the auxin analog is dissolved in DMSO, to control group was treated with the same DMSO amount. At 6 hpf, the treated group was induced with 5-Ph-IAA and the expression of GFP together with tracer mCherry was acquired by time-lapse imaging over 26 hours (Figure 5 B).

The GFP-signal in the non-injected and untreated degron injected *pmm2-GFP* embryos remained visible over time. In the treated embryos, induction with 5 µM 5-Ph-IAA caused reduction of GFP signal. Interestingly, even degradation of maternally contributed Pmm2-GFP occurred in the yolk of degron-injected and induced embryos (Figure 5 B, white arrow).

Analysis of the kinetics of the Pmm2-GFP depletion revealed no basal (non-induced) degradation of GFP (Figure 5 C, purple curve). In the treated group an immediate decrease in GFP signal was visible after induction and plateaued at around 30 hours post induction. To estimate the degradation rate, the half-life of Pmm2-GFP was calculated to be 6.9 hours based on fitted decay curves (Supplementary Figure 1 C).

To confirm that reduction in GFP fluorescence actually corresponds to degradation of the Pmm2 enzyme, an established biochemical Pmm2 enzyme activity assay from lysates of stage 23 embryos was performed in collaboration with Virginia Geiger (Thiel Lab, Heidelberg University Hospital). The assay confirmed successful reduction in Pmm2 net activity to below 50 % in the degron injected and 5 µM 5-Ph-IAA induced embryos (Figure 5 D).

These findings show that the TIR1(F74G) variant together with the mAID-GFP-nanobody enables efficient knockdown of endogenously expressed and maternally contributed GFP-tagged proteins in a developing medaka embryo. The resulting reduced enzyme activity of less than 50 % is comparable to the reported enzyme activity PMM2-CDG patients (Pajusalu et al., 2024).

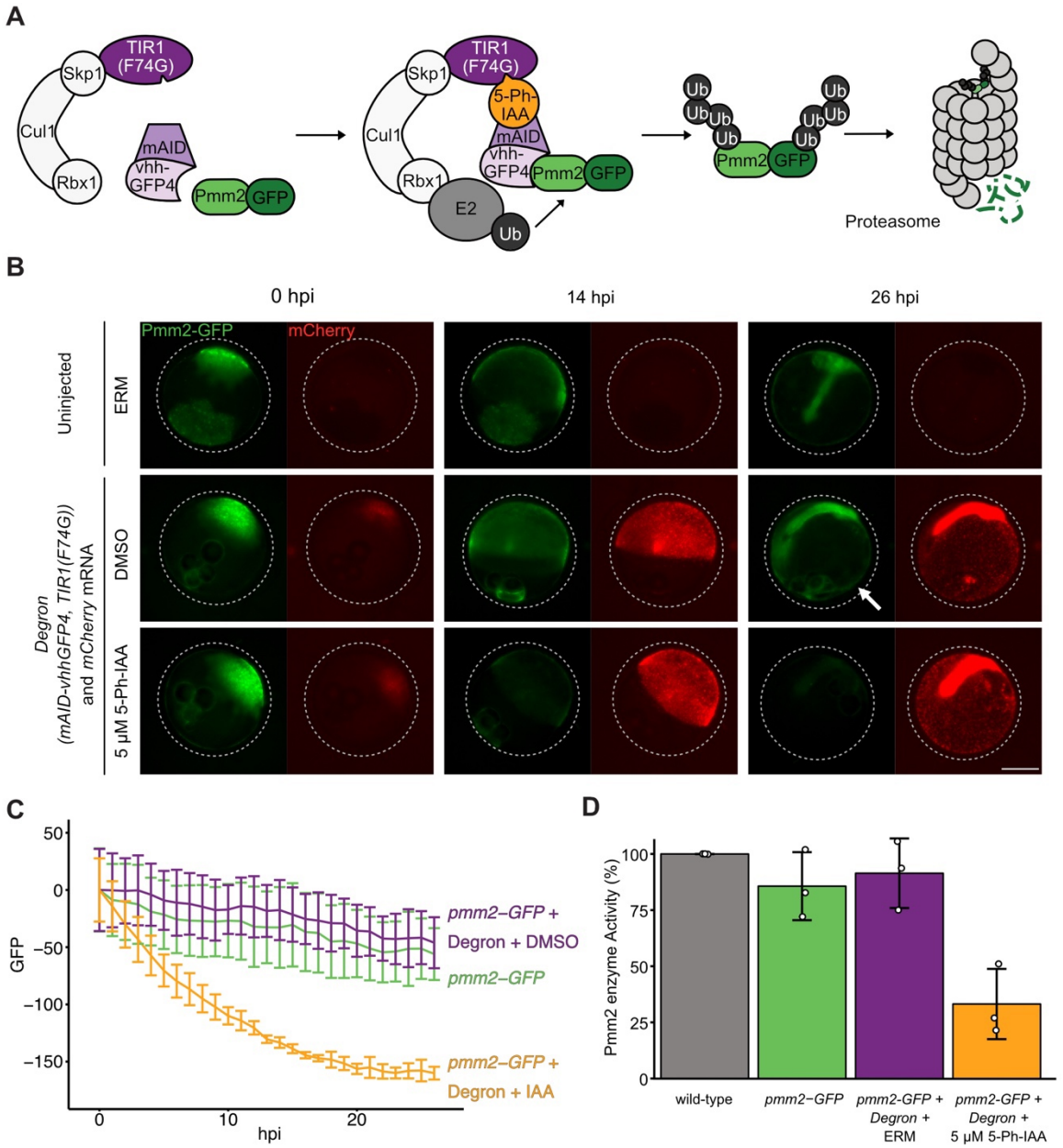

Figure 5: Acute and inducible depletion of Pmm2-GFP in medaka mimics reduced enzyme activity reported from PMM2-CDG patients. A) Representation of the TIR1(F74G) variant together with mAID-GFP-nanobody (vhhGFP4) as degron system (Daniel et al., 2018; Yesbolatova et al., 2020) to degrade Pmm2-GFP in an auxin-analog (5-Ph-IAA) inducible manner. B) Time-lapse imaging of uninjected, degron-injected incubated in ERM and degron-injected induced with 5 µM 5-Ph-IAA *pmm2-GFP* embryos. Scale bar: 500 µm C) Measurement of baseline correction mean GFP fluorescence intensity over 26 hours post-injection (hpi). The data represents the mean ± sd from triplicate samples: uninjected *pmm2-GFP* control (total n = 15), degron/mCherry-injected and induced embryos (total n = 65), and non-induced embryos (total n = 61). D) Pmm2 enzyme activity assay comparing wild-type, *pmm2-GFP* uninjected, degron injected and degron injected and induced with 5 µM 5-Ph-IAA embryos. The data shows the mean ± sd from triplicates (n=85-93 in each triplicate). Pmm2 enzyme assay data produced jointly with Virginia. hpi, hour post induction; 5-Ph-IAA, auxin analog. Figure adapted from Pakari et al., 2025.

2.1.2 Injections of mRNA into 1-cell stage embryos cause baseline phenotypes in transgenic *pmm2-GFP* line

After I confirmed the reduction of Pmm2 enzyme activity by applying the degron system in medaka, I investigated how the acute protein knockdown affects the early development in medaka embryos.

For this, six experimental conditions were compared for occurring phenotypes: uninjected wild-type Cab, uninjected homozygous *pmm2-GFP,* only *mCherry* mRNA injected homozygous *pmm2-GFP* induced with 5-Ph-IAA or kept in ERM and degron (*TIR1(F74G)* and *mAID/GFP-nanobody*) injected *pmm2-GFP* treated (5 µM 5-Ph-IAA) or untreated (DMSO) embryos. In the very early stages of development no phenotypes could be detected. Therefore, phenotypes were assessed at two later stages: before hatching at 4 dpf and at hatch. The two stages were chosen to evaluate effects of the early and late development.

At 4 dpf appearing phenotypes included: wild-type looking or delayed development, blood-clotting, misdeveloped embryos, embryos with only axis formation or heart abnormalities (Figure 6 A). After hatching, the following phenotypes could be observed: wild-type looking or delayed in development, unhatched embryos, enlarged yolk sacs, arrow-like formation or kinks in the back (Figure 6 A). Quantification of the phenotypic distribution shows high rates of abnormal developed embryos in all injected groups, and no exclusively appearing in degron injected and induced groups (Figure 6 B).

Transient loss of Pmm2-GFP did not result in any additional phenotypes or increased ratios of specific phenotypes, suggesting that this temporary degradation had no detectable impact on development and that reduced Pmm2 enzyme activity can be compensated for during early development. However, the *pmm2-GFP* tagged line exposed a general susceptibility to injection stress.

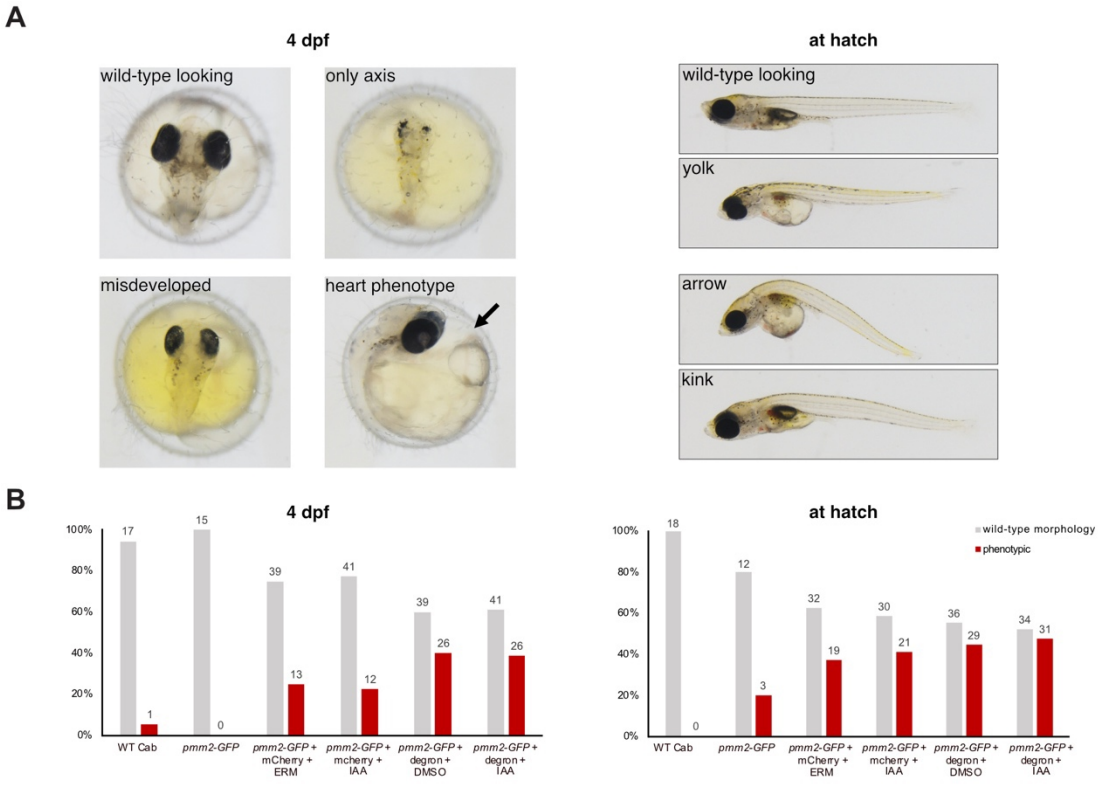

Figure 6: Injection of mRNA causes phenotypes in *pmm2-GFP* line. A) Representative images of homozygous *pmm2-GFP* embryos exhibiting various phenotypes after injection with degron system mRNA or *mCherry* mRNA, compared to non-injected wild-type Cab embryos and non-injected homozygous *pmm2-GFP* embryos at 4 dpf and at hatch. Observed phenotypes include: wild-type looking, axis formation only, misdeveloped and embryos with heart phenotypes (black arrow indicated edema around the heart). B) Quantification of the phenotypic distribution of wild-type and phenotypic looking individuals at 4 dpf and at hatch. Numbers from three independent injections with total number of individuals depicted on top of the bars. dpf, days-post-fertilization

2.1.3 Generation and validation of a stable medaka line expressing degron components ubiquitously

Injections of any mRNA seem to cause phenotypes in the probably susceptible homozygous *pmm2-GFP* line, due to tagging of an essential enzyme. To avoid the injection of the degron components to mimic the patient-like PMM2 reduction, I next attempted to generate a medaka line stably expressing these components. Ubiquitous expression of low levels of the degron components is expected to reduce the observed baseline phenotypes, as no injections are performed. Additionally, a stable line would allow for temporal control as induction can be performed at any stage of development, and one could control the degradation systematically in all cell-types with ubiquitous promotors or even spatially with tissue-specific promotors. Furthermore, varying concentrations of inducer could titrate the enzyme activity to different levels (Figure 7 A). To generate a stable line, I cloned a plasmid containing a ubiquitous promotor to drive the expression,

the degron components TIR1(F74G) and mAID/GFP-nanobody, an RFP separated by a T2A as reference fluorophore for presence of the construct and flanking meganuclease sites for integration into the medaka genome (Figure 7 B).

As the *pmm2-GFP* line appears to be susceptible towards injections, I injected the plasmid into wild-type Cab embryos to later cross the injected F0 generation to the homozygous *pmm2*-GFP line to generate a heterozygous *pmm2-GFP* degron line. After injection and screening of the hatchlings, RFP-positive individuals were raised. RFP signal indicates successful integration of the construct and was visible in the muscles of F0 generation in a mosaic pattern (Figure 7 C). After reaching adulthood, the potential founder fish were outcrossed to the homozygous *pmm2-GFP* line. The offspring was screened for positive RFP and GFP signal indicating the presence of both, the degron construct and Pmm2-GFP (Figure 7 C). A dim RFP fluorescence was visible after hatch in the whole body of the hatchlings. Double-positive F1 fish were grown to adulthood and after reaching maturity, fish were incrossed to generate F2 individuals with stable expression of Pmm2-GFP and the degron components ubiquitously. With this line, knockdown efficiencies of Pmm2-GFP were tested, in a stable line expressing the degron components ubiquitously.
Double positive F2 hatchlings were imaged before induction with 10 µM 5-Ph-IAA, instead of 5 µM like in embryos, and afterwards imaged daily until 4 days post induction. Then, the auxin analog solution was removed and hatchlings were kept in standard ERM media to assess the reversibility of the degradation (Figure 7 D). No reduction in GFP fluorescence was visible upon induction with 5-Ph-IAA and GFP expression did not reoccur after washing away the inducer. It is possible, that the degron expression levels were too low to cause any effect.

In summary, I demonstrate that a mRNA-based degron system can be used to induce the knockdown of Pmm2-GFP in medaka. The data show that after induction with 5-Ph-IAA, Pmm2-GFP levels decrease rapidly with a half-life of approximately 6.9 hours. A Pmm2 enzyme activity assay proves the reduction of net enzyme activity to pathogenic levels similar to levels reported from PMM2-CDG patients. Even maternally contributed Pmm2-GFP was degraded, which cannot be targeted in a genetic model. However, the injection of mRNA caused stress to the developing embryos and triggered unwanted phenotypes in the Pmm2-GFP tagged line, likely due to the essential role of *pmm2*. The stable line expressing the degron components did not lead to efficient GFP degradation due to insufficient expression levels. This suggests that an mRNA-based approach is more effective than a stable line, as it successfully degraded GFP.

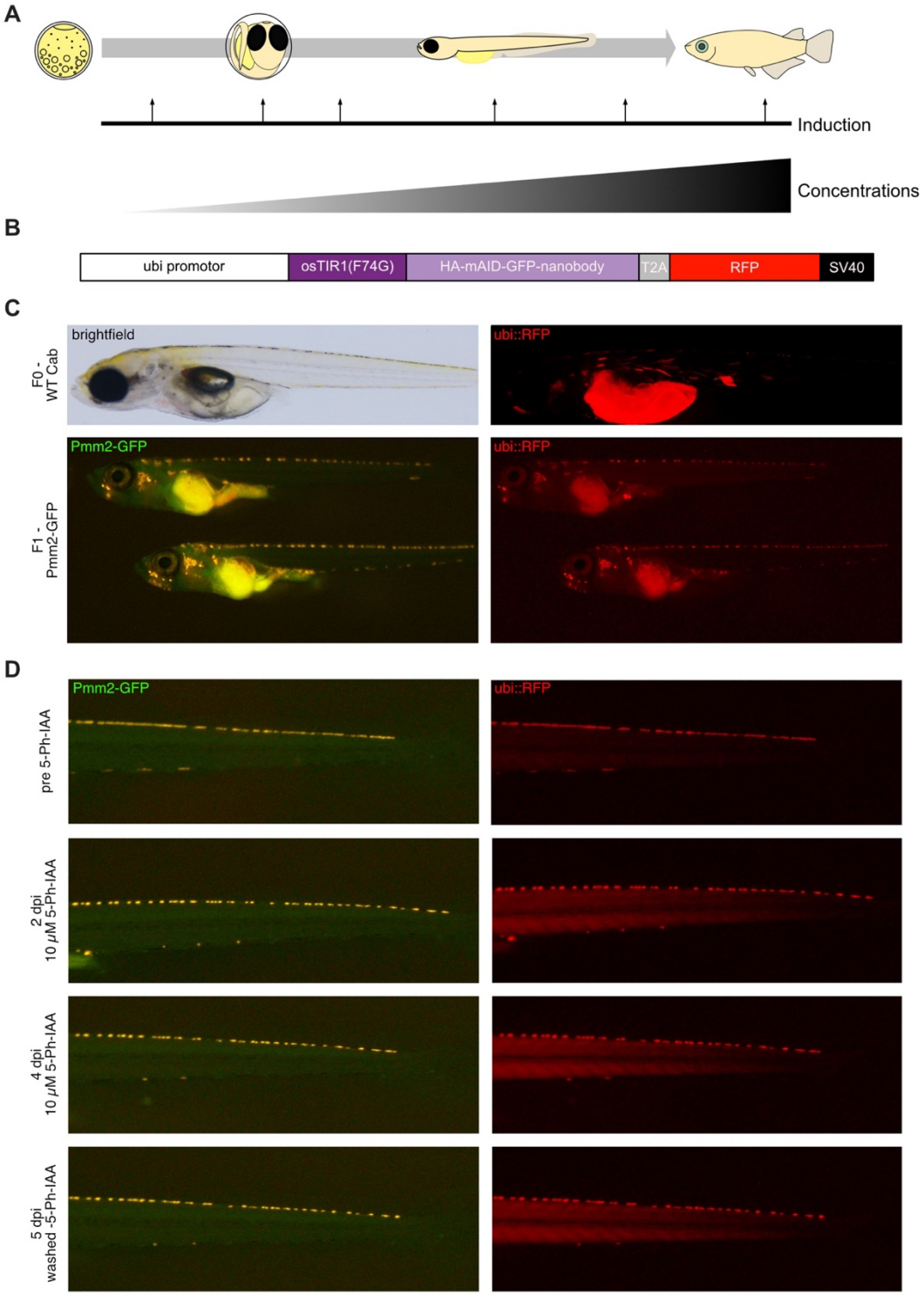

Figure 7: Generation and validation of a stable *pmm2-GFP* line expressing the degron system ubiquitously. A) Schematic illustration of the benefits with a stable line expressing the degron system ubiquitously and endogenously: induction at any stage of development and induction with different concentrations to titrate effects of knockdown. B) Outline of the genetic construct for generation of the stable expressing line. The ubiquitous promotor is driving the expression of TIR1(F74G), mAID/vhhGFP4 nanobody and T2A-RFP for presence of the construct. C) Screening of injected F0 and stable F1 generation for successful integration of the construct via RFP fluorescence signal. D) Induction of stable *pmm2*-GFP line expressing degron components with 10 µM 5-Ph-IAA. Images of hatchlings tails are taken before and after induction with 5-Ph-IAA until 4 days post induction as well as after removal of the inducer. dpi, days post induction

2.2 Generation of patient specific Pmm2 mutations

Next to an acute knockdown of Pmm2, I aimed to genetically modify the enzyme activity by the introduction of reported patient mutations. These exact loci are not accessible with the classical application of base editors as there is no PAM in the correct distance. In the following chapter I describe how I expand the base editing scope with established cytosine and adenine base editors to introduce patient specific mutations in medaka via new PAM generation.

Parts of the text and indicated figures from the following section 3.2. have been adapted from the original publication Pakari et al., 2023.

2.2.1 Inception: reduce base editing limitations by creating PAMs *de novo*

The two most common mutations found in patients suffering from PMM2-CDG are p.F119L and p.R141H and are characterized as hypomorphic alleles (Andreotti et al., 2015; Schollen et al., 2000; M.-A. Vals et al., 2017). Mimicking these human mutations in a model organism, closely resembling the patient's situation would provide a valuable model for translational approaches. As PMM2 is highly conserved between human and medaka, I aim to create the exact patient mutations in medaka using CRISPR/Cas9 base editors.

Classical CRISPR/Cas9 approaches are not suitable for generating presumable hypomorphic patient-based mutations as these induce DNA double-strand breaks and cause insertions and deletions. Recently CRISPR/Cas9-based base editors have been established that can introduce point mutations by only nicking the DNA. These genome editing tools are better suited to introduce precise point mutations as no double-strand breaks are introduced.

In medaka, the adenine (ABEs) and cytosine (CBEs) base editors have been demonstrated to precisely and efficiently introduce point mutations, allowing phenotypic investigations already in the injected generation (Cornean et al., 2022).

However, due to the absence of a PAM site in the required distance from the desired orthologous patient mutation location in the medaka genome, the exact mutation positions are not accessible for editing. An alternative, more flexible CRISPR/Cas9 based systems utilizing near-PAM-less Cas9 variants have been developed, but the relaxation comes at the cost of potentially increased off-target effects (Walton et al., 2020) and higher lethality in medaka (Cornean, 2022). To avoid off-target effects and reach more target sites to specifically introduce patient mutations, a new idea is the creation of *de novo* PAMs to expand the base editing scope. Taking advantage of the ABE base editor,

adenosine-to-guanine base editing of nucleotide triplets with the sequence NAA, NGA or NAG can be converted into NGG sites, i.e. a novel PAM motif. With this strategy, a new guide RNA target site becomes available, allowing editing of previously inaccessible sites. In this approach, two guide RNAs act in a serial manner when administered simultaneously in one-shot, e.g., injected at the same time in the case of medaka. Moreover, two different types of base editors can be introduced at the same time in combination with diverse guide RNAs. The first guide RNA introduces a new PAM site with the ABE, while a second guide is designed to recognize the novel PAM and can sequentially edit nucleotides 27-36 base pairs upstream of the initial PAM with either CBE or ABE (Figure 8).

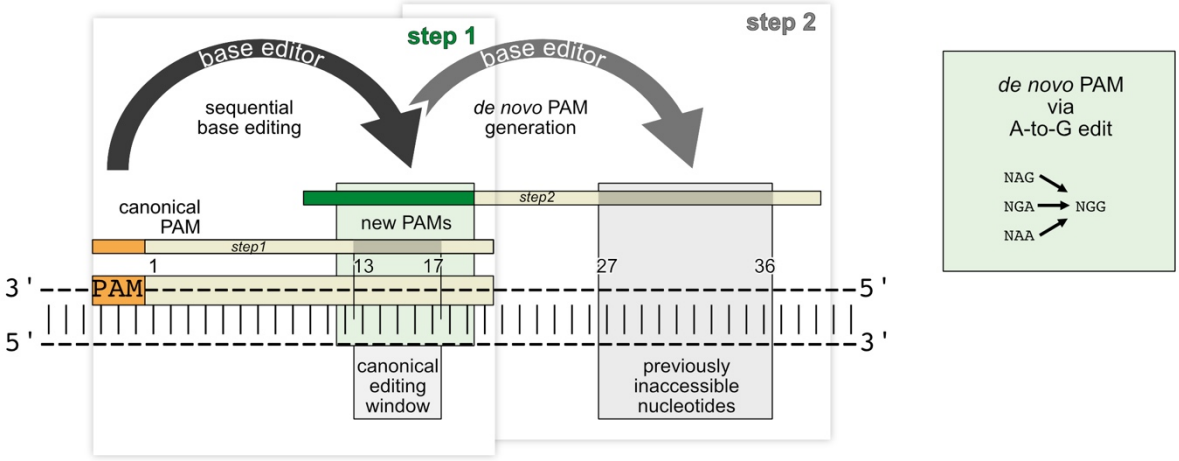

Figure 8: Inception approach expands available target sites for base editing via new PAM generation. The idea of inception is to use two guide RNAs and one or two different base editors at the same time but acting sequentially. In the first step the adenine base editor generates new PAM sites by editing NAG, NGA or NAA triplets to NGG. The new PAM in green allows for the second guide RNA to edit 27-36 nucleotides upstream of the canonical PAM in orange. Adapted from Pakari et al., 2023. PAM, protospacer adjacent motif.

2.2.2 Testing applicability of Inception at the *oca2* locus

To test the applicability of the inception approach, I targeted the oculocutaneous albinism II (*oca2*) gene. Oca2 is responsible for the pigmentation in the eye and body of medaka. After bi-allelic editing, Oca2 is lost and a pigmentation loss becomes visible in the pronounced eye of medaka embryos (Lischik et al., 2019). Two guide RNAs targeting the *oca2* locus were designed to assess the outcome of the inception approach. The first guide RNA binds to an endogenous PAM motif and introduces a NGG motif by CAG to CGG editing with the adenine base editor which causes a synonymous change of the amino acid alanine at position 337. This new PAM enable binding of the second guide RNA which introduces a premature STOP codon with the cytosine base editor by editing CAG to TAG

at the amino acid glutamine at position 333 and a non-synonymous change by editing ACC to ATT at the amino acid threonine at position 332 (Figure 9 A).

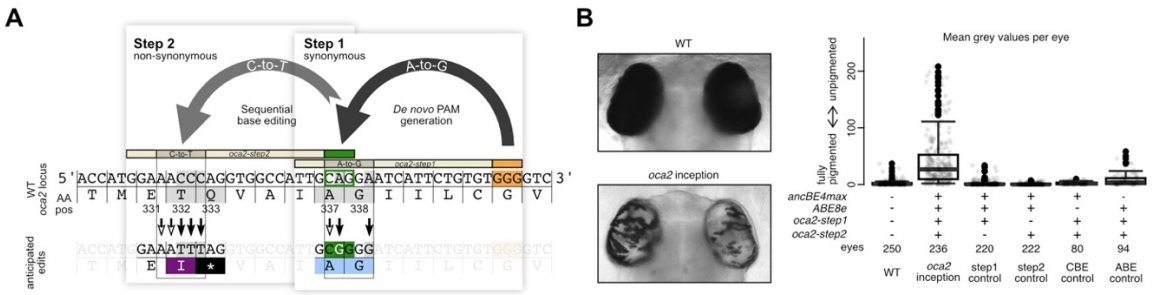

Figure 9. Knock-out by introduction of premature stop codon in the pigmentation gene *oca2* via inception. A) Premature stop codon (PTC) mutations were induced by two steps at the *oca2* locus: synonymous de novo PAM generation in step 1 (ABE, CAG>CGG=p.A337A) and subsequent non-synonymous editing (CBE, CAG>TAG=p.Q333* and ACC>ATT=p.T332I) to introduce non-synonymous codon changes leading to a PTC at p.T332 and p.Q333 in step 2. Expected edits are shown with black arrows and additional possible edits from using both A-to-G and C-to-T base editors are shown with white arrows. B) Pigmentation loss after injection of the *oca2* inception mix was assessed 4.5 days post-fertilization by measuring mean gray values of each eye. The inception mix contained *ABE* and *CBE* mRNA, and *oca2-step1* and *oca2-step2* guide RNAs. Multiple control injections were performed, each lacking one ingredient and only in the case of the ABE control (mix without the *CBE* mRNA), mild loss of pigmentation was visible. Boxplot shows median with boundaries representing the 25th and 75th percentiles. Whiskers extend to a maximum of 1.5 times the interquartile range. Figure legend and Figure adapted from Pakari et al., 2023.

After injection of 1-cell stage medaka embryos with the inception mix (*ABE*, *CBE*, *oca2-step1* guide RNA and *oca2-step2* guide RNA), loss of pigmentation was visible in the eye of 4.5 days post-fertilization (dpf) “editants” (base edited embryos) (Figure 9 B). The degree of loss of pigmentation resulting from the *oca2* perturbation was determined by imaging of fixed 4.5 dpf editants with the Acquifer Imaging machine. The eyes were manually segmented from the images, thresholded and the mean grey values were extracted from each eye (Thumberger et al., 2022) (Figure 9 B). Zero values correspond to fully pigmented eyes and pixel values of 255 to completely unpigmented ones.

To validate that the loss of pigmentation is not caused by the *de novo* PAM editing or by premature stop codon introduction by the second guide RNA in the absence of a PAM, I performed four control injections. The control mixes were injected lacking one of the four components of the inception injection mix: step1 guide RNA, step2 guide RNA, ABE base editor mRNA or CBE base editor mRNA. The controls with ABE and CBE editors which were lacking one of the guide RNAs did not cause any loss of pigmentation (Figure 9 B). Injection of both guide RNAs with the CBE also had no effect on pigmentation, while with the ABE mild loss of pigmentations was detected (Figure 9 B).

The genome editing efficiency was validated via Illumina sequencing of the targeted *oca2* locus. Analysis of three pools of eight editants (24645 sequencing reads in total, Figure 10) showed 70.3±8.3 % new PAM generation (c.1011A>G) with the *oca2-step1* guide RNA. Sequential editing with the *oca2-step2* guide RNA was up to 48.5±10.1 % at the codon of T332 (c. 996C>T) and 23.0±5.8 % of the alleles revealed premature STOP codon editing of the codon Q333 (c.997C>T) (Figure 10). Illumina sequencing or Sanger sequencing of the four control injection mixes confirmed the visual readout. The mix lacking the second guide RNA showed 80.6±7.3 % new PAM generation, while the mix lacking the first guide RNA did not result in any notable editing. Injection mixes containing both guide RNAs and only the CBE, similarly did not cause any editing. In contrast, when injecting the ABE with both guide RNAs efficient new PAM generation was detected with 91 % conversion rate and subsequent T332A and Q333A editing - explaining the visible pigmentation loss in the eyes (Figure 10).

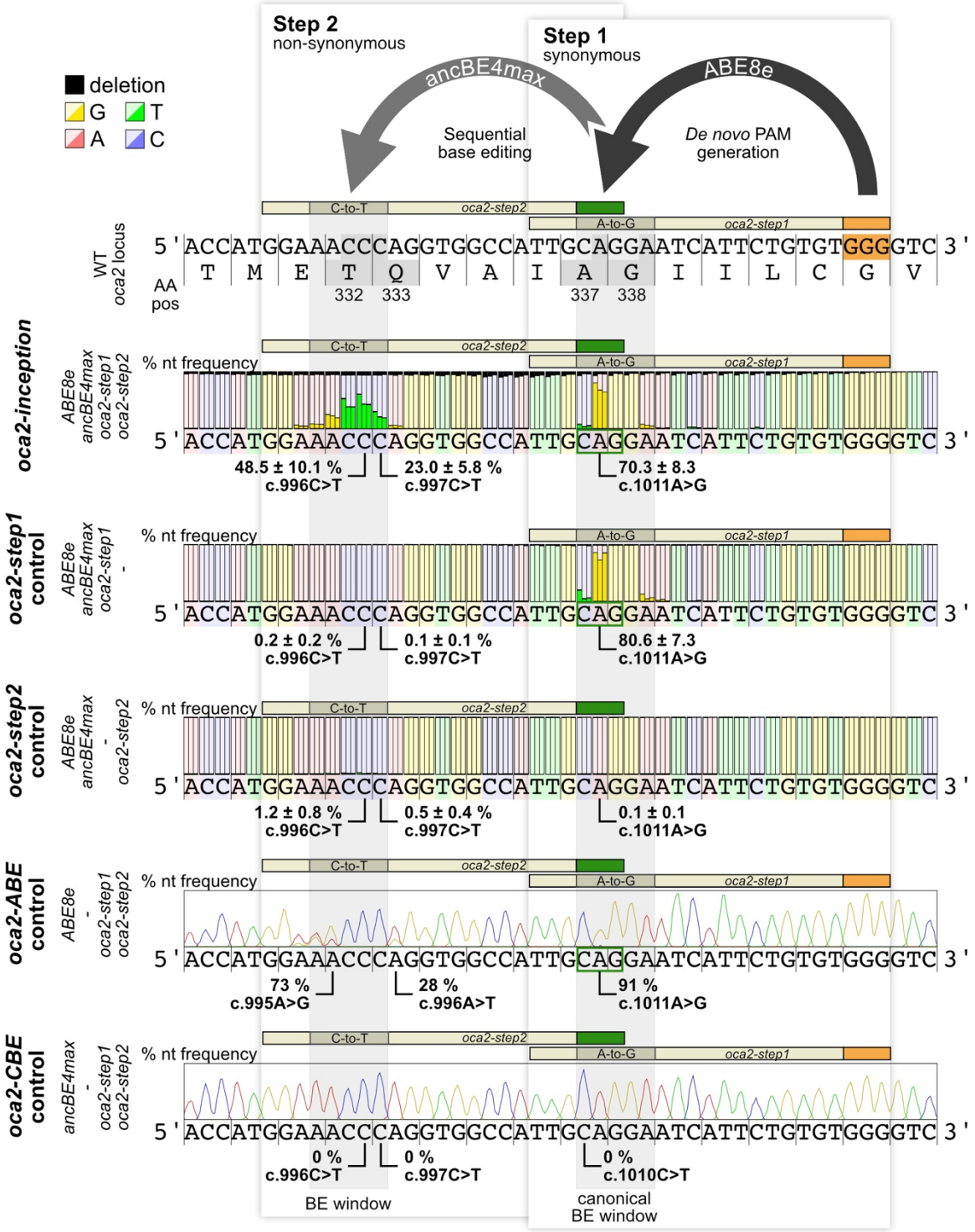

Figure 10: "Sequencing results of *oca2* inception and control editants. Illumina amplicon sequencing analyses of oca2-editants (three replicates each) injected with the respective injection mixes: oca2-inception (3 pools of 8 editants; 246045 reads total), oca2-step1 control (3 pools of 1 to 8 editants, 82182 reads total) and oca2-step2 control (3 pools of 8 editants, 124571 reads total). Barplot representation of nucleotide frequency of the three replicates per nucleotide position. Highlighted nucleotide changes represented as mean ± standard deviation. Chromatograms of oca2-ABE (5 editants) and oca2-CBE controls (8 editants) resulting from Sanger sequencing with indicated nucleotide changes derived from EditR (Kluesner et al., 2018) analysis." (Pakari et al., 2023) Figure and figure legend from Pakari et al.,2023. AA pos, amino acid position; canonical PAM (orange); de novo PAM (green); nt, nucleotide; PTC, pre-termination STOP codon; WT, wild-type

To further evaluate the inception efficiency (sequential editing following new PAM introduction), I analyzed the sequenced alleles to count how many contained both a new PAM and a loss-of-function allele. The expected synonymous mutations at the new PAM site caused a second editing event installing non-synonymous changes at the codons T332 and Q333. In total, 48.4 % of analyzed alleles confirmed generation of loss-of-function changes: 28.6 % showed a T332 alteration and 19.9 % carried a Q333* mutation (Figure 11). All of these alleles also contained the synonymous A337A new PAM change whereas only 15.8 % remained non-edited wild-type alleles.

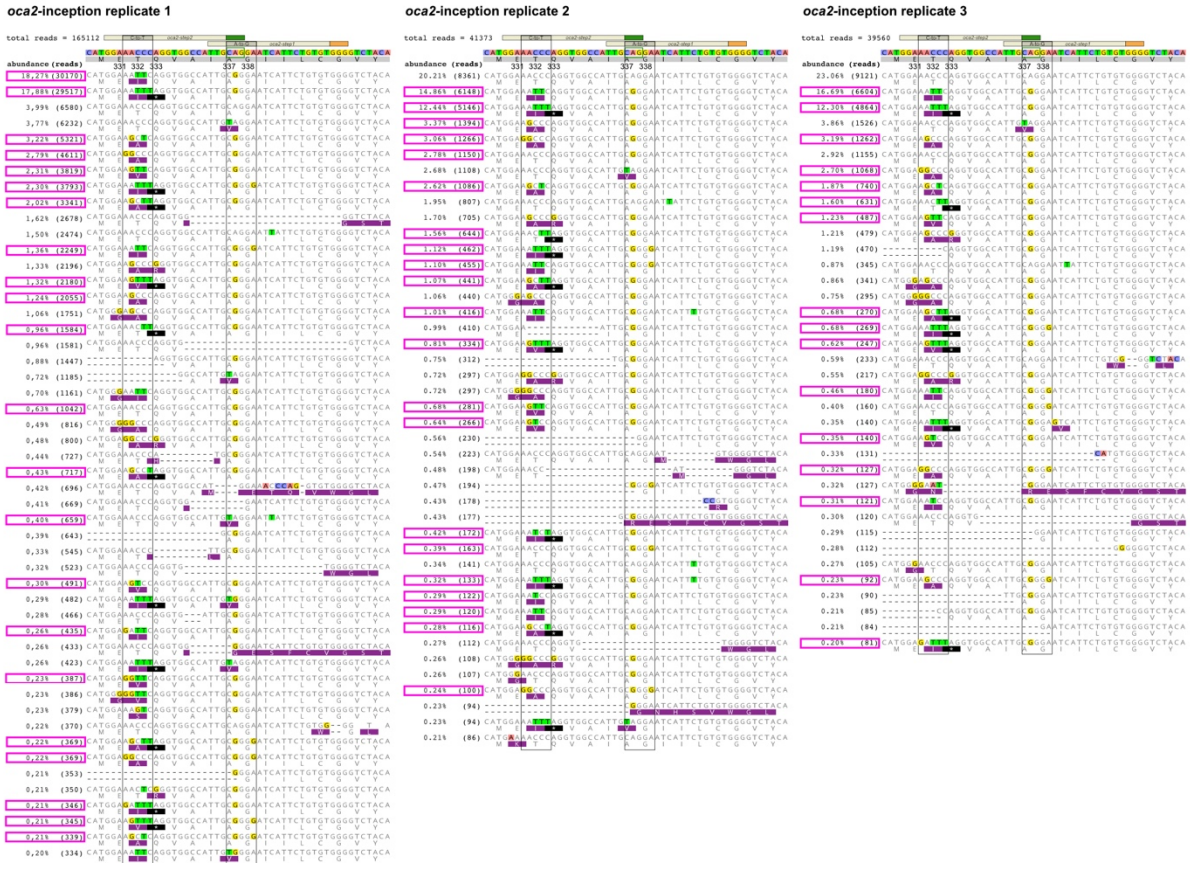

Figure 11: Allele frequency analysis and amino acid translation of Illumina sequencing amplicons from oca2 inception injections. The alleles correspond to the three replicates from injection of the inception mix containing *ABE* and *ABE* mRNA, and *oca2-step1* and *oca2-step2* guide RNAs. The sequencing reads were analyzed with the CRISPResso2 tool (Clement et al., 2019). The alleles frequency table was used for analysis with a cut-off at 0.2 % read abundance in each replicate. The guide RNAs are indicated at the top and alleles are ordered by frequency. Differences in alignment of the reads to the wild-type reference are shown by colors: adenine, red; guanine, yellow; thymidine, green; cytosine, blue; -, deletions. Figure adapted from Pakari et al., 2023. Anticipated alleles, pink outlined box; base editing window, black outlined box; canonical PAM (orange); de novo PAM (green); non-synonymous codon changes, purple box; pre-termination STOP codon, black box

2.2.3 Generation of previously inaccessible patient mutation F119L with inception

After successfully applying the inception approach and evaluating the editing outcome at the *oca2* locus, I turned to generate the exact patient mutations from PMM2-CDG patients. The human p.F119L corresponds to the medaka p.F122L mutation, a codon that can be reach by a two-step inception editing approach. The first guide RNA (*pmm2-newPAM*) creates intronically a *de novo* PAM site with the A-to-G base editor and a second guide RNA (*pmm2-inception*) can subsequently reach the F122 codon and induce a F122L substitution via A>G editing (Figure 12 A). After injection of the ABE base editor with both guide RNAs, efficient editing of new PAM motif was detected but no subsequent editing event. Carefully analyzing the target site and editing outcome, I recognized that for efficient binding of the *pmm2-inception* guide RNA, additional edits which take place in the canonical base editing window (~5 base pairs long) of the first guide RNA need to be considered. For binding to the target site, guide RNAs contain a 17-20 bp long sequence complementary to the locus sequence. The crucial part for binding and editing is the “seed” sequence consisting of the first 12 nucleotides upstream of the PAM and in general PAM-proximal mismatches are less tolerated (Hsu et al., 2013). As the first guide RNA of the inception approach edits bases in this seed sequence within the base editing window, the second step guide RNA needed to be sequence adjusted to enable binding. For this *pmm2* case, the first nucleotide upstream of the new PAM will be edited by the ABE from A>G (Figure 12 A, red box) hence the second gRNA was adjusted to bind to the edited target (Figure 12 A, yellow part of *pmm2-inception-adjusted*).

Injection of ABE base editor with the two guide RNAs resulted in a two-step editing event, reaching the F122 codon. Sanger sequencing of a pool of injected F0 embryos revealed efficient *de novo* PAM generation and subsequent synonymous T121 and non-synonymous F122P substitution (Figure 12 B). I had intended editing of F122 to F122L in order to create the human mutation but as the base editing window is ~5 base pairs long, bystander edits can occur.

Outcrossing the grown F0 adults to wild-type fish and genotyping of the F1 generation revealed individuals with both edits: F122P and the anticipated F122L mutations (Figure 12 C).

Incrossing of p.F122L and analysis of the progeny led to a dramatic phenotype in a subset of individuals. Genotyping the offspring unexpectedly exposed the global phenotype only occurring in heterozygous individuals (Figure 12 D). Homozygous ones showed slightly smaller body sizes and no food in the digestive tract (Figure 12 D). This raised the

possibility of a dominant negative effect or the presence of additional mutations within the intronic region that could not be resolved genetically via sanger sequencing.

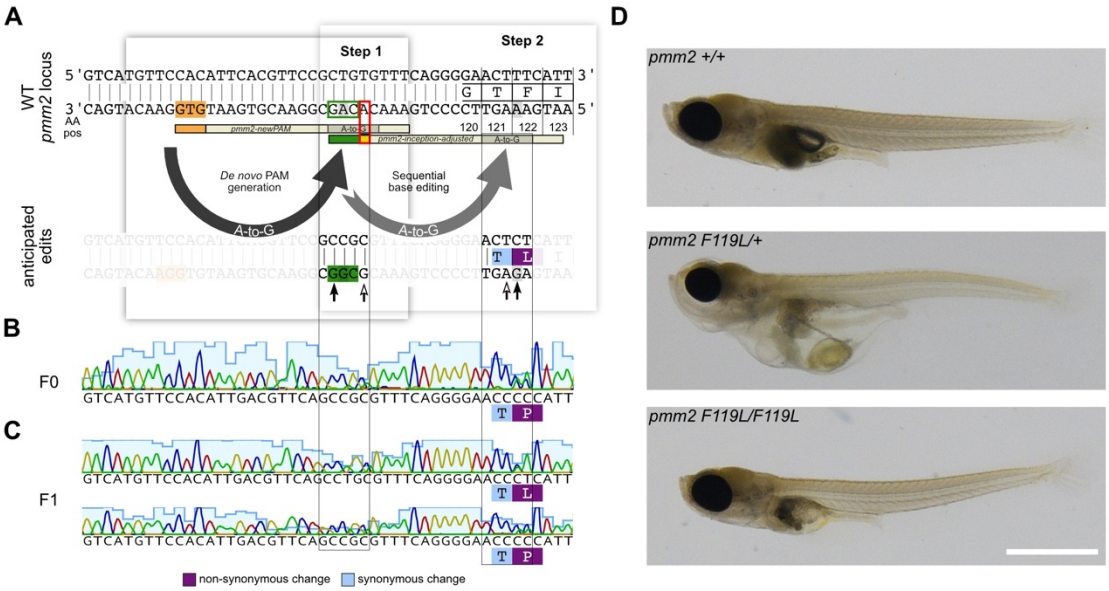

Figure 12: Generation of exact patient mutation *pmm2 p.F122L* with the inception approach. A) Two step base editing strategy to reach F119L position: first guide RNA (*pmm2-newPAM*) generates intronically a new PAM site and a second guide RNA (*pmm2-inception-adjusted,* yellow part of guide RNA is adjusted) edits the desired F122 codon. Anticipated edits are indicated with black arrows and additional edits that may occur are indicated with white arrows. B) Sanger sequencing of the injected F0 generation of pooled embryos (n=3) shows generation of F122P mutation. C) Sequencing of F1 generation after outcrossing F0 editants to wild-type background reveals individuals with F122P but also F122L mutations. D) Incrossing of *pmm2 F122L* heterozygous individuals causes a more dramatic phenotype in heterozygous hatchlings compared to homozygous ones. Scale bar 1 mm. AA pos., amino acid position; WT, wild-type. red box indicates A>G adjustment in *pmm2-inception-adjusted* guide RNA; yellow; orange indicates canonical PAM; green indicates *de novo* PAM; P, prolin; L, leucin

The locus surrounding exon 5 of *pmm2* is particularly challenging to genotype due to a nearly 10,000 bp long repetitive region downstream and a 20-bp long guanine-stretch upstream of exon 5 (Figure 13 A). Designing primers is challenging, not only due to the aforementioned flanking regions, but also as some primer pairs preferentially amplified either the mutant or wild-type allele exclusively. Additionally multiple single nucleotide polymorphisms (SNPs) are present in the wild-type Heidelberg Cab strains (HD Cab) compared to the reference strain HdrR (Figure 13 A). To detect both mutant and wild-type alleles in equal ratios in Sanger sequencing reads, the sole reliable primer binds over 100 times in the intronic region downstream of exon 5 (Figure 13 A, green triangles). By PRC amplification with this forward primer and a reverse primer binding at the 3‘end of exon 5 both alleles were amplified equally (Figure 13 B, green arrows). Sanger sequencing with the reverse primer gave consistent genotyping results for exon 5 PCR products. The intronic region remained unresolvable with Sanger sequencing. Therefore, unintended

editing in the intronic region cannot be excluded which may contribute to the observed phenotype.

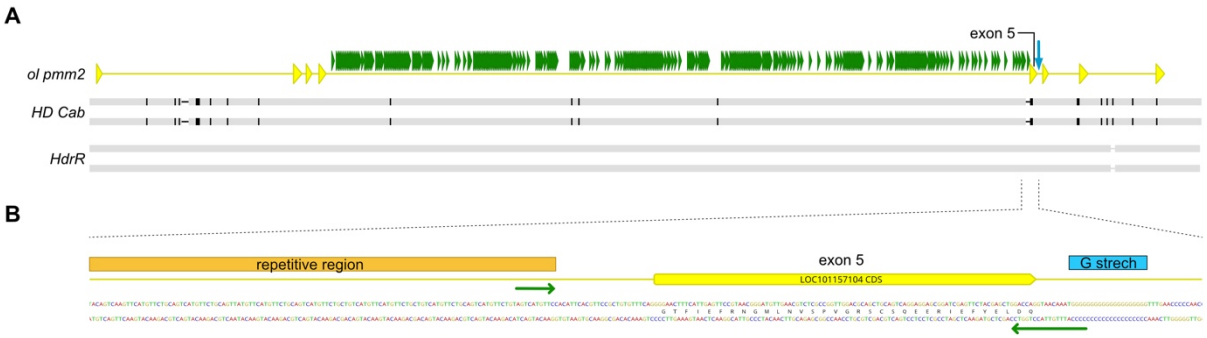

Figure 13: The *pmm2* intron 5 is highly repetitive. A) Alignment of reference sequence from Heidelberg Cab strain and HdrR strain. Exons 1-8 are shown in yellow and the primer alignment in green represents the highly repetitive region within *pmm2* intron 5. Blue arrow indicates a 20-base pair long guanine-stretch. B) Zoom-in view of exon 5 of *pmm2.* Highlighted in blue is a 20-base pair long guanine stretch, in orange a repetitive region and PCR genotyping primers are indicated as green arrows. HD, Heidelberg

In summary, the inception approach offers a valuable extension to the existing base editing CRISPR/Cas9 toolbox. Due to technical limitations, sequencing of repetitive regions is difficult and should be considered for validation of editing approaches in general. The sequential editing is highly efficient demonstrated in two loci: *oca2* and *pmm2*. Especially in the case of introducing loss-of-function mutations or specific patient bases mutations that were inaccessible before, inception offers an efficient multi-base editing in a single step.

2.3 Generation and characterization of a genetic patient-based PMM2-CDG medaka model to study onset of disease progression

In this chapter I describe the generation and characterization of a patient-based PMM2-CDG model in medaka. I used CRISPR/Cas9 based approaches to introduce hypomorphic alleles which allow to study the effect of Pmm2 loss on development and the onset of disease progression. As described in 3.2.3, the *pmm2* locus around exon 5, harboring the two most common mutations reported from PMM2-CDG patients in human, is challenging to sequence due to the repetitive locus. The previous attempt to generate the exact patient mutations was inconclusive hence other mutations will be generated.

2.3.1 Disruption of Pmm2 causes early embryonic lethality in medaka

To generate a *pmm2* mutant line in medaka, I first attempted to create a knockout of the *pmm2* gene. Complete loss-of-function mutations of PMM2 presumably cause lethality in human (Freeze, 2009) and early lethality has been reported in several animal models (Chan et al., 2016; Cline et al., 2012; Himmelreich et al., 2015; Parkinson et al., 2016; Thiel et al., 2006).
I assessed whether a full knockout is lethal in medaka and screened for phenotypes upon loss of Pmm2. If the knockout would be viable, heterozygous individuals can be maintained and incrossed to obtain homozygous individuals to study disease progression.

I generated the knockout by injecting 1-cell stage wild-type medaka embryos with *CRISPR/Cas9* mRNA together with guide RNAs targeting exon 2, which contains the catalytic center and exon 5, harboring the most common patient mutations (Figure 14 A). Resulting phenotypes were assessed 6 days post fertilization (dpf), as by this developmental stage all aspects of potential developmental defects like heart defects, eye abnormalities and growth defects can be detected. Phenotypic analysis of the injected embryos named “crispants”, revealed severe developmental defects (Figure 14 B). Quantification of the phenotypic distribution showed the dramatic impact of the knockout of *pmm2* on the developing medaka crispants (Figure 14 C). In non-injected controls 89 % (n = 17) were wild-type like and 11 % died (n = 2). Only 1 % (n = 1) of injected embryos showed a wild-type appearance whereas 71 % (n = 49) had an aberrant phenotype and 28 % (n = 19) died until 6 dpf. Sanger sequencing of exon 2 confirmed disruption of the locus in genomic DNA extracted from a pool of five injected embryos at 3 dpf (Figure 14 D). The observed developmental defects underline the essential role of *pmm2* and indicate that a complete loss-of-function is incompatible with life, also in medaka. As expected, full

knockout by CRISPR/Cas9 editing of *pmm2* in medaka dramatically impairs embryonic development and causes early lethality, making the establishment of a stable knockout line not feasible.

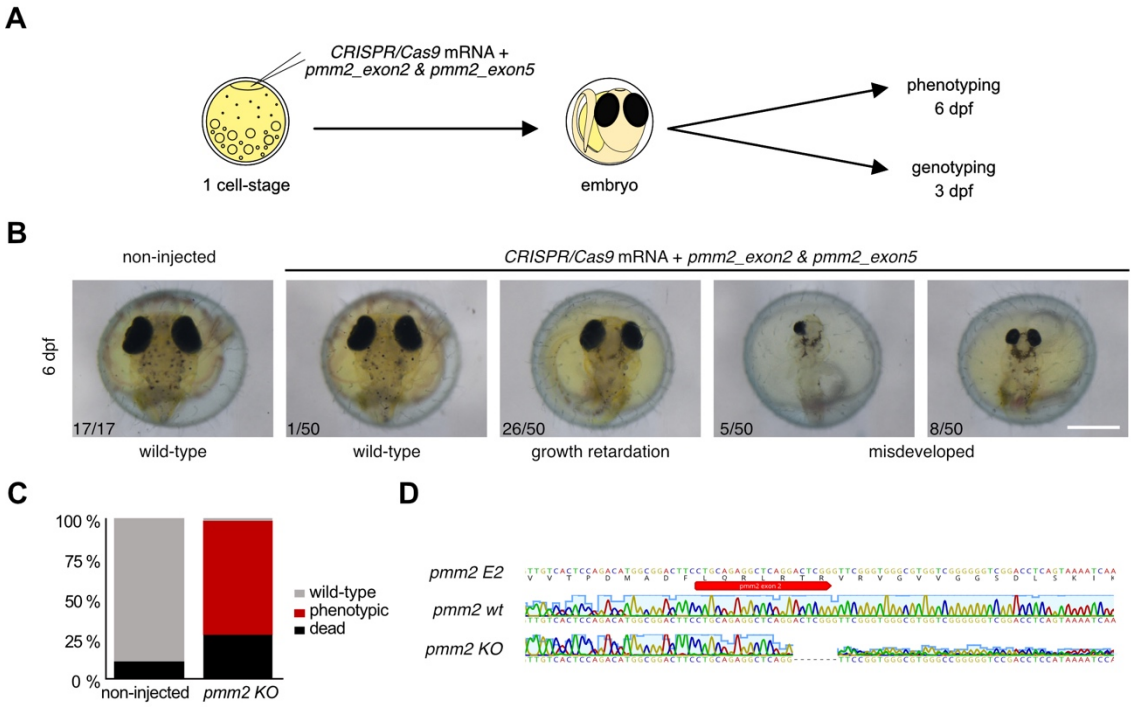

Figure 14: Knockout of *pmm2* with CRISPR/Cas9 affects embryonic development. A) Medaka embryos were injected with *CRISPR/Cas9* mRNA and guide RNAs targeting exon 2 and exon 5. A pool of crispants was genotyped 3 dpf and remaining embryos were phenotyped 6 dpf. B) Spectrum of phenotypes visible at 6 dpf include: only axis formed, misdeveloped and globally affected embryos. Scale bar 500 µM. C) Quantified phenotypic distribution at 6 dpf of non-injected vs *pmm2* knockout embryos. D) Sanger sequencing shows disruption of exon 2 of *pmm2* after cutting with CRISPR/Cas9 (genomic DNA from pool of five editants). dpf, days post fertilization; E2, exon 2; KO, knockout; wt, wild-type

2.3.2 Generation of presumable hypomorphic patient-based mutations using CRISPR/Cas9 base editors

The previously described lethality could be evaded by generating hypomorphic alleles which permit survival of the genetically modified embryos. I used based editors to precisely produce the hypomorphic alleles. As described before, base editors introduce precise point mutations by nicking the DNA. For the use in medaka, the adenine and cytosine base editors (ABE and CBE) have proven to efficiently install precise point mutations in the injected generation (Cornean et al., 2022).

The exact hypomorphic alleles reported from patients cannot be introduced using the ABE and CBE editors in medaka. For editing, the Cas9 must recognize a PAM motif and point mutations can be introduced within the base editing window at a specific distance from the

motif. However, the most common *PMM2*$^{p.R141H}$ and *PMM2*$^{p.F119L}$ patient mutation lack a PAM located in the proper distance.

In my previous work the close vicinity of the human mutations in exon 5 was screened for potential edits predicted to have an effect. It was found that a cysteine to arginine substitution at amino acid position 139 has a deleterious effect (Pakari, 2021) (Figure 15 A).
To further investigate this mutation, I crossed a single surviving founder fish from the injected generation with wild-type fish to establish a stable F1 generation. Phenotyping of this F1 offspring revealed dramatic phenotypes including misdeveloped embryos (34 %; n = 23) with no head and brain formation and cyclops (4 %; n = 23) with an eye-field separation defects (Figure 15 B) The lethality of the offspring was 46% (n = 31). Quantification of the phenotypic spectrum from five batches showed only 16 % normally developing embryos (Figure 15 C). The phenotypic outcome indicates a potential effect of the *pmm2* mutations on multiple traits of development. As the founder fish was female and Pmm2 is maternally contributed, the strong phenotypic effects in high proportions of the embryos can be explained by the maternal contribution of mutant *pmm2* mRNA and protein, even though it was outcrossed to a wild-type male.

After raising the wild-type looking embryos to adulthood, genotyping of the F1 fish revealed individuals harboring two different mutations: a point mutation (p.C139R) or a 23-base pair deletion (p.V135Gfs*45) (Figure 15 D). Although base editors only nick DNA, unwanted insertions and deletions can be induced at the target site. The point mutation and deletion eliminated a PstI restriction enzyme site which allowed to determine the genotype via PCR and restriction digestion. Transcript analysis of the compound heterozygous F2 offspring from heterozygous F1 incrosses of the *pmm2* point mutation line and the deletion line confirmed the presence of both, the point mutation and deletion alleles (Figure 15 E).

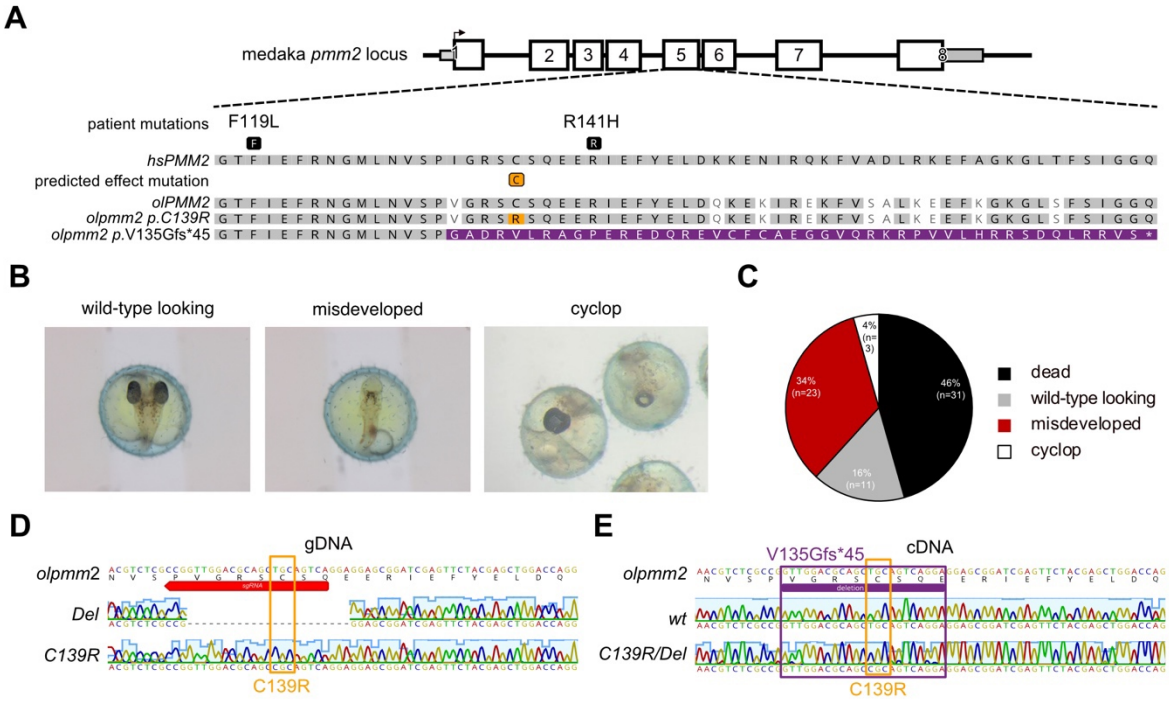

Figure 15: Generation of presumable hypomorphic patient-based *pmm2* mutation using CRISPR/Cas9 base editors. A) Multiple sequence alignment shows high conservation of PMM2 in human and medaka, especially in the region of the two most common patient mutations p.F119L and p.R141H. Cysteine mutation p.C139R in the close vicinity to human mutations is predicted to have an effect on the protein function (Pakari, 2021). Protein variants after genome editing are shown in the multiple sequence alignment. B) Representative images of occurring phenotypes in a female C139R founder fish outcross: wild-type like, misdeveloped and cyclops. C) Quantification of the phenotypic distribution of the offspring from five batches. D) Representative genotyping results from sanger sequencing of genomic DNA of F1 adults reveal point mutation (ABE8e, ACG>GCG, p.Cys139Arg) and deletion (p.Val135Glyfs*45) in *pmm2.* E) Sanger sequencing of cDNA of wild-type and compound heterozygous *pmm2*$^{C139R/V135Gfs*45}$ individuals confirm point mutation and deletion (extra peaks in the background) on transcript levels. cDNA, complementary DNA; Del, deletion; gDNA, genomic DNA; *ol,* Oryzias latipes

2.3.3 Compound heterozygous *pmm2*$^{C139R/V135Gfs*45}$ mutants show a temperature sensitive multisystemic phenotype

Human PMM2-CDG patients are typically compound heterozygous, meaning they carry two different mutant alleles, whereas their heterozygous parents show no symptoms. I incrossed the p.C139R point mutation medaka line with p.V135Gfs*45 deletion line to mimic the compound heterozygous state in medaka and assess the phenotype resulting from sublethal *pmm2* mutations in medaka.

Cysteine mutations have been described to cause thermosensitivity of PMM2 (Yu et al., 2023). Additionally, based on personal communication with Dr. Christian Thiel from the Heidelberg University Hospital, patients that suffer from a fever are often more accurately diagnosed. PMM2 functions as a homodimer and heat could disrupt the interaction which reduces enzyme activity even further. To create a more susceptible environment which

might trigger phenotypes more prominently, I compared the phenotypes at different temperatures. Medaka fish tolerate temperatures from 4 °C up to 35 °C without an impact on the development (Furutani-Seiki & Wittbrodt, 2004). The offspring of the mutant *pmm2* lines were incubated at the following temperatures: 22 °C, 26 °C, 28 °C and 32 °C. The most severely affected individuals showed multiple abnormalities in the compound heterozygous *pmm2* mutants: ocular defects with hypertelorism, reduced snout size, heart defects, intestine abnormalities and edemas all around the body (Figure 16 A). These malformations are also found in CDG-patients (Altassan et al., 2019; Chang et al., 2018; Pajusalu et al., 2024). At 22 °C, the most prominent phenotypic feature was a smaller snout size, indicating craniofacial defects. The higher temperature appeared to create a more susceptible environment, which accumulated the multisystemic phenotype of compound heterozygous fish more prominently (Figure 16 B).

The multisystemic phenotype in the compound heterozygous *pmm2* mutants indicated an effect of *pmm2* mutations on the development and the phenotypes resemble the symptoms of PMM2-CDG patients.

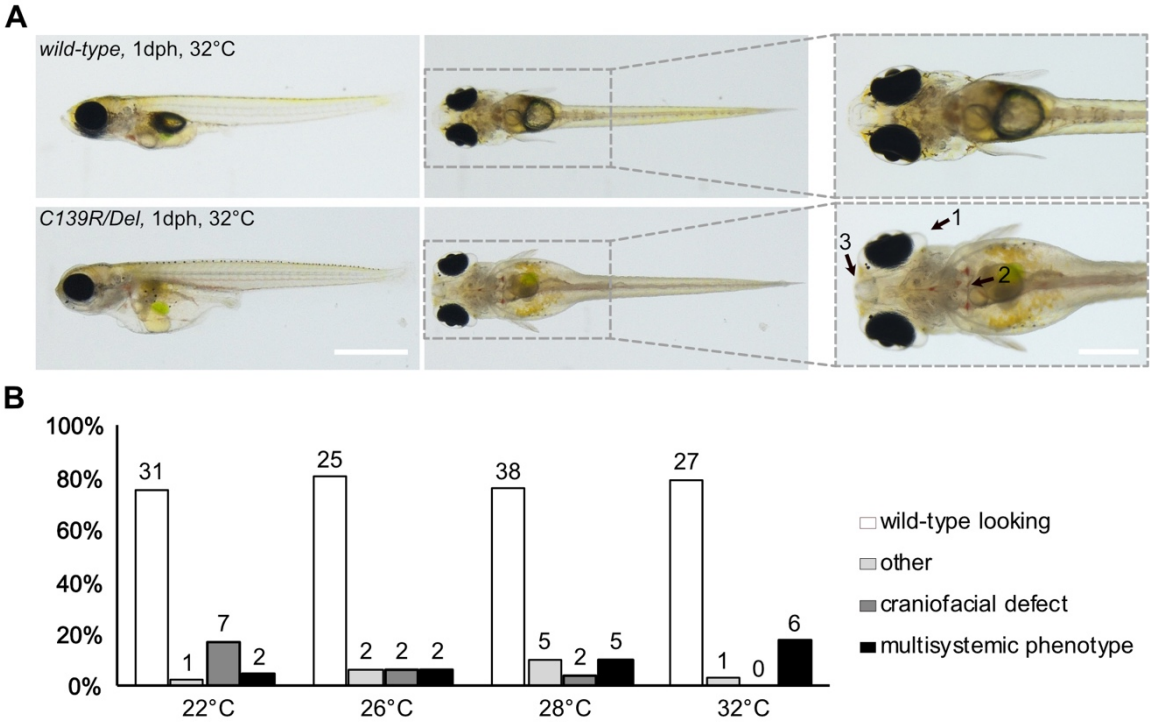

Figure 16: Temperature sensitive multisystemic phenotype in compound heterozygous *pmm2*$^{C139R/V135Gfs*45}$ mutants. A) Incrossing heterozygous *pmm2* p.C139R with *pmm2* p.V135Gfs*45 and incubation at 32 °C revealed a dramatic phenotype in compound heterozygous individuals. Hatchlings showed edemas around the eye (1) and whole body, heart abnormalities (2) and snout phenotypes (3) (indicated with black arrows). B) Quantification of the phenotypes of hatched individuals from heterozygous *pmm2* offspring incubated at 22 °C, 26 °C, 28 °C and 32 °C revealed a temperature-depended effect on the multisystemic phenotype. Scale bar 1 mm. dph, days post hatch

2.3.4 *Pmm2*$^{C139R/V135Gfs*45}$ medaka mutants resemble spectrum of patient symptoms

PMM2-CDG patients exhibit a wide spectrllum of clinical features with craniofacial defects being among the most recognizable. These defects are so specific that digital face recognition tools can predict if patients suffer from PMM2-CDG (Martinez-Monseny et al., 2019). Gross morphological analysis of medaka *pmm2* compound heterozygous mutants showed shorter snout and wider heads which indicated cartilage phenotypes (Figure 16 A).

To characterize the cartilage phenotype in more detail, I performed a double-staining with alcian blue and alizarin red of whole mount hatchlings. Alcian blue visualizes cartilages and alizarin red stains calcified bone structures. Comparing the ventral view revealed that the cartilage structure basihyal (b) was absent in the compound heterozygous hatchling. The bone structures cleithrum (cl) and branchiostegal ray (br) were less calcified or missing in the mutants (Figure 17 A). In the lateral view, the shortened snout morphology was apparent (Figure 17 B).

A previous characterization of a *pmm2* zebrafish mutant showed that the chondrocytes exhibited an aberrant morphology (Cline et al., 2012). Analysis of the *pmm2* medaka mutant revealed similar morphology of the chondrocytes in the meckel`s cartilages (Figure 17 C). The wild-type had ordered long shaped cells whereas the mutant showed round and less ordered chondrocytes. Additionally, the meckel`s and ceratohyal cartilage structures indicated a straightened angle (Figure 17 A). Quantification of the angles of Meckel`s and ceratohyal cartilages shows clear differences between wild-type to mutant *pmm2* hatchlings (Figure 17 D). The angle of the Meckel`s cartilage was 31 % wider in the compound heterozygous mutants and the angles of ceratohyal cartilage was 32 % wider.

The staining suggests that the reduced *pmm2* mutation had an impact on the development of craniofacial structures which lead to differences in cartilage and bone structures and specifically altered chondrocyte morphology.

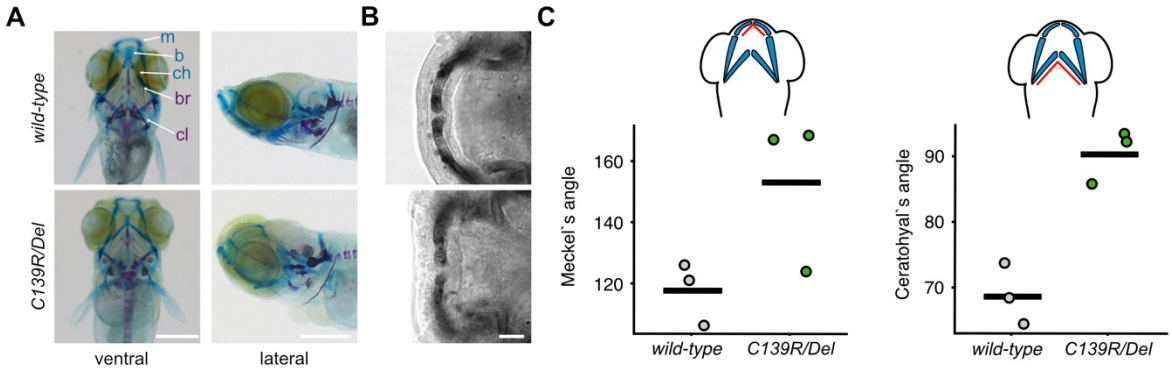

Figure 17: Craniofacial features affected in compound heterozygous *pmm2*$^{C139R/V135Gfs*45}$ mutants. A) Ventral and lateral view of alcian blue and alizarin red stained wild-type and compound heterozygous *pmm2* hatchlings. Mutants revealed defects in cartilage and bone structures. m: meckel`s cartilage, b: basihyal, br: branchiostegal ray, ch: ceratohyal cl: cleithrum; scale bars 500 µM. B) Confocal microscopy of Meckel`s cartilage shows chondrocyte morphology affected in the *pmm2* mutants. Scale bar 50 µM. C) Quantification of Meckel`s cartilage and ceratohyal angels show increased angels in the mutant hatchlings. wt, wild-type

Micro-computed tomography (µCT) enables high-resolution visualization of internal organs. By gross morphology analysis, *pmm2* compound heterozygous mutants showed defect in the intestine and heart (Figure 16 A). Comparing wild-type and mutant hatchlings stained with PTA on µCT images revealed further morphological differences. In sagittal and coronal views of the whole scan stack, the mutants presented a reduced brain size, kyphosis like forwards rounding of the back, intestine abnormalities, unhealthy liver and craniofacial deformations (Figure 18 A). From the ventral view in a single plane, the entire gut was visible. In the mutant hatchling, no food was visible inside the intestine and the anterior part was not coiling properly, indicating a gut-looping defect (Figure 18 B). Additionally, fluid was visible around the heart suggesting cardiac dysfunction (Figure 18 B). These results align with reports describing that patients suffer from similar multisystemic symptoms. This confirmed that the medaka model is suffering from a multisystemic phenotype where all organs are affected and is resembling the symptoms seen in PMM2-CDG patient.

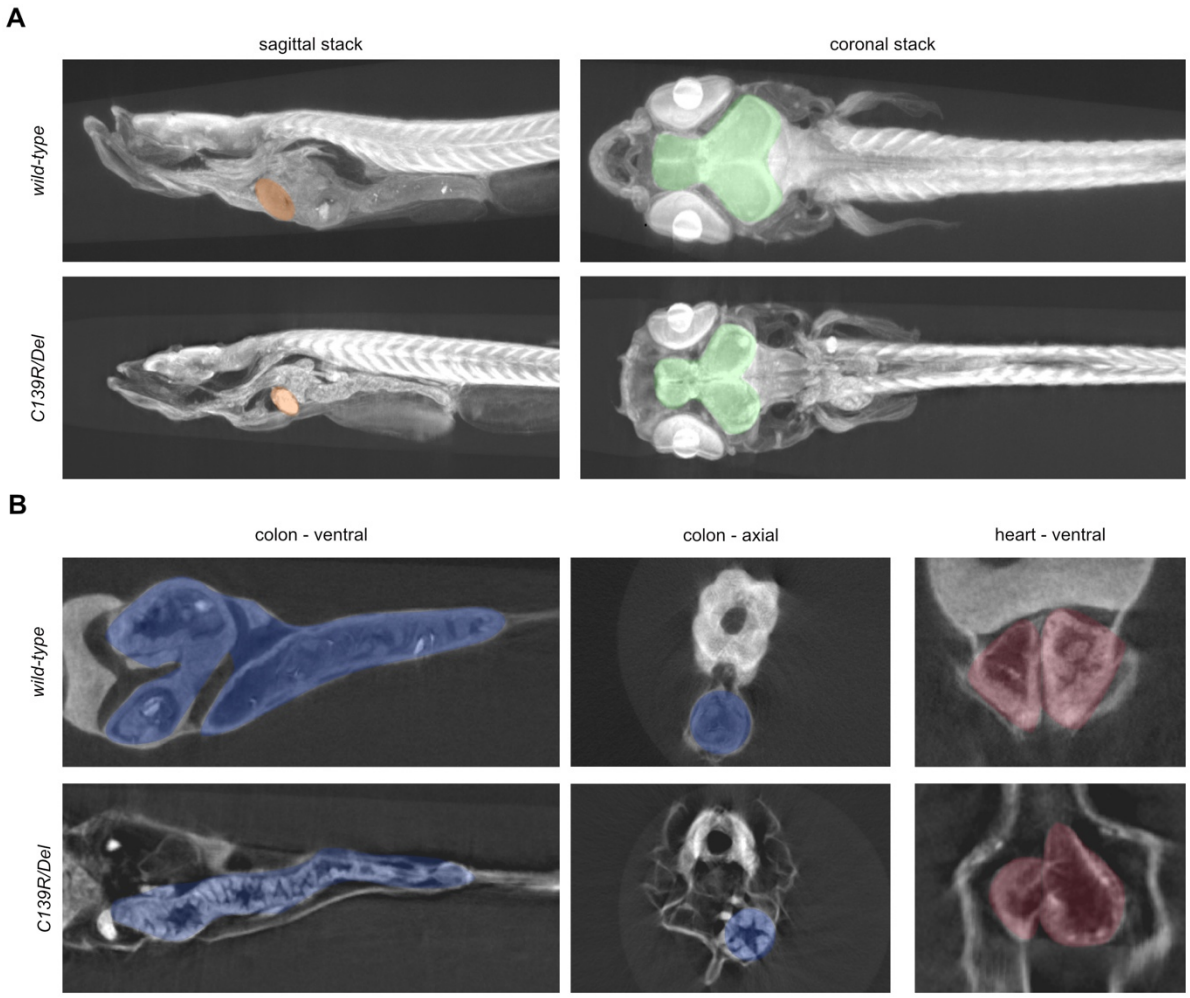

Figure 18: Micro-computed tomography reveals inner organ abnormalities in compound heterozygous *pmm2*$^{C139R/V135Gfs*45}$ mutants. A) Stacks of the whole hatchling of sagittal and coronal view comparing wild-type and compound heterozygous *pmm2* mutants. Liver (orange), brain (green), intestine (blue) and heart abnormalities (red) were visible in the mutant hatchlings. B) Single plain sections of the gut in ventral and axial view and the heart in ventral view showed gut-looping defects and no food in the intestine as well as heart abnormalities in the pmm2 mutant. Data produced jointly with Kristaps Kairiss (Wittbrodt/Weinhardt Lab, Heidelberg University).

2.3.5 Pmm2 mutations reduce enzyme activity and cause general hypoglycosylation of proteins

PMM2-CDG patients only survive because of residual enzyme activity as null mutations are not viable. Therefore, they exhibit protein hypoglycosylation rather than complete loss of glycosylation. The PMM2 enzyme provides mannose-1-phosphate, the precursor GDP-mannose needed during ER-glycosylation. Reduced PMM2 activities lead to reduced GDP-mannose levels and ultimately cause a decrease in complex *N*-glycan types, unoccupied glycosylation sites or trunked glycans to be transferred to nascent proteins. Hence, I wanted to measure the enzyme activity of the mutant *pmm2* fish and assessed the resulting hypoglycosylation state.

To determine whether the genetic mutations result in reduced enzyme activities, I performed an established biochemical PMM2 enzyme activity assay in collaboration with Virginia Geiger (Thiel Lab, Heidelberg University Hospital). Pmm2 enzyme activity showed 5 % remaining activity in compound heterozygous *pmm2* mutants (Figure 19A) which is comparable to the residual PMM2 activity seen in severely affected patients (Westphal et al., 2001b). In the heterozygous individuals the enzyme activity was around 50 % (Figure 19 A), as expected from the heterozygous parents of PMM2-CDG patients.
To prove that reduced enzyme activity causes hypoglycosylation of proteins, I performed lectin blots in collaboration with Andreas Hecker (Thiel Lab, Heidelberg University Hospital). Lectins against concanavalin A (ConA) detected high mannose *N*-glycan precursors and lectins against wheat germ agglutinin (WGA) bound to complex *N*-glycans. Both lectin plots indicated a hypoglycosylation state as the signal was reduced in the compound heterozygous individuals and differences in the lectin patterns of the bands were visible (Figure 19 B'). Quantification of the signal showed 61 % ConA lectin signal in the mutant hatchlings and 64 % for WGA lectins signal compared to the wild-type (Figure 19 B''). Both lectin plots confirmed reduced glycosylation which is expected to result from the reduced Pmm2 enzyme activity.

PMM2 mutations cause altered compositions of *N*-glycans. To assess these changes, *N*-glycan occupancy of wild-type and compound heterozygous *pmm2*$^{C139R/V135Gfs*45}$ hatchlings was analyzed in collaboration with Ivan Andújar-Martínez (Rapp Lab, MPI Magdeburg). Multiplexed capillary gel electrophoresis with laser-induced fluorescence detection (xCGE-LIF) analysis was performed to identify and quantify *N*-glycans. *N*-glycans were released from the proteins with via enzymatic digestion with PNGase F and analyzed with xCGE-LIF. Analysis of the *N*-glycan fingerprint confirmed a general hypoglycosylation state of the compound heterozygous *pmm2* mutants compared to wild-types across all *N*-glycan types (complex, hybrid and mannose-type). Especially the high mannose-type *N*-glycans (Man5-Man9) were reduced and precursor structures (Man3-Man4) were accumulating (Figure 19 C). A shift from high mannose *N*-glycans to low mannose complex *N*-glycan is visible.

These results of the hypoglycosylation situation in the Pmm2-CDG medaka model are comparable to the analysis of *N*-glycans from serum samples of PMM2-CDG patients (Garapati et al., 2024a). The reduced Pmm2 enzyme activity in medaka causes similar effects on the *N*-glycome as reported from human patient fibroblasts and sera samples.

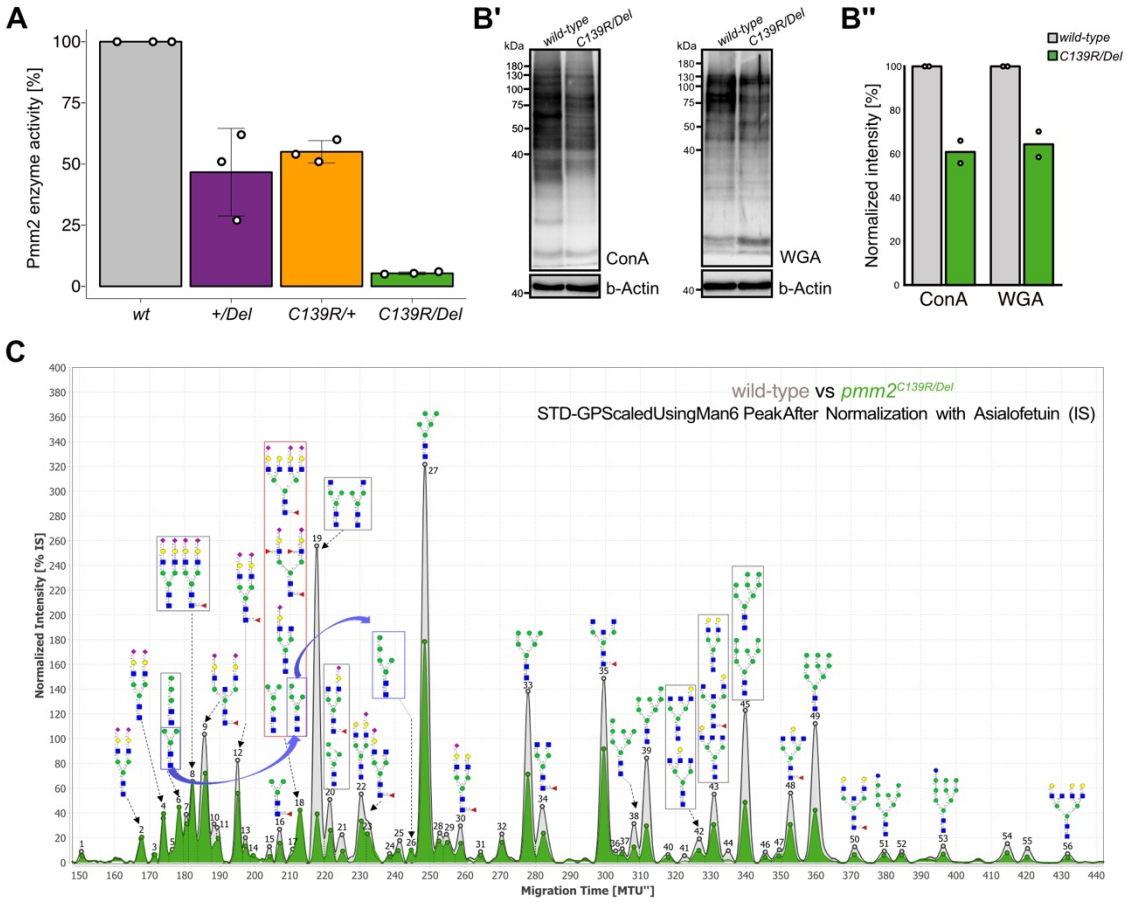

Figure 19: *Pmm2* mutations p.C139R and p.V135Gfs*45 reduce enzyme activity and cause a hypoglycosylation situation. A) Pmm2 enzyme activity assay of the four genotypes arising from crossing *pmm2*$^{p.C139}$ with *pmm2*$^{p.V135Gfs*45}$: wild-type, heterozygous V135Gfs*45, heterozygous C139R and compound heterozygous. Compound heterozygous *pmm2* mutants have 5 % remaining enzyme activity. Data produced jointly with Virginia Geiger (Thiel Lab, Heidelberg University Hospital). Mean ± sd of triplicates (each replicate n = 4 per genotype) shown. B) Lectin plots against ConA and WGA and quantitation of signal prove hypoglycosylation in compound heterozygous *pmm2* mutants compared to wild-types. Data produced jointly with Andreas Hecker (Thiel Lab, Heidelberg University Hospital). Mean of duplicates shown (replicate 1 had n = 4 and replicate 2 had n = 5 per genotype). C) Glycan analysis comparing *wild-type* (n =20) to compound heterozygous *pmm2* mutanst (n = 20) revealed hypoglycosylation state of mutants. Red peaks correspond to *wild-type* and blue peaks correspond to *pmm2*$^{C139R/V135Gfs*45}$. Blue arrows specify *N*-glycan sequences Man3, Man4 and Man5 enriched in the mutant vs. wild-type. Numbers represent *N*-glycan structures shown in Supplementary Table 1. Data produced jointly with Ivan Andújar-Martínez (Rapp Lab, MPI Magdeburg).

2.3.6 Macroscopically visible multisystemic *pmm2* phenotype occurs after hatch and survival of mutants decreases after hatch

After verifying morphologically that the fish model is resembling the patient's symptoms, proving biochemically a reduced enzyme activity and a hypoglycosylation state, I wanted to investigate the onset of phenotypic features in compound heterozygous *pmm2* mutants. Medaka fish develop extrauterine and the early development and hence phenotypic onset can be investigated in great detail in contrast to humans and other mammals.

To assess the early onset of phenotypes, I crossed the $pmm2^{C139R}$ with the $pmm2^{V135Gfs*45}$ line and compared the development from 1-cell stage to hatching (Figure 20 A). Before hatching, there are no macroscopic differences visible between the wild-type and compound heterozygous mutant embryos (Figure 20 B). After hatch a severe phenotype becomes visible: edemas around the eyes and body, abnormal heart phenotypes and no food in the digestive tract (Figure 20 B). Due the global phenotype in the mutant fish, they cannot survive and there is an increase in lethality after hatching at 32 °C (6 dpf) (Figure 20 C). Like in patients there is spectrum of phenotypes visible which can vary from batch to batch in medaka. However, the global dramatic phenotype is consistently observed in every batch and some milder versions might occur.

The fish model seems to mimic the patient situation in which the early development is not affected, but after hatch (equivalent birth in humans) the effects become apparent.

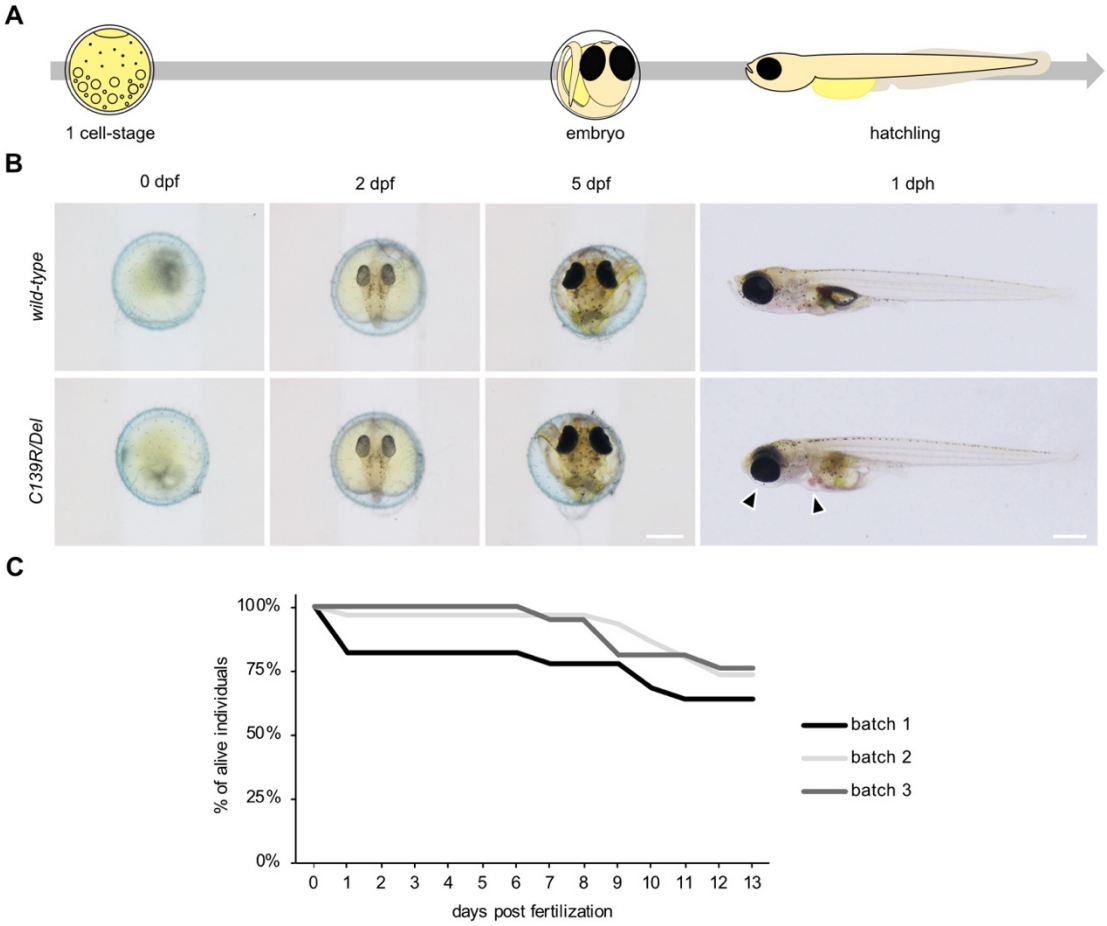

Figure 20: Multisystemic phenotype occurs after hatch in compound heterozygous *pmm2* mutants and reduce the viability. A) Schematic timeline of medaka development from 1-cell stage to hatchling. B) Comparison of the development from 0 dpf to 1 dph of wild-type and compound heterozygous *pmm2*$^{C139R/V135Gfs*45}$ individuals showed occurrence of multisystemic phenotype only after hatching. C) Lethality of offspring from *pmm2*^{C139R} crossed to *pmm2*^{V135Gfs*45} line from 0 to 13 dpf. Scale bar 0.5 mm for embryos and 1 mm for hatchlings. del, deletion; dpf, days post fertilization; dph, days post hatch

2.3.7 Supplementation with D-Mannose does not rescue multisystemic *pmm2*$^{C139R/V135Gfs*45}$ phenotypes

As GDP-mannose levels are lower in patients, supplementing with mannose has been suggested as potential therapy in patients. PMM2-CDG fibroblasts benefited from mannose supplementation via biochemical validation (Rush et al., 2000) and in pregnant mouse feeding mannose rescued early lethality (Schneider et al., 2012). Benefits from supplementation of mannose in PMM2-CDG patients is debated (Taday et al., 2020; Witters et al., 2021).

Gross morphology analysis indicated that the multisystemic phenotypes of *pmm2*$^{C139R/V135Gfs*45}$ mutants becomes apparent only after hatch. This suggests that the early development is not severely affected and raised the question, if supplementation with

sugars like D-mannose could improve physiological defects to prevent subsequent developmental effects.

Because of the findings in mammals, I investigated if the survival of compound heterozygous *pmm2* mutants in medaka can increased by supplementing the media with D-mannose. To test the effect of mannose in the mutant fish, I supplemented the standard ERM media with 25 mM D-Mannose at stage 9 or with 50 mM D-Mannose at stage 32 (Iwamatsu, 2004) (Figure 21 A). Prior to treatment, the embryos were rolled on sandpaper to increase the permeability through the chorion. Both groups were treated until 5 dph and genotyped at 9 dph. Survival of compound heterozygous *pmm2* mutants was not improved with the D-Mannose treatment (Figure 21 B) and multisystemic phenotypes were visible. The supplementation did likely not lead to an effect due to insufficient penetration and uptake of the mannose into the cells.

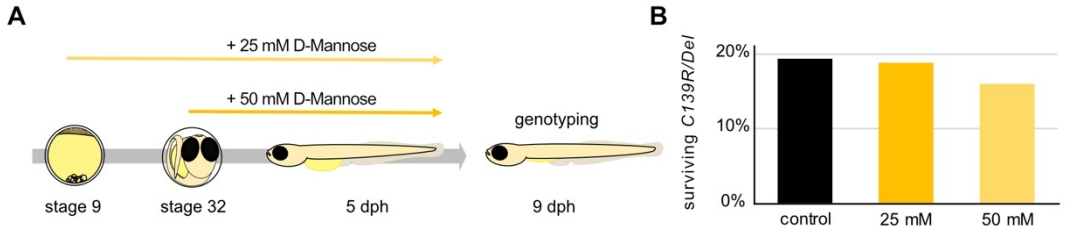

Figure 21: Mannose supplementation in compound heterozygous *pmm2*$^{C139R/V135Gfs*45}$ does not rescue their survival. A) Schematic representation of D-Mannose supplementation screen. Offspring from *pmm2*^{C139R} crossed to *pmm2*^{V135Gfs*45} line were rolled on sandpaper and incubated with 25 mM D-Mannose from stage 9 onwards or with 50 mM D-Mannose from stage 32 onwards. Supplementation of the media with mannose continued until 5 dph and hatchlings were genotyped 9 dph. B) Quantification of surviving compound heterozygous *pmm2* mutants upon D-Mannose supplementation. dph, days post hatch; mM, millimolar

2.3.8 Biotin supplementation slows lethality of *pmm2*$^{C139R/V135Gfs*45}$ mutants

In PMM2-CDG patient derived fibroblasts a reduction of biotinidase activity was identified. Based on these results, biotin was given to patients and it improved their cognitive abilities (Himmelreich et al., 2023). I treated the offspring of heterozygous *pmm2*^{C139R} crossed with *pmm2* ^{V135Gfs*45} mutant lines with biotin to explore the potential of biotin to improve viability and phenotypic defects of *pmm2* deficient medaka. Embryos were dechorinated at stage 34, prior to biotin supplementation for enhanced biotin uptake. As a control, to exclude toxic effects of biotin, wild-type embryos were supplemented with biotin as well. Both groups were treated until from stage 34 to 5 dph and genotyped at 18 dph (Figure 24 A). The lethality rate of offspring from *pmm2*^{C139R} crossed to *pmm2*^{V135Gfs*45} line was slower upon biotin supplementation compared to non-treated offspring and biotin

supplementation did not affect wild-type embryo survival (Figure 24 B). However, no surviving individual was genotyped as compound heterozygous indicating that the supplementation did not rescue developmental defects until 18 dph.

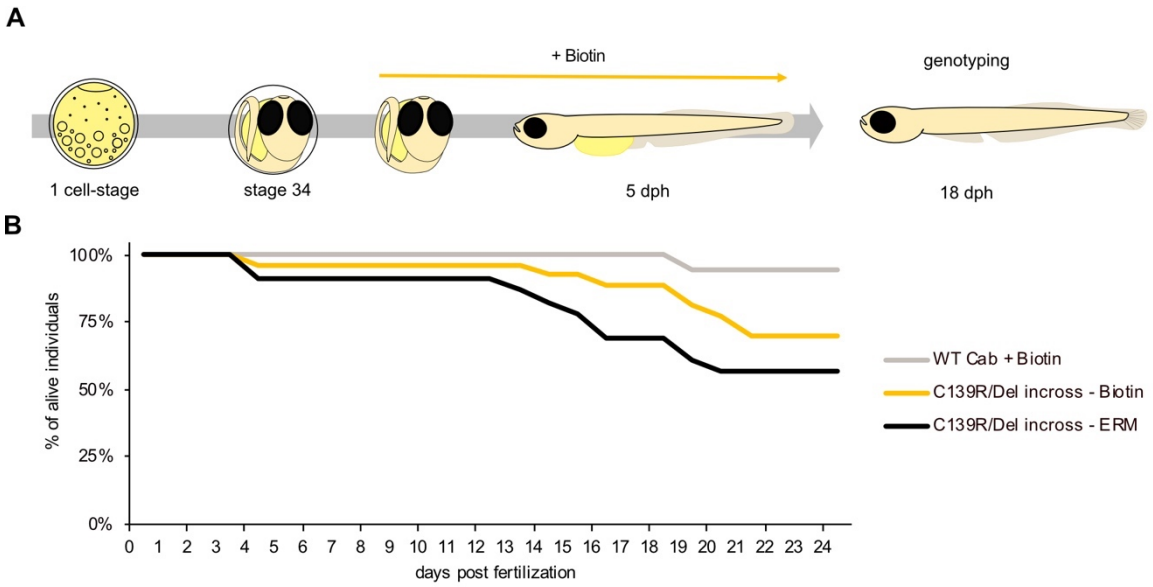

Figure 22: Biotin treatment reduces death rate of compound heterozygous *pmm2*$^{C139R/V135Gfs*45}$ mutants. A) Schematic representation of biotin supplementation in the offspring from *pmm2*^{C139R} crossed to *pmm2*^{V135Gfs*45} line. Embryos were dechorinated at stage 34 and incubated with 0.25 mg/ml biotin in ERM. Supplementation of the media with biotin continued until 5 dph and the experiment was determined at 18 dph. B) Lethality of wild-type control embryos supplemented with biotin, offspring from *pmm2*^{C139R} crossed to *pmm2*^{V135Gfs*45} line incubated with biotin or kept in ERM as control. dph, days post hatch

2.3.9 Functional analysis of *pmm2* mRNA variants and their effect on lethality and phenotypic rescue

2.3.9.1 Providing wild-type medaka *pmm2* mRNA is able the rescue the multisystemic phenotype and reduce death rate

Supplementations with D-Mannose and Biotin could not improve the physiological defects to prevent subsequent developmental effects. As PMM2-CDG patients suffer from reduced enzyme activity which causes the multisystemic phenotypes, boosting the activity of Pmm2 or providing more Pmm2 early on could rescue the developmental phenotype. To test this assumption, I sought to provide more Pmm2 to the offspring of *pmm2* mutants in medaka (Figure 23 A).

Offspring of heterozygous *pmm2*^{C139R} crossed with heterozygous *pmm2*^{V135Gfs*45} mutants had a lethality rate of 38 % until three weeks after hatch (Figure 23 B) and no compound heterozygous individuals survived (Figure 23 A, C). After I injected *pmm2* mRNA into 1-cell stage *pmm2* mutant embryos (Figure 23A), 12 % compound heterozygous individuals

survived and the overall lethality was reduced to 26 % (Figure 23B, C). This confirms that the phenotype is actually caused by reduced Pmm2 enzyme activity as I could rescue the survival of compound heterozygous *pmm2* mutants. Moreover, this experiment rules out any off-target effects caused by genome editing. Providing *pmm2* mRNA at the 1-cell stage boosted enzyme activity early on and could prevent developmental defects occurring after hatch. These results indicate that gene therapy may be a potential therapeutic approach for PMM2-CDG patients.

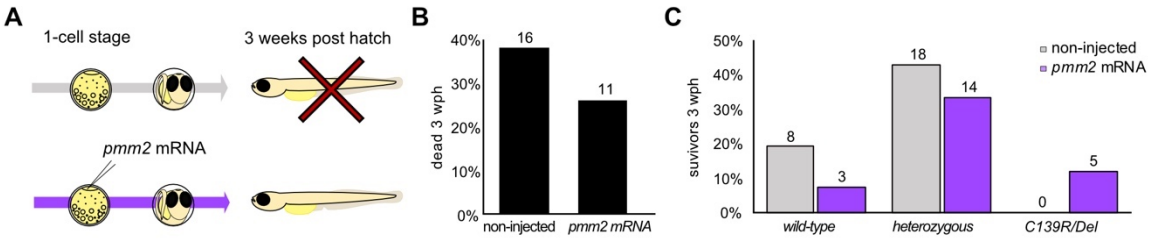

Figure 23: *Pmm2* mRNA injections rescues survival of compound heterozygous *pmm2*$^{C139R/V135Gfs*45}$ mutants. A) Illustration representing the experimental design: typically compound heterozygous *pmm2* mutants do not survive until 3 wph. Injection of *pmm2* mRNA into 1-cell stage embryos may potentially rescue the survival. B) Lethality of individuals until 3 wph of non-injected and *pmm2* mRNA injected individuals from heterozygous *pmm2* crosses. C) Genotypes of surviving hatchlings at 3 wph. wph, weeks post hatch

2.3.9.2 Injections of mutant mRNA F122L rescues the survival of compound heterozygous *pmm2* mutants

As the delivery of *pmm2* mRNA during early development rescued the multisystemic phenotype of *pmm2* mutants in medaka, I investigated next if approaches to enhance Pmm2 activity, e.g., through molecular chaperones or transcriptional enhancers, would rescue the *pmm2* phenotypes. If the phenotype is caused by reduced enzyme activities, rescue by providing more of mutant variants should also be able to rescue phenotypes, reduce lethality and mimic the treatment with pharmacological chaperons.

The human PMM2 p.R141H patient mutation is considered to encode for an inactive enzyme (Kjaergaard et al., 1999) whereas the p.F119L has residual enzyme activity. Therefore, I injected wild-type, the patient based C139R and exact patient ortholog F122L *pmm2* mRNA into 1-cell stage embryos from of heterozygous *pmm2*^{C139R} crossed to heterozygous *pmm2*^{V135Gfs*45} (Figure 24 A). As most of compound heterozygous mutants do not survive longer than 13 days post fertilization, I chose to genotype the offspring at 13 dpf. Contradictory to previous results, injections of wild-type *pmm2* mRNA did not reduce the lethality of the offspring in general (Figure 24 B). However, in compound heterozygous hatchlings, wild-type mRNA injections led to 27 % survival (Figure 24 C) and

rescue of the multisystemic phenotype (Figure 24 D) consistent with my previous results. Providing the mutant mRNAs C139R and F122L did not reduce the lethality rate (Figure 24 B). Injections of mutant C139R *pmm2* mRNA did not increase viability of the mutants but F122L *pmm2* mRNA injected embryos revealed 20 % survival of compound heterozygous individuals. Surprisingly, the multisystemic phenotype occurred in heterozygous individuals in mutant mRNA injected embryos, which might indicate a dominant effect of the mutant mRNA. As the Pmm2 protein acts as a homodimer, providing more of mutant protein into a balanced heterozygous background, might cause reduced enzyme activities. The multisystemic phenotypes are not detected in heterozygous hatchlings injected with wild-type mRNA.

Overall, surviving compound heterozygous *pmm2* mutant upon mutant *pmm2* F122L mRNA injections indicate that the reduced enzyme activity in patients, could be boosted by increased translation of *pmm2* or stabilizing the mutant protein with molecular chaperons.

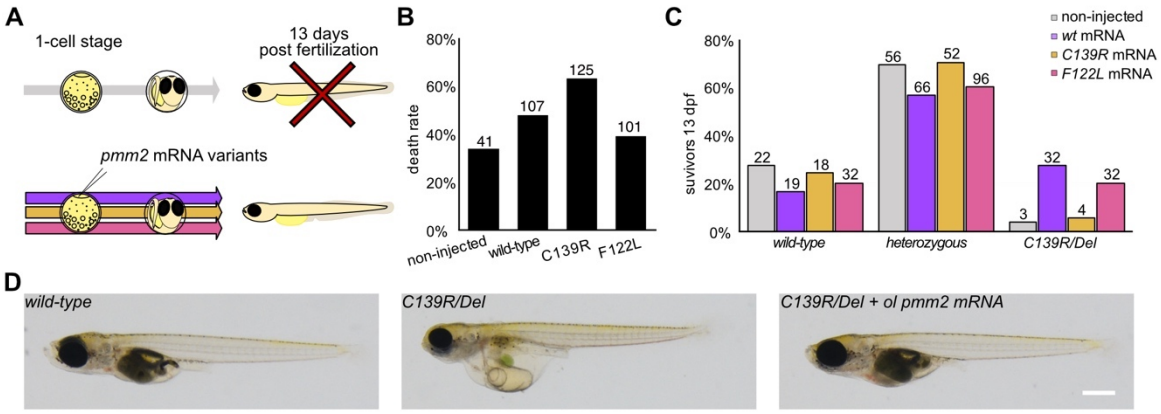

Figure 24: Providing *pmm2* mRNA is able to rescue the multisystemic phenotypes of *pmm2*$^{C139R/V135Gfs*45}$ mutants whereas mutant F122L mRNA can rescue survival until 13 dpf. A) Schematic representation of the experiment: most compound heterozygous individuals from *pmm2* mutants do not survive past 13 dpf. Injection of *pmm2* mRNA variants could potentially improve their survival. B) Lethality of individuals cumulative until 13 dpf of non-injected and *pmm2* mRNA variant injected individuals from heterozygous *pmm2* crosses. C) Survival rate by genotype of surviving hatchlings at 13 dpf. D) Images of offspring at 5 dph injected with wild-type *pmm2* mRNA. Providing wild-type *pmm2* mRNA rescues the multisystemic phenotype of hatchlings from heterozygous *pmm2* crosses. Scale bar 0.5 mm. dph, days post hatch; ol, Oryzias latipes

2.3.9.3 Providing human PMM2 mRNA reduces death rate and rescues multisystemic *pmm2* phenotype

The glycosylation machinery enzymes and Pmm2 are evolutionary highly conserved. I hypothesized that providing human *pmm2* mRNA would similarly rescue the multisystemic compound heterozygous *pmm2* phenotype (Figure 25 A). I injected the human *PMM2*

mRNA into 1-cell stage embryos from heterozygous *pmm2* crosses and counted the dead individuals until 13 dpf and genotyped the surviving hatchlings. The death rate was reduced to 10 % (Figure 25 B) compared to non-injected ones from the previous experiment. Providing human *PMM2* mRNA was able to greatly enhance the survival of compound heterozygous *pmm2* mutants (Figure 25 C). Assessing the gross morphology of hatchlings at 5 dph showed rescue of the multisystemic phenotype of *pmm2* mutants (Figure 25 D).

These results demonstrated that the human *PMM2* mRNA can substitute for its ortholog in medaka in the highly conserved glycosylation pathway, and rescued the corresponding developmental defects.

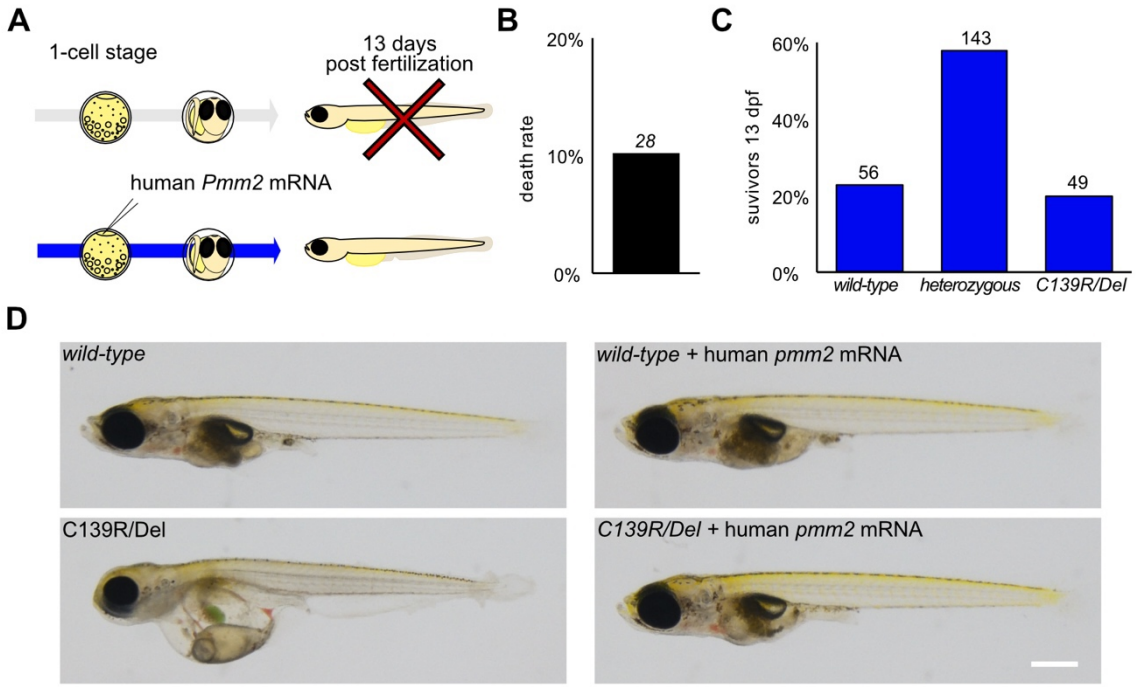

Figure 25: Injections of human *Pmm2* mRNA rescues multisystemic *pmm2* phenotype in medaka. A) Schematic representation of the experiment: typically, non-injected compound heterozygous *pmm2* mutants do not survive past 13 dpf. Injection of human *pmm2* mRNA could potentially rescue their survival. B) Death rate until 13 dpf of human *pmm2* mRNA injected individuals from heterozygous *pmm2* crosses. C) Survival rate by genotype of hatchlings at 13 dpf. D) Images of offspring at 5 dph. Providing human *pmm2* mRNA rescues the multisystemic phenotype of hatchlings from heterozygous *pmm2* crosses. Scale bar 0.5 mm. dph, days post hatch; ol, Oryzias latipes

2.3.10 Identification of candidate proteins affected by hypoglycosylation via proteomics

Providing *pmm2* mRNA at the 1-cell stage successfully rescued the multisystemic *pmm2*$^{C139R/V135Gfs*45}$ phenotype but supplementing with biotin and mannose did not lead to

survival of compound heterozygous *pmm2* mutants. These results suggest that the developmental defects are too severe to be rescued by physiological improvements and raises the questions at what point disease progression starts on a molecular level and which proteins are primarily affected. As PMM2-CDG patients suffer from similar symptoms, it is likely that specific proteins are more susceptible to hypoglycosylation or their function is more dependent on correct glycosylation.

To identify affected proteins and pathways that are differentially regulated due to hypoglycosylation, I performed bottom-up proteomics to analyze the whole proteome. My goal was to compare differentially expressed proteins between wild-type and compound heterozygous *pmm2*$^{C139R/V135Gfs*45}$ mutants. The glycosylation of proteins impacts protects them from proteolytic degradation. Upon hypoglycosylation, misfolded proteins accumulate in the ER and this stress triggers the unfolded protein response (UPR) which promotes degradation of misfolded proteins (Rita Lecca et al., 2005a; Shang et al., 2002; Zdrazilova et al., 2023).

The multisystemic *pmm2* mutant phenotype occurs macroscopically only after hatch, but the underlying defects on the protein level might have already changed at earlier stages. I analyzed the proteomes at two different developmental stages: before and after onset of phenotypes.

Samples for bottom-up mass spectrometry analysis were collected at the embryonic stage 5 dpf (stage 35) and after hatching (5 dph), then snap frozen in liquid nitrogen (Figure 26 A). Lysates were prepared simultaneously for all samples and genotyping was performed directly from the lysates to avoid collecting any material for genotyping (e.g., tail or eyes). To ensure equal sample quality, lysates were assessed by SDS-PAGE (Supplementary Figure 4). The lysates were submitted to Dr. Marcin Luzarowski at the Core Facility for Mass Spectrometry and Proteomics of the Center for Molecular Biology (ZMBH) of Heidelberg University, where proteins were purified with Sp3 beads and digested with trypsin. The final shot-gun proteomics run was performed in data-dependent acquisition mode (DDA).

A total of 8459 proteins were identified of which 5701 proteins remained after filtering for proteins supported by at least two unique peptides and which were detected in at least three out of five replicates, within at least one experimental group. The cut-off criteria for more and less abundant proteins was p-value ≤ 0.05 and log-2-fold change ≥ ± 1. Volcano plots show differentially detected proteins at the two developmental stages (Figure 26 B). More changes were present in the later stage, which comes along with the phenotype being more prominent. Interestingly, at the earlier stage, differentially detected proteins are present (Figure 26 B). Even though the phenotype is macroscopically not yet visible,

the underlying protein levels have changed. Comparison of the differentially abundant proteins between both stages revealed minimal overlap among the upregulated (red) and downregulated (blue) ones (Figure 26 C). Only one protein was found more abundant protein in both stages: prr33. This protein is medaka specific and has not been extensively studied. It is predicted to be a mucin-6-like isoform. Mucins are the major component of mucus and are known to be highly glycosylated proteins. They are heavily *O*-glycosylated and contain a few *N*-glycosylation sites. *N*-glycosylation in the ER precedes *O*-glycosylation in the Golgi and therefore defects in *N*-glycosylation could affect both kinds of glycosylation. Since mucins are known to be glycosylated and prr33 is medaka specific, it was not considered a relevant studying disease progression in a human context but confirmed the feasibility of the approach to detect differentially regulated glycoproteins (Supplementary Figure 4).

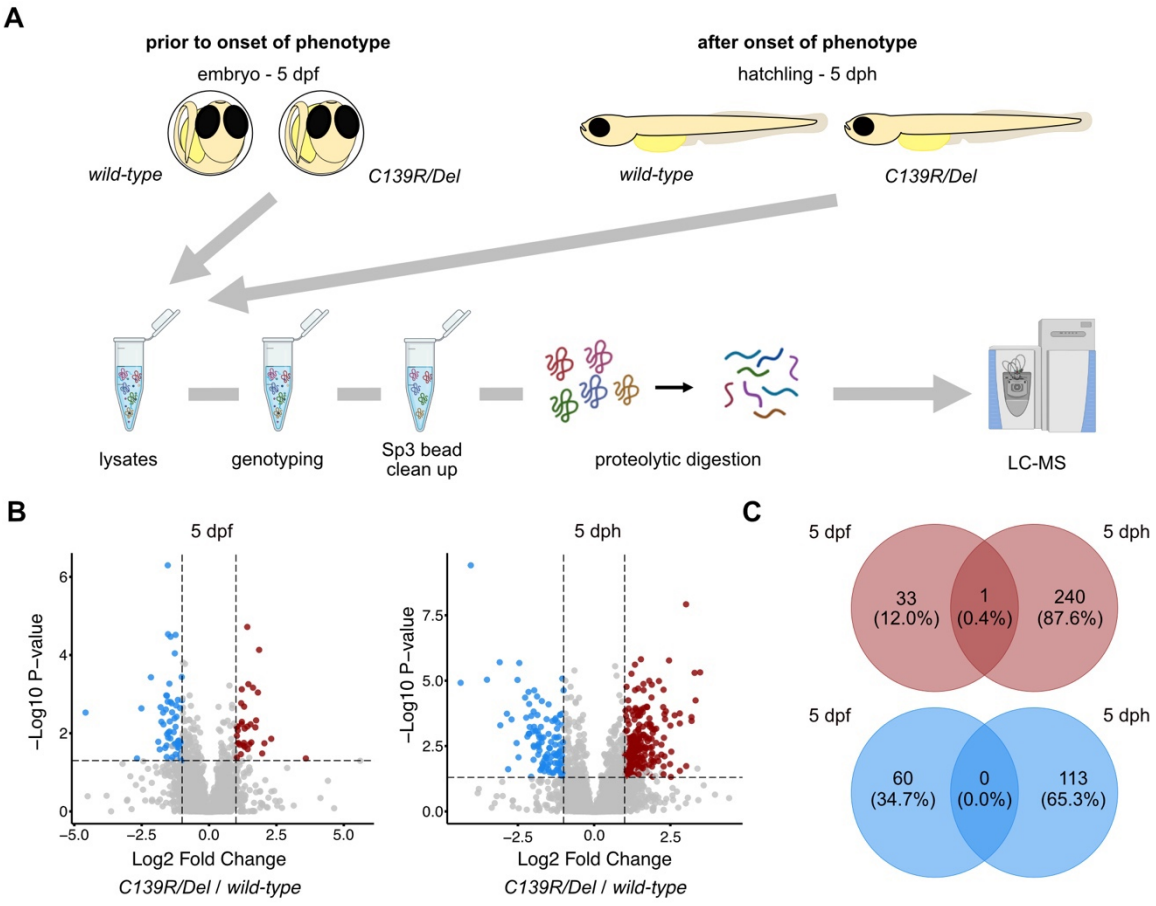

Figure 26: Bottom-up mass spectrometry to find differentially expressed proteins before and after onset of phenotype. A) Schematic representation of the workflow from sample preparation to mass spectrometry run: embryos and hatchlings were collected and lysates were prepared from which genotyping was performed. Sp3 bead clean-up and trypsin digestion was performed. B) Volcano plots at two stages: 5 dpf and 5 dph. Red dots represent significantly upregulated proteins and blue dots downregulated proteins. Cut-off values are p-value ≤ 0.05 and log-2-fold changes ≥ ± 1. C) Venn diagram representing overlapping differentially detected proteins. dpf, days post fertilization; dph, days post hatch

Since the comparison of differentially abundant proteins between the two stages revealed no overlap, I assumed that affected proteins might be identified by comparing fold changes across stages. Interestingly, I observed that some proteins were initially downregulated and later upregulated, or vice versa. This analysis identified five proteins: Abcf3 (H2MZQ6), Rp2 (H2MMY6), Vaspb (H2MDI3), Pgm3 (H2MR65) and Srsf2a (A0A3B3IH33) (Figure 27 A).

ABCF3 belongs to the ATP-binding cassette transport family, is anchored in the ER membrane and plays a role in resistance against flaviviruses infections (Peterson et al., 2019). Two *N*-glycosylation motifs were estimated from the ABCF3 protein sequence (Gupta R, 2022) but so far is has not been identified as a glycoprotein, in contrast to other ABC transporters which are shown to be modified by *N*-glycosylation (Draheim et al., 2010). The protein RP2 (retinitis pigmentosa gene 2) is associated with X-linked retinitis pigmentosa (Dandekar et al., 2004). RP2 is involved in protein trafficking to photoreceptor outer segments in the eye (Holopainen et al., 2010). Although it has three predicted *N*-glycosylation motifs (Gupta R, 2022), there are no studies on its function as a glycoprotein. VASPB (Vasodilator stimulated phosphoprotein b) is involved in cytoskeleton remodeling (Benz et al., 2009). No predicted *N*-glycosylation sites were found in the medaka ortholog. The PGM3 (Phosphoacetylglucosamine mutase) protein converts GlcNAc-6-P into GlcNAc-1-P, an essential step for multiple glycosylation pathways including protein *N*- and *O*-glycosylation. SRSF2a (serine and arginine rich splicing factor 2a) is involved in mRNA splicing and predicted to have one *N*-glycosylation motif (Gupta R, 2022).

Examining the heat map of missing values together with the clustering pattern revealed clear differences between the two developmental stages. The proteomes at dpf and dph exhibit different clusters indicating substantial changes in protein expression over time already in the wild-type (Figure 27 B). The two developmental stages seem to be distinct from each other in terms of development.

Due to the developmental distance of the embryo versus the hatchling, the comparison of their proteomes at two stages to identify progressively lost proteins is not feasible. Instead, the proteomics data shows multiple significant differences comparing wild-type with compound heterozygous *pmm2* mutants within the two developmental stages.

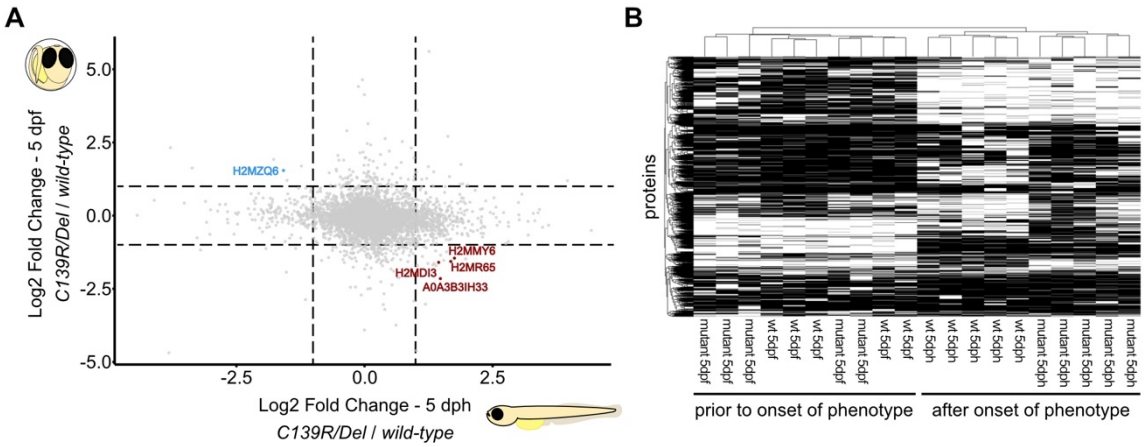

Figure 27: Proteomics data revealed that embryonic and hatching stage proteomes in medaka are distinct. A) Scatter plot comparing fold changes at embryonic (dpf) and hatchling (dph) stages. Blue dots indicate proteins more abundant at dpf and less abundant at dph whereas red dots represent less abundant proteins at dpf and more detected at dph. Colored are only proteins with p-value ≤ 0.05 (for both pairs: *pmm2*$^{C139R/V135Gfs*45}$ 5 dph vs *wild-type* 5 dph and *pmm2*$^{C139R/V135Gfs*45}$ 5 dpf vs *wild-type* 5 dpf) and fold change ± 1. B) Heatmap of missing values with cluster dendrogram of the proteome profiles from wild-type and compound heterozygous *pmm2* mutants at the two stages (dpf and dph) across all five replicates. dpf, days post fertilization; dph, days post hatch; wt, wild-type

2.3.11 Gene enrichment analysis reveal multiple pathways affected in *pmm2* mutants

To characterize the molecular phenotype of *pmm2* mutants, I performed gene enrichment analysis to identify affected biological pathways on differentially detected proteins at embryonic stage 5 dpf (Figure 28 A) and at hatching stage 5 dph (Figure 28 B) separately. The significant hits went through Gene Ontology (GO) term enrichment analysis in ShinyGO v0.82 (Ge et al., 2020) in the main class of biological processes. Among the 94 differentially up- and downregulated proteins at 5 dpf, processes involved retinal layer formation (GO:0010842), regulation of mRNA splicing via spliceosome (GO:0048024), regulation of mRNA processing (GO:0050684) and mRNA processing (GO:0006397) (Figure 28 A). At 5 dph, 354 differentially up- and downregulated proteins were subjected to GO term analysis and the top differentially regulated processes were cristae formation (GO:0042407), proteolysis (GO:0006508) and two overarching groups involved in localization/transport of proteins and catabolic/metabolic processes (Figure 28 B).

N-glycosylation primarily occurs on secreted or membrane-bound proteins. To identify candidate glycoproteins affected by *pmm2* mutations, I filtered the significantly differentially detected proteins based on their subcellular location data from UniProt. I selected those annotated as “membrane”, “secreted”, “Golgi” and “extracellular” and removed those annotated as “mitochondria”. For 5 dpf, 18 differentially detected proteins were submitted to GO term enrichment analysis. Differentially regulated processes

involved axon regeneration (GO:0031103), neuron projection regeneration (GO:0031102), response to axon injury (GO:0048678) and epithelium development (GO:0060429) (Figure 28 C). For 5 dph, 96 proteins were analyzed for their biological processes after filtering for their subcellular localization. The top differentially regulated pathways were homotypic cell-cell adhesion (GO:0034109), platelet aggregation (GO:0070527), protein kinase C signaling (GO:0070528), axis elongation (GO:0003401) and multiple processes involved in the transport/localization (Figure 28 D).

The heat shock protein A5 (hspa5), also known as immunoglobulin protein (BiP), is a well-characterized chaperone and master regulator of the UPR. BiP interacts with unfolded proteins and activates UPR stress sensors. Remarkably, hspa5 was more abundant in the compound heterozygous *pmm2* mutants at the hatchling stage and indicates upregulation of the UPR pathway.

Collectively, this analysis suggests that *pmm2* mutations affect multiple molecular pathways. In the embryonic stage before onset of the multisystemic *pmm2* mutant phenotype mRNA regulation and eye formation pathways appear dysregulated. After hatching when the severe phenotype is present, mitochondria are affected together with transport and metabolic processes.

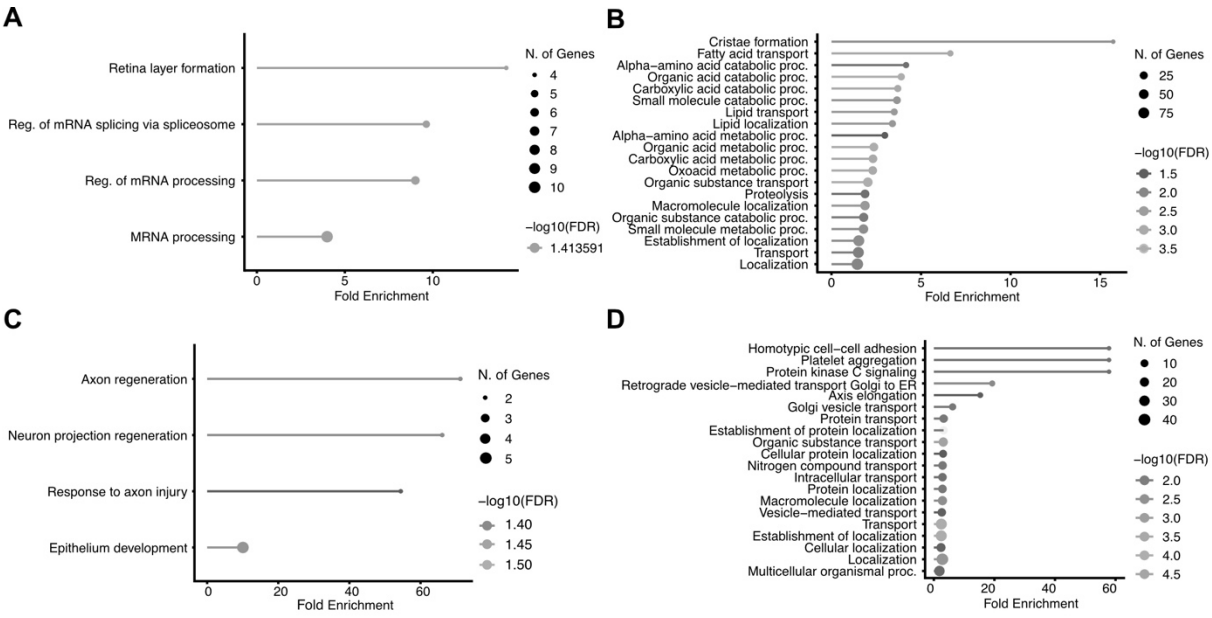

Figure 28: Gene Ontology term enrichment analysis for biological processes shows molecular pathways affected in compound heterozygous *pmm2*$^{C139R/V135Gfs*45}$ mutants. A) GOBP of 94 differentially regulated proteins at 5 dpf. B) Top 20 GOBP of 354 differentially regulated proteins at 5 dph. C) GOBP of 18 differentially regulated proteins filtered for subcellular location in membrane, secreted, Golgi and extracellular at 5 dpf. D) Top 20 GOBP of 96 differentially regulated proteins filtered for subcellular location in membrane, secreted, Golgi and extracellular at 5 dph. dpf, days post fertilization; dph, days post hatch; ER, endoplasmic reticulum; GOBP, Gene Ontology Biological Process

2.3.12 Selecting candidate genes associated with Pmm2-CDG phenotype

To identify potential candidates' contributions to the phenotypes in *pmm2* mutants, I selected genes for functional validation using CRISPR/Cas9 and base editors. Candidates were selected based on differential abundance from the proteomics analysis, presence of predicted *N*-glycosylation sequon, expression data and their molecular function.

I separately subjected the significantly differentially upregulated and downregulated proteins to GO term enrichment analysis (Figure 29 A). Additionally, I examined the top 10 differentially regulated proteins. Potential candidates were screened for predicted *N*-glycan motifs in medaka and, if present, their human ortholog was screened for potential predicted *N*-glycosylation motifs with NetNGlyc (Gupta R, 2022). Existing *in situ* data from the ZFIN database (Bradford et al., 2022) was examined for expression patterns of the candidate proteins and their molecular functions were investigated to make educated guesses about their involvement in disease progression of the *pmm2* phenotype (Figure 29 A). Ultimately, a list of ten potential glycoprotein candidates was compiled and guide RNAs were designed to target them preferentially in the predicted *N*-glycosylation motif. If the *N*-glycosylation sequon could not be targeted, guide RNAs were designed to install premature termination codons or loss of function mutations (Figure 29 B).

A

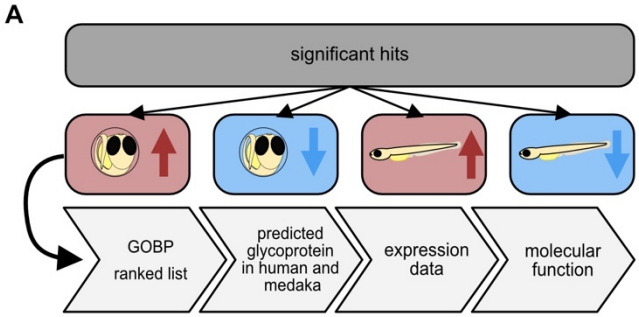

B

gene	*N*-Glyco sites	target
rfc4	1	N102xS > S/G/DxS
rp2	4	N200xS > NxG
srsf2a	1	Q88 > *
acsl5	1	W130 > *
immt	2	N232xS > NxF
crk	1	N112xS > NxF
mucin	5	Q34 > *
emc10	1	KO exon 3

Figure 29: Selection of potential Pmm2-CDG phenotype causing candidates. A) Filtering pipeline for candidates: Significantly differentially regulated proteins in the two stages 5 dpf and 5 dph were submitted to gene ontology biological process (GOBP) enrichment analysis and the top 10 differentially regulated proteins were analyzed. Candidate protein sequences were screened for predicted *N*-glycosylation motifs, existing *in situ* data from zebra fish and molecular functions were considered. B) List of 10 candidates with gene name, predicted number of *N*-glycosylation sites and crRNA target site with predicted editing outcome in red. KO; knockout; *, stop codon

2.3.13 Loss of rod photoreceptors in *pmm2* medaka mutants hint towards retinitis pigmentosa – a symptom seen in PMM2-CDG patients

The embryonic stage at 5 dpf, before the macroscopic phenotype was observed, is particularly interesting as proteomic analysis revealed that molecular changes have already taken place. GO term analysis revealed mainly two differentially regulated pathways before the onset of phenotypes: eye development and mRNA processing.

As the eyes of medaka are accessible neural tissue which can be analyzed morphologically, I examined the eyes of the mutant *pmm2* fish. Measurements of the eye size and distance revealed smaller eyes with increased inter-ocular distance in the *pmm2* mutant hatchlings compared to the wild-type siblings (Figure 30 A). Additionally, histological sections of eyes were performed in collaboration with Encarnación Sánchez Salvador (Wittbrodt Lab, Heidelberg University). Cryosections were stained with DAPI to label the nuclei and showed the characteristic three cell layers in the retina: the ganglion cell layer (GCL), the inner nuclear layer (INL) and the outer nuclear (ONL) layer in which the photoreceptors reside (Figure 30 B). In the wild-type, the ONL consists of two cell layers containing rod and cone photoreceptors. In contrast, only one cell layer is visible in the mutant fish. The loss of photoreceptors disrupts the typical lamination pattern of the outer nuclear layer. Cone cells were visualized with immunostaining against Zpr1 to differentiate whether rod or cone photoreceptors were affected. Present Zpr1 signal showed that cone photoreceptors are not affected in the mutant fish, implying that the rods are likely selectively affected (Figure 30 B). The other two cell layers seem unaffected.

This phenotype implies a retinal degenerative condition called retinitis pigmentosa (RP). RP is characterized by a progressive loss of rod photoreceptors, a symptom commonly seen in human PMM2-CDG patients. The Pmm2-CDG medaka model therefore seems to closely resemble the patient symptom.

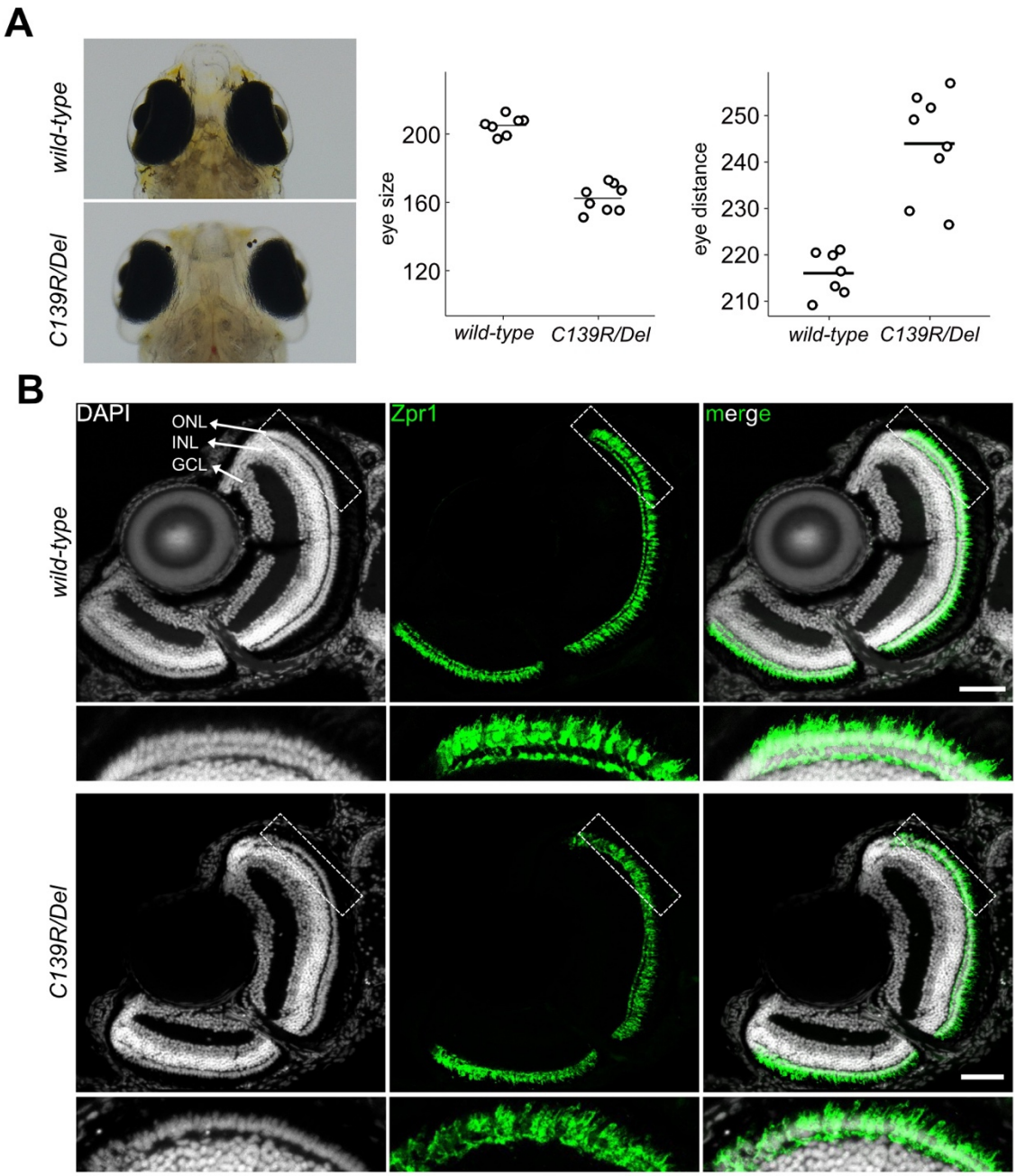

Figure 30: Defects in lamination of the outer nuclear layer in compound heterozygous *pmm2*$^{C139R/V135Gfs*45}$ mutants. Eyes of compound heterozygous *pmm2* mutants are smaller and wider apart. B) Maximum projections of cryosections from *wild-type* and compound heterozygous *pmm2*$^{C139R/V135Gfs*45}$ hatchling heads stained with DAPI (grey) to label nuclei and with antibodies against Zpr1 (green) to label cone photoreceptors. Outer nuclear layer (ONL), inner nuclear layer (INL) and ganglion cell layer (GCL) are indicated with white arrows. Data produced jointly with Encarnación Sánchez Salvador (Wittbrodt Lab, Heidelberg University). Scale bar 50 µM. wt, wild-type

2.3.14 CRISPR/Cas9 knockout of *rp2* and *rfc4* show retinal defects

The candidate list of genes encoding proteins potentially affected in *pmm2* mutants contain *rp2* and *rfc4*, which could cause eye phenotypes. Mutations in the retinitis pigmentosa 2 gene (*RP2)* are associated with X-linked retinitis pigmentosa but RP2 has not been characterized as a glycoprotein. Replication factor C gene (*RFC4)* has not been described in the context of retinal diseases and is not characterized as glycoprotein. However, *RFC4* is described to act in camera-type eye development. To investigate if *rp2* and *rfc4* contribute to the defect in the lamination the outer nuclear layer seen in *pmm2* medaka mutants, I performed CRISPR/Cas9 knockouts of both genes.

I injected 1-cell stage wild-type medaka embryos with *CRISPR/Cas9* mRNA together with guide RNAs targeting the predicted *N*-glycosylation motif of *rp2* and *rfc4* (Figure 31 A). At 3 dpf, pools of embryos were taken for genomic DNA extraction to verify the edit. Remaining editants were fixed after hatching. Their heads were stained with DAPI to label the nuclei and imaged with confocal microscopy. In the control injection where I targeted the *oca2* locus, two cell layers were visible in the ONL (Figure 31 B). Upon disruption of the *rp2* gene I observed defects in the lamination of the ONL, which is expected as RP2 mutation cause RP in patients. Knockout of *rfc4* resulted in massive defects in the layering of the eye. Nuclei appeared to be forming abnormal bridges spanning from the GCL across the INL to the ONL.
The observed eye defects upon knockout indicated a crucial role in photoreceptor maintenance for *rp2* and eye layering for *rfc4*.

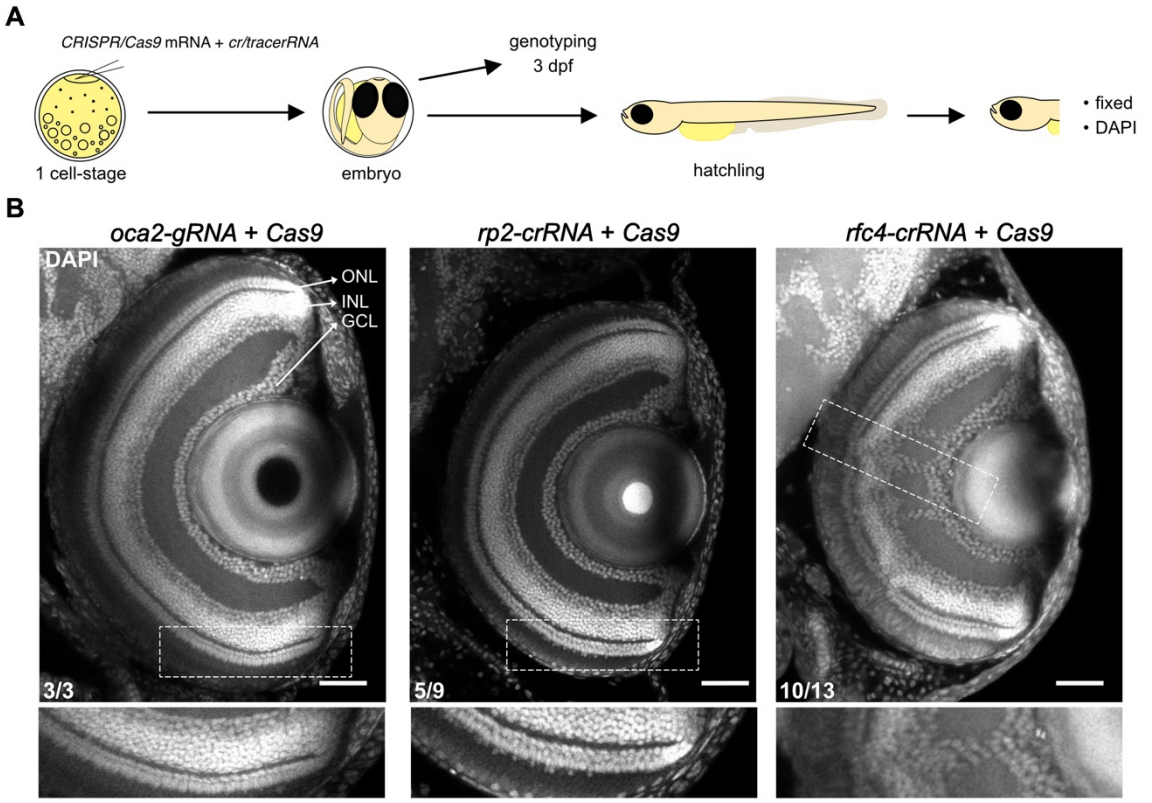

Figure 31: Eye defects in *rp2* and *rfc4* crispants. A) Schematic outline of the workflow. Wild-type medaka Cab embryos were injected with *CRISPR/Cas9* mRNA and guide RNAs targeting the *rp2* and *rfc4* gene and control injected with guide RNAs targeting *oca2.* A pool of crispants was genotyped 3 dpf. Remaining individuals were fixed after hatching and their heads were stained with DAPI. B) Confocal images of single plains of wholemount heads from *oca2* control, *rp2* and *rfc4* crispants stained with DAPI to label nuclei. Zoom-in shown below. The outer nuclear layer (ONL), the inner nuclear layer (INL) and the ganglion cell layer (GCL) are indicated with white arrows. Scale bar 50 µM. dpf, days post fertilization

2.3.15 Precise base editing of *N*-glycosylation motif of *rfc4* shows retinal defects

The protein RFC4 is highly conserved between species and the medaka ortholog shares the same predicted *N*-glycosylation motif as human RFC4 (Figure 32 A). During conventional bottom-up mass spectrometry, peptides with post-translational modifications are not detected. This means that peptides harboring glycosylation motifs are omitted from the analyses. Notably in our analysis, the tryptic peptide “VLELNASDER” of Rfc4, which contains the potential *N*-glycosylation site “NAS”, was exclusively detected in the compound heterozygous *pmm2* mutant samples at hatchling stage (Figure 32 B, red bars), suggesting that this sequence was not post-translationally modified in the *pmm2* mutant. Rfc4 is not a characterized glycoprotein therefore I mutated the predicted *N*-glycosylation sequon to assess whether missing the motif contributes to the observed layering defects

visible in the eye. This would indicate that Rfc4 requires glycosylation for proper function and that a hypoglycosylation situation impairs its activity.

I injected guides targeting the *N*-glycosylation sequon with an adenine base editor. The goal was to mutate the *N*-glycosylation motif “NXS/T” in the *rfc4* sequence. The injected editants were genotyped 3 dpf and the heads of editants of the remaining embryos were fixed and stained with DAPI after hatching. Imaging of the wholemount heads revealed identical phenotypes in the retina: bridges from the GCL to the ONL were formed (Figure 32 C). Sanger sequencing confirmed successful editing of the *N*-glycosylation motif from “NAS” to either “SAS” or “GAS” (Figure 32 D).

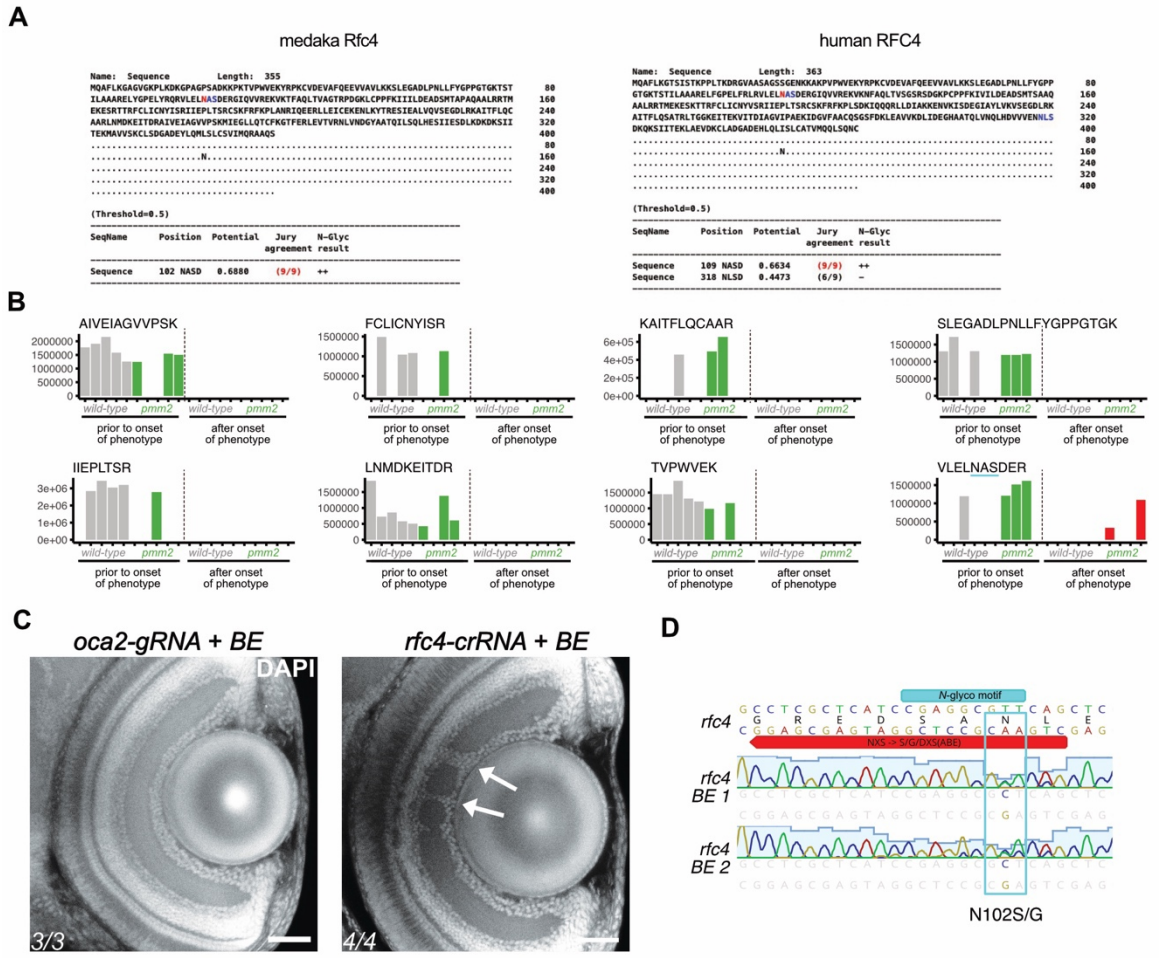

Figure 32: Irregular bridges form in the retina of medaka upon mutation of a predicted *N*-glycosylation motif within *rfc4*. A) Prediction of potential *N*-glycosylation sequons in medaka Rfc4 and human RFC4 via NetNGlyc (Gupta R, 2022). B) Absolute intensities of tryptic peptides from bottom-up mass spectrometry analysis assigned to Rfc4 across all 5 replicates from wild-type and compound heterozygous *pmm2* mutants at the two stages (prior onset of phenotype 5 dpf and after onset of phenotype 5 dph). Predicted *N*-Glycosylation motif “NAS” is marked in cyan and red bars represent exclusively detected in the *pmm2* mutant sample 5 dph. C) Confocal images of single plains from wholemount heads from *oca2* control and *rfc4* editants stained with DAPI to label nuclei. Abnormal bridges are indicated with white arrows. Scale bar: 50 µM. D) Sanger sequencing of editants at 3 dpf (n=1 and pool with n=2) shows editing of *N*-glycosylation motif via asparagine to serin or glycine (N102 to S102 or G102) substitution. BE, base editor

These results indicate that Rfc4 could be a glycoprotein as mutations in predicted the *N*-glycosylation site disrupt its proper function in medaka. Conditions like hypoglycosylation could impair the proteins activity and cause conditions like retinitis pigmentosa.

This validation suggests that from the mass spectrometry data one can select candidates and targeted the glycosylation site with base editors to precisely remove the sequon and validate the phenotypic consequences of the potential loss of *N*-glycosylation. The absolute intensities of tryptic peptides can additionally hint towards the glycosylation state of proteins if peptides with predicted *N*-glycosylation motif are detected exclusively in the mutants.

3. Discussion

Rare genetic diseases caused by mutations in essential genes raise a puzzling question: How can there be patients who survive considering the essential role of the mutated gene? This is a fundamental question of disorders affecting basic biological processes like protein glycosylation.
Congenital Disorders of Glycosylation (CDG) are caused by different mutations affecting enzymes involved in glycosylation. Most patients have a mutation in PMM2. The existence of PMM2-CDG patients arises due to hypomorphic variants, as complete loss of function is embryonically lethal. Clinical phenotypes seen in patients range on a spectrum from mild phenotypes to multisystemic severe phenotypes. Over a hundred different *PMM2* mutations have been identified via whole exome sequencing. This explains to some extend the variability of symptoms but intronic and regulatory regions have not been analyzed and could have compensatory effects. Nature selects for survivors at the viable end of the spectrum and severe genotypes are lost during early development. Studying the hypomorphic variants compatible with life are critical for understanding disease onset, mechanism and progression and open the possibility to develop targeted therapies.

In this work, I aimed to generate hypomorphic models in medaka fish which resemble the human PMM2-CDG disease. I established two technical methods to mimic the reduced enzyme activities reported from patients. The first method was based on a degron system to lower the Pmm2 protein abundance which results in reduced net enzyme activity. Transient expression of the degron components allowed to degrade GFP tagged Pmm2 during the early development. The second approach involved precisely installing the exact patient mutations into the medaka genome with a new base editing approach only after overcoming the PAM motif constrains. This method now allows to reach desired target sites initially out of scope and in a more flexible manner. In addition to patient mutations, I successfully introduced mutations close to the human mutations in medaka to generate a genetic Pmm2-CDG model organism resembling the patients multisystemic symptoms in medaka. The model showed reduced enzyme activities and a hypoglycosylation state. Proteomics analysis identified differently abundant proteins and revealed multiple molecular pathways affected in the *pmm*2 mutants, already in early stages of development where no phenotypes are observed yet.

3.1 Reduced enzyme activities reported from PMM2-CDG patients can be mimicked by reduction of Pmm2 enzyme abundance in medaka

PMM2-CDGs are primarily physiological disorders with developmental consequences. Deficient enzymes lead to biochemically detectable glycosylation defects which result in multisystemic developmental symptoms that affect all organs. Understanding the developmental defects is essential, as compensating for physiological effects after birth is not curative.

In human, the first signs of disease typically develop within the first years of life. However, studying the early onset in human or other mammal model organisms is challenging due to intrauterine development. In contrast, medaka fish develop extrauterine therefore embryos can be manipulated at the 1-cell stage and the early development can be investigated.

In traditional genetic models, homozygous PMM2 mutants suffer from severe developmental defect, while heterozygous carriers typically maintain sufficient enzyme levels to mask disease phenotypes. Offspring of heterozygous mothers are not suitable for studying the early onset of CDG phenotypes, as maternal contribution of Pmm2 masks early embryonic effects. To investigate the acute effects of Pmm2 loss during early embryonic development, I hypothesized that reducing protein abundance can mimic the reduced enzyme activity observed from patients. By combining the TIR1(F74G) and mAID-GFP-nanobody, I achieved an acute and efficient knockdown of endogenously GFP-tagged Pmm2 in a developing medaka embryo. The targeted knockdown successfully mimicked reduced enzyme activities reported from patients.

Delivering the degron system as mRNA offers a systemic knockdown approach with precise temporal control of protein levels upon induction and allows to effectively deplete maternal and zygotic Pmm2. Such tools are especially valuable for disease modeling during early developmental stages. GFP expression dropped immediately and rapidly upon induction, especially considering constant Pmm2-GFP production in the developing embryo. Pmm2-GFP depletion occurs within a narrow time window, peaking around 30 hpf (stage 20 in medaka). Despite maximum depletion, no early phenotypes were observed in degron-injected and induced embryos, likely due to buffering by mannose-1-phosphate which is already available due to maternally contributed protein.

Compared to a stable line, the mRNA-based degron system provides multiple benefits: 1) It demonstrated effective degradation of maternally contributed Pmm2-GFP, an effect that cannot be achieved using conventional approaches like RNAi or morpholinos, as these target RNA transcripts rather than proteins directly, 2) the injection amounts and inducer

concentrations could possibly tune the degradation in a fine manner to desired levels and 3) this system can be injected in any already available GFP-tagged line. Importantly, mRNA injections permitted ubiquitous expression of degron components early on. In contrast, stable lines are limited as ubiquitous promotors already active during early embryogenesis are not available hence no maternal contributed proteins and no proteins expressed early in development can be degraded.

This mRNA-based degron system provides a powerful and flexible tool next to classical gene knockout strategies, particularly for studying loss of maternally provided proteins.

While the line is susceptible to stress, as injection of any mRNA induced unusual phenotypes, no additional aberrant phenotypes were observed beyond the ones in control injections. This suggest that the transient knockdown is not causing long-term developmental defects other than baseline injection effects. A stable line could prevent aberrant injection phenotypes and allow to induce knockdown at any time during development. However, in this particular case the mRNA-based system outperformed the stable line as the results suggest that high enough levels of degron component expression are not reached to effectively degrade endogenously expressed proteins. As no acute effects on development were macroscopically visible, proteomics or transcriptomics analysis could provide insight about the acute knockdown effect of Pmm2 loss in a developing system.

By establishing the auxin-inducible acute protein knockdown system for the use in medaka fish, I demonstrate the functionality of a GFP-nanobody in combination with the Tir1(F74G) variant. This approach provides a versatile and widely applicable protein depletion system in medaka, especially when targeting endogenous GFP-fusion proteins. This method has not only relevant for studying CDGs but also for applications in developmental biology where conditional and reversible protein depletion is required.

3.2 Complexity of the *Pmm2* locus complicates genetic modeling

There is a lack of viable animal models to study the rare human disease PMM2-CDG. To be able to find therapies for patients, it is important to understand the pathogenic mechanisms causing the disease. Genetic animal models recapitulating the human disease showed either not full penetrance of disease affecting all organs or, especially mammalian models, suffered from embryonic lethality (Chan et al., 2016; Thiel et al., 2006). Generation of the most prevalent mutations known from PMM2-CDG patients are prime candidates to generate in medaka, as these usually single nucleotide changes would resemble the patient situation most accurately and are known to render the PMM2 protein hypomorphic in human. With the established CRISPR/Cas9 toolbox, there are

several ways to achieve these small edits, all with their individual drawback. Canonical Cas9 approaches that introduce a double strand break can be used to integrate a DNA donor via homology directed repair (HDR). With further optimizations on the nuclear localization of the Cas9 enzyme and biotinylation of the DNA-donor 5' ends, HDR has become a reliable and precise method (Gutierrez-Triana et al., 2018; Seleit et al., 2021; Thumberger et al., 2022). Yet HDR is restricted to G2/S phase of the cell cycle, leading to rather low efficiencies (Hustedt & Durocher, 2017). In parallel, the introduced double strand breaks are as well repaired by the error-prone non-homologous end-joining, changing the target site when improperly sealed which will remove such edited loci from further HDR integration attempts. In addition, these insertions and deletions (indels) can have severe consequences in essentials genes like *pmm2,* as the knockouts are embryonically lethal.

Base editors in contrast have proven to be highly efficient and precise for creating point mutations with minimal off-target effects in medaka (Cornean et al., 2022) but are dependent on the presence of a PAM motif in the proper distance to the desired edit. Base editors with expanded PAM recognition, allow for targeted nucleotide conversions with higher flexibility, yet they often induce phenotypic abnormalities due to likely increased off-target effects. Base editing is further strongly influenced by the nucleotides surrounding the target nucleotide impacting on overall editability. The next Cas9-evolution - prime editing - would offer an alternative since it only nicks the genomic DNA and no additional DNA donor template molecule is required. This promising method is yet to be optimized for the use in medaka.

Considering the benefits and drawbacks, I chose to generate *pmm2* mutations with the established adenine and cytosine base editors due to their highly efficient editing and low off-target risks.

During the generation and screening for founder fish, I discovered that the genomic landscape of the *pmm2* locus surrounding exon 5, i.e., the site for the two most common mutations in patients, is flanked by a 10,000 bp long highly repetitive region downstream and a 20-bp long guanine-stretch upstream. In addition, single nucleotide polymorphisms (SNPs) complicated designing of primers with reliable amplification of both alleles.

Sanger sequencing provides consistent results but requires PCR amplification and carefully selected primers, which is particularly difficult in this region. Amplification-free sequencing methods from Oxford Nanopore Technologies (ONT) (Branton et al., 2008) and single molecule real-time (SMRT) sequencing developed by Pacific Bioscience (PacBio) (Rhoads & Au, 2015) as these allow long sequencing reads. Both methods enable single molecule sequencing whereas PacBio relies on a DNA-polymerase for sequencing and ONT detects current changes as a DNA strand is pulled through a

nanopore. To sequence this region reliably, one strategy could involve cutting the region using CRISPR/Cas9 with guide RNAs flanking the *pmm2* locus and enrich for the locus by pulling with a dead Cas9 and specific guide RNAs for the *pmm2* sequence to extract the region. This approach would provide PCR-free long reads for sequencing with ONT or PacBio. However, for time- and cost-efficient sequencing these are not optimal solutions for routine genotyping. I tested multiple primer sets and ultimately reached reliable equal amplification of both alleles using a forward primer that binds over 100 times in the intronic region downstream of exon 5 and a reverse primer at the 3‘-end of exon 5. Sanger sequencing with the reverse primer revealed consistent genotyping results for exon 5, reliably resolving the exonic sequence which was essential for all genome editing attempts in this locus.

3.3 Inception: expanding the CRISPR/Cas9 toolbox through combinatorial use of base editors

With conventional base editing to date, it was not possible to install the patient-specific mutations in *pmm2* exon 5, due to the lack of PAM motifs in the appropriate distance from the desired editing site. To reach the exact patient mutation p.F119L in medaka, I expanded the established Base Editing toolbox with the so-called “inception” approach. Here, a first guide RNA and the adenine base editor create a new PAM site which subsequently creates a novel, second target site and enables sequential editing with a second guide RNA provided at the same time. Depending on the desired edit and the sequences of the targeted locus, guide RNAs may be chosen for the first step introducing synonymous changes, while the second editing introduces the desired mutation. In general, this inception approach can be applied to introduce loss-of-function mutation or multiple codon changes at once in a less stringent manner. The inception efficiency depends on the efficiency of each guide RNA involved and is highly dependent on the sequence of the target locus. Once a new PAM site was generated, the sequential edit occurred almost quantitively. This could in theory allow sequential PAM generation multiple times until the desired target is reached. The applied base editors (ABE8e (Richter et al., 2020), ancBE4max (Koblan et al., 2018) and evoBE4max (Thuronyi et al., 2019)) recognize the same PAM motif (SpyCas9, NGG) and guide RNA backbone (SpyCas9). Thus, both applied guide RNAs can form a complex with either ABE and CBE editors, leading to further “unwanted” edits in both base editing windows. To prevent these unintended edits, Cas9 ortholog-based base editors with different PAM recognitions could be combined and broaden the targeting range even further. The field of base editing is rapidly evolving and new Cas9 variants called (near) PAM-less (Walton et al., 2020) or

PAM-free (Tan et al., 2022) are established. These variants likely harbor more off-target effects whereas inception provides a balance of the high specificity of traditional editors while still expanding their targeting range.

Proof of principle of the inception concept was performed in three different settings: premature STOP codon introduction via synonymous PAM generation, intronic PAM generation and subsequent splice acceptor modulation and introduction of multiple non-synonymous codon changes, calculated to increase overall target sites by 64.8 % and published in Pakari et al., 2023.

Using the inception approach, I generated p.F122L (human p.F119L) in medaka by intronic new PAM generation followed by sequential editing of F122L position. The offspring of heterozygous parents showed severe multisystemic phenotypes expected from *pmm2* mutations in medaka, but only in the heterozygous state. This unexpected outcome suggested that additional unintended mutations have been generated in the close by intronic region which were impossible to resolve due to the high intronic repetitiveness of the *pmm2* locus.

3.4 Conformational effects of Pmm2 dimers on enzyme activity

Alternatively, the unexpected aberrant phenotype observed in the heterozygous individuals could result from a dominant negative effect of the F122L variant. PMM2 functions as a homodimer by interaction though a hydrophobic core which can be disrupted by pathogenic mutations (Quental et al., 2010; Yuste-Checa et al., 2015). Splice site prediction using NetGene2 did not indicate any changes in splicing after inception introduced mutations (Brunak et al., 1991; Hebsgaard, 1996), suggesting conformational changes. Depending on how the mutations affect the protein, formation of heterodimers could have a more deleterious effect than homodimers and could account for the severe phenotypes seen in the heterozygous F122L individuals. Such an effect is not expected from human PMM2 studies. In a mouse model carrying the two most common patient mutations in the *Pmm2* mouse ortholog, the embryonic lethality was higher than reported from humans (Chan et al., 2016). Similarly, medaka models could exhibit more dramatic outcomes due to species-specific differences. Even though glycosylation is highly conserved, the impact of mutations in PMM2 orthologs may differ across species. Interestingly, in a comparative injection screen during a research project, Johanna Rasch observed that injections of *pmm2* mutant variant mRNAs into wild-type embryos induced aberrant phenotypes. This strongly suggests that increased levels of mutant protein can disrupt the dimeric balance and perturb enzyme activity.

3.5 Generation of hypomorphic patient-based mutations show patient specific disease phenotypes

All performed nucleotide changes in the medaka *pmm2* exon 5 lead to medaka embryos fully resembling the PMM2-CDG patients' symptoms. I thus focused on the compound heterozygous *pmm2*$^{C139R/V135Gfs*4}$ mutation line which could be efficiently genotyped/identified using the described PCR genotyping regime. This Pmm2-CDG medaka model serves as a valuable model for studying the underlying mechanism of PMM2 deficiency and its associated phenotypes. Analysis of the inner organs with micro-CT revealed an aberrant liver, reduced brain size, intestinal loop defects, absence of food in the gut as well as heart abnormalities. All organs which are also found to be similarly affected in PMM2-CDG patients (Krasnewich et al., 2007; Muthusamy et al., 2024a). Additionally, cartilage phenotypes in *pmm2* mutants resemble facial dysmorphisms reported from patients (Ferreira et al., 2018). Analysis of the eyes revealed lamination defects in the of the outer nuclear layer of the retina, a characteristic feature of retinitis pigmentosa which is commonly observed in patients (Monin et al., 2014).

Most PMM2-CDG patients are diagnosed within the first few years of life after a healthy pregnancy and uncomplicated birth (Pérez-Cerdá et al., 2017; M. Vals et al., 2017). Since medaka embryos are transparent and develop externally, early development can be continuously examined in detail.

In medaka *pmm2* mutants, the early development appears normal and morphological defects only become apparent after hatching, thus similar to patients' post-partum. Since the phenotypic abnormalities are macroscopically only distinct post hatching, it can be hypothesized that the source of disease manifestation is indeed physiological rather than an early developmental defect. The medaka *pmm2* model offers accessibility to all stages of development allowing to dissect the molecular onset of disease. The model offers to investigate the onset and progression of PMM2-CDG related disease phenotypes.

Hypoglycosylation in CDG patients causes accumulation of misfolded proteins in the ER which triggers cellular stress that activates the unfolded protein response (UPR) (Rita Lecca et al., 2005; Shang et al., 2002; Zdrazilova et al., 2023). The UPR subsequently facilitates the degradation of these misfolded proteins. In mouse and zebrafish PMM2-CDG models, upregulated transcription of UPR related genes were detected (Edmondson, Budhraja, et al., 2025; Matheny-Rabun et al., 2024). In the mass spectrometry data from *pmm2* medaka mutants hspa5, known as "binding immunoglobulin protein" (BiP), was found to be upregulated compared to wild-types. Hspa5 is the master regulator of UPR and its upregulation indicates hypoglycosylation-induced protein misfolding and UPR, also in the Pmm2-CDG medaka model. Dnajc3, a co-chaperone of BiP, was upregulated in

CDG patient fibroblasts (Rita Lecca et al., 2005b) and was also found upregulated in *pmm2* mutant hatchlings.

CDGs and mitochondrial disease have been described to develop clinically similar features (Briones et al., 2001; Gardeitchik et al., 2018). This led to studies on mitochondrial function in PMM2-CDG derived fibroblasts and confirmed their disfunction in patients (Himmelreich et al., 2023; Ligezka et al., 2023). Gene ontology enrichment analysis revealed the cristea formation pathway, which is the invagination of the inner mitochondrial membrane, to be highly upregulated in mutant *pmm2* medaka hatchlings – mirroring the mitochondrial disfunction reported from the aforementioned studies. Analysis of potentially glycosylated proteins in the secreted pathway, based on the subcellular location, revealed neurological involvement already in the embryonic stage. This is consistent with the fact that neurological defects are a key phenotype of PMM2-CDG patients (Altassan et al., 2019; Edmondson, Budhraja, et al., 2025; Lam & Krasnewich, 2005; Muthusamy et al., 2024b). Overall, the observed phenotypic and molecular phenotypes closely resemble those reported in human PMM2-CDG patients and from studies in patient-derived fibroblasts.

3.6 *N*-glycosylation fingerprint indicates flippase enzymes as potential therapeutic target

The results on hypoglycosylation state in the Pmm2-CDG medaka model mirrors those reported from the serum or derived iPSCs from fibroblasts of PMM2-CDG patients, suggesting that reduced Pmm2 enzyme activity leads to comparable changes in *N*-glycosylation pattern (Garapati et al., 2024b; Thiesler et al., 2016). xCGE-LIF analysis revealed overall reduced levels of all *N*-glycan types. This is expected as the Pmm2 provides mannose-1-phosphate, the precursor of GDP-Man which essential for the synthesis of the LLOs in the ER. Reduced levels thus quantitatively reduce the abundance of released glycans detectable after PNGase F digestion and identification. Interestingly, high mannose *N*-glycans built in the ER (Man6-Man9) and mature glycans generated in the Golgi were found to be reduced while precursor structures (Man3-Man5) assembled on the cytosolic side were accumulating (Figure 33).

N-glycosylation takes place in the ER and Golgi. The process initiates with dolichol phosphate on the cytoplasmic side of the ER first receiving *N*-acetylglucosamine-1-phosphate followed by consecutive elongation with five mannoses using GDP-mannose as donor. This intermediate is flipped into the ER lumen where it is further enzymatically extended with four mannoses and three glucoses from dolichol-phosphate-mannose and dolichol-phosphate-glucose.

The accumulation of cytosolic precursor structures (Man3-Man4) and Man5 together with a reduction in high mannose structures (Man6-Man9), suggests that GDP-mannose on the cytosolic side can be utilized normally. However, the addition of mannoses inside the ER lumen seems affected.

One possible explanation could be an insufficient activity of flipping enzyme RFT1. Fibroblasts from RFT1-CDG patients showed accumulation of the intermediate Man5GlcNAc2-PP-dolichol (Vleugels et al., 2009), a structure I also observed in the glycan analysis from *pmm2* mutants. Although RFT1 is not *N*-glycosylated and its essential flippase activity is debated (S. Chen et al., 2024; Frank et al., 2008; Hirata et al., 2024), boosting *RTF1* activity could be a possible approach to reduce or overcome hypoglycosylation (Figure 33, RFT1 colored in yellow).

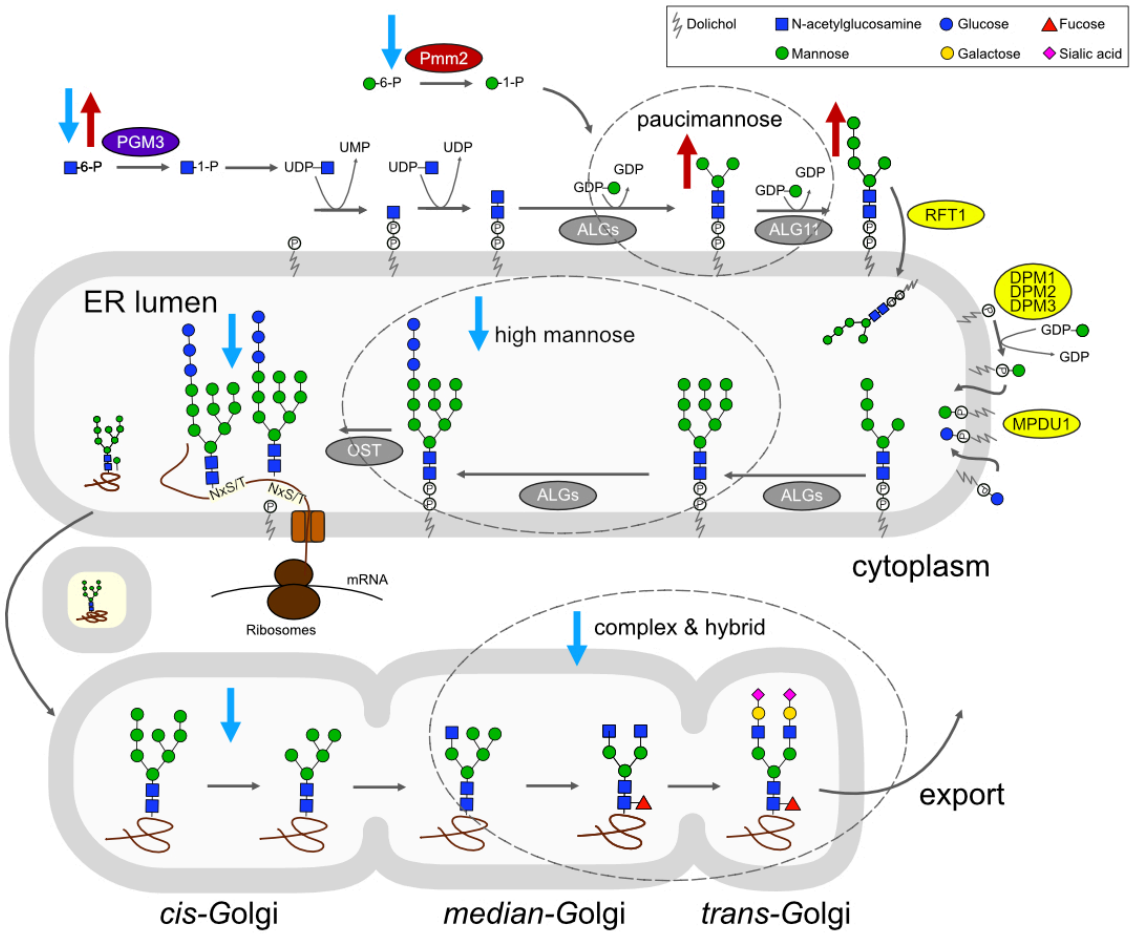

Figure 33: Consequences of reduced Pmm2 enzyme activity. xCGE-LIF analysis revealed changes in the *N*-glycan composition comparing wild-type to *pmm2* mutants. The mutants show general hypoglycosylation and reduction in oligomannose-type (Man5-Man9) together with complex-type *N*-glycans. The hypoglycosylation is accompanied by accumulation of Man3 to Man5 structures. Enzymes marked in yellow could be potential targets for therapeutical approaches to boost import of immature glycans and increase transport of donor sugars into the ER. PGM3 was first downregulated (embryonic stage) and later upregulated (hatchling stage) in the bottom-up mass spectrometry analysis in *pmm2* mutants. Figure adapted from *Varki et al., 2022* (Essentials in Biology Figure 9.3 and 9.4.)

Another bottleneck in the disrupted *N*-glycosylation pathway could involve the availability of Dolichol-phosphate-mannose (Dol-P-Man) donors. These are assembled on the cytoplasmic side but need to be flipped across the ER membrane into the lumen. The observed reduction of high mannose structures led to the hypothesis that enhancing Dol-P-Man transport into the ER could improve the hypoglycosylation. Targeting this flippase might present a potential therapeutic strategy as well as increasing the activity of MPDU1 and/or the DPM complex (DPM1, DPM2, and DPM3) through pharmacological modulators (Figure 33, enzymes colored in yellow). This could elevate the availability of mannose donors within the ER and increase the synthesis of high mannose LLO structures (Man6–Man9).

Analysis of the *N*-glycan fingerprint across different tissues will allow to assess glycosylation heterogeneity and identify which organs are more affected from reduced Pmm2 activities. This would allow for a detailed examination of glycan composition and glycan structure variation among different tissues.

3.7 Proteomics analysis revealed changes in molecular pathways before onset of visible phenotype

To understand the consequences of hypoglycosylation, proteomics analysis provides the most direct insight compared to other omics approaches as the abundance of proteins can be determined. To study the onset and progression of disease, I chose to analyze two timepoints in development: before (stage 35) and after onset of severe the multisystemic *pmm2* mutant phenotypes (hatchling, 5 dph). Proteomics analysis confirmed that multiple pathways were affected at the hatchling stage which is consistent with the presence of the *pmm2* mutant phenotype at that time.

Overall, a direct comparison of the proteomes of the developmentally distant stages (embryonic versus hatchling) could not be made as they differed greatly. As a consequence of the developed phenotype at the hatching stage, affected protein levels might not only reveal glycoproteins affected by the hypoglycosylation but are secondary differences, downstream of the altered functionality of phenotype causing factors. I initially aimed to compare commonly up- and downregulated proteins between the two stages and associate their progression of abundance to effects from hypoglycosylation. Glycoproteins might be less affected in the earlier stage and more profoundly affected after hatch. As the stages are developmentally more distant than expected, the analysis of disease progression was not feasible. This implied that affected proteins might be identified by comparing the fold changes of the two stages. I assumed affected proteins could be initially

downregulated due to the hypoglycosylation and later upregulated to compensate for the loss, or vice versa. One interesting candidate was Pgm3 (Phosphoglucomutase 3) that converts acetylglucosamine 6-phosphate (GlcNAc-6-P) into *N*-acetylglucosamine 1-phosphate (GlcNAc-1-P). GlcNAc-1-P is an essential precursor for generation of Dol-P-P-GlcNAc, which is extended to Dol-P-P-GlcNAc2Man5 before flipping into the ER during *N*-glycosylation. Pgm3 was found to be downregulated in the embryonic stage and upregulated only after hatch in the *pmm2* mutant.
The *N*-glycan analysis revealed accumulation of Man3-Man5 structures and reduction in high mannose glycans as described earlier. Therefore, I speculated about a connection of upregulated Pgm3 activity and accumulation of Man3-Man5 structures on the cytosolic side of the ER. I hypothesize that reducing Pgm3 activity could reduce assembly of Dol-P-P-GlcNAc2Man5 and push the available GDP-man towards Dol-P-Man formation which could promote extension of high mannose structures inside in ER.

From the embryonic stage, before a scorable phenotype was macroscopically visible, primary effects were more likely to become visible. The proteomics analysis revealed two distinct groups of molecular pathways affected: mRNA processing and eye formation.
Differential regulation of the mRNA processing pathways including splicing, indicates an overall cellular response of the organism to hypoglycosylation. To prevent the accumulation of misglycosylated proteins, mRNA processing may be downregulated to reduce protein translation.

3.8 Potential identification of misglycosylated proteins via comparison of absolute intensities of tryptic peptides

In the bottom-up mass spectrometry run, only unmodified peptides are detected, as post-translational modifications hamper peptide identification. This limitation becomes relevant for potential glycoproteins, as their peptides containing glycans are usually not identified.
Interestingly, for two candidate proteins analyzed, rfc4 and prr33 the specific peptide predicted to contain glycosylation sites appeared at higher frequencies in the *pmm2* mutant samples compared to wild-type samples. The shift from certain peptides exclusively or mostly detected in mutant samples could indicate potential glycosylation of this motif in the wild-type condition, i.e., not being identified in the *pmm2* wild-type samples. In return, their increased appearance in mutant samples could reflect a loss or reduction of glycosylation of the associated protein.

To my knowledge, predicting glycosylation from peptides which are detected selectively in mutant backgrounds is not common practice in proteomics or glycoproteomics. However, this observation represents a useful indicator for identifying potential glycoproteins.
Further validation is needed to confirm the glycosylation state of these proteins. To prove the presence of a *N*-glycan, one approach could be the enzymatic removal of *N*-glycans from proteins in the wild-type samples with PNGase F, followed by mass spectrometry analysis before and after digestion. Alternatively, a new method could include glycan sequencing and profiling on single proteins using nanopore technology (Stuber et al., 2023).

The eye associated RFC4 protein has not been described as a glycoprotein. Knockout of *rfc4* and specific editing of the predicted *N*-glycosylation motif (N102S/G) revealed dramatic retina layering defects and formed “cellular bridges” of cells spanning from the ganglion cell layer to the outer nuclear layer of the medaka retina.
This suggests that Rfc4 requires glycosylation in medaka for proper function and that hypoglycosylation could impair its activity. Prediction of the folding with Re-glyco did not reveal obvious changes in the structure of wild-type Rfc4 compared to the N102S/G variant (Ives et al., 2024). RFC4 (Replication Factor subunit 4) is essential for DNA replication and shows specific mRNA expression in the peripheral region of the eye, where retinal ganglion cells (RGC) and retinal stem cells reside, visible in *in situ* hybridization data from zebrafish at hatching stage (Thisse & Thisse, 2004). Recently, RFC4 has been described as a target of notch signaling (Liu et al., 2021). Notch signaling is involved in controlling RGC proliferation (Mills & Goldman, 2017; Nelson et al., 2006) thus, the loss of RFC4 could stimulate excessive proliferation of RGC. Furthermore, glycosylation plays a role in Notch signaling (Takeuchi & Haltiwanger, 2014). Hypoglycosylation in *pmm2* mutants could interfere upstream of Notch target genes and misregulate Notch signaling, which could lead to downregulated Rfc4 protein levels regardless of the glycosylation state of Rfc4.

Although the glycosylation of RFC4 remains elusive in this study, the CRISPR phenotype was striking and requires further validation to understand the nature of the cell types affected which form the bridges. Future experiments could include cell type specific staining to identify the cell type(s) contributing to the bridge formations. Additional pulse-chase experiments may help tracking the fate of the cells.
Specific glycoproteomics would allow to identify which glycoproteins are ultimately affected by hypoglycosylation. However, protocols for such analyses have not yet been established in medaka. Additionally, current methods primarily enrich for membrane-localized proteins,

limiting our ability to assess overall protein turnover. Moreover, bottom-up proteomics has the drawback of preferentially detecting more abundant proteins, potentially overlooking low-abundant yet functionally relevant targets.

3.9 Genetic *pmm2* medaka model provides a platform to screen for functional studies of mutant *pmm2* variants

The successful rescue experiments with wild-type *pmm2* mRNA demonstrated that providing Pmm2 protein early on is sufficed to rescue developmental defects. The rescue with human *PMM2* mRNA highlighted the conservation of the glycosylation pathway across species. Since the mutant *pmm2* phenotypes result from reduced enzyme activity, increasing levels of mutant *pmm2* variants might improve outcomes, reduce lethality, and replicate the effects of pharmacological chaperones or transcriptional enhancers. The sequence variant *pmm2 F122L* mRNA was able to improve survival of compound heterozygous mutants, while the *pmm2 C139R* variant did not show such rescue effect. This suggests that not all mutations affect protein function in the same way and some may retain residual activity to be useful as therapeutic targets when boosted. Since PMM2-CDG is a rare disease that often is diagnosed only after birth, gene therapy options are limited. Identifying variants that can rescue aspects of the disease could help guide future treatment strategies.

Further experiments measuring enzyme activity after *pmm2* mRNA injection could help clarify why early developmental expression is sufficient for long-term rescue. One possibility is that the Pmm2 protein remains stable and active after hatching, maintaining elevated enzymatic activity. Alternatively, early Pmm2 expression during development may be sufficient to correct developmental defects while physiological defects after hatching are effectively compensated.

Understanding this could be key to determining whether early intervention alone is sufficient for life-long benefits. The survival of compound heterozygous PMM2 mutants following injection of mutant *pmm2 F122L* mRNA suggests that boosting PMM2 translation or stabilizing the mutant protein may suffice to restore enzyme function by application of molecular chaperones or transcriptional enhancers.

The stable genetic *pmm2* line generated in this work, can be used to study the structure/function of additional *pmm2* variants derived from patients and their effect on the survival of compound heterozygous individuals in the future.

3.10 Disease onset and therapeutical intervention window

In the mutant *pmm2* medaka line, disease symptoms become apparent after hatching, reflecting the onset of observed symptoms in PMM2-CDG patients. Mannose supplementation has been suggested to improve glycosylation defects (Körner et al., 1998; Rush et al., 2000), similar to its described benefits for MPI-CDG patients (Niehues et al., 1998). Likewise, biotin has been proposed to enhance cognitive abilities in PMM2-CDG patients, as biotinidase activity was reduced in patient fibroblasts (Himmelreich et al., 2023).

To investigate the effect of the potential therapeutic strategies in medaka, I tested supplementation with D-mannose and biotin in *pmm2* mutant offspring. While patients receive sugar or biotin by oral intake, in medaka the components were provided within the rearing medium (ERM + supplement). It is unclear whether these substances are permeable and whether medaka can absorb them from the medium into their body. Medaka hatchlings begin to require food at 5 dph as they use up their yolk reserves (Myosho et al., 2025).

No rescue effects were observed in compound heterozygous *pmm2* mutants exposed to biotin or mannose in the rearing medium. This may be due to the mannose and biotin not fully penetrating through the skin of medaka or because the developmental defects are too severe, rendering physiological benefits insufficient at hatching stages. In PMM2-CDG mouse models, feeding mannose to pregnant mice reduced embryonic lethality (Schneider et al., 2012), which indicates that early interventions are crucial for rescuing the severe effects of *PMM2* mutations. The proteomics data support this idea, as molecular changes are already present before hatching, suggesting that therapeutic interventions may be needed at earlier developmental stages.

Pmm2 converts mannose-6-phophate to mannose-1-phosphate, the precursor of GDP-mannose. Providing the activated mannose-1-phophate directly could offer a more targeted therapy. Due to its high polarity, it cannot penetrate the cell membrane and efforts have been made to synthesize membrane-permeable derivates (Rutschow et al., 2002). Moreover, liposome-encapsulated mannose-1-phospate has been tested and should improve stability and delivery of the sugar (Budhraja et al., 2024).

One limitation of the medaka fish model is the delivery of drugs. Dissolving them in the rearing medium is applicable especially during early stages of developments and oral supplementation only becomes feasible around 5 dph, and intravenous injections are not practical. Nevertheless, the ability to expose large numbers of medaka embryos simultaneously to a set of compounds provides a distinct advantage over other animal models. Additionally, the medaka model allows to assess multiple stages with several

omics approaches to identify the onset of disease and define exactly optimal timing for therapeutic interventions.

3.11 Mechanistic insight into reduced Pmm2 activity during development

The generated medaka models for Pmm2-CDG revealed that reducing Pmm2 abundance during early development led to lower enzyme activity but did not cause long-term phenotypic abnormalities. Any interference in the susceptible *pmm2* lines through mRNA injections, overexpression of *pmm2* variants or heat could disrupt the tightly regulated glycosylation process and led to developmental defects. Genetic models exhibited no phenotype until hatching but after hatch defects similar to those observed in humans emerged. Interestingly, not all cells were affected equally, as revealed by the specific loss of only one cell type in the eye. Analysis of *N*-glycan fingerprints and proteomics data indicated that Pmm2 deficiency led to impaired protein glycosylation in the ER lumen, triggering cellular responses. Rescue by providing *pmm2* mRNA during early stages was sufficient to mitigate these effects, whereas supplementation later on was ineffective.

Taking everything into account, I propose the following mechanism for disease onset in PMM2-CDG. The glycosylation pathway is a sensitive system with Pmm2 playing a central role. Reduced Pmm2 activity led to impaired glycosylation of proteins, especially due to accumulation of precursor glycans on the cytosolic side, reduced LLO assembly in the ER lumen and consequently reduced maturation in the Golgi. Misglycosylated proteins are recognized by quality control mechanisms activating the unfolded protein response. This suppresses mRNA processing to decrease protein translation to prevent accumulation of further misglycosylated proteins. Maternally contributed glycosylation enzymes, early available Mannose-1-Phosphate and activated sugar donors help to compensate for reduced Pmm2 activity during early development. This buffering capacity allows cells to tolerate hypoglycosylation until hatch. Afterwards defects emerge which predominantly are associated with mitochondrial dysfunction and disrupted metabolism likely due to disturbed intracellular protein/compound trafficking. Developmental defects cannot be rescued by improving physiological effects anymore and early interventions are required to prevent disease manifestation.

Interestingly, although systemic defects occur, some cell types appear to be more susceptible to hypoglycosylation. In the eye only the photoreceptors were absent. This selective susceptibility is likely caused by the microheterogeneity and cell-type specific glycosylation (Chrysinas et al., 2024; Dworkin et al., 2022; Kellman et al., 2024). Specific

cell types mighty rely on proteins with differing glycan occupancy. Upon hypoglycosylation, cell types which depend on highly glycosylated proteins with all sequons being occupied by glycans might have a stronger compensatory response. This could induce stronger repressed translation and more active UPR pathways to clear the accumulating misglycosylated proteins, compared to the other cell types.

3.12 Relevance of the genetic model for future studies

Medaka and humans are evolutionarily quite distant but medaka fish have proven to be valuable models for studying human diseases. Previous publications have shown that medaka resembles the complexity of human biology and offers insights into conserved molecular mechanisms and gene functions (Doering et al., 2023; Gücüm et al., 2021; Hammouda et al., 2021). Many genes associated with human disorders have orthologs in medaka (Howe et al., 2013; Vilella et al., 2009), which allows to perform functional studies in a vertebrate system. Further, the medaka genome is well annotated (Kasahara et al., 2007) and there are multiple molecular and genetic tools available (Kirchmaier et al., 2015).

The established Pmm2-CDG medaka model provides a genetic vertebrate system that complements and extends existing PMM2-CDG models. Studies on patient-derived fibroblasts, serum and blood samples provide insight into cell-type-specific aspects of the disease and other vertebrate animal models suffer from early embryonic lethality or do not recapitulate the multisystemic symptoms. The medaka model can be analyzed and manipulated at whole-organism level involving all organs and features of the disease. Such systemic studies are essential in a pleiotropic disease in which the pathogenic mechanism is driven by the interplay of several proteins rather than the misregulation of a single one. In this study, I analyzed for the first time the changes at the proteome level across the entire organism during embryonic stages before onset of the *pmm2* mutant phenotype. This provides valuable insight into the molecular onset of Pmm2-CDG and contributes to our understanding of how developmental defects originate. Targeting differentially regulated candidate proteins identified at this early stage in functional validation experiments will reveal their involvement in disease progression.

4. Conclusion

In this study, I generated medaka models to study PMM2-CDG in order to investigate early acute effects and developmental consequences arising from reduced PMM2 activity. I established a degron system to reduce Pmm2 abundance and generated a patient-based genetic Pmm2-CDG model in medaka which closely recapitulate the human syndrome. The models provide valuable insights into the early molecular and developmental processes that occur prior to the onset of symptoms in human PMM2-CDG patients and highlight potential therapeutic strategies. The impact of reduced Pmm2 activity seems to be less dramatic in the very early embryonic stages. Afterwards, the reduced Pmm2 activity negatively impacts embryogenesis, causing developmental defects that manifest and become apparent after hatch.

The temporal activation of the degron-based system to reduce Pmm2-levels in an induced manner, can be used in follow-up studies to detect primary targets affected by hypoglycosylation throughout embryogenesis. The genome editing approach furthered in this thesis (‘inception’) is a valuable mode of precise genome editing reaching beyond the scope of (patient-based) allele mutation as it offers the possibility to precisely introduce point mutations in previously inaccessible genomic regions for a broad range of applications and model systems.

The genetic compound heterozygous Pmm2-CDG model fully resembled the human disease phenotypes and provides a platform for therapeutic compound screening and structural-functional analysis of PMM2 variants. Moreover, a protein atlas at developmental stages before and after onset of disease phenotype stages is available through this work. Investigation of tissue specific effects and identification of affected glycoproteins together with transcriptomics analysis will allow to dissect disease progression in further studies. This study underscores the potential of medaka as powerful models for human disease and represents a highly relevant resource for PMM2-CDG research.

Contributions

Here I detail the contributions of involved collaborators, colleagues and student assistants including experimental design, data curation and data analysis. Contributions to specific figures are mentioned in the corresponding figure legends.

Virginia Geiger and **PD Dr. Christian Thiel** prepared lysates and performed Pmm2 enzyme assays of wild-type Cab embryos, *pmm2-GFP* embryos and degron injected *pmm2-GFP* embryos. They also prepared lysates and performed Pmm2 enzyme assays of offspring from *pmm2*^{C139R} crossed to *pmm2*^{V135Gfs*45} line.

Dr. Thomas Thumberger designed guide RNAs for the *oca2* inception approach.

Kristaps Kairiss acquired micro computed tomography data and performed rendering of images of wild-type and *pmm2* mutants.

Andreas Hecker prepared lysates and lectin blots of wild-type and *pmm2* mutants.

Marlen Brodbeck genotyped *pmm2* mutants.

Johanna Rasch genotyped *pmm2* mutants, prepared *pmm2* variant mRNAs and maintained fish lines.

Lea Adams cloned the construct for stable degron line generation.

Encarnación Sánchez Salvador prepared cryosections, antibody staining and confocal imaging of wild-type and *pmm2* mutants.

Ivan Andújar-Martínez, Robert Burock and **Dr. Erdmann Rapp** prepared lysates, performed xCGE-LIF run, data analysis and plotted the *N*-glycome analysis in wild-type and *pmm2* mutants.

Dr. Marcin Luzarowski: performed mass spectrometry sample preparation, ran the samples and performed data analysis.

Tanja Kellner prepared the mRNA of base editors and Cas9.

5. Material and Methods

The following section describes the materials and methods used in this thesis. Several of the experimental procedures have been previously published in the following publication and are described for completeness: Pakari et al., 2023 and Pakari et al., 2025.
For additional information on contributions, see the Contributions section.

5.1 Material

Medaka fish lines used or created in this thesis are listed in Table 1. The transgenic lines were created either by microinjection of CRISPR/Cas9 base editors or meganuclease (I-SceI) in one-cell stage medaka embryos. The respective injection mixes are listed in Table 20.

Table 1: Medaka (*Oryzias latipes*) lines used in this work.

Fish lines	Internal stock number	Source
Wild-type Cab	#10052, #10346, #10542, #11057, #11332	lab stock
CR(Pmm2-GFP) C2F5, C2F6, C2F6	#10343, #10554, #11289	Pakari et al., 2025
ABE(Pmm2_V132Gfs*45)	#10475, #10791, #11039, #11471	this thesis
ABE(Pmm2_C136R)	#10475, #10768, #11011, #11439	this thesis
ABE(Pmm2_C136R) F0	#10110	Pakari et al., 2021
ABE(Pmm2_F119L)	#10365, #10575, #10786	this thesis
SC(ubi::Flag-myc-NES-Tir1F74G-E2A-mAID-nanobody-T2A-mRFP-pA) F0	#10719	this thesis
CR(Pmm2-GFP_het)_SC(ubi::Flag-myc-NES-Tir1F74G-E2A-mAID-nanobody-T2A-mRFP-pA) F1	#11030	this thesis
CR(Pmm2-GFP)_SC(ubi::Flag-myc-NES-Tir1F74G-E2A-mAID-nanobody-T2A-mRFP-pA) F2, F3	#11203, #11456	this thesis

5.1.1 Bacteria

Mach1T1 phage-resistant chemically competent *E.coli* from Thermo Fisher Scientific were used in this thesis.

5.1.2 Plasmids

All plasmids used in this thesis are listed in Table 2. Degron constructs from Daniel et al., 2018 were cloned into pCS2+ plasmids from pCDNA5FRT/TO_HA-mAID-nanobody

(Addgene plasmid # 117713; http://n2t.net/addgene:117713; RRID:Addgene_117713) and Flag-myc-NES-Tir1 which were both gifts from Joerg Mansfeld (Addgene plasmid # 117717; http://n2t.net/addgene:117717; RRID:Addgene_117717). The TIR1F74G point mutation (Yesbolatova et al., 2020) was introduced via Q5 mutagenesis to the Flag-myc-NES-Tir1 plasmid. The base editor plasmids evoBE4max, pCMV_AncBE4max (Addgene 112094) and pCMV_ABE8e (Addgene 138489) were gifts from David Liu.

Table 2: Plasmids used in this thesis.

Plasmid name	**Internal stock number**	**Source**
pCS2+	#221	lab stock
GFP	#883	lab stock
mCherry	#1924	lab stock
DR274(sgRNA_57_Oca2_ex9_T1)	#5357	Lischik et al., 2019
evoBE4max	#5797	Cornean et al., 2022
ancBE4max	#5811	Addgene #112094, Koblan et al., 2018
ABE8e	#5812	Addgene #138489, Richter et al., 2020
Flag-myc-NES-TIR1	#6088	Daniel et al., 2018
HA-mAID-nanobody	#6090	Daniel et al., 2018
pCS2+(Flag-myc-NES-Tir1F74G)	#6149	this thesis
pGG_SC(ubi::Flag-myc-NES-Tir1F74G-E2A-mAID-nanobody-T2A-mRFP-pA)	#6191	this thesis
pCS2+(kozak_Pmm2_full-length-cDNA)	#6301	this thesis
pCS2+(kozak_Pmm2(C136R)_full-length-cDNA)	#6315	this thesis
pCS2+(kozak_Pmm2(F122L)_full-length-cDNA)	#6317	this thesis
pCS2(heiCas9)	#6342	Thumberger et al., 2022
pCS2+(hPMM2_cDNA)	#6343	this thesis

5.1.3 Primers

Table 3: Primers used in this thesis.

Name	Internal nr.	Sequence (5' to 3' direction)
OCA2_T7_F	JW3292	GTTAAAACAGTTTCTTAAAAAGAACAGGA
OCA2_T7_R	JW3293	AGCAGAAGAAATGACTCAACATTTTG
pmm2_rev	JW5869	TGAGGTCACATCCCGTGTTG
pmm2_t2_R	JW5908	AAACGCAGAGGCTCAGGACTCG
pmm2_N_seq_F	JW6257	ACGTAGCACAGGTGCGTTTCCCG
pmm2_N_seq_R	JW6258	CGTTCTTGTAGGCCACCAGACCG
pmm2_inin_T4_R	JW8374	AAACATGACTGGAGAATGGAGC
oca2_Q333_HTS_genewiz_F	JW10815	ACACTCTTTCCCTACACGACGCTCTTCCGATCTCGTTAGAGTGGTATGGAGAACTGT
oca2_Q333_HTS_genewiz_R	JW10816	GACTGGAGTTCAGACGTGTGCTCTTCCGATCTATGGTCCTCACATCAGCAGC
TIR1_F74G_Q5 mut_F	JW10885	TAAACCACATGGAGCTGATTTCAATTTGG
TIR1_F74G_Q5 mut_R	JW10886	CCCTTAACTGTAAGTGCC
pmm2_CBE_T4_R	JW10263	TAACGGGATGTTGAACGT
pmm2_Exon5_R	JW11288	CCCCATTTGTTACCTGGTCC
pmm2_Exon5_F	JW11292	GCTGTGTTTCAGGGGAAC
pmm2_Ex5_F	JW11375	AGTGATGTTCTGCAGTCATGTTC
pmm2_cDNA_R	JW11404	ATTATTTCTAGATCAGCAGAAGAAGAGCTGTTCG
pmm2_cDNA_F	JW11412	ATTATTGAATTCGCTGCCAACATGAACGACGCCACGG
pmm2_F122L_F	JW11751	AGGGGAACTTTCATTGAGTTCCG
pmm2_F122L_R	JW11752	CTTCTTGGGCAGCTT
pmm2_C136R_F	JW11753	GACGCAGCTGCAGTCAGGAGGAG
pmm2_C136R_R	JW11754	CAACCGGCGAGACGTTCA
rfc4_Ex4_F	JW11997	AAGTAACGGACTGGCACCTG
rfc4_Ex4_R	JW11998	GCAGCAAAGCAAGCATGAGT
rp2_Ex2_F	JW11999	CAGCCCATCATCGAGTCCTC
rp2_Ex2_R	JW12000	TGCTCCAAAACGAGTGGTGT

5.1.4 sgRNAs

Table 4: Single guide RNAs used in this thesis.

Guide nr.	Target	Target site [PAM]	Source
sgRNA57	*oca2*	GAAACCCAGGTGGCCATTGC[AGG]	Lischik et al., 2019
sgRNA58	*oca2*	TTGCAGGAATCATTCTGTGT[GGG]	Lischik et al., 2019
sgRNA442	*oca2_newPAM*	CTGCCTCAGGTCATCAGTGC[AGG]	Pakari et al., 2023
sgRNA443	*oca2_inception*	GATGACTCAGACTTCTGCCT[CAG]	Pakari et al., 2023
sgRNA521	*pmm2 exon 5*	AGACGTTCAACATCCCGTTA[CGG]	Pakari, 2021
sgRNA523	*pmm2 exon 2*	TCCTGCAGAGGCTCAGGACT[CGG]	Pakari, 2021

5.1.5 crRNAs

Table 5: CRISPR guide RNAs used in this thesis.

Guide nr.	Target	Target site [PAM]	Source
crRNA572	*pmm2_newPAM*	AACACAGCGGAACGTGAATG[TGG]	this thesis
crRNA573	*pmm2_newPAM_SNP*	AACACAGCTGAACGTCAATG[TGG]	this thesis
crRNA585	*pmm2_inception_SNP*	ATGAAGGTTCCCCTGAAACg[CGG]	this thesis
crRNA634	*rfc4*	CTGAACGCCTCGGATGAGCG[AGG]	this thesis
crRNA635	*rp2*	CAACTGGAGCCTACTGCCGG[AGG]	this thesis

5.1.6 Antibiotics

Table 6: Antibiotics used in this thesis.

Antibiotics	Stock conc.	Working conc.	Company
Ampicillin	100 mg/ml	100 µg/ml	Roth
Kanamycin	50 mg/ml	50 µg/ml	Roth

5.1.7 Enzymes and buffers

Table 7: Enzymes and buffers used in this thesis.

Enzyme	Buffer	Source
I-SceI meganuclease (5 U/µl)	I-SceI buffer (10x)	New England Biolabs
BamHI-HF (20 U/µl)	rCutSmart buffer (10x)	New England Biolabs

Benzonase nuclease (5 KU)		Millipore
DNAse I 1500U	DNA Digestion Buffer	Zymo Research
DpnI (20 U/µl)	rCutSmart buffer (10x)	New England Biolabs
EcoRI-HF (20 U/µl)	rCutSmart buffer (10x)	New England Biolabs
FastAP Thermosensitive Alkaline Phosphatase (1 U/µl)		Thermo Fisher Scientific
Hatching enzyme		Homemade
Klenow Exonuclease		Roche
KpnI-HF (20 U/µl)	rCutSmart buffer (10x)	New England Biolabs
NotI-HF (20 U/µl)	rCutSmart buffer (10x)	New England Biolabs
PacI (10 U/µl)	rCutSmart buffer (10x)	New England Biolabs
ProteinaseK (20 mg/ml)		Roche
PstI-FD	FastDigest Green buffer (10x)	Thermo Fisher Scientific
Q5 High-Fidelity DNA Polymerase (2 U/µl)	Q5 Reaction buffer (5x)	New England Biolabs
RiboLock (20 U/µl)	Reaction buffer (5x)	Thermo Fisher Scientific
SnaBI (5 U/µl)	rCutSmart buffer (10x)	New England Biolabs
T4 DNA Ligase (5 U/µl)	10x T4 DNA Ligase buffer	Thermo Fisher Scientific
T4 Polynucleotide Kinase (10 U/µl)		New England Biolabs
TURBO DNase (2 U/µl)	DNase I buffer (10x)	Invitrogen
XbaI (20 U/µl)	rCutSmart buffer (10x)	New England Biolabs
XcmI (5 U/µl)	rCutSmart buffer (10x)	New England Biolabs

5.1.8 Chemicals and reagents

Table 8: Chemicals and reagents used in this thesis.

Name	Source
4',6-diamidino-2-phenylindole (DAPI)	Sigma-Aldrich
2-mercaptoethanol	Sigma-Aldrich
2-Propanol	Sigma-Aldrich
2X RNA loading dye	Life Technologies

30% Acrylamide (29:1)	BioRad
5-phenyl-indole-3-acetic acid (5-Ph-IAA)	MedChemExpress
6x TriTrack DNA loading dye	Thermo Fisher Scientific
Acetic acid (96%)	Merck
Adenosine triphosphate (ATP)	Thermo Fisher Scientific
Agar	VWR
Agarose	Sigma-Aldrich
Agarose low melting	Roth
Alcian Blue 8GX	Sigma-Aldrich
Alizarin Red	Sigma-Aldrich
Alt-R CRISPR-Cas9 crRNA	Integrated DNA Technologies
Alt-R CRISPR-Cas9 tracrRNA	Integrated DNA Technologies
Ammonium persulfate	Sigma-Aldrich
Ammonium persulfate (APS)	Sigma-Aldrich
Ampicillin	Roth
ATP (100 mM)	Thermo Fisher Scientific
Bacto-Trypton	Gibco
Bromophenol blue	Sigma-Aldrich
cOmpleteTM EDTA-free Protease Inhibitor Cocktail	Roche
Coomassie Brilliant Blue R-250 Staining Solution	Bio-Rad
D-Biotin (Vitamin B7)	Sunday Natural
Deoxynucleotide triphosphate (dNTPs)	Sigma-Aldrich
Dimethyl sulfoxide (DMSO)	Roth
D-mannose	Sigma-Aldrich
dNTPs (10 mM)	Sigma-Aldrich
D-sorbitol	Sigma-Aldrich
Ethanol 70% (EtOH) denatured	Roth
Ethanol 96% (EtOH) denatured	Roth
Ethanol 99% (EtOH)	Sigma-Aldrich
Ethidium Bromide (EtBr) 10% solution	Roth
Ethylenediaminetetraacetic acid (EDTA)	Roth
Formamide	Sigma-Aldrich
GeneRuler DNA Ladder Mix	Thermo Fisher Scientific
Glacial acetic acid	Merck
Glycerol (Glycerin) ≥99%	Merck
Glycine	Sigma-Aldrich

HEPES (4-(2-hydroxyethyl)-1-piperazineethanesulfonic acid)	Roth
Hydrogen chloride (HCl) 37%	Merck
Hydrogen peroxide (H_2O_2) 30%	Sigma-Aldrich
Kanamycin	Roth
Magnesium chloride (MgCl2)	AppiChem
Methanol (MeOH) 100%	Roth
Methylcellulose	Sigma-Aldrich
Methylene blue trihydrate	Sigma-Aldrich
Nail polish	Essence
Normal Goat Serum (NGS)	Gibco
Nuclease-Free Duplex Buffer	Integrated DNA Technologies
Orange G	Sigma-Aldrich
PageRuler Prestained Protein Ladder, SDS, 10-180 kDa	Thermo Fisher Scientific
Paraformaldehyde (PFA)	Sigma-Aldrich
Phosphotungstic acid (PTA)	Sigma-Aldrich
Poly(ethylene glycol) (PEG) 4000	Thermo Fisher Scientific
Potassium chloride (KCl)	Roth
Potassium dihydrogen phosphate (KH2PO4)	Merck
Potassium hydrogen phosphate (K2HPO4)	Merck
Potassium hydroxide (KOH)	Merck
RIPA Lysis and Extraction Buffer	Thermo Fisher Scientific
Sodium acetate NaAc	Roth
Sodium chloride (NaCl)	Sigma-Aldrich
Sodium dodecyl sulphate sodium salt (SDS) 20%	Roth
Sodium hydrogen carbonate (NaHCO3)	Merck
Sodium hydroxide (NaOH)	Roth
Sucrose	Sigma-Aldrich
Tetramethylethylenediamine (TEMED)	Roth
Tricaine (C9H11NO2 · CH4SO3, MS-222)	Sigma-Aldrich
Tris Base	Roth
Tris-hydrochloride (Tris-HCl)	Sigma-Aldrich
Triton X-100	Roth
TRIzol reagent	Life Technologies
Tryptone bacteria	Roth
Tween20	Sigma-Aldrich

Urea	Sigma-Aldrich
Yeast extract	Roth

5.1.9 Antibodies

Table 9: Antibiotics used in this thesis.

Antibody	Host	Dilution	Company
Zpr1	mouse	1:500	ZIRC
Anti-mouse IgG (H+L), alexa fluor 488	goat	1:500	Life Technologies
β-actin-HRP	mouse	1:10000	Proteintech

5.1.10 Commercial kits

Table 10: Commercial kits used in this thesis

Name	Source
Direct-zol RNA Microprep Kit	Zymo Researcher
MEGAscript T7 Transcription Kit	Life Technologies
mMESSAGE mMACHINE Sp6 Transcription Kit	Life Technologies
Monarch DNA Gel Extraction Kit	New England Biolabs
Monarch PCR & DNA Cleanup Kit	New England Biolabs
Pierce™ BCA Protein Assay Kit	Thermo Fisher Scientific
QIAGEN Plasmid Mini Kit	Qiagen
QIAquick PCR Purification Kit	Qiagen
RNeasy Mini Kit	Qiagen
RevertAid First Strand cDNA Synthesis Kit	Thermo Fisher Scientific

5.1.11 Buffer and Solutions

Table 11: Media and solutions used in this thesis. All buffer were prepared in water if not stated otherwise.

Medium	Component	Concentration
1.5 % agarose in water	agarose	1.5 % w/v
	boil in water	
Alcian Blue staining solution	Alcian Blue 8GX	0.02 % w/v
	MgCl2	1 M
	EtOH	70 %

Alizarin red solution	Alizarin red	0.5 % (w/v)
Ampicillin	Ampicillin (100 mg/µl)	100 µg/µl
	EtOH	50 %
Bleaching solution	KOH	0.5 % v/v
	H2O2	1.5 % v/v
Destaining solution	methanol	40 %
	glacial acetic acid	10 %
6x DNA Orange G Loading dye	Orange G	1.2 mg/ml
	Glycerol	25 % v/v
ERM (Embryos Rearing Medium)	NaCl	17 mM
	KCl	0.4 mM
	$CaCl_2 \cdot 2H_20$	0.27 mM
	$MgSO_4 \cdot 7H_20$	0.66 mM
	HEPES pH 7.3	17 mM
	pH 7.1	
70% EtOH	99% EtOH	70 % v/v
70% EtOH, Nuclease-free water	99% EtOH	70 % v/v
	Nuclease-free H2O	
EtBr bath	EtBr 10 mg/ml	0.02 %
	1x TAE	
Fin-Clip buffer	Tris-HCl pH 8.5	100 mM
	EDTA pH 8	10 mM
	NaCl	200 mM
	SDS	2%
Fin-clip buffer with Proteinase K	Fin-clip buffer	95 %
	Proteinase K (20 mg/ml)	5 %
Kanamycin	Kanamycin (50 mg/µl)	50 µg/µl
4x Laemmli Buffer	SDS	8 %
	Glycerol	40%
	Tris-base	250 mM
	bromophenol blue	200 mg / 50 ml
	2-mercaptoethanol	20 % (added freshly)

LB-bacterial Plates	Bacto-Tryptone	10 g/l
	Yeast extract	5 g/l
	NaCl	10 g/l
	Agar	15 g/l
LB-medium	Bacto-Tryptone	10 g/l
	Yeast extract	5 g/l
	NaCl	10 g/l
Medaka Hatch Medium	NaCl	17 mM
	KCl	0.4 mM
	$CaCl_2 \cdot 2H_20$	0.27 mM
	$MgSO_4 \cdot 7H_20$	0.66 mM
	HEPES pH 7.3	17 mM
	Methylene blue trihydrate	0.0001 %
	pH 7.1	
3 M NaAc	NaAc	246.1 g/l
	Nuclease-free H2O	
Optical clearing solution (Zhu et al., 2019)	Urea	20 % w/v
	D-sorbitol	30 % w/v
	glycerol in DMSO	5 %
Oligo annealing buffer	Tris	10 mM
	NaCl	30 mM
	pH 7.5-8	
1x PBS	NaCl	137 mM
	KCl	2.7 mM
	KH_2PO_4	240 mg/l
	Na_2HPO_4	1.44 g/l
	pH 7.4	
P1 buffer	Glucose	50 mM
	Tris-HCL	20 mM
	EDTA	10 mM
	RNase A	100 µg/ml
	pH 8.0	

P2 buffer	NaOH	0.2 M
	SDS	1 % SDS
P3 buffer	KAc	5 M
	pH 5.5	
4 % PFA	Paraformaldehyde	4 %
	in 1x PBS	
	or 1x PTW	
1x PTW	Tween20	0.05 %
	in 1x PBS	
2x RNA loading dye	Xylene cyanol	0.25 % w/v
	Bromphenol Blue	0.25 % (w/v)
	SDS	0.025 % (v/v)
	EDTA	5 mM (pH 8.0)
	Formamide	95 % (v/v)
10x Running buffer	Tris	250 mM
	Glycine	2 M
	SDS	30 mM
	pH 8.3	
4x Separation Buffer	Tris-HCl	1.5 M
	SDS	1 %
	pH 8.8	
4x Stacking buffer	Tris-HCl	0.5 M
	SDS	0.4%
	pH 6.8	
1x TAE	Tris-base	242 g/l
	Glacial acetic acid	5.71 %
	EDTA	50 mM
	pH 8.5	
TB-medium	Bacto-Tryptone	12 g/l
	Yeast extract	24 g/l
	Glycerin	0.4 %
	KH2PO4	2.13 g/l
	K2HPO4	12.45 g/l

10x TBS	Tris-HCl	0.15 M
	Tris base	0.05 M
	NaCl	1.5 M
	pH 7.6	
1x TBST	Tris-HCl	15 mM
	Tris base	5 mM
	NaCl	0.15 M
	Tween20	0.1 %
	pH 7.6	
Tissue Clearing	Glycerol	20 % / 50%
	KOH	0.25 %
	in water	
20x Tricaine	Tricaine	4 g/l
	$Na_2HPO_4 \cdot 2H_20$	10 g/l
	pH 7-7.5	
50x Tris-Acetate-EDTA buffer (TAE)	Tris base	242 g/l
	Glacial acetic acid	5.71 %
	EDTA	50 mM
	pH 8.5	
10 x Yamamoto buffer	NaCl	0.75 g/l
	KCl	2.4 g/l
	$CaCl_2$	0.02 g
	$NaHCO_3$	20 mg/l
	pH 7.3	

5.1.12 Consumables

Table 12: Consumables used in this work.

Consumable	**Company**
96-well plate, U-bottom	Thermo Fisher Scientific
96-well plate, flat bottom (Nunc Microwell)	Thermo Fisher Scientific
Aluminum foil lids	Beckman Coulter
Cell saver tips 200 µl, 1 ml	Biozym
Cover slips	Roth

Filter paper	Whatman
Filter tips	Starlab
Gas permeable adhesive foil (moisture barrier seal 96)	4titude
Gel Loading Tips	Thermo Fisher Scientific
Glass beads	Roth
Glass dish	Roth
Glass petri dishes	Roth
Glass vials	Roth
Injection molds	House made
Injection needles GC100F-10	Harvard Apparatus
Low-binding tubes 1.5 ml, 2.0 ml	Thermo Fisher Scientific
MatTek dish	Mattek
Micro pestles 1.5/ 2.0 ml	Eppendorf
Micro pestles 0.5/1.5 ml	Laborversand Hartmann
Microloader tips	Eppendorf
Microloader tips for Western Blot	VWR
Nitrile gloves	Starlab
Nitrile gloves	TouchNTuff
Parafilm M	Amcor
Pasteur pipettes	Kisker / Sarstedt
PCR stripes and lids	Sarstedt
PCR tubes	Kisker
Petri dished dishes 92mm + 60 mm	Greiner
Pipette tips	Starlab
PVDF membrane- Immobilion-P	Merck
Reaction tubes 1.5ml, 2ml, 5ml	Sarstedt
Sandpaper 1000 grit	Bauhaus
Scalpel bladder	Roth
Scalpel blades	Braun
Serological pipettes 2 ml, 5 ml, 10 ml, 25 ml	Sarstedt
Superfrost plus microscope slides	Thermo Fisher Scientific
Tissue Freezing Medium	Leica
Tubes 15 ml, 50 ml	Sarstedt
Tubes for bacterial cultures, 13 ml PP	Sarstedt
Well plates, 6-well, 12-well, 24-well, 96-well	Roth, Corning
Whatman paper	Whatman

5.1.13 Equipment and Instruments

Table 13: Equipment and Instruments used in this thesis.

Name	Company
Bacterial Shaker INNOVA 44	New Brunswick
Bioruptor® Pico sonication device	Diagenode
Centrifuges 5417C, 5425, 5430R, 5810R	Eppendorf
Cold light source for stereomicroscope KL 1500 LCD	Schott
DeNovix DS-11 spectrophotometer	DeNovix
Electrophoresis chambers and combs	homemade and Peqlab
FemtoJet express	Eppendorf
Fish incubator	RuMed
Fish incubators	Heraeus instruments and RuMed
Forceps 5, 55 Inox stainless steel	Dumont
Freezer -20 °C	Liebherr
Freezer -80 °C	Thermo Fisher Scientific
Fridge 4 °C	Liebherr
Gel chamber	custom-made
HIVE data module	ACQUIFER from Bruker Corporation
Imaging Machine IM04	ACQUIFER from Bruker Corporation
Incubator 32 °C, 37 °C, 60 °C	Binder
InjectMan NI2	Eppendorf
Leica TCS Sp8	Leica
Macro pipette controller	Brand
Microinjector 5242	Eppendorf
Microwave	Samsung
Milli-Q water filtration station	Millipore Corporation
Mini centrifuge C1301B	Labnet
Mini centrifuge SU1555	Sunlab
Mini-PROTEAN® Tetra Handcast Systems	Bio-Rad
MS1 Minishaker	IKA
Multichannel pipette	Starlab / VWR
Multipette plus	Eppendorf
MyBlock mini dry bath	Benchmark Scientific
Needle puller P-30	Sutter Instrument Co USA

Nikon SMZ18 stereomicroscope	Nikon
Olympus SZX7	Olympus
PCR C1000 Touch Thermal Cycler	Bio-Rad
pH-Meter	Sartorius
Pipettes 10 µl, 20 µl, 200 µl, 1 ml	Starlab
Power supply PowerPac Basic	Bio-Rad
PowerPac 300	Bio-Rad
Rocking shaker DRS-12	neolab
Rotating arm	homemade
Scale	Sartorius
Scale Entris	Sartorius
Scale Extend	Sartorius
Shakers CAT S 20, DRS-12	neolab
Stereomicroscope Zeiss Stemi 2000	Zeiss
Transferpette® electronic pipette, single channel	Brand
UV table	Vilber Lourmat
UV-Gel Documentation System	Intas
Vortex-Genie 2	Scientific Industries

5.1.14 Software and online tools

The software and online tool used in this thesis are listed in Table 14. GitHub Copilot was used in Rstudio to provide code suggestions for data plotting. Perplexity was exclusively used for literature research. OpenAI's ChatGPT and YoKi were used for code suggestions for data plotting and exclusively for proof-reading of selected text passages and no text was generated. DeepL was used to help translating parts of the abstract into German.

Table 14: Software and online tool used in this thesis.

Software/online tools	**Source**
ACEofBASEs	Cornean et al., 2022
Affinity Designer 2 (v2.6)	Serif (Europe) Ltd
CCTop	Stemmer et al., 2015
ChatGPT	OpenAI
CRISPResso2	Clement et al., 2019
DeepL	DeepL SE

EditR	Kluesner et al., 2018
FileMaker	Filemaker Inc.
Geneious Prime 2019.2.3	Biomatters Limited
GitHub Copilot	GitHub
ImageJ v 2.14.0/1.54f	Schindelin et al., 2012
LasX	Leica
Mendeley Reference Manager v. 2.134.0	Elsevier
Microsoft Office	Microsoft
Medical Imaging Interaction Toolkit (MITK)	German Cancer Research Center
NEBaseChanger	New England Biolabs
NEBioCalculator v 1.17.2	New England Biolabs
Perplexity	Perplexity AI
R (v4.4.2)	R Core Team, 2021
Rstudio Version (2024.4.2.764)	Posit team, 2024
ShinyGO 0.82	Ge et al., 2020
Tm Calculator v 1.16.7	New England Biolabs
Uniprot	www.uniprot.org
YoKi v. Meta-llama/Meta-Llama-3.1-70BInstruct	Heidelberg University

5.2 Methods

5.2.1 Fish husbandry

Adult medaka fish (*Oryzias latipes*) stocks were bred (fish husbandry, permit number 35–9185.64/BH Wittbrodt) and experiments (permit number 35–9185.81/G-271/20 Wittbrodt) were performed in accordance with local animal welfare standards (Tierschutzgesetz §11, Abs. 1, Nr. 1) and European Union animal welfare guidelines (Bert et al., 2016). Fish were maintained as closed stocks at 28 °C on a 14 h light/10 h dark cycle at Heidelberg University. The fish facility is under the supervision of the local representative of the animal welfare agency.

5.2.2 Molecular cloning

5.2.2.1 Q5 polymerase PCR

PCRs (polymerase chain reactions) were carried out in a total volume of 50 µl with, typically, 1 µl of template DNA in a standard PCR reaction containing the ingredients listed in Table 15. If PCR failed, “pipetting without pipetting” was used for adding the template DNA to the PCR mix: 50 µl DNA was aspirated with a 200 µl tip and incubated for 10 secs.

The DNA was released and the tip was washed in 50 µl water by pipetting once up and down. The same tip was then used to aspirate the PCR mix for 10 secs to dissolve the DNA from the tip walls into the PCR mixture. The standard settings for the thermal cycler are depicted in Table 16. The primer annealing temperatures were determined with NEB's online Tm Calculator and the extension times were estimated from the polymerase extension rate of approximately 1 kb per 20–30 secs.

Table 15: Standard components of PCR Master Mix

Component	**50 µl Reaction**	**Final conc.**
Q5 reaction buffer (5x)	10 µl	1x
dNTPs (10 mM)	1 µl	200 µM
Forward Primer (10 µM)	2.5 µl	0.5 µM
Reverse Primer (10 µM)	2.5 µl	0.5 µM
Template DNA	variable	< 200 ng
Q5 High-Fidelity DNA Polymerase (2U/µl)	0.2 µl	0.4 U
MilliQ Water	To 50 µl	

Table 16: Standard PCR settings

Step	**Temperature**	**Time**
Initial Denaturation	98 °C	2 min
30 x cycles	98 °C	30 sec
	X °C	30 sec
	72 °C	X sec
Final extension	72 °C	10 min
Hold	10 °C	1 min

5.2.2.2 Agarose gel electrophoresis

Agarose gels were prepared by heating agarose powder in 1x TAE buffer using a microwave until fully dissolved. Gels with agarose concentrations varying between 1 % and 3 % (w/v) were prepared, depending on the size of DNA or RNA samples. The agarose was poured into a gel casting tray sealed with tape and a comb was inserted to form wells. Once the gel had solidified the comb was removed and the tray was placed into an electrophoresis chamber filled with 1x TAE buffer. DNA or RNA samples were mixed with DNA or RNA loading dye and together with a DNA Ladder the samples were loaded into the wells. Electrophoresis was first run at 90 V for 5 min followed by 120 V until desired separation was reached. After electrophoresis gels were stained in a 0.2 µg/ml ethidium

bromide in 1x TAE solution for 20 min. Visualization was performed under UV illumination. If needed, selected DNA bands were excised from the gel with a scalpel and purified directly or stored at -20 °C.

For RNA gel electrophoresis the comb, gel casting tray and electrophoresis chamber were treated with 0.1 N NaOH for 20 min under a fume hood to minimize RNase contamination. Then the components were rinsed using Milli-Q water directly from the filtration system. The agarose gel was freshly prepared using RNase-free 1x TAE buffer. Moreover, a fresh ethidium bromide staining solution was prepared for each use.

5.2.2.3 DNA gel extraction

DNA from agarose gel was extracted using the Monarch Gel Extraction Kit (NEB) according to manufacturer's protocol. The final elution was always carried out in prewarmed Milli-Q water. The DNA concentration was determined using a Nanodrop spectrophotometer.

5.2.2.4 Restriction digestion

Restriction digests were prepared in a total volume of 20 µl for test digestions or 50 µl when preparing linearized plasmid mRNA templates. All reactions contained the appropriate restriction enzyme and buffer, DNA and nuclease-free water. Test digestions of miniprepped DNA were incubated at 37 °C for 1 hour or overnight (O/N). Digestion efficiency was assessed by gel electrophoresis using either 200 ng of DNA or the entire digestion.

If digested DNA was used further for cloning, digestions were either purified using the Monarch PCR & DNA Cleanup Kit / the QIAquick PCR Purification Kit (Qiagen) or recovered from an agarose gel using the Monarch DNA Gel Extraction Kit.

5.2.2.5 DNA Ligation

Ligation reactions were performed either for 10-30 min at room temperature or O/N at 4 °C. The ligation was prepared in a total volume of 10 µl, using the components listed in Table 17. A 3:1 molar ratio of insert to vector was used and the required DNA mass was calculated using the online NEBioCalculator tool.

Table 17: Ligation reaction components.

Component	10 µl Reaction
10x T4 Ligation buffer	1 µl
Insert	x µl
Vector (40 ng)	y µl
T4 Ligase (5 U/µl)	1 µl
(PEG 4000)	optional
Milli-Q water	z µl

5.2.2.6 Q5-site directed mutagenesis

Primers for Q5 site-directed mutagenesis were designed using the online tool NEBaseChanger. Standard PCR was performed using the mutagenesis primers. The resulting PCR product was analyzed by gel electrophoresis and the band corresponding to the expected size was excised and purified. KLD (kinase, ligase, DpnI) treatment was then carried out according to Table 18.

Table 18: Components of KDL treatment of PCR product.

Component	15 µl Reaction
PCR product	1 µl
Milli-Q water	9.5 µl
rCutSmart buffer (10x)	1.5 µl
ATP (10 mM)	1.5 µl
PNK (NEB)	0.5 µl
T4 Ligase (5U)	0.5 µl
DpnI (20 U/µl)	0.5 µl

5.2.2.7 Transformation

For transformations chemical competent Mach1 T1 bacteria were thawed. 5 µl of ligation reaction was added to 50 µl of bacteria and gently mixed by flicking the tube. The mixture was incubation on ice for 15 min. The cells were then heat-shocked for 45 sec at 42 °C and snap cooled on ice for 2 min. Then, 300 µl TB medium was added and the cells were incubated at 37 °C on the shaker for either 45 min (ampicillin) or 1 hour (kanamycin) depending on the antibiotic resistance gene. Meanwhile LB agar plates containing the respective antibiotics were prewarmed at 37 °C for 1 hour. 50–250 µl of the transformed

cells were plated on agar plates using sterile glass beads and plates were incubated O/N at 37 °C.

5.2.3 Plasmid preparation

5.2.3.1 Minipreparation

For minipreparation of plasmids, single *E.coli* colonies were picked from agar plates using autoclaved toothpicks and inoculated in 3 ml of LB medium with the corresponding antibiotics. The cultures were incubated O/N at 37 °C while shaking at 180 rpm. On the following day 2 ml of each bacteria culture was transferred into 2 ml microcentrifuge tubes and centrifuged at 14000 rpm for 2 min at room temperature. The remaining bacterial cultures were stored at 4 °C as backup or for following BigMini preparations.
The bacterial pellet was resuspended in 200 µl of P1 buffer by sliding the tubes across a rack. Cell lysis was performed by adding 200 µl of P2 buffer and inverting of the tube 5-6 times. To neutralize the solution 200 µl of P3 buffer was added and the tubes were again inverted 5-6 times. Samples were centrifuged for 10 min at 14000 rpm and 4 °C. The supernatant was transferred to a fresh 1.5 ml tube.
To precipitate the plasmid DNA, 500 µl isopropanol was added to the supernatant and the tube was vortexed. After 15 min centrifugation at 14000 rpm and 4 °C the supernatant was discarded and the DNA pellet was washed with 500 µl of 70 % EtOH. After centrifugation for 5 min at 14000 rpm and room temperature, the ethanol was removed and the DNA pellet was air dried for ~5 min. Finally, the DNA pellet was dissolved in 40 µl of Milli-Q water.

5.2.3.2 Big Minipreparation

Around 50 µl from an O/N bacterial culture were used to inoculate 20 ml of LB medium with the respective antibiotics (ampicillin or kanamycin) in a 300 ml Erlenmeyer flask. The cultures were then incubated O/N at 37 °C with shaking at 180 rpm. Next, 8 ml of each O/N culture was collected and centrifuged for 2 min at 8000 rpm at room temperature to pellet the cells. DNA was subsequently extracted using the QIAprep Spin Miniprep Kit (QIAGEN) according to the manufacturer's protocol and the purified DNA was eluted in 50 µl Milli-Q water.

5.2.4 mRNA *in vitro* synthesis

The mRNAs for micro injections were *in vitro* transcribed from the plasmids listed in Table 19.
Of each plasmid, 5–10 µg was linearized O/N at 37°C. After verification of linearization on an agarose gel, digestions were either purified using the QIAquick PCR Purification Kit

(Qiagen) or recovered from an agarose gel using the Monarch® DNA Gel Extraction Kit (NEB). mRNA synthesis was carried out using the mMESSAGE mMACHINE SP6 or T7 Transcription Kit (Invitrogen) following the manufacturer's instructions, and RNA was purified with the RNeasy Mini Kit (Qiagen). The mRNA quality was evaluated by running an RNA test gel.

Table 19: Plasmids used for *in vitro* mRNA synthesis are listed together with the corresponding enzymes used for linearization and promoters driving transcription.

mRNA	Plasmid nr.	Enzyme	Promotor
evoBE4max	#5797	NotI	SP6
ancBE4max	#5811	SapI	T7
ABE8e	#5812	SapI	T7
HA-mAID-nanobody	#6090	NotI	SP6
Flag-myc-NES-Tir1F74G	#6149	NotI	SP6
ol pmm2	#6301	NotI	SP6
ol pmm2 C136R	#6315	NotI	SP6
ol pmm2 F122L	#6317	NotI	SP6
heiCas9	#6342	NotI	SP6
human PMM2	#6343	NotI	SP6

5.2.5 crRNA

CRISPR RNAs (crRNA) were evaluated for potential off-target effects using CCTop (Stemmer et al., 2015) and ACEofBASES (Cornean et al., 2022) using standard settings. The guide RNAs designed for this thesis are listed in Table 5. Synthetic crRNAs and tracrRNA (custom Alt-R crRNA) were ordered from IDT. Both, crRNA and tracrRNA were resuspended in nuclease-free duplex buffer (IDT) to a final concentration of 100 µM and stored at -20 °C. A duplex mixture of 40 µM crRNA:tracerRNA was prepared by mixing 4 µl of each RNA with 2 µl of nuclease-free duplex buffer. The mixture was incubated at 95 °C for 5 min, allowed to cool down to room temperature and stored at -20 °C. For injections, 1 µl was used in a 10 µl injection mix for 4 µM final concentration.

5.2.6 Microinjections and phenotyping

Microinjections were performed in wild-type Cab embryos and in homozygous *pmm2-GFP* embryos. Individual mixes are listed in Table 20. The night before injections, adult medaka fish were separated and paired on the next morning for mating. Freshly fertilized eggs

were collected in ice-cold 1x ERM after 15 min and separated using forceps. The eggs were aligned in the grooves of a 1.5 % agarose in water mold covered in cold 1 x ERM. Injection needles were pulled from glass capillaries with a needle puller. Approximately 2.5 µl injection mix was loaded into the needle and opened by scratching the chorion. The injection parameters were initially set to 1000 hPa for the injection pressure and 180 hPa for the holding pressure but they were individually adjusted during injections to adapt to needle requirements. Embryos were injected at the one-cell stage with the corresponding injection mixes. Injection volumes were estimated visually to around 10% of the cell volume. After injections, embryos were transferred into fresh ERM and incubated at 26 °C, 28 °C or 32 °C depending on the experimental requirements. Embryos were screened for the presence of fluorescence mRNA tracer 4-8 hours after injections for GFP signal or on the next day for mCherry positive embryos. If resulting phenotypes were assessed, embryos or hatchlings were imaged with a stereomicroscope equipped with an attached Nikon DXM1200 digital camera at the indicated timepoints. For imaging of hatchlings, they were anesthetized using 1x Tricaine prepared in 1x ERM.

Table 20: List of injection mixes used in this thesis.

Injection mix	**Injection mix components**	**final concentration**
degron mRNA	*Tir1(F74G)* mRNA	50 ng/µl
	mAID-vhhGFP4 mRNA	10 ng/µl
	GFP mRNA	10 ng/µl
	mCherry mRNA	10 ng/µl
degron mRNA	*Tir1(F74G)* mRNA	50 ng/µl
	mAID-vhhGFP4 mRNA	10 ng/µl
	mCherry mRNA	10 ng/µl
mCherry control	*mCherry* mRNA	10 ng/µl
degron stable line	plasmid	5 ng/µl
	I-SceI meganuclease	0.2 U
	10x ISceI buffer	0.5 x
	10 x Yamamoto buffer	0.5 x
oca2-inception	*ancBE4max* mRNA	150 ng/µl
	ABE8e mRNA	15 ng/µl
	oca2-step1 sgRNA	15 ng/µl
	oca2-step2 sgRNA	30 ng/µl
	GFP mRNA	10 ng/µl

oca2-step1 control	*ancBE4max* mRNA	150 ng/µl
	ABE8e mRNA	15 ng/µl
	oca2-step1 sgRNA	15 ng/µl
	GFP mRNA	10 ng/µl
oca2-step2 control	*ancBE4max* mRNA	150 ng/µl
	ABE8e mRNA	15 ng/µl
	oca2-step2 sgRNA	30 ng/µl
	GFP mRNA	10 ng/µl
oca2-ABE	*ABE8e* mRNA	150 ng/µl
	oca2-step1 sgRNA	15 ng/µl
	oca2-step2 sgRNA	30 ng/µl
	GFP mRNA	10 ng/µl
oca2-CBE	*ancBE4max* mRNA	150 ng/µl
	oca2-step1 sgRNA	15 ng/µl
	oca2-step2 sgRNA	30 ng/µl
	GFP mRNA	10 ng/µl
pmm2-ABE	*ABE8e* mRNA	150 ng/µl
	pmm2 new-PAM cr/tracerRNA	4 µM
	pmm2 new-PAM-SNP cr/tracerRNA	4 µM
	pmm2 inception cr/tracerRNA	4 µM
	GFP mRNA	10 ng/µl
pmm2-KO	*heiCas9* mRNA	150 ng/µl
	pmm2_exon2 sgRNA	4 µM
	pmm2_exon5 sgRNA	4 µM
	GFP mRNA	10 ng/µl
pmm2 WT	*pmm2 WT mRNA*	300 ng/µl
	GFP mRNA	10 ng/µl
pmm2 F122L	*pmm2 F112L* mRNA	300 ng/µl
	GFP mRNA	10 ng/µl
pmm2 C139R	*pmm2 C139R* mRNA	300 ng/µl
	GFP mRNA	10 ng/µl
pmm2 human	*pmm2 human* mRNA	300 ng/µl
	GFP mRNA	10 ng/µl

rfc4-KO	*heiCas9* mRNA	150 ng/µl
	rfc4 cr/tracerRAN	4 µM
	GFP mRNA	10 ng/µl
rp2-KO	*heiCas9* mRNA	150 ng/µl
	rp2 cr/tracerRAN	4 µM
	GFP mRNA	10 ng/µl
rfc4-BE	*ABE8e* mRNA	150 ng/µl
	rfc4 cr/tracerRAN	4 µM
	GFP mRNA	10 ng/µl

5.2.7 Auxin analog 5-Ph-IAA and toxicity test

The auxin analog 5-phenyl-indole-3-acetic acid (5-Ph-IAA) powder (MedChemExpress, # HY-134653) was dissolved in 100 µl DMSO to a final concentration of 198.98 mM using an ultrasonic water bath. From this, 10 mM stock solutions were prepared in 1x PBS and stored at -80 °C. Working concentrations were diluted with ERM from the stock solution as needed.

For the toxicity assay, wild-type Cab embryos from adult crosses were collected and maintained in ERM until stage10 (~6 hours post fertilization). Embryos were then treated with 1 µM, 2.5 µM, 5 µM, 10 µM 5-Ph-IAA and 0.005 % DMSO as vehicle control and incubated at 26 °C. The auxin solution was refreshed every 48 hours and resulting phenotypes were assessed daily with a stereomicroscope equipped with an attached Nikon DXM1200 digital camera until hatch.

5.2.8 Cloning of Tir1(F74G) point mutation

The point mutation for Tir1(F74G) was introduced via Q5 mutagenesis (5.2.2.6). The following primers were used for generation the *F74G* mutation: *fwd* 5'-TAAACCACATGGAGCTGATTTCAATTTGG and *rev* 5'- CCCTTAACTGTAAGTGCC. The plasmid Flag-myc-NES-TIR1 was used as template. *In vitro* mRNA synthesis was performed as describes before in 5.2.4

5.2.9 5-Ph-IAA induction

For validation of the degron system in wild-type Cab medaka embryos, microinjected embryos were kept at 26 °C and induced 6 hours post fertilization with 5 µM of the auxin analog 5-Ph-IAA. Prior to induction, dead and mCherry negative embryos were removed. Images were captured at the indicated timepoints using an epifluorescence

stereomicroscope (Nikon SMZ18) with a light source (Lumencor, SOLA-SE) for detecting GFP and mCherry signal.

5.2.10 Time-lapse acquisition and quantification of Pmm2-GFP degradation

Time-lapse imaging of degron-injected *Pmm2-GFP*$^{+/+}$ embryos was performed as described in Pakari et al., 2025. Images were acquired on an ACQUIFER imaging Machine (ACQUIFER Imaging GmbH, Heidelberg, Germany). Injected embryos and controls were transferred to a 96-well plate with 100 µl 1x ERM. Then 100 µl of either 10 µM 5-Ph-IAA, or 0.007 % DMSO or 1x ERM were added to reach 200 µl total volume. Imaging was conducted at 26°C for 26 hours. Every hour, a series of 5 z-slices with 300 µm each slice was captured in bright field, in the 561 nm and in the 470 nm fluorescence channels using a 2x NA 0.06 objective (Nikon, Düsseldorf, Germany).

To analyze the degron kinetics, a custom ImageJ macro was written. For each timepoint, a maximum projection of the z-stack was generated for both fluorescence channels. The maximum-projection images were then cropped with a rectangular mask in which the embryos were centered in the middle to minimize background interference. Fluorescence intensities from individual embryos at each time-point was used to calculate the degradation kinetics of GFP. To facilitate comparison between the different groups, mean GFP fluorescence values were baseline normalized by subtracting the initial time zero value from every point in the curve.

Moreover, to quantify the decay of GFP, the curve was fitted to a one phase decay model (Y = (Y0-Plateau)*exp(-k*X)+Plateau). All plots were visualized with RStudio.

5.2.11 Pmm2 enzyme activity assay

Biochemical Pmm2 enzyme activity assays were performed as described in Pakari et al., 2025.

Samples were prepared by me (5.2.12) and submitted to the Lab of PD Dr. Christian Thiel (Center for Child and Adolescent Medicine, Department Pediatrics I, Heidelberg University, 69120 Heidelberg, Germany) where Virginia Geiger performed the assays (5.2.12.1).

5.2.12 Sample preparation for stage 23 embryos

Stage 23 embryos were first rolled on fine sandpaper to remove surface hairs and then incubated in glass vials with hatching enzyme at 28 °C for approximately 40 min. Following enzymatic treatment, embryos were rinsed four times with ERM and transferred to a glass dish containing 1x ERM. Remaining chorions were carefully removed, and the yolk sac

was manually ripped open using forceps. Embryos were transferred to 5 ml tubes with ice-cold 1x PBS supplemented with Protein inhibitor cocktail and stored on ice until all samples were prepared. The embryos were washed for 5 min at 4 °C on a rocking table and were transferred to low-protein binding tubes with cell-saver tips. After centrifugation at 956 g for 2 min at 4 °C, the supernatant was discarded. The pellets were snap-frozen in liquid nitrogen and stored at -80°C.

5.2.12.1 Biochemical Pmm2 enzyme assay

Sample pellets were resuspended in a detergent-free lysis buffer containing protease inhibitors. The Pmm2 activity assay was based on the method established by Körner (Korner et al., 1998). Briefly, 30 µg of total protein was mixed with a reaction mixture containing NADP, $MgCl_2$, glucose-1-phosphate, mannose-6 phosphate isomerase (MPI) and phosphoglucose isomerase (PGI). To ensure that Pmm2 acts as a rate-limiting enzyme of the reaction, MPI and PGI were added in excessive for oversaturation. The resulting conversion of NADP to NADPH was measured at 340 nm for 2 hours. Each sample was analyzed in triplicates.

5.2.13 Image acquisition and phenotyping of oca2 Inception editants

Analysis of *oca2* inception knockouts was performed as previously described in Pakari et al., 2023 and Thumberger et al., 2022. Embryos were fixed 4.5 days post fertilization (Iwamatsu, 2004) in 4 % paraformaldehyde in 1x PBS on a rocking table at 4 °C O/N. On the following day, embryos were washed three times in 1x PBS at room temperature for 10 min per wash on a rocking table. For imaging, properly developed embryos were mounted in 1 % agarose using water molds and the heads were imaged with the high-throughput ACQUIFER Imaging Machine. Images were analysed using ImageJ. Eye regions were manually segmented by drawing elliptical selections. Minimum intensity projections were locally thresholded with the Phansalkar algorithm using the following parameters: r = 20, p = 0.4, k = 0.4). Selections of the eyes were used to extract mean grey values for each individual eye. Grey values ranged from 0 (fully pigmented eyes) to 255 (completely unpigmented). These values were used for plotting in RStudio.

5.2.14 Genotyping and targeted amplicon sequencing by Illumina

Genotyping of *oca2* inception knockouts was performed as previously described in Pakari et al., 2023 and Thumberger et al., 2022. The genomic DNA (gDNA) from editants was extracted from up to eight embryos by grounding the embryos with plastic pestles and lysing them in 100 µl fin-clip buffer with Proteinase K. Samples were then incubated at 60 °C O/N and on the following day the samples were diluted 1:2 with nuclease-free water

and proteinase K was heat inactivated at 95 °C for 20 min. Samples were afterwards stored at 4 °C.

For the *oca2* inception pools, eight phenotypically edited embryos were selected per replicate. For the corresponding controls *oca2*-step1, 1–8 embryos per replicate were genotyped and for *oca2*-step2 control, eight randomly chosen editants per replicate were processes. The targeted region was amplified by PCR using Q5 High-Fidelity DNA Polymerase and *oca2* primers containing 5′ overhangs with partial Illumina adapter sequences (*fwd* 5'-ACACTCTTTCCCTACACGACGCTCTTCCGATCTCGTTAGAGTGGT ATGGAGAACTG and *rev* 5'- GACTGGAGTTCAGACGTGTGCTCTTCCGATCTATGGT CCTCACATCAGCAGC).

PCR products were visualized by agarose gel electrophoresis, cut out of the gel and purified using the Monarch DNA Gel Extraction Kit. Amplicons were pooled at equal concentrations (20 ng/µl) and submitted for next-generation sequencing via GeneWiz (Azenta Life Sciences) using the Amplicon-EZ service (Illumina MiSeq, 2x250 bp, paired-end). Sequencing data was analyzed using CRISPResso2 v2.1.2 (Clement et al., 2019). Parameters were mostly set to default values with exception of the quantification_window_center (17), the plot_window_size (25) and the quantification_window_size (50). Nucleotide abundance plots were generated in R (v3.6.3) within the RStudio environment. The nucleotide composition and indel frequencies were averaged across the three replicates based on the Nucleotide Frequency Table output from CRISPResso2. Allelic variants were aligned and translated using Geneious Prime referencing the Allele Frequency Table output. Only alleles with cut off at 0.2 % of total reads in a replicate were considered.

5.2.15 Genotyping via Sanger sequencing of oca2 inception controls

For the inception *oca2-ABE* control injection, genotyping was performed on a pooled sample of five phenotypic embryos. For the *oca2-CBE* control group, a pool of eight randomly selected edited embryos was used for gDNA extraction. The extraction and genotyping PCR was done as described above (5.2.14). The following *oca2* primers were used: *fwd* 5'- GTTAAAACAGTTTCTTAAAAAGAACAGGA and *rev* 5'- AGCAGAAGAAATGACTCAACATTTTG. PCRs were run with standard settings with 62 °C annealing and 25 sec extension (Table 16). After purification the PCR products were sent for Sanger sequencing (Eurofins Genomics). Sequencing data was analyzed using EditR version 1.0.10 (Kluesner et al., 2018).

5.2.16 Genotyping of pmm2 F122L inception editants and stable lines

For genotyping of *pmm2 F122L* editants injected with cr/tracerRNAs and base editor mRNA (Table 20), embryos were crushed in 100 µl fin-Clip buffer with Proteinase K with a plastic pestle for gDNA extraction. Samples were incubated at 60 °C O/N. On the next day, the lysates were diluted by adding 200 µl water and incubation at 95 °C for 20 min to heat-inactivate the Proteinase K. Genomic DNA were stored at 4 °C. 1 µl of gDNA was used for a 50 µl PCR reaction (Table 15). Following *pmm2* primers were used: *fwd* 5'-AGTGATGTTCTGCAGTCATGTTC and *rev* 5'- CCCCATTTGTTACCTGGTCC. PCRs were run with standard settings with 66 °C annealing and 25 sec extension (Table 16). Amplicons were run on a 1 % agarose test gel. PCRs were cleaned-up with the Monarch PCR & DNA Cleanup Kit according to the manufacturer's protocol and sent for Sanger sequencing (Eurofins Genomics).

For genotyping of adult medaka fish, gDNA was extracted from fin-clipped fish which were anesthetized in 1x tricaine in 1x ERM. Fin-clipped samples were incubated in fin-clip buffer O/N at 60°C. After incubation, water was added in 1.5x of the volume and extracts were incubated at 95°C for 20 min. The gDNA was stored at 4 °C and genotyping was performed the same way as described above for the embryos.

5.2.17 Genotyping of *pmm2* knockout crispants

For genotyping of *pmm2* knockout crispants injected with sgRNAs and *heiCas9* mRNA (Table 20), embryos were treated as described in 5.2.15. The following *pmm2* primers were used: *fwd* 5'-ACGTAGCACAGGTGCGTTTCCCG and *rev* 5'-CGTTCTTGTAGGCCACCAGACCG. PCRs were run with standard mixture and standard settings with 72 °C annealing and 10 sec extension (Table 15, Table 16). Amplicons were run on a 1 % agarose test gel. PCRs were cleaned-up with the Monarch PCR & DNA Cleanup Kit according to the manufacturer's protocol and sent for Sanger sequencing (Eurofins Genomics).

5.2.18 Genotyping of *pmm2^{C139R}* and *pmm2^{V135Gfs*45}*

5.2.18.1 Genomic DNA and restriction digestion PCR

Genotyping of *pmm2^{C139R}* and *pmm2^{V135Gfs*45}* or compound heterozygous *pmm2$^{C139R/V135Gfs*45}$* individuals was performed on gDNA from whole embryos, hatchlings, hatchling tails or fin-clips from hatchlings or adult medaka. For gDNA extraction from embryos, they were ground with a plastic pestle in 100 µl fin-Clip buffer with Proteinase K. Whole hatchlings, tails of hatchlings and fin-clips were directly placed in 50 or 100 µl fin-Clip buffer with Proteinase K.

For micro fin-clips of hatchlings, the hatchlings were anesthetized with 1x tricaine in 1x ERM and placed on top of a 1.5 % agarose in water mold. Using a stereomicroscope, the tip of the caudal peduncle fin was cut off with a scalpel. The hatchlings were immediately placed in 1x Hatch media to wake up. The micro fin-clip was placed in 50 µl fin-Clip buffer with Proteinase K.

Samples were incubated at 60°C O/N. On the next day, the lysates were diluted by 1:2 with water and incubated at 95 °C for 20 min to heat-inactivate the Proteinase K.

For genotyping PCR, the following *pmm2* primers were used: *fwd* 5'- TAACGGGATGTTGAACGT and *rev* 5'- AAACATGACTGGAGAATGGAGC. PCRs were run with standard settings with 66 °C annealing and 25 sec extension (Table 16). Again, 1 µl gDNA was used as template in the standard PCR mixture (Table 15). To not waste any sample, only positive (wild-type gDNA) and negative (no template) PCR controls were run on a 1 % agarose test gel.

5.2.18.2 PCR product precipitation by sodium acetate and isopropanol

Pmm2 PCR products were purified by precipitation with sodium acetate (NaAc) and isopropanol. To each 50 µl PCR reaction, 4 µl of 3 M NaAC and 43 µl of isopropanol were added. Samples were mixed thoroughly and centrifuged for 30 min at 7 °C at full speed at 4000 rpm in a swing-out rotor. The supernatant was carefully removed using a multichannel pipette. The resulting pellet was washed with 150 µl of 70 % ethanol and centrifuged again for 10 min at 4000 rpm. After discarding the supernatant, the pellet was air-dried at room temperature for approximately 10 min. Finally, DNA was resuspended in 10 µl of nuclease-free water and incubated overnight at room temperature.

5.2.18.3 PstI digestion and genotyping

The PCR product was digested with the restriction enzyme PstI to differentiate between *pmm2* wild-type, $pmm2^{C139R/+}$, $pmm2^{V135Gfs*45}$ and $pmm2^{C139R/V135Gfs*45}$ alleles. The point mutation (C139R) and the frameshift mutation (V135Gfs*45) remove a native *PstI* recognition site which results in distinct digestion patterns. Digestion reactions were performed using either 10 µl of precipitated PCR product or 25 µl of unpurified PCR product, with reaction volumes and enzyme amounts specified in Table 21. Digestions were incubated overnight at 37 °C. The digested samples were separated on 3 % agarose gels to visualize allele-specific patterns and enable genotyping based on fragment size differences (Figure 34 A).

Table 21: PstI digestion master mix.

Component	Precipitated PCR	Unpurified PCR
PCR	10 µl	25 µl
water	7.7 µl	19.5 µl
FastDigest Green buffer (10x)	2 µl	5
PstI-FD	0.3 µl	0.5 µl
total	20 µl	50 µl

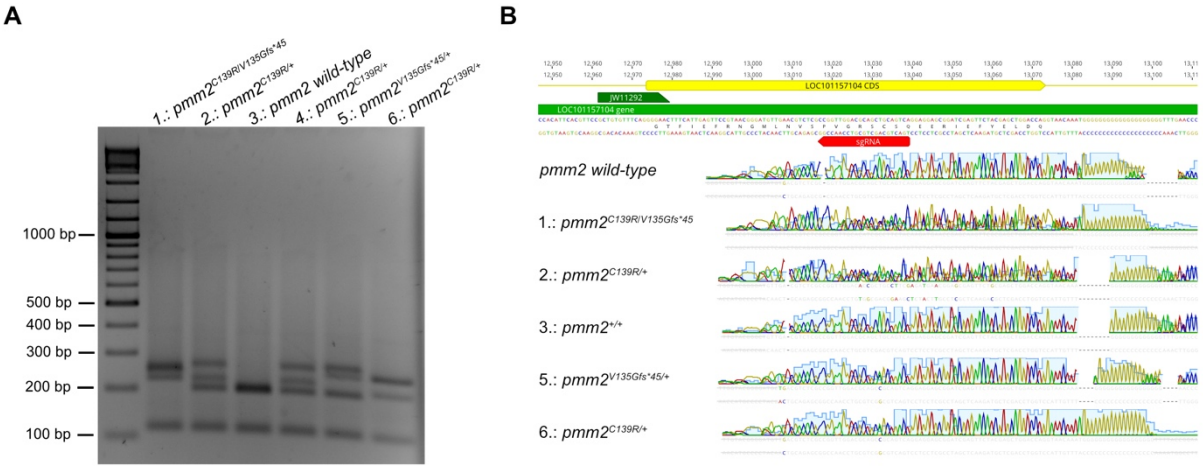

Figure 34: Genotyping of offspring from incrosses of *pmm2*^{C139R} and *pmm2*^{V135Gfs*45} mutant lines. A) A representative restriction digestions of PCR product with PstI can differentiate between the 4 resulting genotypes on a 3 % agarose gel. B) Sanger sequencing of the 4 *pmm2* genotypes with mutations in exon 5.

5.2.18.4 Genotyping by sanger sequencing

For genotyping PCR by Sanger sequencing of *pmm2*^{C139R} and *pmm2*^{V135Gfs*45} or compound heterozygous *pmm2*$^{C139R/V135Gfs*45}$ the following *pmm2* primers were used: *fwd* 5'-AGTGATGTTCTGCAGTCATGTTC and *rev* 5'- AAACATGACTGGAGAATGGAGC. PCRs were run with standard settings with 66 °C annealing and 30 sec extension (Table 16). Again, 1 µl gDNA was used as template in the standard PCR mixture (Table 15). 8 µl of PCR products was run on a 1 % agarose test gel. The remaining PCR products were cleaned-up with the Monarch PCR & DNA Cleanup Kit according to the manufacturer's protocol and sent for Sanger sequencing (Eurofins Genomics) with following primer: *fwd* 5'-GCTGTGTTTCAGGGGAAC (Figure 34 B).

5.2.18.5 Complementary DNA

Total RNA was extracted from two wild-type and two *pmm2*$^{C139R/V135Gfs*45}$ hatchlings by homogenizing the tissue with a plastic pestle in 300 µl TRIzol Reagent. Homogenization was followed by purification with the Direct-zol RNA MicroPrep Kit according to the manufacturer's protocol. Complementary DNA (cDNA) was synthesized from the isolated

RNA using the RevertAid First Strand cDNA Synthesis Kit. For amplification, primers targeting exon 2 of *pmm2* (*fwd* 5'-AAACGCAGAGGCTCAGGACTCG) and the 3' untranslated region (*rev* 5'-TGAGGTCACATCCCGTGTTG) were using for PCR with an annealing temperature of 64 °C and an extension time of 30 sec. PCR products were resolved on a 1.5 % agarose gel in 1x TAE buffer. Bands of the correct size were excised and purified from the agarose gel with the Monarch DNA Gel Extraction Kit (New England Biolabs) and sent for Sanger sequencing (Eurofins Genomics).

5.2.18.6 Alcian Blue and Alizarin Red staining

Bone and cartilage staining was performed using an acid-free Alcian Blue and Alizarin Red double-staining protocol as described in Walker & Kimmel, 2007. Hatchlings were anesthetized in 1x tricaine dissolved in 1x ERM and fixed overnight at 4 °C in 4 % PFA in 1x PBS on a rocking platform. On the following day samples were washed four times for 15 min each at room temperature with 1x PBS. Rehydration was carried out by incubating the hatchlings in 50 % ethanol for 10 min at room temperature.

Staining was performed overnight at room temperature with gentle rocking in an acid-free double-stain solution containing 0.02 % (w/v) Alcian Blue 8GX in 70 % ethanol, 200 mM $MgCl_2$, and 0.5 % (w/v) Alizarin Red. On the next day, staining solution was removed and samples were rinsed with water. To bleach the hatchlings the samples were incubated for 20 min at room temperature in a bleaching solution containing 1.5 % hydrogen peroxide and 1 % potassium hydroxide (KOH).

Tissue clearing was started by incubating samples in 20 % glycerol with 0.25 % KOH for 30 min to O/N at room temperature on a rocking table. Next, samples were incubated in 50 % glycerol with 0.25 % KOH for 2 hours to O/N under the same conditions. Samples were imaged using stereomicroscope equipped with an attached Nikon DXM1200 digital camera or the Sp8 confocal microscope with 20x glycerol objective. For long-term storage, samples were transferred to 50 % glycerol containing 0.1 % KOH and stored at 4 °C.

The cartilage angels of Meckel`s cartilage and ceratohyal angles were measured using the angle tool from ImageJ.

5.2.19 X-ray computed tomography

Sample preparation of hatchlings for micro computed tomography was done by myself (5.2.19.1) and Kristaps Kairiss (Wittbrodt/Weinhardt Lab, Heidelberg University) mounted the samples and performed with image acquisition (5.2.19.2-5.2.19.3).

5.2.19.1 Sample preparation

The offspring of the *pmm2*^{C139R} and the *pmm2*^{V135Gfs*45} line was collected and incubated at 32 °C. Phenotypic and wild-type looking hatchlings were fixed 4 days post hatching in 4 % PFA in 1x PBS at 4 °C on a rocking platform. After three days of fixing, the samples were washed three times in 1x PBS for ten min each time. Afterwards, the hatchlings were placed into 1.5 ml Eppendorf tubes and rinsed three times with 1x PBS for 10 min each. Following the washes, the samples were dehydrated using a graded ethanol series of 10 %, 25 %, 50 % and 70 % in double-distilled water for 20 min each step. After the final dehydration step, the ethanol was replaced with a 0.33 % (w/v) phosphotungstic acid solution (PTA) in 70% ethanol and the samples were stained for three days. Before mounting, the samples were moved to fresh 1.5 ml Eppendorf tubes and washed three times with 70 % ethanol for 10 min each. All steps were performed at room temperature on a rocking table.

5.2.19.2 Sample mounting

Hatchlings were mounted in 200 µl pipette tips and fixed in position using 1 % low-melting agarose. To prevent samples from drying, both sides of the pipette tips were sealed with parafilm. Mounted samples were placed with the large opening on the rotation stage and fixed in place using paraffin wax.

5.2.19.3 Image acquisition micro computed tomography

Computed tomography (CT) data was acquired using the SkyScan 1272 CMOS edition (Bruker, Belgium). A total of 3600 projections were captured over a full 360-degree rotation, with a rotation step of 0.1 degrees. Frame averaging was set to 3 and each projection had an exposure time of 1331 milliseconds. The camera binning was set to 2x2. The X-ray source was set to 40 kV and 100 µA with no filter applied. This setup produced a pixel size of 1.5 µm. Reconstruction of the acquired data was performed using NRecon software, version 2.2.0.6 (Bruker, Belgium).

5.2.20 Lectin blots

Sample preparation of hatchlings for the lectin was done by myself (5.2.19.1) and protein lysis and lectin blots (5.2.20.2-5.2.20.5) were performed by Andreas Hecker (Center for Child and Adolescent Medicine, Department Pediatrics I, Heidelberg University, 69120 Heidelberg, Germany).

5.2.20.1 Sample preparation

The offspring of the *pmm2*^{C139R} and the *pmm2*^{V135Gfs*45} line was collected and incubated at 32 °C in 1x hatching medium. At 5 days post hatch, the hatchlings were anesthetized in 1 % Tricaine in 1x ERM and images of each individual were taken. On top of a 1.5 % agarose in water mould as a support, the tail of each hatchling was cut off with a scalpel. The body was transferred into 1x PBS for washing followed by transfer into low protein-binding tubes, snap-frozen in liquid nitrogen and stored at -80 °C.
The tails were incubated in 50 µl of FinClip buffer supplemented with 2.5 µl of Proteinase K. For genomic DNA extraction the tails were incubated O/N at 60 °C. On the following morning 100 µl of water was added and the samples were incubated at 95 °C for 20 min.
After genotyping of the samples described in 5.2.18, only compound heterozygous *pmm2* and wild-type *pmm2* hatchlings were handed over on dry ice to Andreas Hecker for performing lectin blots.

5.2.20.2 Total lysate preparation

Hatchlings were homogenized in 100 µl of RIPA buffer supplemented with 1x protease inhibitor cocktail (Roche Diagnostics) using a micro-pestle. The lysate was sonicated to enhance cell lysis and subsequently incubated on ice for 30 min. Samples were mechanically sheared by passing them 20 times through a 22G x 1½" safety needle to ensure complete disruption. Lysates were then centrifuged at 18000 *rfc* for 30 min at 4 °C. The supernatant was collected and the total protein concentration was determined.

5.2.20.3 Total protein quantification

Quantification of protein concentrations was performed using the DC Protein Assay (Bio-Rad) based on the Lowry method according to the manufacturer's instructions. For each sample 5 µl of protein lysate was transferred into a well of a 96-well plate. If necessary, samples were diluted. Reagents A and B from the DC assay kit were added to each well in volumes of 25 µl and 200 µl, respectively. Plates were incubated at room temperature for 15 min on a shaker to allow color development. Absorbance was measured at 750 nm using a microplate reader. A standard curve was generated using bovine serum albumin (BSA) standards ranging from 0 to 2 mg/ml, prepared in RIPA buffer to match sample conditions.

5.2.20.4 SDS-PAGE

SDS-PAGE (sodium dodecyl sulfate polyacrylamide gel electrophoresis) was used to separate proteins based on their molecular weight using a two-layer acrylamide gel system with a stacking gel and a separation gel. The gels were prepared in-house (Table 22). The

stacking gel concentrates and aligns protein samples in a narrow band before they enter the resolving gel where proteins migrate at different rates depending on their size. After pouring the resolving gel into the gel cassette a thin layer of isopropanol was gently added to the surface to ensure a flat interface and to prevent drying during polymerization. Once polymerization was complete, the isopropanol was carefully removed using Whatman filter paper. The stacking gel was then poured on top of the polymerized resolving gel and a comb (10- or 15-well format) was inserted to create wells for sample loading. Gels were allowed to polymerize fully before use in electrophoresis.

Table 22: Composition of 12.5 % separation gel and stacking gel.

Compound	Separation gel (12.5 %)	Stacking gel
Rotiphorese 30	2500 µl	338 µl
Separation gel buffer	1500 µl	-
Stacking gel buffer	-	338 µl
APS (10 %)	60 µl	30 µl
TEMED	6 µl	3 µl
H_2O	2000 µl	1500 µl

For each sample, 10 µg of total protein (adjusted with water) was mixed with 1x SDS loading buffer and denatured by heating at 95 °C for 5 min. The PageRuler Prestained Protein Ladder (Thermo Fisher Scientific) was included as a molecular weight reference. Electrophoresis was started at 100 V to allow proteins to migrate through the stacking gel. After approximately 10 min, when the dye front reached the interface with the resolving gel the voltage was increased to 140 V to facilitate separation. The run was terminated once the dye front left the gel or when optimal resolution of protein bands was achieved.

5.2.20.5 Lectin blot

Proteins separated by SDS-PAGE were transferred onto a nitrocellulose membrane (GE Healthcare) using a semi-dry transfer system. The transfer stack consisted of three layers of Whatman paper, the SDS-PAGE gel, the nitrocellulose membrane, and three additional Whatman papers. The transfer was carried out at 47 mV per blot (1 mA/cm²) for 50 min.
To block nonspecific binding, membranes were incubated in 5 % milk in 0.1 % PBS-T for 20 min, followed by blocking in 0.5 % milk in 0.1 % TBS-T for 20 min. After rinsing with PBS-T and TBS-T, membranes were incubated overnight at 4 °C with biotinylated lectins (1:400 in 0.1 % TBS-T). The next day, membranes were washed three times for 5 min in the appropriate buffer.

For detection, membranes were incubated for 45 min at room temperature with HRP-conjugated streptavidin (Vector Laboratories, SA5004). Signal development was performed using ECL Plus Western Blot substrate (Thermo Fisher). Membranes were incubated in the substrate for 5 min in the dark and imaged using a Fusion SL4 chemiluminescence system (Peqlab). As a loading control, β-ACTIN-HRP antibody (Proteintech, HRP-60008) was used.

5.2.21 N-glycan analysis – xCGE-LIF

The sample for the xCGE-LIF (multiplexed capillary gel electrophoresis with laser-induced fluorescence detection) run were collected by me (5.2.21.1) and sent to the MPI Magdeburg where the samples were prepared, measured and analyzed by Ivan Andújar-Martínez**, Robert Burock** and **Dr. Erdmann Rapp** (5.2.21.2-5.2.21.5).

5.2.21.1 Sample preparation

Sample preparation was done the same way as describes earlier in 5.2.20.1.
After genotyping of the samples, compound heterozygous *pmm2* and wild-type *pmm2* hatchlings were shipped to Ivan Andújar-Martínez (Max Planck Institute for Dynamics of Complex Technical Systems, Germany).

5.2.21.2 Hatchlings lysis

For sample preparation, hatchling samples were processed separately, with 20 hatchlings per vial. The lysis buffer was prepared by filling a glass beaker with 10.5 ml of UPX Protein Extraction buffer (abcam, ab270054) and dissolving one tablet of cOmplete™ EDTA-free Protease Inhibitor Cocktail (Roche, 1183617001). Each sample vial (containing 20 hatchlings) was then supplemented with 500 µl of the prepared UPX + cOmplete solution. Tissue and cell disruption was performed using a Branson Sonifier (Marshall Scientific), applying a pulse mode with 30% amplitude for 1 min while keeping the samples on ice. This was followed by thermal disruption through incubation at 100 °C for 10 min in a Thermoblock (VWR, Thermal Shake *lite*). Finally, the samples were centrifuged at 15000xg for 10 min, and the supernatants are carefully transferred to new 1.5 ml Eppendorf tubes for further analysis.

5.2.21.3 Methanol/Chloroform precipitation

Samples were purified with methanol/chloroform protein extraction protocol according to Wessel and Flügge (1984). For that, 100 µl of sample was taken. To this, 4x volume of methanol was added, achieving a final concentration of 80%. The mixture was vortexed and centrifuged for 1 min at 9000 rpm. Next, 100 µl of chloroform was added, followed by vortexing and centrifuging for 1 min at 9000 rpm. Then, 300 µl of Milli-Q water was added,

vortexed, and centrifuged for 1 min at 9000 rpm. The upper phase was carefully removed and discarded.
Subsequently, 300 µl of methanol was added, and the mixture was vortexed and centrifuged for 2 min at 9000 rpm. The supernatant was removed, and the protein pellet was dried and stored until further use.

5.2.21.4 FASP tryptic digestion

Prior to analysis, the whole protein pellet was reconstituted in 200 µl 8 M urea (in 0.1 M Tris-HCl, pH 8.5). The Nanosep centrifugal filter unit (10K Omega membrane, Pall Corporation) was then rinsed by adding 50 µl of urea buffer and centrifuging at 14000 x g for 5 min at room temperature (RT). Subsequently the 200 µl of the reconstituted protein pellet was added, followed by vortexing and incubation for 5 min in a thermomixer. The protein solution was centrifuged at 14000 x g for 5 min at RT. The flow-through was discarded.
To reduce disulfide bonds, 100 µl of 40 mM 1,4-Dithiothreitol (DTT, Sigma-Aldrich) solution was added to the filter unit, mixed for 1 min at 600 rpm using a thermomixer at RT, and incubated at 56 °C for 20 min with gentle agitation (300 rpm). The filter unit was centrifuged at 14,000 x g for 10 min at RT, and the flow-through was discarded. Next, 100 µl of 55 mM Iodoacetamide (IAA, Sigma-Aldrich) solution was added, mixed for 1 min at 600 rpm using a thermomixer at RT, and incubated for 20 min in the dark. The filter unit was centrifuged at 14000 x g for 10 min at RT, and the flow-through was discarded.
The filter unit was washed three times with 100 µl of urea buffer. For each wash, buffer was added, incubated for 1 min at RT at 600 rpm, centrifuged for 10 min, and the flow-through was discarded. This process was repeated three times with 100 µl of 1x Ammonium bicarbonate (ABC) buffer (50 mM, Sigma-Aldrich).
To prevent enzyme solution leakage during digestion, the filter tube cap was cut and retained to seal the filter unit. Using clean gloves, the filter unit was transferred to a new 2 ml Eppendorf tube. The enzyme solution was prepared by diluting trypsin (Promega) in 50 mM ABC buffer containing 5% acetonitrile (ACN, Sigma-Aldrich) and 1 mM Calcium chloride ($CaCl_2$, Sigma-Aldrich), with a final enzyme-to-substrate ratio of 1:100 and a total volume of 100 µl. The enzyme solution was added to the filter unit, mixed for 1 min at 600 rpm using a thermomixer, and incubated at 37 °C O/N with gentle agitation (350 rpm).
Post-digestion, the filter unit was centrifuged at 8000x g for 7 min at RT. Care was taken to avoid releasing the filter unit at high speeds, and the flow-through was retained. Additional washes were performed by adding 50 µl of digestion buffer (50 mM ABC buffer with 5 % ACN) and 50 µl of Milli-Q water, centrifuging each time at 8000x g for 7 min at RT, and retaining the flow-through.

The digest was dried in a SpeedVac and stored at −20 °C until use.

5.2.21.5 N-glycan sample preparation and xCGE-LIF analysis

Thereafter, *N*-glycans were prepared and analyzed as previously described by Hennig et al. (2015 and 2016), with slight modifications. Briefly, to each dried sample, 2 µl of 1X PBS was added, followed by 4 µl of 2% SDS solution prepared in 1x PBS. The samples were mixed and centrifuged. Subsequently, the samples were incubated for 10 min at 60 °C. After incubation, 4 µl of 8% IGEPAL (Sigma-Aldrich) solution in 1x PBS was added to each sample. The samples were mixed and centrifuged again. *N*-glycans were released from protein backbone by PNGase F incubation (Sigma-Aldrich) for 12 h at 37 °C. Released *N*-glycans were labeled with 8-aminopyrene-1,3,6-trisulfonic acid (APTS, Synchem) using reduX (glyXera) as non-toxic but highly efficient reducing agent, followed by a sample cleanup step (HILIC-SPE) to remove excess label, salt, and other impurities. The purified labeled *N*-glycans were analyzed by xCGE-LIF. Using the glycoanalysis system glyXboxCE [glyXera; incl. 4-capillary xCGE-LIF instrument, software (glyXtoolCE v6.1.0) and database (glyXbaseCE)]. The generated *N*-glycan electropherogram data (migration times) were aligned to an orthogonal internal standard (GeneScanTM 500 LIZ Size Standard; Thermo Fisher Scientific & glyXalign GA2; glyXera), resulting in so-called "*N*-glycan fingerprints" with highly reproducible (orthogonally aligned) migration times. Subsequently, glyXtoolCE was utilized for automated peak picking, integration, and relative quantification, as well as for the structural assignment of the *N*-glycan peaks by migration time matching to the *N*-glycan database glyXbaseCE. To confirm *N*-glycan structures, a comprehensive exoglycosidase sequencing was performed, using the enzymes β(1-2,3,4,6)-N-Acetylglucosaminidase (Agilent), α-(2–3,6,8) sialidase (Agilent), and α(1–2,3,6) mannosidase (New England BioLabs). All exoglycosidase digests were carried out at 37 °C and at the reaction conditions recommended by the respective enzyme supplier. The APTS-labeled *N*-glycan mixture from each sample, after being resuspended, was digested O/N with the corresponding exoglycosidases. Subsequently, HILIC-SPE was performed again, with washing using only 80% ACNaq and elution in 500 µl of Milli-Q water. The samples were then dried until their re-analysis with glyXboxCE.
The symbolic representations of *N*-glycans in Supplementary Table 1 and in figures were drawn using GlycoWorkbench (Ceroni et al., 2008) according to the guideline of the Consortium for Functional Glycomics (Varki et al., 2009).

5.2.22 D-Mannose supplementation

The offspring of the *pmm2*^{C139R} and the *pmm2*^{V135Gfs*45} mutant lines were collected and incubated at 32 °C. Embryos were treated with D-Mannose at two developmental stages:

25 mM at stage 9 and 50 mM at stage 32 (Iwamatsu, 2004). To enhance permeability of the chorion, embryos were gently rolled on fine sandpaper prior to treatment. Supplementation of both groups were carried out until 5 days post hatching and the media was changed every day. At 9 days post hatching, individuals were euthanized using an overdose of Tricaine, imaged under a binocular and genotyped by restriction digestion as previously described in in 5.2.18.

5.2.23 Biotin supplementation

For Biotin supplementation, the offspring of the *pmm2*^{C139R} and the *pmm2*^{V135Gfs*45} mutant lines and wild-type Cab embryos were collected and incubated at 32 °C. Embryos were treated with 0.25 mg/ml biotin in ERM at stage 34. To enhance permeability, embryos were gently rolled on fine sandpaper and dechorinated with hatching enzyme at 28 °C for approximately 30 min. Following enzymatic treatment, embryos were rinsed four times with ERM and transferred to a glass dish containing 1x ERM. Remaining chorions were carefully removed with forceps. Treatments of wild-type and *pmm2* mutants were carried out until 5 days post hatching and the supplementation media was changed every two days. At 18 days post hatching, individuals were micro fin-clipped and genotyped as previously described in 5.2.18.

5.2.24 mRNA rescue injections of *pmm2*$^{C139R/V135Gfs*45}$

5.2.24.1 Cloning of constructs

Wild-type *pmm2* mRNA was cloned from stage 32 wild-type Cab cDNA using PCR. The forward primer (5′-ATTATTTCTAGATCAGCAGAAGAAGAGCTGTTCG-3′) and reverse primer (5′-ATTATTGAATTCGCTGCCAACATGAACGACGCCACGG-3′) introduced XbaI and EcoRI restriction sites. The resulting PCR product was digested with *XbaI* and *EcoRI* and ligated into a pCS2+ vector backbone that was digested with the same enzymes. All steps were performed as described earlier in 5.2.2. The point mutations for *pmm2 F122* and *C139R* mutant mRNA were introduced via Q5 mutagenesis (5.2.2.6). Following primers were used for generating the *F122L* mutation: *fwd* 5'-AGGGGAACTTTCATTGAGTTCCG and *rev* 5'- CTTCTTGGGCAGCTT. For generation of the *C139R* mutations following primers were used: *fwd* 5'-GACGCAGCTGCAGTCAGGAGGAG and *rev* 5'- CAACCGGCGAGACGTTCA.
The human wild-type *Pmm2* sequence cloned into pGEM-T Easy backbone was provided by Dr. Christian Thiel (Center for Child and Adolescent Medicine, Department Pediatrics I, Heidelberg University, 69120 Heidelberg, Germany). The vector was digested with NotI and blunted with Klenow Exconuclease. The human *Pmm2* was cloned into the SnaBI digested pCS2+ vector which was dephosphorylated with FastAP Thermosensitive

Alkaline Phosphatase. *In vitro* mRNA synthesis was performed as described before in 5.2.4

5.2.24.2 Injections and genotyping

For micro injections the *pmm2*$^{C139R/+}$ was crossed with the *pmm2*$^{V135Gfs*45/+}$ mutant lines and embryos were injected in the 1-cell stage with 300 ng/µl mRNA. The specific mixes are listed in Table 20. Injected embryos were incubated at 32 °C until hatching. Afterwards, they were kept at room temperature and fed once a day. Genomic extraction of DNA of hatchlings was performed three weeks post hatch or 13 days post hatch via micro fin-clipping as previously described in in 5.2.18. Genotyping was completed by restriction digestion as described in 5.2.18.

5.2.24.3 Bottom-up mass spectrometry

Sample and lysate preparation of embryos and hatchlings for bottom-up mass spectrometry was performed by me (5.2.24.4) and Dr. Marcin Luzarowski (Core Facility for Mass Spectrometry and Proteomics of the Center for Molecular Biology (ZMBH) of Heidelberg University) performed further sample preparation, mass spectrometry run and data analysis (5.2.24.7-5.2.24.9). Downstream Gene Ontology (GO) term enrichment analysis was performed by myself (5.2.24.10).

5.2.24.4 Sample collection and preparation of lysates

The offspring of the *pmm2*^{C139R} and the *pmm2*^{V135Gfs*45} line were collected and incubated at 32 °C. At 5 dpf, when embryos reached stage 35 (Iwamatsu, 2004) sample preparation started for the embryonic stage samples. Embryos were rolled on fine sandpaper and manually dechorinated with sharp forceps. Following dechorionation, embryos were washed 4 times with 1x ERM and were transferred to clean glass Petri dishes containing 1x ERM. The yolk sacs were ripped using sharp forceps to separate embryonic tissue from the yolk. The embryos were then transferred to a 15 ml falcon tube containing ice-cold 1x PBS and gently shaken at 4 °C for 5 min. PBS was replaced with fresh ice-cold 1x PBS and the embryos were shaken again for 5 min at 4 °C. After this step, embryos were returned to a glass dish for removal of remaining yolk using forceps. Embryos were individually transferred into 1.5 ml low protein-binding microcentrifuge tubes. All liquid was removed from each tube before snap freezing the samples in liquid nitrogen. Frozen embryos were stored at −80 °C until further use.

At 11 days post fertilization (4-5 days post hatch), hatchlings were euthanized using tricaine prior to sample preparation. Brightfield images were acquired for documentation purposes. The hatchlings were washed in 1x PBS and transferred individually into 1.5 ml

low protein-binding tubes. After removing all remaining liquid, samples were snap frozen in liquid nitrogen and stored at −80 °C until further processing.

5.2.24.5 Preparation of lysates and genotyping

Lysates of the samples were prepared by adding 50 µl (stage 35 embryos) and 95 µl (hatchlings) of RIPA Lysis and Extraction Buffer supplemented with cOmpleteTM EDTA-free Protease Inhibitor Cocktail. Samples were homogenized by 6 cycles each 10 sec on and 30 sec off at 4 °C in a Diagenode Bioruptor (Prof. Dr. Jan Lohmanns Lab, COS Heidelberg). Lysates were quickly spun down at 4 °C and incubated on ice for 20 min. In the meantime, a PCR master mix was prepared as described in section 5.2.18.1. As template DNA, 1 µl of protein lysate was used and 31 PCR cycles were run. Following PCR, the lysates were snap-frozen in liquid nitrogen and stored at -80 °C.

5.2.24.6 Measuring protein concertation and SDS-PAGE

After genotyping (5.2.18.1.), only wild-type and compound heterozygous *pmm2* samples were kept. Frozen lysates were thawed on ice and two stage 35 (5 dpf) embryos were pooled into a single tube. To degrade nucleic acids and reduce lysate viscosity samples were treated with Benzonase nuclease. Benzonase was added to the lysates and incubated for 20 min at 4 °C followed by 5 min at 37 °C to maximize enzymatic activity.
Samples were centrifuged at 12000 g for 10 min at 4 °C. The supernatant was carefully transferred to fresh 1.5 ml low-protein-binding tubes. Protein concentration was determined using the Pierce BCA Protein Assay Kit according to the manufacturer's instructions. Measurements were performed in duplicates using flat bottom 96-well plates. Lysates were aliquoted and diluted with RIPA buffer to reach a final concentration of 10 µg protein in 50 µl total volume. Aliquots were snap-frozen in liquid nitrogen and stored at -80 °C. From the remaining lysate 10 µg were boiled in 4x Laemmli sample buffer for 10 min at 95 °C and stored at -80 °C. Samples were run on a self-made SDS-PAGE consisting of a 10 % separation gel and a 4.5 % stacking gel (as described earlier in 5.2.20.4). Gels were run at 65 V for the first 30 min and at 100 V for approximately 1 hour. The gels were washed for 5 min in water and then stained with Coomassie Brilliant Blue staining for 2 hours on a shaker at room temperature. Destaining was performed using destaining solution and washing the gels four times each 30 min at room temperature on the shaker. Lysates were handed over on dry ice to Dr. Marcin Luzarowski.

5.2.24.7 Sample clean-up and digestion

Protein samples (10 µg) were prepared for digestion using the Single Tube Solid Phase Sample Preparation (SP3) method on a KingFisher Apex platform (Hughes et al., 2019).

To ensure optimal results, all reagents, solutions, and vessels were of high purity and keratin-free. Magnetic bead-based sample preparation was carried out in a 96-well plate format using a prototype magnetic bead slurry (Promega, Cat. No. 916738) and a total of 1000 µl liquid per sample for binding. Beads were washed three times with dH_2O and reconstituted to a final concentration of 100 µg/µl. Protein reduction and alkylation were performed in the presence of 10 mM TCEP, 40 mM CAA, and 1 % SDS. Samples were incubated at 95 °C for 5 min, followed by 25 min at 70 °C with mixing, and then cooled to room temperature. Following reduction and alkylation, 2 µl of magnetic bead slurry was added to each sample, followed by the addition of ethanol to a final concentration of 80%. Samples were incubated at 24 °C for 20 min with mixing to enable protein binding. Beads were subsequently washed three times with 1 ml of 80% ethanol and once with 1 ml of 80 % acetonitrile (ACN), with each wash lasting 4 min and including mixing. Protein digestion was performed with trypsin at a 1:50 enzyme-to-protein ratio. The reaction was carried out at 37 °C for 4 hours with mixing. Digestion was quenched by the addition of trifluoroacetic acid (TFA), and samples were stored O/N at 4 °C. On the following day, the pH of each sample was confirmed to be below 2 before proceeding to StageTip desalting and LC-MS (Liquid Chromatography-Mass Spectrometry) analysis. Digested peptides were desalted using self-assembled C18 Empore® extraction discs (3M, Maplewood, MN) (Rappsilber et al., 2007).

5.2.24.8 LC-MS/MS analysis and data processing

Samples were suspended in 0.1 % TFA and analyzed using an Ultimate 3000 liquid chromatography system coupled to an Orbitrap QE HF (Thermo Fisher) as described before (Pedre et al., 2023). Briefly, peptides were separated in a 120 min linear gradient starting from 3 % B and increasing to 23 % B over 100 min and to 38 % B over 20 min, followed by washout with 95 % B. The mass spectrometer was operated in data-dependent acquisition mode, automatically switching between MS and MS2. MS spectra (m/z 400–1600) were acquired in the Orbitrap at 60,000 (m/z 400) resolution and MS2 spectra were generated for up to 15 precursors with a normalized collision energy of 27 and an isolation width of 1.4 m/z. The MS/MS spectra were searched against the UniProt O. latipes (UP000001038, November 2019), and a customized contaminant database using Proteome Discoverer 2.5 with Sequest HT. The fragment ion mass tolerance was set to 0.02 Da, and the parent ion mass tolerance to 5 ppm. Trypsin was specified as an enzyme. The following variable modifications were allowed: Oxidation (M), Deamidation (N, Q), Acetylation (N-terminus), Met-loss (M), and a combination of Met-loss and acetylation (N-terminus), whereas Carbamidomethylation (C) was set as a fixed

modification. Peptide quantification was done using a precursor ion quantifier node with the Top N Average (n = 3) method set for protein abundance calculation.

5.2.24.9 Data Analysis

To identify potential interaction partners of the protein(s) of interest, protein quantification data exported from Proteome Discoverer 2.5 were analyzed in R Studio (R Core Team, 2021). Proteins supported by fewer than two peptides and those not designated as master proteins within their respective protein groups were excluded. The remaining data were normalized to the median intensity across all samples, under the assumption that medians should be comparable across experimental conditions and replicates. Proteins quantified in at least three out of four replicates in at least one experimental group were considered reliably detected and retained for further analysis. Missing values were imputed using the missForest algorithm (Stekhoven & Bühlmann, 2012). Statistical analysis was performed using one-way ANOVA followed by Benjamini-Hochberg correction to adjust for multiple comparisons. Pairwise group differences were assessed using Tukey's Honest Significant Difference (Tukey-HSD) test. Data visualization was carried out using the ggplot2 package in R.

5.2.24.10 Gene Ontology (GO) term enrichment with ShinyGO.82

Gene Ontology (GO) term enrichment analysis was performed with ShinyGo v0.82 (Ge et al., 2020) in the main class of biological processes. Medaka was set as species (Japanese medaka HdrR genes ASM223467v1) and as background all proteins detected in the bottom-up mass spectrometry run were provided. Gene enrichment analysis of differentially expressed proteins at embryonic stage 5 dpf and at hatching stage 5 dph was performed separately for up- and downregulated proteins at both stages: prior (stage 35) and after onset of phenotypes (hatchling).

5.2.25 Immunostaining against Zpr1

Sample preparation of hatchlings for cryosections was performed by me (5.2.25.1) and Encarnación Sánchez Salvador (Wittbrodt Lab, Heidelberg University) performed cryosections, antibody staining and confocal imaging of wild-type and *pmm2* mutant sections (5.2.25.2-5.2.25.3).

5.2.25.1 Sample preparation

Medaka hatchlings were fixed in 4 % PFA in 1x PTW O/N at 4 °C. Afterwards, hatchlings were washed in 1x PTW and transferred to 30 % sucrose in 1x PTW for O/N incubation at 4 °C, followed by 3 washes in 1x PBS and transferred to 30 % sucrose in 1x PBS at 4 °C.

After at least 5 days, media was exchanged to a 1:1 solution of 30 % sucrose in 1x PBS and tissue freezing media (TFM) for at least one night at 4 °C.

5.2.25.2 Cryosectioning

For cryosections, hatchlings were placed in plastic molds filled with TFM and snap-frozen in liquid nitrogen. Samples were immediately placed in a cryostat for 10 min to equilibrate. The heads of the hatchlings were sectioned with 16 µm thickness on the cryostat (Leica CM 3050S). Cryosections were dried O/N at 4 °C on Superfrost plus microscope slides.

5.2.25.3 Immunohistochemistry on cryosections and imaging

On the next day, sections were rehydrated for 30 min in 1x PBS at RT in a pipette tip box. Samples were blocked for 2 hours in 10 % NGS in 1x PBS at RT and slides were covered with parafilm to avoid evaporation. After the blocking solution was removed slides were washed 2 times for 5 min with 1x PBS. Next, the sections were stained with anti-Zpr1 antibody (1:500) in 1 % NGS in 1x PBS and covered with parafilm O/N at 4 °C. Sections were then washed 6 time with 1x PBS for 5 min each washing step. The secondary goat anti-rabbit IgG Alexa Fluor 488 antibody (1:500) was applied in 1 % NGS in 1x PBS together with DAPI (1:500 dilution) overnight at 4 °C in the dark. Slices were washed again 3 times for 5 min with 1x PBS. The slides were mounted in 100 µl of 60 % glycerol in 1x PBS and a coverslip was place on top and sealed with nail polish. Slides were stored at 4 °C in darkness until imaging was performed. Imaging was done on a Leica SP8 confocal microscope. Images were processed with ImageJ.

5.2.26 Whole mount imaging of DAPI stained heads

5.2.26.1 Genotyping of rp2 and rfc4 editants

Wild-type *Cab* embryos were microinjected at the one-cell stage with the injection mixes stated in Table 20. After injections, the embryos were incubated at 28 °C until hatching. Genomic DNA was extracted from editants 3 dpf using the standard protocol (5.2.15). Following primers were used: *rfc4 fwd* 5'- AGTGATGTTCTGCAGTCATGTTC and *rfc4 rev* 5'- GCAGCAAAGCAAGCATGAGT and *rp2 fwd* 5'- CAGCCCATCATCGAGTCCTC and *rfc4 rp2* 5'- TGCTCCAAAACGAGTGGTGT. PCRs were run with standard settings with 68 °C annealing and 30 sec extension time (Table 16). PCR products were separated on a 1 % agarose gel. Bands of the correct size were cut out and purified with the Monarch DNA Gel Extraction Kit according to the manufacturer's protocol and sent for Sanger sequencing to verify editing (Eurofins Genomics).

5.2.26.2 Sample preparation, staining and Sp8 imaging

Hatchlings were fixed in 4 % PFA in 1x PBS O/N at 4 °C on a shaker. The next day, samples were washed three times with 1x PBS. Samples were then bleached using a standard bleaching solution on a shaker at room temperature for 20–40 min. Afterwards, they were washed three times in 1x PTW for 30 min each. Heads were dissected using forceps and incubated overnight at 4 °C in DAPI staining solution (10 ng/µl in 1x PTW) on a shaker. On the next day, samples were washed five times with 1x PTW for 5 min each. For imaging, heads were mounted ventrally in clearing solution in MatTek glass-bottom dishes. Imaging was performed using a Leica SP8 confocal microscope equipped with a 20x glycerol immersion objective.

5.2.27 Data visualization

In general, microscopy images were processed with ImageJ (Schindelin et al., 2012). Graphical data visualization and analysis were performed with ggplot2 (Wickham, 2016) in RStudio (Posit team, 2024). Sequencing data was analyzed in Geneious Prime. Figures were assembled using Affinity Designer 2.

Appendix

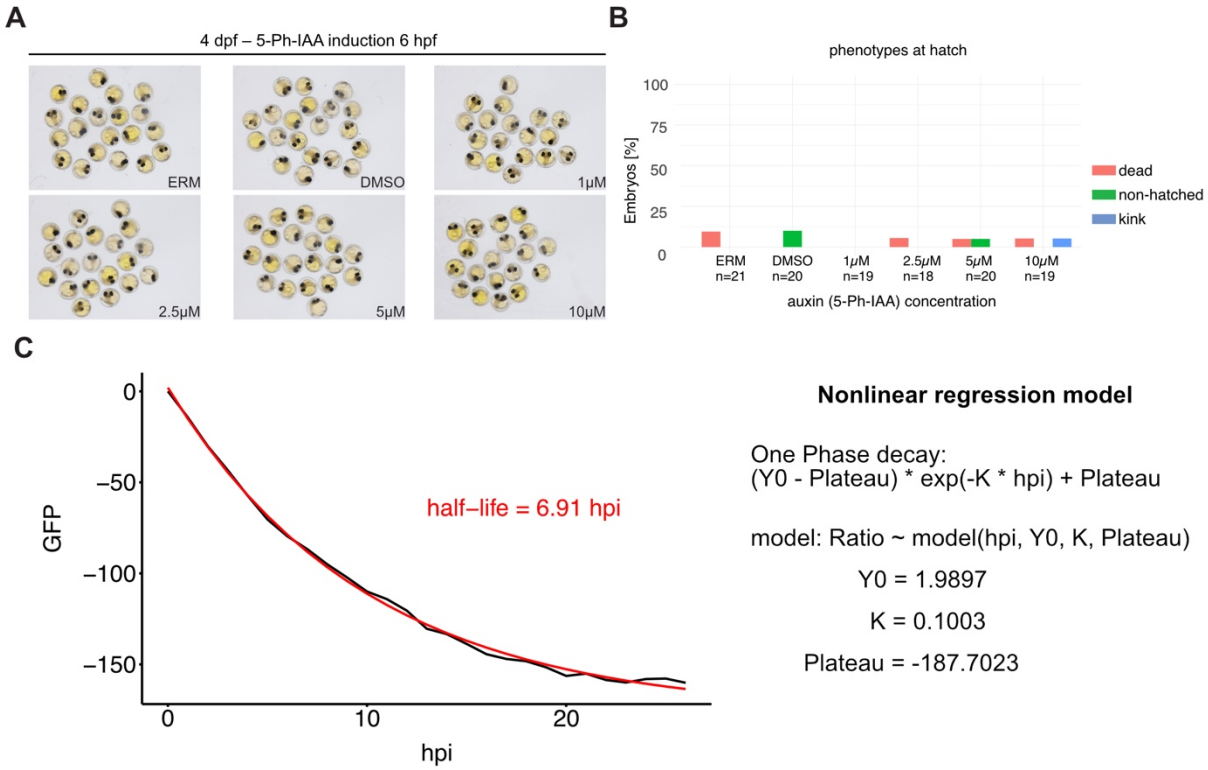

Supplementary Figure 1: Auxin toxicity test in wild-type embryos and half-life of Pmm2-GFP degradation. A) 5-Ph-IAA induced wild-type embryos with different concentrations and DMSO vehicle control at 6 hpf. B) Determination of half-life of Pmm2-GFP degradation by degron system. Baseline corrected mean GFP fluorescence are fitted to a one-phase exponential decay model (Y = (Y0-Plateau)exp(-k*X)+Plateau) C) Extracted values from Pmm2-GFP depletion kinetics fitted against one-phase exponential decay model. Adapted from Pakari et al., 2025. Dpf, days post fertilization; hpf, hours post fertilization; 5-Ph-IAA, auxin analog

Supplementary Table 1: *N*-Glycan structures assigned by migration time matching with glyXbaseCE) to the peaks of the xCGE-LIF *N*-glycan fingerprints, derived from the proteomes of 20 wild-type and 20 compound heterozygous *pmm2*$^{C139R/V135Gfs*45}$ hatchlings. Peak intensities are normalized to *N*-glycans derived from 1 µg Asialofetuin as an internal standard. The most intense *N*-glycan peak (A3G3) from Asialofetuin was set to 100 % IS intensity (see Supplementary Figure 2). Therefore, some values exceed 100%. Data provided by Ivan Andújar-Martínez (Rapp Lab, MPI Magdeburg).

Peak	*N*-glycan structures	*N*-Glycan Names (Adapted from Oxford Nomenclature by GlyXera)	Relative Peak Heights (%IS)	
			***pmm2* wild-type**	***pmm2* mutants**
1	_	_	8.917	5.376
2	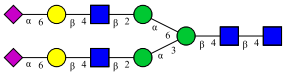	A2G2S2(2,6)	19.130	20.407

3	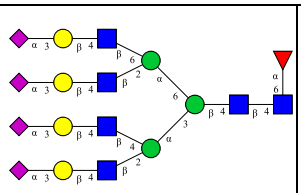	FA4G4S4(2,3)	6.354	6.211
4	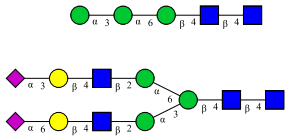	Man3[b] A2G2S1(2,6)S1(2,3)	35.728	39.459
5	–	–	10.540	–
6	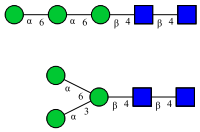	Man3 Man3[c]	17.003	44.666
7	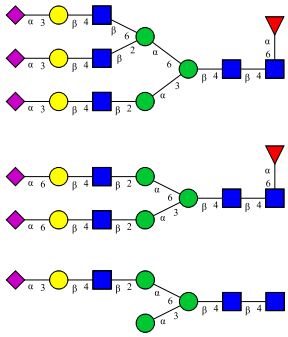	FA3G3S3(2,3)[2,6] FA2G2S2(2,6) A1G1S1(2,3)[6]	38.872	31.390
8	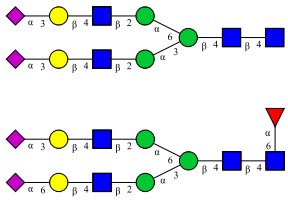	A2G2S2(2,3) FA2G2S1(2,3)S1(2,6)	65.471	65.419
9	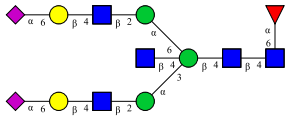	FA2BG2S2(2,6)	103.624	72.088
10	–	–	31.180	
11	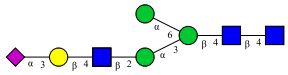	A1G1S1(2,3)[3]	28.260	19.487
12	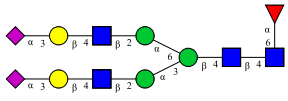	FA2G2S2(2,3)	82.633	55.871

13	–	–	19.984	13.348
14	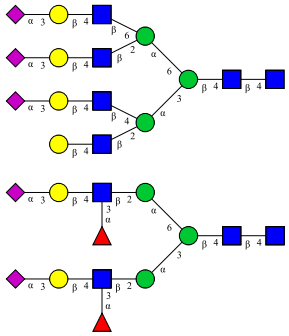	A4G4S3(2,3) A2F2(1,3)G2S2(2,3)	–	5.647
15	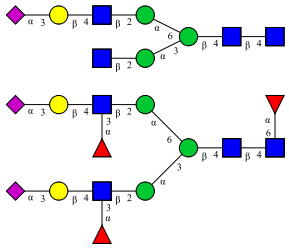	A2G1S1(2,3)[6] FA2F1(1,3)G2S2(2,3)	12.877	4.818
16	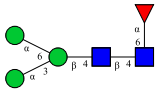	FMan3	26.800	15.532
17	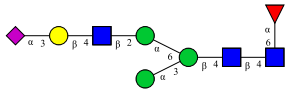	FA1G1S1(2,3)	10.783	–
18	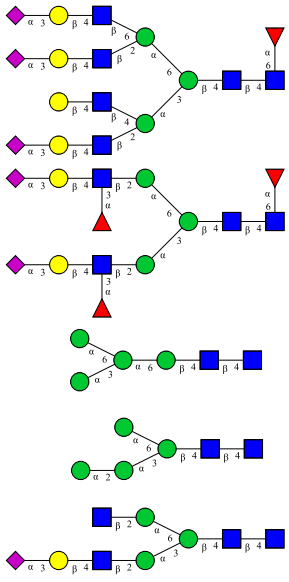	FA4G4S3(2,3) FA2G2F2(1,3)S2(2,3) Man4↑ A2G1S1(2,3)[3]	14.593	42.287
19	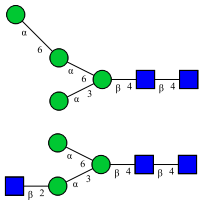	Man4[6]↓ A1G0[3] A1G0[6]	255.814	39.268

	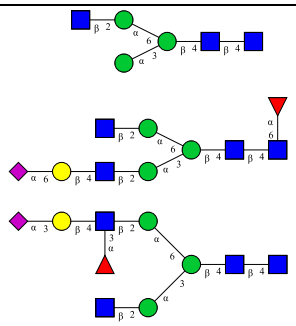	FA2G1S1(2,6)[3] A2F1(1,3)[6]G1[6]S1(2,3)[6]		
20	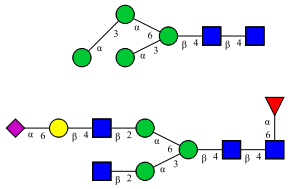	Man4[3]↓ FA2G1S1(2,6)[6]	50.890	26.002
21	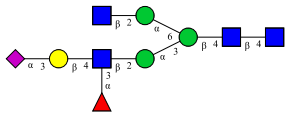	A2F1(1,3)[6]G1[6]S1(2,3)[3]	22.496	9.156
22	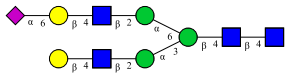	A2G2S1(2,6)	55.288	33.522
23	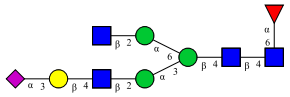	FA2G1S1(2,3)	–	23.163
24	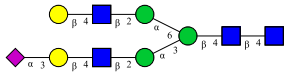	A2G2S1(2,3)	7.161	4.660
25	–	–	17.711	9.645
26	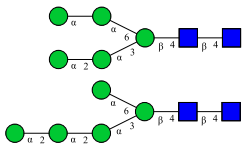	Man5(unusual ER isomer) Man5	–	10.033
27	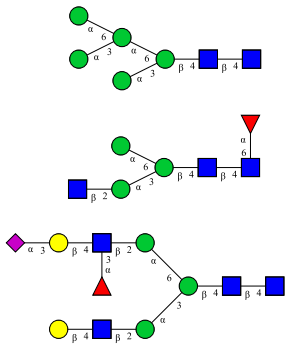	Man5 FA1G0[3] A2F1(1,3)G2S1(2,3)[6]	321.704	178.467

28	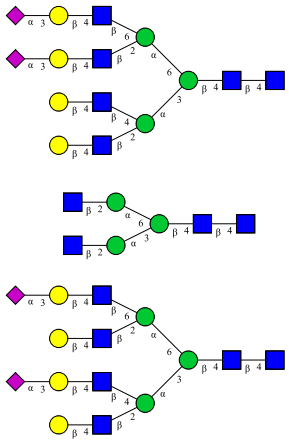	A4G4S2(2,3) A2G0	23.855	17.360
29	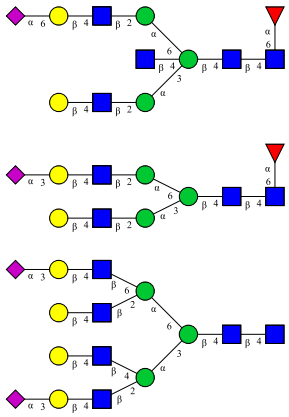	FA2BG2S1(2,6) FA2G2S1(2,3)[6] A4G4S2(2,3)	22.740	16.155
30	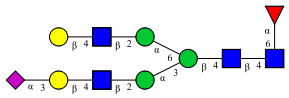	FA2G2S1(2,3)[3]	29.585	15.432
31	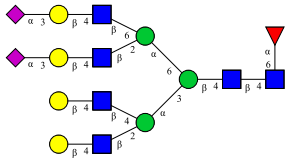	FA4G4S2(2,3)	8.652	5.519
32	–	–	23.008	16.303
33	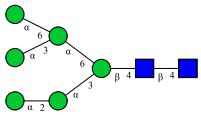	Man6	138.383	71.359
34	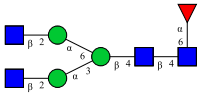	FA2G0	45.289	23.652
35	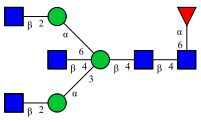	FA2BG0 FA3G3S1(2,6)[2,6]	148.763	91.802

	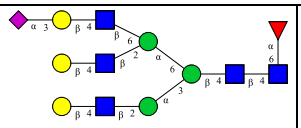			
36	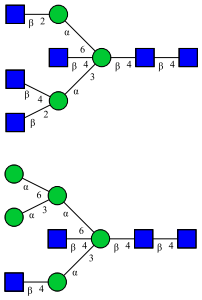	A3BG0[2,4] Man5-A1B	9.279	–
37	–	–	11.108	6.968
38	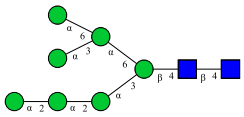	Man7[D1]	31.393	12.532
39	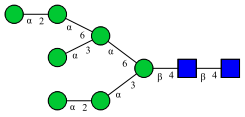	Man7[D3]	84.357	29.552
40	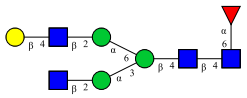	FA2G1[6]	6.327	4.286
41	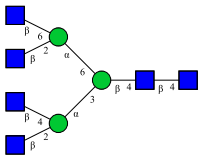	A4G0	5.524	–
42	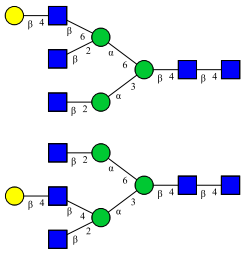	A3G1[2,6] A3G1[2,4]	19.113	9.747
43	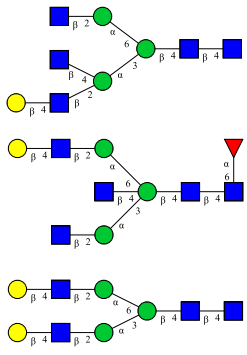	A3G1[2,4] FA2BG1[6] A2G2	55.180	30.596

44	–	–	9.541	–
45	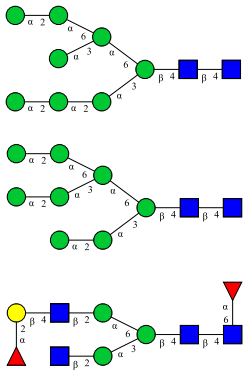	Man8[D1D3] Man8 FA2G1F1(1,2)[6]	122.976	48.577
46	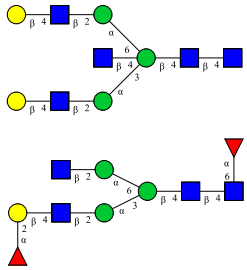	A2BG2 FA2G1F1(1,2)[3]	8.428	4.198
47	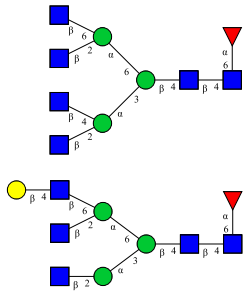	FA4G0 FA3G1[2,6]	10.258	5.388
48	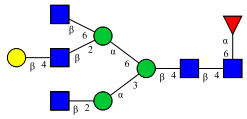	FA3G1[2,6]	56.084	30.637
49	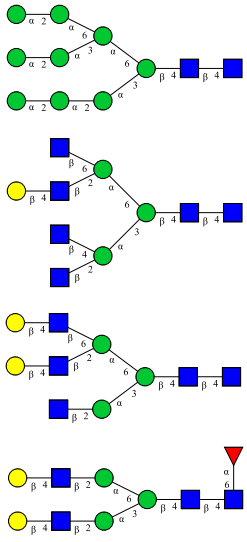	Man9 A4G1 A3G2[2,6] FA2G2	112.227	42.183

50	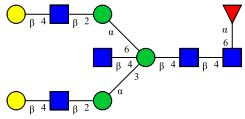	FA2BG2	12.687	6.364
51	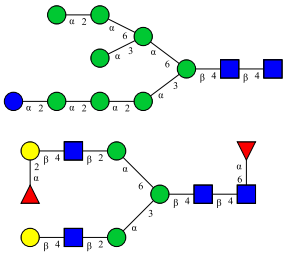	Man8Glc1 FA2G2F1(1,2)[6]	9.172	5.601
52	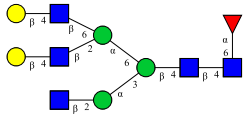	FA3G2[2,6]	8.958	5.730
53	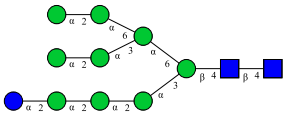	Man9Glc1	13.265	6.694
54	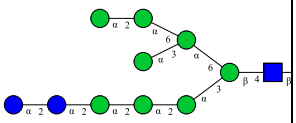	Man8Glc2	15.235	7.853
55	–	–	11.362	4.435
56	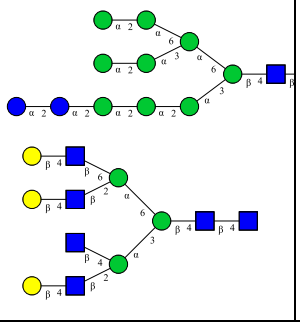	Man9Glc2 A4G3	7.050	4.061

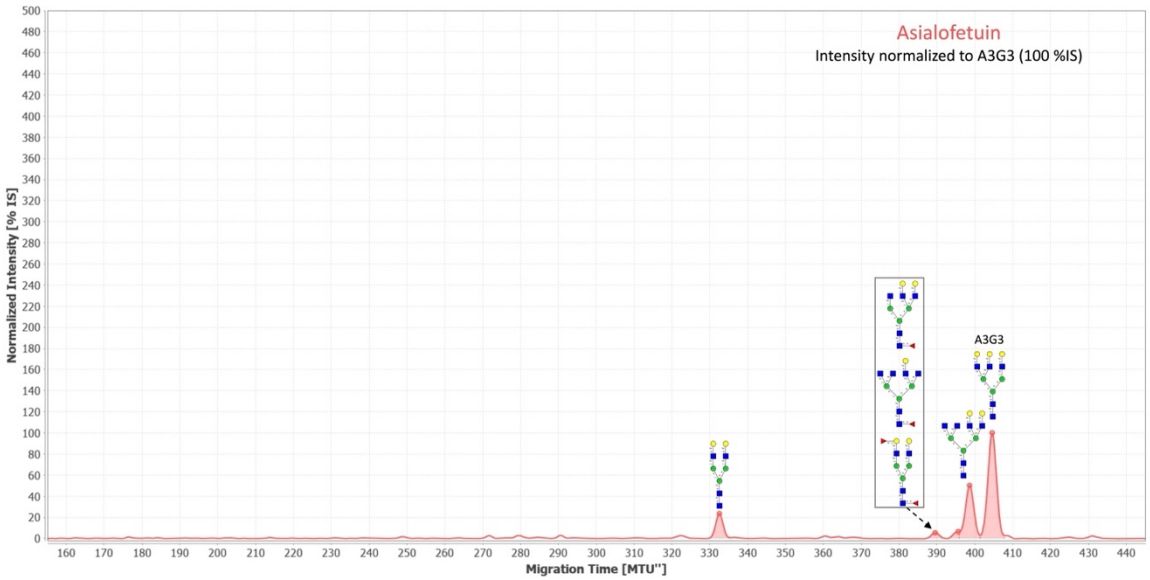

Figure 10. Normalized glyco-fingerprint for the Asialofetuin.
Grey framed the peaks potentially corresponding to multiple structures.

Supplementary Figure 2: Normalized glyco-fingerprint for Asialofetuin. Grey framed peaks potentially correspond to multiple structures. Data provided by Ivan Andújar-Martínez (Rapp Lab, MPI Magdeburg).

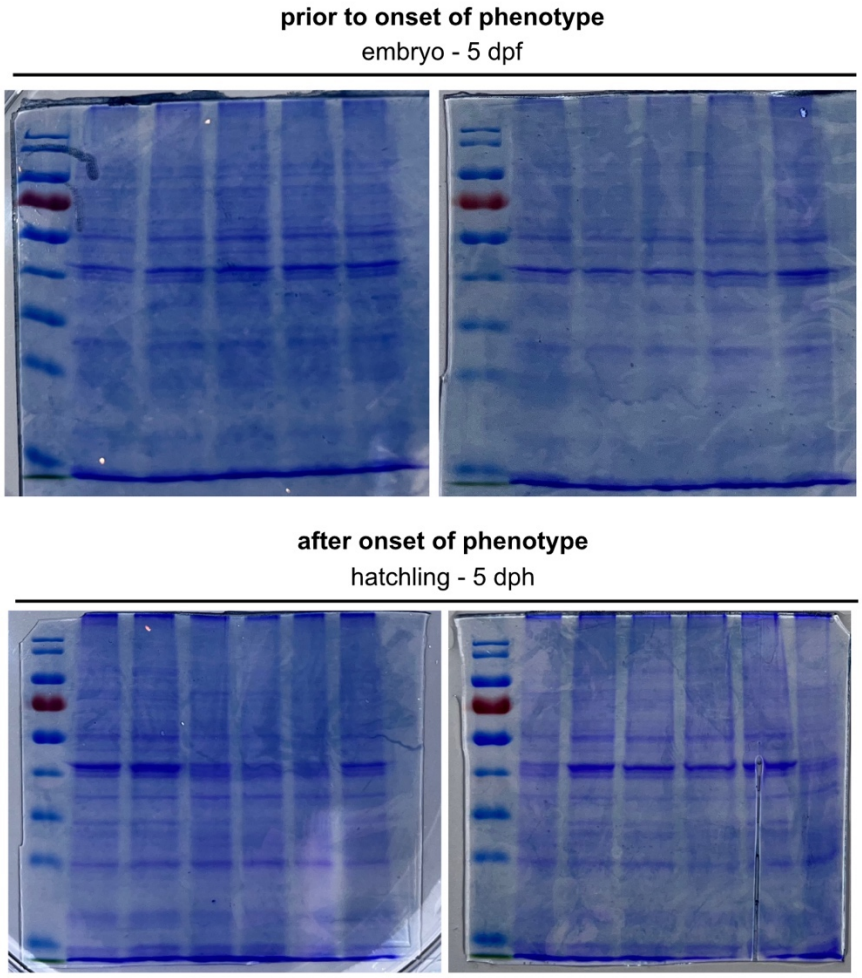

Supplementary Figure 3: Quality control of protein lysates from *wild-type* and *pmm2*$^{C139R/V135Gfs*45}$. SDS-PAGEs stained with Coomassie blue show all lysates from *pmm2* wild-type and compound heterozygous mutants prepared for bottom-up mass spectrometry. Sample are from two stages: prior and after onset of phenotype. dpf, days post fertilization; hpf, hour post fertilization

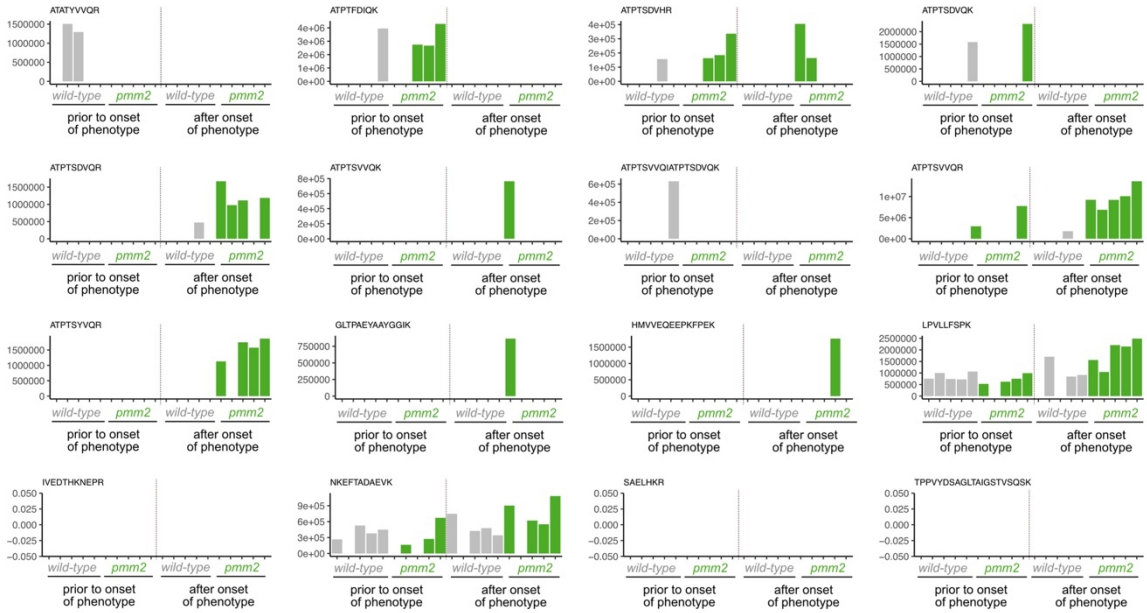

Supplementary Figure 4: Absolute intensities of tryptic peptides from bottom-up mass spectrometry analysis assigned to A0A3B3HGK5 (prr33). Peptides across all 5 replicates from wild-type and compound heterozygous pmm2 mutants at the two stages (5 dpf and 5 dph). dpf, days post fertilization; hpf, hour post fertilization; mut, compound heterozygous; wt, wild-type

References

Aebi, M. (2013). N-linked protein glycosylation in the ER. *Biochimica et Biophysica Acta (BBA) - Molecular Cell Research*, *1833*(11), 2430–2437. https://doi.org/10.1016/j.bbamcr.2013.04.001

Altassan, R., Péanne, R., Jaeken, J., Barone, R., Bidet, M., Borgel, D., Brasil, S., Cassiman, D., Cechova, A., Coman, D., Corral, J., Correia, J., de la Morena-Barrio, M. E., de Lonlay, P., Dos Reis, V., Ferreira, C. R., Fiumara, A., Francisco, R., Freeze, H., … Morava, E. (2019). International clinical guidelines for the management of phosphomannomutase 2-congenital disorders of glycosylation: Diagnosis, treatment and follow up. *Journal of Inherited Metabolic Disease*, *42*(1), 5–28. https://doi.org/10.1002/jimd.12024

An, H. J., Froehlich, J. W., & Lebrilla, C. B. (2009a). Determination of glycosylation sites and site-specific heterogeneity in glycoproteins. *Current Opinion in Chemical Biology*, *13*(4), 421–426. https://doi.org/10.1016/j.cbpa.2009.07.022

An, H. J., Froehlich, J. W., & Lebrilla, C. B. (2009b). Determination of glycosylation sites and site-specific heterogeneity in glycoproteins. *Current Opinion in Chemical Biology*, *13*(4), 421–426. https://doi.org/10.1016/j.cbpa.2009.07.022

Andreotti, G., Cabeza de Vaca, I., Poziello, A., Monti, M. C., Guallar, V., & Cubellis, M. V. (2014). Conformational Response to Ligand Binding in Phosphomannomutase2. *Journal of Biological Chemistry*, *289*(50), 34900–34910. https://doi.org/10.1074/jbc.M114.586362

Andreotti, G., Monti, M. C., Citro, V., & Cubellis, M. V. (2015). Heterodimerization of Two Pathological Mutants Enhances the Activity of Human Phosphomannomutase2. *PLOS ONE*, *10*(10), e0139882. https://doi.org/10.1371/journal.pone.0139882

Bause, E., & Hettkamp, H. (1979). Primary structural requirements for *N* -glycosylation of peptides in rat liver. *FEBS Letters*, *108*(2), 341–344. https://doi.org/10.1016/0014-5793(79)80559-1

Benz, P. M., Blume, C., Seifert, S., Wilhelm, S., Waschke, J., Schuh, K., Gertler, F., Münzel, T., & Renné, T. (2009). Differential VASP phosphorylation controls remodeling of the actin cytoskeleton. *Journal of Cell Science*, *122*(21), 3954–3965. https://doi.org/10.1242/jcs.044537

Bradford, Y. M., Van Slyke, C. E., Ruzicka, L., Singer, A., Eagle, A., Fashena, D., Howe, D. G., Frazer, K., Martin, R., Paddock, H., Pich, C., Ramachandran, S., & Westerfield, M. (2022). Zebrafish information network, the knowledgebase for *Danio rerio* research. *Genetics*, *220*(4). https://doi.org/10.1093/genetics/iyac016

Branton, D., Deamer, D. W., Marziali, A., Bayley, H., Benner, S. A., Butler, T., Di Ventra, M., Garaj, S., Hibbs, A., Huang, X., Jovanovich, S. B., Krstic, P. S., Lindsay, S., Ling, X. S., Mastrangelo, C. H., Meller, A., Oliver, J. S., Pershin, Y. V, Ramsey, J. M., … Schloss, J. A. (2008). The potential and challenges of nanopore sequencing. *Nature Biotechnology*, *26*(10), 1146–1153. https://doi.org/10.1038/nbt.1495

Breitling, J., & Aebi, M. (2013). N-Linked Protein Glycosylation in the Endoplasmic Reticulum. *Cold Spring Harbor Perspectives in Biology*, *5*(8), a013359–a013359. https://doi.org/10.1101/cshperspect.a013359

Briones, P., Vilaseca, M. A., García-Silva, M. T., Pineda, M., Colomer, J., Ferrer, I., Artigas, J., Jaeken, J., & Chabás, A. (2001). Congenital disorders of glycosylation (CDG) may be underdiagnosed when mimicking mitochondrial disease. *European Journal of Paediatric Neurology*, *5*(3), 127–131. https://doi.org/10.1053/ejpn.2001.0483

Briso-Montiano, A., Del Caño-Ochoa, F., Vilas, A., Velázquez-Campoy, A., Rubio, V., Pérez, B., & Ramón-Maiques, S. (2022). Insight on molecular pathogenesis and pharmacochaperoning potential in phosphomannomutase 2 deficiency, provided by novel human phosphomannomutase 2 structures. *Journal of Inherited Metabolic Disease*, *45*(2), 318–333. https://doi.org/10.1002/JIMD.12461

Brunak, S., Engelbrecht, J., & Knudsen, S. (1991). Prediction of human mRNA donor and acceptor sites from the DNA sequence. *Journal of Molecular Biology*, *220*(1), 49–65. https://doi.org/10.1016/0022-2836(91)90380-O

Budhraja, R., Radenkovic, S., Jain, A., Muffels, I. J. J., Ismaili, M. H. A., Kozicz, T., Pandey, A., & Morava, E. (2024). Liposome-encapsulated mannose-1-phosphate therapy improves global N-glycosylation in different congenital disorders of glycosylation. *Molecular Genetics and Metabolism*, *142*(2), 108487. https://doi.org/10.1016/j.ymgme.2024.108487

Carchon, H. A., Chevigné, R., Falmagne, J.-B., & Jaeken, J. (2004). Diagnosis of Congenital Disorders of Glycosylation by Capillary Zone Electrophoresis of Serum Transferrin. *Clinical Chemistry*, *50*(1), 101–111. https://doi.org/10.1373/clinchem.2003.021568

Caussinus, E., & Affolter, M. (2016). *deGradFP: A System to Knockdown GFP-Tagged Proteins* (pp. 177–187). https://doi.org/10.1007/978-1-4939-6371-3_9

Caussinus, E., Kanca, O., & Affolter, M. (2011). Fluorescent fusion protein knockout mediated by anti-GFP nanobody. *Nature Structural & Molecular Biology*, *19*(1), 117–121. https://doi.org/10.1038/nsmb.2180

Ceroni, A., Maass, K., Geyer, H., Geyer, R., Dell, A., & Haslam, S. M. (2008). GlycoWorkbench: A Tool for the Computer-Assisted Annotation of Mass Spectra of

Glycans. *Journal of Proteome Research*, *7*(4), 1650–1659. https://doi.org/10.1021/pr7008252

Chan, B., Clasquin, M., Smolen, G. A., Histen, G., Powe, J., Chen, Y., Lin, Z., Lu, C., Liu, Y., Cang, Y., Yan, Z., Xia, Y., Thompson, R., Singleton, C., Dorsch, M., Silverman, L., Su, S.-S. M., Freeze, H. H., & Jin, S. (2016). A mouse model of a human congenital disorder of glycosylation caused by loss of PMM2. *Human Molecular Genetics*, *25*(11), 2182–2193. https://doi.org/10.1093/hmg/ddw085

Chang, I. J., He, M., & Lam, C. T. (2018). Congenital disorders of glycosylation. *Annals of Translational Medicine*, *6*(24), 477–477. https://doi.org/10.21037/atm.2018.10.45

Chen, P. J., & Liu, D. R. (2023). Prime editing for precise and highly versatile genome manipulation. *Nature Reviews Genetics*, *24*(3), 161–177. https://doi.org/10.1038/s41576-022-00541-1

Chen, S., Pei, C.-X., Xu, S., Li, H., Liu, Y.-S., Wang, Y., Jin, C., Dean, N., & Gao, X.-D. (2024). Rft1 catalyzes lipid-linked oligosaccharide translocation across the ER membrane. *Nature Communications*, *15*(1), 5157. https://doi.org/10.1038/s41467-024-48999-3

Cho, S. W., Kim, S., Kim, J. M., & Kim, J.-S. (2013). Targeted genome engineering in human cells with the Cas9 RNA-guided endonuclease. *Nature Biotechnology*, *31*(3), 230–232. https://doi.org/10.1038/nbt.2507

Chrysinas, P., Venkatesan, S., Ang, I., Ghosh, V., Chen, C., Neelamegham, S., & Gunawan, R. (2024). Cell- and tissue-specific glycosylation pathways informed by single-cell transcriptomics. *NAR Genomics and Bioinformatics*, *6*(4). https://doi.org/10.1093/nargab/lqae169

Clement, K., Rees, H., Canver, M. C., Gehrke, J. M., Farouni, R., Hsu, J. Y., Cole, M. A., Liu, D. R., Joung, J. K., Bauer, D. E., & Pinello, L. (2019). CRISPResso2 provides accurate and rapid genome editing sequence analysis. *Nature Biotechnology*, *37*(3), 224–226. https://doi.org/10.1038/s41587-019-0032-3

Cline, A., Gao, N., Flanagan-Steet, H., Sharma, V., Rosa, S., Sonon, R., Azadi, P., Sadler, K. C., Freeze, H. H., Lehrman, M. A., & Steet, R. (2012). A zebrafish model of PMM2-CDG reveals altered neurogenesis and a substrate-accumulation mechanism for N-linked glycosylation deficiency. *Molecular Biology of the Cell*, *23*(21), 4175–4187. https://doi.org/10.1091/mbc.e12-05-0411

Cong, L., Ran, F. A., Cox, D., Lin, S., Barretto, R., Habib, N., Hsu, P. D., Wu, X., Jiang, W., Marraffini, L. A., & Zhang, F. (2013). Multiplex Genome Engineering Using CRISPR/Cas Systems. *Science*, *339*(6121), 819–823. https://doi.org/10.1126/science.1231143

Cornean, A. (2022). *he role of the medaka protein O-mannosyltransferase 2 across tissues, development and dystroglycanopathies* .

Cornean, A., Gierten, J., Welz, B., Mateo, J. L., Thumberger, T., & Wittbrodt, J. (2022). Precise in vivo functional analysis of DNA variants with base editing using ACEofBASEs target prediction. *ELife*, *11*. https://doi.org/10.7554/eLife.72124

Dandekar, S. S., Ebenezer, N. D., Grayson, C., Chapple, J. P., Egan, C. A., Holder, G. E., Jenkins, S. A., Fitzke, F. W., Cheetham, M. E., Webster, A. R., & Hardcastle, A. J. (2004). An atypical phenotype of macular and peripapillary retinal atrophy caused by a mutation in the RP2 gene. *The British Journal of Ophthalmology*, *88*(4), 528–532. https://doi.org/10.1136/bjo.2003.027979

Daniel, K., Icha, J., Horenburg, C., Müller, D., Norden, C., & Mansfeld, J. (2018). Conditional control of fluorescent protein degradation by an auxin-dependent nanobody. *Nature Communications*, *9*(1), 3297. https://doi.org/10.1038/s41467-018-05855-5

Doering, L., Cornean, A., Thumberger, T., Benjaminsen, J., Wittbrodt, B., Kellner, T., Hammouda, O. T., Gorenflo, M., Wittbrodt, J., & Gierten, J. (2023). CRISPR-based knockout and base editing confirm the role of MYRF in heart development and congenital heart disease. *Disease Models & Mechanisms*, *16*(8). https://doi.org/10.1242/dmm.049811

Draheim, V., Reichel, A., Weitschies, W., & Moenning, U. (2010). N-glycosylation of ABC transporters is associated with functional activity in sandwich-cultured rat hepatocytes. *European Journal of Pharmaceutical Sciences*, *41*(2), 201–209. https://doi.org/10.1016/J.EJPS.2010.06.005

Dworkin, L. A., Clausen, H., & Joshi, H. J. (2022). Applying transcriptomics to study glycosylation at the cell type level. *IScience*, *25*(6), 104419. https://doi.org/10.1016/j.isci.2022.104419

Edmondson, A. C., Budhraja, R., Xia, Z., Melendez-Perez, A., Cai, C., Radenkovic, S., Collins, A. M., Shiplett, E. J., Hill, S. F., Somarowthu, A., Dam, J., Pai, L.-L., Santi, M., Kim, S., He, M., Goldberg, E. M., Kozicz, T., Morava, E., Pandey, A., & Zhou, Z. (2025). *Novel mouse model reveals neurodevelopmental origin of PMM2-CDG brain pathology*. https://doi.org/10.1101/2025.06.01.657261

Edmondson, A. C., Honzík, T., Lam, C., Õunap, K., McWilliams, P., & Morava, E. (2025). Incidence and prevalence of phosphomannomutase 2-congenital disorder of glycosylation: Past, present, and future. *Molecular Genetics and Metabolism*, 109188. https://doi.org/10.1016/J.YMGME.2025.109188

Feichtinger, R. G., Hüllen, A., Koller, A., Kotzot, D., Grote, V., Rapp, E., Hofbauer, P., Brugger, K., Thiel, C., Mayr, J. A., & Wortmann, S. B. (2021). A spoonful of L-fucose—an efficient therapy for GFUS-CDG, a new glycosylation disorder. *EMBO Molecular Medicine*, *13*(9). https://doi.org/10.15252/emmm.202114332

Ferreira, C. R., Altassan, R., Marques-Da-Silva, D., Francisco, R., Jaeken, J., & Morava, E. (2018). Recognizable phenotypes in CDG. *Journal of Inherited Metabolic Disease*, *41*(3), 541–553. https://doi.org/10.1007/s10545-018-0156-5

Footitt, E. J., Karimova, A., Burch, M., Yayeh, T., Dupré, T., Vuillaumier-Barrot, S., Chantret, I., Moore, S. E. H., Seta, N., & Grunewald, S. (2009). Cardiomyopathy in the congenital disorders of glycosylation (CDG): a case of late presentation and literature review. *Journal of Inherited Metabolic Disease*, *32*(S1), 313–319. https://doi.org/10.1007/s10545-009-1262-1

Francisco, R., Marques-da-Silva, D., Brasil, S., Pascoal, C., dos Reis Ferreira, V., Morava, E., & Jaeken, J. (2019). The challenge of CDG diagnosis. *Molecular Genetics and Metabolism*, *126*(1), 1–5. https://doi.org/10.1016/J.YMGME.2018.11.003

Frank, C. G., Sanyal, S., Rush, J. S., Waechter, C. J., & Menon, A. K. (2008). Does Rft1 flip an N-glycan lipid precursor? *Nature*, *454*(7204), E3–E4. https://doi.org/10.1038/nature07165

Freeze, H. H. (2009). Towards a therapy for phosphomannomutase 2 deficiency, the defect in CDG-Ia patients. *Biochimica et Biophysica Acta (BBA) - Molecular Basis of Disease*, *1792*(9), 835–840. https://doi.org/10.1016/j.bbadis.2009.01.004

Freeze, H. H., Eklund, E. A., Ng, B. G., & Patterson, M. C. (2015). Neurological Aspects of Human Glycosylation Disorders. *Annual Review of Neuroscience*, *38*(1), 105–125. https://doi.org/10.1146/annurev-neuro-071714-034019

Furutani-Seiki, M., & Wittbrodt, J. (2004). Medaka and zebrafish, an evolutionary twin study. *Mechanisms of Development*, *121*(7–8), 629–637. https://doi.org/10.1016/j.mod.2004.05.010

Gallego, D., Serrano, M., Cordoba-Caballero, J., Gámez, A., Seoane, P., Perkins, J. R., Ranea, J. A. G., & Pérez, B. (2024). Transcriptomic analysis identifies dysregulated pathways and therapeutic targets in PMM2-CDG. *Biochimica et Biophysica Acta (BBA) - Molecular Basis of Disease*, *1870*(5), 167163. https://doi.org/10.1016/J.BBADIS.2024.167163

Garapati, K., Budhraja, R., Saraswat, M., Kim, J., Joshi, N., Sachdeva, G. S., Jain, A., Ligezka, A. N., Radenkovic, S., Ramarajan, M. G., Udainiya, S., Raymond, K., He, M., Lam, C., Larson, A., Edmondson, A. C., Sarafoglou, K., Larson, N. B., Freeze, H. H., … Pandey, A. (2024a). A complement C4–derived glycopeptide is a biomarker for PMM2-CDG. *JCI Insight*, *9*(7). https://doi.org/10.1172/jci.insight.172509

Garapati, K., Budhraja, R., Saraswat, M., Kim, J., Joshi, N., Sachdeva, G. S., Jain, A., Ligezka, A. N., Radenkovic, S., Ramarajan, M. G., Udainiya, S., Raymond, K., He, M., Lam, C., Larson, A., Edmondson, A. C., Sarafoglou, K., Larson, N. B., Freeze, H. H., … Pandey, A. (2024b). A complement C4–derived glycopeptide is a biomarker for PMM2-CDG. *JCI Insight*, *9*(7). https://doi.org/10.1172/jci.insight.172509

Gardeitchik, T., Wyckmans, J., & Morava, E. (2018). Complex Phenotypes in Inborn Errors of Metabolism: Overlapping Presentations in Congenital Disorders of Glycosylation and Mitochondrial Disorders. *Pediatric Clinics of North America*, *65*(2), 375–388. https://doi.org/10.1016/j.pcl.2017.11.012

Gaudelli, N. M., Komor, A. C., Rees, H. A., Packer, M. S., Badran, A. H., Bryson, D. I., & Liu, D. R. (2017). Programmable base editing of A•T to G•C in genomic DNA without DNA cleavage. *Nature*, *551*(7681), 464–471. https://doi.org/10.1038/nature24644

Ge, S. X., Jung, D., & Yao, R. (2020). ShinyGO: a graphical gene-set enrichment tool for animals and plants. *Bioinformatics*, *36*(8), 2628–2629. https://doi.org/10.1093/bioinformatics/btz931

Giurgea, I., Michel, A., Le Merrer, M., Seta, N., & De Lonlay, P. (2005). Underdiagnosis of mild congenital disorders of glycosylation type Ia. *Pediatric Neurology*, *32*(2), 121–123. https://doi.org/10.1016/J.PEDIATRNEUROL.2004.06.021

Glycomine, Inc. (2022). *24-Week Study to Assess the PD, Safety, Tolerability, and PK of GLM101 in Participants With PMM2-CDG*. NCT05549219. https://clinicaltrials.gov/study/NCT05549219#more-information

Gücüm, S. (2021). *Modeling hypo-N-glycosylation in medaka, Oryzias latipes, to decipher mechanisms of Congenital Disorders of Glycosylation* .

Gücüm, S., Sakson, R., Hoffmann, M., Grote, V., Becker, C., Pakari, K., Beedgen, L., Thiel, C., Rapp, E., Ruppert, T., Thumberger, T., & Wittbrodt, J. (2021). A patient-based medaka alg2 mutant as a model for hypo-N-glycosylation. *Development*, *148*(11). https://doi.org/10.1242/dev.199385

Gupta R, B. S. (2022). Prediction of glycosylation across the human proteome and the correlation to protein function. *Pac Symp Biocomput.* , *310*(22).

Gutierrez-Triana, J. A., Tavhelidse, T., Thumberger, T., Thomas, I., Wittbrodt, B., Kellner, T., Anlas, K., Tsingos, E., & Wittbrodt, J. (2018). Efficient single-copy HDR by 5’ modified long dsDNA donors. *ELife*, *7*. https://doi.org/10.7554/eLife.39468

Hammouda, O. T., Wu, M. Y., Kaul, V., Gierten, J., Thumberger, T., & Wittbrodt, J. (2021). In vivo identification and validation of novel potential predictors for human cardiovascular diseases. *PLOS ONE*, *16*(12), e0261572. https://doi.org/10.1371/journal.pone.0261572

He, M., Zhou, X., & Wang, X. (2024). Glycosylation: mechanisms, biological functions and clinical implications. *Signal Transduction and Targeted Therapy*, *9*(1), 194. https://doi.org/10.1038/s41392-024-01886-1

Hebsgaard, S. (1996). Splice site prediction in Arabidopsis thaliana pre-mRNA by combining local and global sequence information. *Nucleic Acids Research*, *24*(17), 3439–3452. https://doi.org/10.1093/nar/24.17.3439

Helenius, A., & Aebi, M. (2004). Roles of N-Linked Glycans in the Endoplasmic Reticulum. *Annual Review of Biochemistry*, *73*(1), 1019–1049. https://doi.org/10.1146/annurev.biochem.73.011303.073752

Himmelreich, N., Kaufmann, L. T., Steinbeisser, H., Körner, C., & Thiel, C. (2015). Lack of phosphomannomutase 2 affects *Xenopus laevis* morphogenesis and the non-canonical Wnt5a/Ror2 signalling. *Journal of Inherited Metabolic Disease*, *38*(6), 1137–1146. https://doi.org/10.1007/s10545-015-9874-0

Himmelreich, N., Kikul, F., Zdrazilova, L., Honzik, T., Hecker, A., Poschet, G., Lüchtenborg, C., Brügger, B., Strahl, S., Bürger, F., Okun, J. G., Hansikova, H., & Thiel, C. (2023). Complex metabolic disharmony in PMM2-CDG paves the way to new therapeutic approaches. *Molecular Genetics and Metabolism*, *139*(3), 107610. https://doi.org/10.1016/j.ymgme.2023.107610

Hirata, E., Sakata, K.-T., Dearden, G. I., Noor, F., Menon, I., Chiduza, G. N., & Menon, A. K. (2024). Molecular characterization of Rft1, an ER membrane protein associated with congenital disorder of glycosylation RFT1-CDG. *The Journal of Biological Chemistry*, *300*(8), 107584. https://doi.org/10.1016/j.jbc.2024.107584

Holopainen, J. M., Cheng, C. L., Molday, L. L., Johal, G., Coleman, J., Dyka, F., Hii, T., Ahn, J., & Molday, R. S. (2010). Interaction and localization of the retinitis pigmentosa protein RP2 and NSF in retinal photoreceptor cells. *Biochemistry*, *49*(35), 7439–7447. https://doi.org/10.1021/bi1005249

Howe, K., Clark, M. D., Torroja, C. F., Torrance, J., Berthelot, C., Muffato, M., Collins, J. E., Humphray, S., McLaren, K., Matthews, L., McLaren, S., Sealy, I., Caccamo, M., Churcher, C., Scott, C., Barrett, J. C., Koch, R., Rauch, G.-J., White, S., … Stemple, D. L. (2013). The zebrafish reference genome sequence and its relationship to the human genome. *Nature*, *496*(7446), 498–503. https://doi.org/10.1038/nature12111

Hsu, P. D., Scott, D. A., Weinstein, J. A., Ran, F. A., Konermann, S., Agarwala, V., Li, Y., Fine, E. J., Wu, X., Shalem, O., Cradick, T. J., Marraffini, L. A., Bao, G., & Zhang, F. (2013). DNA targeting specificity of RNA-guided Cas9 nucleases. *Nature Biotechnology*, *31*(9), 827–832. https://doi.org/10.1038/nbt.2647

Hughes, C. S., Moggridge, S., Müller, T., Sorensen, P. H., Morin, G. B., & Krijgsveld, J. (2019). Single-pot, solid-phase-enhanced sample preparation for proteomics

experiments. *Nature Protocols*, *14*(1), 68–85. https://doi.org/10.1038/s41596-018-0082-x

Hustedt, N., & Durocher, D. (2017). The control of DNA repair by the cell cycle. *Nature Cell Biology*, *19*(1), 1–9. https://doi.org/10.1038/ncb3452

Ives, C. M., Singh, O., D'Andrea, S., Fogarty, C. A., Harbison, A. M., Satheesan, A., Tropea, B., & Fadda, E. (2024). Restoring protein glycosylation with GlycoShape. *Nature Methods*, *21*(11), 2117–2127. https://doi.org/10.1038/s41592-024-02464-7

Iwamatsu, T. (2004). Stages of normal development in the medaka Oryzias latipes. *Mechanisms of Development*, *121*(7–8), 605–618. https://doi.org/10.1016/J.MOD.2004.03.012

Iyer, S., Sam, F. S., DiPrimio, N., Preston, G., Verheijen, J., Murthy, K., Parton, Z., Tsang, H., Lao, J., Morava, E., & Perlstein, E. O. (2019). Repurposing the aldose reductase inhibitor and diabetic neuropathy drug epalrestat for the congenital disorder of glycosylation PMM2-CDG. *Disease Models & Mechanisms*. https://doi.org/10.1242/dmm.040584

Jaeken, J. (2013). Congenital disorders of glycosylation. *Handbook of Clinical Neurology*, *113*, 1737–1743. https://doi.org/10.1016/B978-0-444-59565-2.00044-7

Jaeken, J., Hennet, T., Matthijs, G., & Freeze, H. H. (2009). CDG nomenclature: Time for a change! *Biochimica et Biophysica Acta (BBA) - Molecular Basis of Disease*, *1792*(9), 825–826. https://doi.org/10.1016/j.bbadis.2009.08.005

Jaeken, J., & Matthijs, G. (2001). Congenital Disorders of Glycosylation. *Annual Review of Genomics and Human Genetics*, *2*(1), 129–151. https://doi.org/10.1146/annurev.genom.2.1.129

Jaeken, J., van Eijk, H. G., van der Heul, C., Corbeel, L., Eeckels, R., & Eggermont, E. (1984). Sialic acid-deficient serum and cerebrospinal fluid transferrin in a newly recognized genetic syndrome. *Clinica Chimica Acta; International Journal of Clinical Chemistry*, *144*(2–3), 245–247. https://doi.org/10.1016/0009-8981(84)90059-7

Jinek, M., Chylinski, K., Fonfara, I., Hauer, M., Doudna, J. A., & Charpentier, E. (2012). A programmable dual-RNA-guided DNA endonuclease in adaptive bacterial immunity. *Science (New York, N.Y.)*, *337*(6096), 816–821. https://doi.org/10.1126/science.1225829

Jinek, M., East, A., Cheng, A., Lin, S., Ma, E., & Doudna, J. (2013). RNA-programmed genome editing in human cells. *ELife*, *2*. https://doi.org/10.7554/eLife.00471

Kasahara, M., Naruse, K., Sasaki, S., Nakatani, Y., Qu, W., Ahsan, B., Yamada, T., Nagayasu, Y., Doi, K., Kasai, Y., Jindo, T., Kobayashi, D., Shimada, A., Toyoda, A., Kuroki, Y., Fujiyama, A., Sasaki, T., Shimizu, A., Asakawa, S., … Kohara, Y. (2007).

The medaka draft genome and insights into vertebrate genome evolution. *Nature*, *447*(7145), 714–719. https://doi.org/10.1038/nature05846

Kellman, B. P., Sandoval, D., Zaytseva, O. O., Brock, K., Baboo, S., Nachmanson, D., Irvine, E. B., Armingol, E., Mih, N., Zhang, Y., Jeffris, M., Bartels, P., Nguyen, T., Tam, A., Gasman, S., Ilan, S., Shamie, I., Diedrich, J. K., Wang, X., … Lewis, N. E. (2024). *Protein structure, a genetic encoding for glycosylation*. https://doi.org/10.1101/2024.05.15.594261

Kirchmaier, S., Naruse, K., Wittbrodt, J., & Loosli, F. (2015). The Genomic and Genetic Toolbox of the Teleost Medaka (*Oryzias latipes*). *Genetics*, *199*(4), 905–918. https://doi.org/10.1534/genetics.114.173849

Kiyomitsu, A., Nishimura, T., Hwang, S. J., Ansai, S., Kanemaki, M. T., Tanaka, M., & Kiyomitsu, T. (2024). Ran-GTP assembles a specialized spindle structure for accurate chromosome segregation in medaka early embryos. *Nature Communications*, *15*(1), 981. https://doi.org/10.1038/s41467-024-45251-w

Kjaergaard, S., Skovby, F., & Schwartz, M. (1999). Carbohydrate-deficient glycoprotein syndrome type 1A: expression and characterisation of wild type and mutant PMM2 in E. coli. *European Journal of Human Genetics*, *7*(8), 884–888. https://doi.org/10.1038/sj.ejhg.5200398

Klaver, E. J., Dukes-Rimsky, L., Kumar, B., Xia, Z.-J., Dang, T., Lehrman, M. A., Angel, P., Drake, R. R., Freeze, H. H., Steet, R., & Flanagan-Steet, H. (2021). Protease-dependent defects in N-cadherin processing drive PMM2-CDG pathogenesis. *JCI Insight*, *6*(24). https://doi.org/10.1172/jci.insight.153474

Kluesner, M. G., Nedveck, D. A., Lahr, W. S., Garbe, J. R., Abrahante, J. E., Webber, B. R., & Moriarity, B. S. (2018). EditR: A Method to Quantify Base Editing from Sanger Sequencing. *The CRISPR Journal*, *1*(3), 239–250. https://doi.org/10.1089/crispr.2018.0014

Kobata, A. (1992). Structures and functions of the sugar chains of glycoproteins. *European Journal of Biochemistry*, *209*(2), 483–501. https://doi.org/10.1111/j.1432-1033.1992.tb17313.x

Koblan, L. W., Doman, J. L., Wilson, C., Levy, J. M., Tay, T., Newby, G. A., Maianti, J. P., Raguram, A., & Liu, D. R. (2018). Improving cytidine and adenine base editors by expression optimization and ancestral reconstruction. *Nature Biotechnology*, *36*(9), 843–846. https://doi.org/10.1038/nbt.4172

Komor, A. C., Kim, Y. B., Packer, M. S., Zuris, J. A., & Liu, D. R. (2016). Programmable editing of a target base in genomic DNA without double-stranded DNA cleavage. *Nature*, *533*(7603), 420–424. https://doi.org/10.1038/nature17946

Korner, C., Lehle, L., & von Figura, K. (1998). Abnormal synthesis of mannose 1-phosphate derived carbohydrates in carbohydrate-deficient glycoprotein syndrome type I fibroblasts with phosphomannomutase deficiency. *Glycobiology*, *8*(2), 165–171. https://doi.org/10.1093/glycob/8.2.165

Körner, C., Lehle, L., & von Figura, K. (1998). Carbohydrate-deficient glycoprotein syndrome type 1: correction of the glycosylation defect by deprivation of glucose or supplementation of mannose. *Glycoconjugate Journal*, *15*(5), 499–505. https://doi.org/10.1023/A:1006939104442

Kozlov, G., & Gehring, K. (2020). Calnexin cycle - structural features of the ER chaperone system. *The FEBS Journal*, *287*(20), 4322–4340. https://doi.org/10.1111/febs.15330

Krasnewich, D., O'Brien, K., & Sparks, S. (2007). Clinical features in adults with congenital disorders of glycosylation type Ia (CDG-Ia). *American Journal of Medical Genetics Part C: Seminars in Medical Genetics*, *145C*(3), 302–306. https://doi.org/10.1002/ajmg.c.30143

Lam, C., & Krasnewich, D. M. (2005). *PMM2-CDG*. https://pubmed.ncbi.nlm.nih.gov/20301289/

Ligezka, A. N., Budhraja, R., Nishiyama, Y., Fiesel, F. C., Preston, G., Edmondson, A., Ranatunga, W., Van Hove, J. L. K., Watzlawik, J. O., Springer, W., Pandey, A., Morava, E., & Kozicz, T. (2023). Interplay of Impaired Cellular Bioenergetics and Autophagy in PMM2-CDG. *Genes*, *14*(8), 1585. https://doi.org/10.3390/genes14081585

Ligezka, A. N., Radenkovic, S., Saraswat, M., Garapati, K., Ranatunga, W., Krzysciak, W., Yanaihara, H., Preston, G., Brucker, W., McGovern, R. M., Reid, J. M., Cassiman, D., Muthusamy, K., Johnsen, C., Mercimek-Andrews, S., Larson, A., Lam, C., Edmondson, A. C., Ghesquière, B., … Morava, E. (2021). Sorbitol Is a Severity Biomarker for <scp>PMM2-CDG</scp> with Therapeutic Implications. *Annals of Neurology*, *90*(6), 887–900. https://doi.org/10.1002/ana.26245

Lischik, C. Q., Adelmann, L., & Wittbrodt, J. (2019). Enhanced in vivo-imaging in medaka by optimized anaesthesia, fluorescent protein selection and removal of pigmentation. *PLOS ONE*, *14*(3), e0212956. https://doi.org/10.1371/journal.pone.0212956

Liu, L., Tao, T., Liu, S., Yang, X., Chen, X., Liang, J., Hong, R., Wang, W., Yang, Y., Li, X., Zhang, Y., Li, Q., Liang, S., Yu, H., Wu, Y., Guo, X., Lai, Y., Ding, X., Guan, H., … Tian, H. (2021). An RFC4/Notch1 signaling feedback loop promotes NSCLC metastasis and stemness. *Nature Communications*, *12*(1), 2693. https://doi.org/10.1038/s41467-021-22971-x

Maggie's Pearl, L. (2022). *Oral Epalrestat Therapy in Pediatric Subjects With PMM2-CDG*. NCT04925960. https://clinicaltrials.gov/study/NCT04925960

Mali, P., Yang, L., Esvelt, K. M., Aach, J., Guell, M., DiCarlo, J. E., Norville, J. E., & Church, G. M. (2013). RNA-Guided Human Genome Engineering via Cas9. *Science*, *339*(6121), 823–826. https://doi.org/10.1126/science.1232033

Marques-da-Silva, D., dos Reis Ferreira, V., Monticelli, M., Janeiro, P., Videira, P. A., Witters, P., Jaeken, J., & Cassiman, D. (2017). Liver involvement in congenital disorders of glycosylation (CDG). A systematic review of the literature. *Journal of Inherited Metabolic Disease*, *40*(2), 195–207. https://doi.org/10.1007/s10545-016-0012-4

Martinez-Monseny, A., Cuadras, D., Bolasell, M., Muchart, J., Arjona, C., Borregan, M., Algrabli, A., Montero, R., Artuch, R., Velázquez-Fragua, R., Macaya, A., Pérez-Cerdá, C., Pérez-Dueñas, B., Pérez, B., & Serrano, M. (2019). From gestalt to gene: early predictive dysmorphic features of PMM2-CDG. *Journal of Medical Genetics*, *56*(4), 236–245. https://doi.org/10.1136/jmedgenet-2018-105588

Martínez-Monseny, A. F., Bolasell, M., Callejón-Póo, L., Cuadras, D., Freniche, V., Itzep, D. C., Gassiot, S., Arango, P., Casas-Alba, D., de la Morena, E., Corral, J., Montero, R., Pérez-Cerdá, C., Pérez, B., Artuch, R., Jaeken, J., & Serrano, M. (2019). AZATAX: Acetazolamide safety and efficacy in cerebellar syndrome in PMM2 congenital disorder of glycosylation (PMM2-CDG). *Annals of Neurology*, *85*(5), 740–751. https://doi.org/10.1002/ana.25457

Matheny-Rabun, C., Mokashi, S. S., Radenkovic, S., Wiggins, K., Dukes-Rimsky, L., Angel, P., Ghesquiere, B., Kozicz, T., Steet, R., Morava, E., & Flanagan-Steet, H. (2024). O-GlcNAcylation modulates expression and abundance of N-glycosylation machinery in an inherited glycosylation disorder. *Cell Reports*, *43*(11), 114976. https://doi.org/10.1016/j.celrep.2024.114976

Matthijs, G., Schollen, E., Van Schaftingen, E., Cassiman, J.-J., & Jaeken, J. (1998). Lack of Homozygotes for the Most Frequent Disease Allele in Carbohydrate-Deficient Glycoprotein Syndrome Type 1A. *The American Journal of Human Genetics*, *62*(3), 542–550. https://doi.org/10.1086/301763

Mills, E. A., & Goldman, D. (2017). The Regulation of Notch Signaling in Retinal Development and Regeneration. *Current Pathobiology Reports*, *5*(4), 323–331. https://doi.org/10.1007/s40139-017-0153-7

Monin, M.-L., Mignot, C., De Lonlay, P., Héron, B., Masurel, A., Mathieu-Dramard, M., Lenaerts, C., Thauvin, C., Gérard, M., Roze, E., Jacquette, A., Charles, P., de Baracé, C., Drouin-Garraud, V., Van Kien, P. K., Cormier-Daire, V., Mayer, M., Ogier, H., Brice, A., … Héron, D. (2014). 29 French adult patients with PMM2-congenital

disorder of glycosylation: outcome of the classical pediatric phenotype and depiction of a late-onset phenotype. *Orphanet Journal of Rare Diseases*, *9*(1), 207. https://doi.org/10.1186/s13023-014-0207-4

Monticelli, M., Liguori, L., Allocca, M., Andreotti, G., & Cubellis, M. V. (2019). β-Glucose-1,6-Bisphosphate Stabilizes Pathological Phophomannomutase2 Mutants In Vitro and Represents a Lead Compound to Develop Pharmacological Chaperones for the Most Common Disorder of Glycosylation, PMM2-CDG. *International Journal of Molecular Sciences*, *20*(17), 4164. https://doi.org/10.3390/ijms20174164

Moremen, K. W., Tiemeyer, M., & Nairn, A. V. (2012). Vertebrate protein glycosylation: diversity, synthesis and function. *Nature Reviews. Molecular Cell Biology*, *13*(7), 448–462. https://doi.org/10.1038/nrm3383

Mukaigasa, K., Tsujita, T., Nguyen, V. T., Li, L., Yagi, H., Fuse, Y., Nakajima-Takagi, Y., Kato, K., Yamamoto, M., & Kobayashi, M. (2018). Nrf2 activation attenuates genetic endoplasmic reticulum stress induced by a mutation in the phosphomannomutase 2 gene in zebrafish. *Proceedings of the National Academy of Sciences*, *115*(11), 2758–2763. https://doi.org/10.1073/pnas.1714056115

Muthusamy, K., Perez-Ortiz, J. M., Ligezka, A. N., Altassan, R., Johnsen, C., Schultz, M. J., Patterson, M. C., & Morava, E. (2024a). Neurological manifestations in PMM2-congenital disorders of glycosylation (PMM2-CDG): Insights into clinico-radiological characteristics, recommendations for follow-up, and future directions. *Genetics in Medicine*, *26*(2), 101027. https://doi.org/10.1016/j.gim.2023.101027

Muthusamy, K., Perez-Ortiz, J. M., Ligezka, A. N., Altassan, R., Johnsen, C., Schultz, M. J., Patterson, M. C., & Morava, E. (2024b). Neurological manifestations in PMM2-congenital disorders of glycosylation (PMM2-CDG): Insights into clinico-radiological characteristics, recommendations for follow-up, and future directions. *Genetics in Medicine*, *26*(2), 101027. https://doi.org/10.1016/J.GIM.2023.101027

Myosho, T., Kashima, M., Iguchi, T., & Kobayashi, T. (2025). Effects of Non-Feeding on Development in a Teleost, Minami-Medaka, <scp> *Oryzias latipes* </scp> : Identification of Eleutheroembryonic Stage for Potential Alternative Regulatory Toxicology Tests Along the 3R Principles. *Journal of Applied Toxicology*, *45*(6), 935–947. https://doi.org/10.1002/jat.4757

Natsume, T., Kiyomitsu, T., Saga, Y., & Kanemaki, M. T. (2016). Rapid Protein Depletion in Human Cells by Auxin-Inducible Degron Tagging with Short Homology Donors. *Cell Reports*, *15*(1), 210–218. https://doi.org/10.1016/J.CELREP.2016.03.001

Nelson, B. R., Gumuscu, B., Hartman, B. H., & Reh, T. A. (2006). Notch Activity Is Downregulated Just prior to Retinal Ganglion Cell Differentiation. *Developmental Neuroscience*, *28*(1–2), 128–141. https://doi.org/10.1159/000090759

Ng, B. G., Freeze, H. H., Himmelreich, N., Blau, N., & Ferreira, C. R. (2024). Clinical and biochemical footprints of congenital disorders of glycosylation: Proposed nosology. *Molecular Genetics and Metabolism*, *142*(1), 108476. https://doi.org/10.1016/j.ymgme.2024.108476

Niehues, R., Hasilik, M., Alton, G., Körner, C., Schiebe-Sukumar, M., Koch, H. G., Zimmer, K. P., Wu, R., Harms, E., Reiter, K., von Figura, K., Freeze, H. H., Harms, H. K., & Marquardt, T. (1998). Carbohydrate-deficient glycoprotein syndrome type Ib. Phosphomannose isomerase deficiency and mannose therapy. *Journal of Clinical Investigation*, *101*(7), 1414–1420. https://doi.org/10.1172/JCI2350

Nishimura, K., Fukagawa, T., Takisawa, H., Kakimoto, T., & Kanemaki, M. (2009). An auxin-based degron system for the rapid depletion of proteins in nonplant cells. *Nature Methods*, *6*(12), 917–922. https://doi.org/10.1038/nmeth.1401

Nishimura, K., Yamada, R., Hagihara, S., Iwasaki, R., Uchida, N., Kamura, T., Takahashi, K., Torii, K. U., & Fukagawa, T. (2020). A super-sensitive auxin-inducible degron system with an engineered auxin-TIR1 pair. *Nucleic Acids Research*, *48*(18), e108–e108. https://doi.org/10.1093/nar/gkaa748

Pacesa, M., Pelea, O., & Jinek, M. (2024). Past, present, and future of CRISPR genome editing technologies. *Cell*, *187*(5), 1076–1100. https://doi.org/10.1016/j.cell.2024.01.042

Pajusalu, S., Vals, M.-A., Serrano, M., Witters, P., Cechova, A., Honzik, T., Edmondson, A. C., Ficicioglu, C., Barone, R., De Lonlay, P., Bérat, C.-M., Vuillaumier-Barrot, S., Lam, C., Patterson, M. C., Janssen, M. C. H., Martins, E., Quelhas, D., Sykut-Cegielska, J., Mousa, J., … Õunap, K. (2024). Genotype/Phenotype Relationship: Lessons From 137 Patients With PMM2-CDG. *Human Mutation*, *2024*(1). https://doi.org/10.1155/2024/8813121

Pakari, K. (2021). *Establishing patient-based and conditional knockdown models to study the role of Pmm2 in medaka fish* [Master Thesis].

Pakari, K., Jakab, S., Sanchez Salvador, E., Thiel, C., Wittbrodt, J., & Thumberger, T. (2025). Establishing an auxin-inducible GFP nanobody-based acute protein knockdown system to mimic hypomorphic mutations during early medaka embryogenesis. *BioRxiv*, 2025.05.23.655727. https://doi.org/10.1101/2025.05.23.655727

Pakari, K., Wittbrodt, J., & Thumberger, T. (2023a). CRISPR-Fortschritte — Schnitt für Schnitt zu neuen Möglichkeiten. *BIOspektrum*, *29*(1), 25–28. https://doi.org/10.1007/s12268-023-1893-z

Pakari, K., Wittbrodt, J., & Thumberger, T. (2023b). *De novo* PAM generation to reach initially inaccessible target sites for base editing. *Development*, *150*(2). https://doi.org/10.1242/dev.201115

Park, C., & Zhang, J. (2011). Genome-wide evolutionary conservation of N-glycosylation sites. *Molecular Biology and Evolution*, *28*(8), 2351–2357. https://doi.org/10.1093/molbev/msr055

Parkinson, W. M., Dookwah, M., Dear, M. L., Gatto, C. L., Aoki, K., Tiemeyer, M., & Broadie, K. (2016). Synaptic roles for phosphomannomutase type 2 in a new *Drosophila* congenital disorder of glycosylation disease model. *Disease Models & Mechanisms*, *9*(5), 513–527. https://doi.org/10.1242/dmm.022939

Pedre, B., Talwar, D., Barayeu, U., Schilling, D., Luzarowski, M., Sokolowski, M., Glatt, S., & Dick, T. P. (2023). 3-Mercaptopyruvate sulfur transferase is a protein persulfidase. *Nature Chemical Biology*, *19*(4), 507–517. https://doi.org/10.1038/s41589-022-01244-8

Peng, T., Lv, C., Tan, H., Huang, J., He, H., Wang, Y., Zeng, M., Yi, D., Li, J., Deng, H., Shi, X., & Xiao, H. (2020). Novel PMM2 missense mutation in a Chinese family with non-syndromic premature ovarian insufficiency. *Journal of Assisted Reproduction and Genetics*, *37*(2), 443–450. https://doi.org/10.1007/s10815-019-01675-8

Pérez-Cerdá, C., Girós, M. L., Serrano, M., Ecay, M. J., Gort, L., Pérez Dueñas, B., Medrano, C., García-Alix, A., Artuch, R., Briones, P., & Pérez, B. (2017). A Population-Based Study on Congenital Disorders of Protein N- and Combined with O-Glycosylation Experience in Clinical and Genetic Diagnosis. *The Journal of Pediatrics*, *183*, 170-177.e1. https://doi.org/10.1016/j.jpeds.2016.12.060

Peterson, E., Shippee, E., Brinton, M. A., & Kaur, P. (2019). Biochemical characterization of the mouse ABCF3 protein, a partner of the flavivirus-resistance protein OAS1B. *The Journal of Biological Chemistry*, *294*(41), 14937–14952. https://doi.org/10.1074/jbc.RA119.008477

Piedade, A., Francisco, R., Jaeken, J., Sarkhail, P., Brasil, S., Ferreira, C. R., Rijoff, T., Pascoal, C., Gil, A., Lourenço, A. B., Abreu, M., Gomes, M., Videira, P. A., & dos Reis Ferreira, V. (2022). Epidemiology of congenital disorders of glycosylation (CDG)—overview and perspectives. *Journal of Rare Diseases*, *1*(1), 3. https://doi.org/10.1007/s44162-022-00003-6

Posit team. (2024). *RStudio: Integrated Development Environment for R*. Posit Software, PBC, Boston, MA. http://www.posit.co/

Pothukuchi, P., Agliarulo, I., Russo, D., Rizzo, R., Russo, F., & Parashuraman, S. (2019). Translation of genome to glycome: role of the Golgi apparatus. *FEBS Letters*, *593*(17), 2390–2411. https://doi.org/10.1002/1873-3468.13541

Quelhas, D., & Jaeken, J. (2024). Treatment of congenital disorders of glycosylation: An overview. *Molecular Genetics and Metabolism*, *143*(1–2), 108567. https://doi.org/10.1016/J.YMGME.2024.108567

Quental, R., Moleirinho, A., Azevedo, L., & Amorim, A. (2010). Evolutionary History and Functional Diversification of Phosphomannomutase Genes. *Journal of Molecular Evolution*, *71*(2), 119–127. https://doi.org/10.1007/s00239-010-9368-5

R Core Team. (2021). *R: A language and environment for statistical computing.* Vienna, Austria. https://www.R-project.org/

Radenkovic, S., Ligezka, A. N., Mokashi, S. S., Driesen, K., Dukes-Rimsky, L., Preston, G., Owuocha, L. F., Sabbagh, L., Mousa, J., Lam, C., Edmondson, A., Larson, A., Schultz, M., Vermeersch, P., Cassiman, D., Witters, P., Beamer, L. J., Kozicz, T., Flanagan-Steet, H., … Morava, E. (2023). Tracer metabolomics reveals the role of aldose reductase in glycosylation. *Cell Reports Medicine*, *4*(6), 101056. https://doi.org/10.1016/j.xcrm.2023.101056

Rappsilber, J., Mann, M., & Ishihama, Y. (2007). Protocol for micro-purification, enrichment, pre-fractionation and storage of peptides for proteomics using StageTips. *Nature Protocols*, *2*(8), 1896–1906. https://doi.org/10.1038/nprot.2007.261

Reily, C., Stewart, T. J., Renfrow, M. B., & Novak, J. (2019). Glycosylation in health and disease. *Nature Reviews Nephrology*, *15*(6), 346–366. https://doi.org/10.1038/s41581-019-0129-4

Rhoads, A., & Au, K. F. (2015). PacBio Sequencing and Its Applications. *Genomics, Proteomics & Bioinformatics*, *13*(5), 278–289. https://doi.org/10.1016/j.gpb.2015.08.002

Richter, M. F., Zhao, K. T., Eton, E., Lapinaite, A., Newby, G. A., Thuronyi, B. W., Wilson, C., Koblan, L. W., Zeng, J., Bauer, D. E., Doudna, J. A., & Liu, D. R. (2020). Phage-assisted evolution of an adenine base editor with improved Cas domain compatibility and activity. *Nature Biotechnology*, *38*(7), 883–891. https://doi.org/10.1038/s41587-020-0453-z

Rita Lecca, M., Wagner, U., Patrignani, A., Berger, E. G., & Hennet, T. (2005a). Genome-wide analysis of the unfolded protein response in fibroblasts from congenital disorders of glycosylation type-I patients. *The FASEB Journal*, *19*(2), 1–21. https://doi.org/10.1096/fj.04-2397fje

Rita Lecca, M., Wagner, U., Patrignani, A., Berger, E. G., & Hennet, T. (2005b). Genome-wide analysis of the unfolded protein response in fibroblasts from congenital disorders of glycosylation type-I patients. *The FASEB Journal*, *19*(2), 1–21. https://doi.org/10.1096/fj.04-2397fje

Rudd, P. M., Karlsson, N. G., Khoo, K. H., Thaysen-Andersen, M., Wells, L., & Packer, N. H. (2022). Glycomics and Glycoproteomics. In A. Varaki (Ed.), *Essentials in Glycobiology* (4th ed., pp. 689–704). Cold Spring Harbor Laboratory Press. Format:

Rush, J. S., Panneerselvam, K., Waechter, C. J., & Freeze, H. H. (2000). Mannose supplementation corrects GDP-mannose deficiency in cultured fibroblasts from some patients with Congenital Disorders of Glycosylation (CDG). *Glycobiology*, *10*(8), 829–835. https://doi.org/10.1093/glycob/10.8.829

Rutschow, S., Thiem, J., Kranz, C., & Marquardt, T. (2002). Membrane-Permeant derivatives of mannose-1-phosphate. *Bioorganic & Medicinal Chemistry*, *10*(12), 4043–4049. https://doi.org/10.1016/S0968-0896(02)00269-9

Schachter, H., & Freeze, H. H. (2009). Glycosylation diseases: Quo vadis? *Biochimica et Biophysica Acta (BBA) - Molecular Basis of Disease*, *1792*(9), 925–930. https://doi.org/10.1016/j.bbadis.2008.11.002

Schindelin, J., Arganda-Carreras, I., Frise, E., Kaynig, V., Longair, M., Pietzsch, T., Preibisch, S., Rueden, C., Saalfeld, S., Schmid, B., Tinevez, J.-Y., White, D. J., Hartenstein, V., Eliceiri, K., Tomancak, P., & Cardona, A. (2012). Fiji: an open-source platform for biological-image analysis. *Nature Methods*, *9*(7), 676–682. https://doi.org/10.1038/nmeth.2019

Schjoldager, K. T., Narimatsu, Y., Joshi, H. J., & Clausen, H. (2020). Global view of human protein glycosylation pathways and functions. *Nature Reviews Molecular Cell Biology*, *21*(12), 729–749. https://doi.org/10.1038/s41580-020-00294-x

Schneider, A., Thiel, C., Rindermann, J., DeRossi, C., Popovici, D., Hoffmann, G. F., Gröne, H.-J., & Körner, C. (2012). Successful prenatal mannose treatment for congenital disorder of glycosylation-Ia in mice. *Nature Medicine*, *18*(1), 71–73. https://doi.org/10.1038/nm.2548

Schollen, E., Kjaergaard, S., Legius, E., Schwartz, M., & Matthijs, G. (2000). Lack of Hardy-Weinberg equilibrium for the most prevalent PMM2 mutation in CDG-Ia (congenital disorders of glycosylation type Ia). *European Journal of Human Genetics*, *8*(5), 367–371. https://doi.org/10.1038/sj.ejhg.5200470

Schwarz, F., & Aebi, M. (2011). Mechanisms and principles of N-linked protein glycosylation. *Current Opinion in Structural Biology*, *21*(5), 576–582. https://doi.org/10.1016/J.SBI.2011.08.005

Seleit, A., Aulehla, A., & Paix, A. (2021). Endogenous protein tagging in medaka using a simplified CRISPR/Cas9 knock-in approach. *ELife*, *10*. https://doi.org/10.7554/eLife.75050

Shang, J., Korner, C., Freeze, H., & Lehrman, M. A. (2002). Extension of lipid-linked oligosaccharides is a high-priority aspect of the unfolded protein response: endoplasmic reticulum stress in Type I congenital disorder of glycosylation fibroblasts. *Glycobiology*, *12*(5), 307–317. https://doi.org/10.1093/glycob/12.5.307

Sharma, V., Ichikawa, M., & Freeze, H. H. (2014). Mannose metabolism: More than meets the eye. *Biochemical and Biophysical Research Communications*, *453*(2), 220–228. https://doi.org/10.1016/j.bbrc.2014.06.021

Shirakura, T., Krishnamoorthy, L., Paliwal, P., Hird, G., McCluskie, K., McWilliams, P., He, M., & Ismaili, M. H. A. (2024). In vitro treatment with liposome-encapsulated Mannose-1-phosphate restores N-glycosylation in PMM2-CDG patient-derived fibroblasts. *Molecular Genetics and Metabolism*, *143*(1–2), 108531. https://doi.org/10.1016/j.ymgme.2024.108531

Silvaggi, N. R., Zhang, C., Lu, Z., Dai, J., Dunaway-Mariano, D., & Allen, K. N. (2006). The X-ray Crystal Structures of Human α-Phosphomannomutase 1 Reveal the Structural Basis of Congenital Disorder of Glycosylation Type 1a. *Journal of Biological Chemistry*, *281*(21), 14918–14926. https://doi.org/10.1074/jbc.M601505200

Spiro, R. G. (2002). Protein glycosylation: nature, distribution, enzymatic formation, and disease implications of glycopeptide bonds. *Glycobiology*, *12*(4), 43R-56R. https://doi.org/10.1093/glycob/12.4.43R

Stanley, P. (2011). Golgi glycosylation. *Cold Spring Harbor Perspectives in Biology*, *3*(4). https://doi.org/10.1101/cshperspect.a005199

Stanley, P., Moremen, K., Lewis, N., Taniguchi, N., & Aebi, M. (2022). N-Glycans. In *Essentials in Glycobiology* (4th ed.).

Stekhoven, D. J., & Bühlmann, P. (2012). MissForest—non-parametric missing value imputation for mixed-type data. *Bioinformatics*, *28*(1), 112–118. https://doi.org/10.1093/bioinformatics/btr597

Stemmer, M., Thumberger, T., del Sol Keyer, M., Wittbrodt, J., & Mateo, J. L. (2015). CCTop: An Intuitive, Flexible and Reliable CRISPR/Cas9 Target Prediction Tool. *PLOS ONE*, *10*(4), e0124633. https://doi.org/10.1371/journal.pone.0124633

Stuber, A., Schlotter, T., Hengsteler, J., & Nakatsuka, N. (2023). *Solid-State Nanopores for Biomolecular Analysis and Detection* (pp. 283–316). https://doi.org/10.1007/10_2023_240

Suzuki, T., Cummings, R. D., Aebi, M., & Parodi, A. (2022). Glycans in Glycoprotein Quality Control. In *Essentials of Glycobiology*. (4th ed., pp. 529–538). Cold Spring Harbor Laboratory Press.

Taday, R., Grüneberg, M., DuChesne, I., Reunert, J., & Marquardt, T. (2020). Dietary mannose supplementation in phosphomannomutase 2 deficiency (PMM2-CDG). *Orphanet Journal of Rare Diseases*, *15*(1), 258. https://doi.org/10.1186/s13023-020-01528-z

Takeuchi, H., & Haltiwanger, R. S. (2014). Significance of glycosylation in Notch signaling. *Biochemical and Biophysical Research Communications*, *453*(2), 235–242. https://doi.org/10.1016/j.bbrc.2014.05.115

Tan, J., Zeng, D., Zhao, Y., Wang, Y., Liu, T., Li, S., Xue, Y., Luo, Y., Xie, X., Chen, L., Liu, Y., & Zhu, Q. (2022). PhieABEs: a PAM-less/free high-efficiency adenine base editor toolbox with wide target scope in plants. *Plant Biotechnology Journal*, *20*(5), 934–943. https://doi.org/10.1111/pbi.13774

Thiel, C., Lübke, T., Matthijs, G., von Figura, K., & Körner, C. (2006). Targeted Disruption of the Mouse Phosphomannomutase 2 Gene Causes Early Embryonic Lethality. *Molecular and Cellular Biology*, *26*(15), 5615–5620. https://doi.org/10.1128/MCB.02391-05

Thiesler, C. T., Cajic, S., Hoffmann, D., Thiel, C., van Diepen, L., Hennig, R., Sgodda, M., Weißmann, R., Reichl, U., Steinemann, D., Diekmann, U., Huber, N. M. B., Oberbeck, A., Cantz, T., Kuss, A. W., Körner, C., Schambach, A., Rapp, E., & Buettner, F. F. R. (2016). Glycomic Characterization of Induced Pluripotent Stem Cells Derived from a Patient Suffering from Phosphomannomutase 2 Congenital Disorder of Glycosylation (PMM2-CDG). *Molecular & Cellular Proteomics : MCP*, *15*(4), 1435–1452. https://doi.org/10.1074/mcp.M115.054122

Thisse, B., & Thisse, C. (2004). Fast Release Clones: A High Throughput Expression Analysis. *ZFIN Direct Data Submission*. http://zfin.org

Thumberger, T., Tavhelidse-Suck, T., Gutierrez-Triana, J. A., Cornean, A., Medert, R., Welz, B., Freichel, M., & Wittbrodt, J. (2022). Boosting targeted genome editing using the hei-tag. *ELife*, *11*. https://doi.org/10.7554/eLife.70558

Thuronyi, B. W., Koblan, L. W., Levy, J. M., Yeh, W.-H., Zheng, C., Newby, G. A., Wilson, C., Bhaumik, M., Shubina-Oleinik, O., Holt, J. R., & Liu, D. R. (2019). Continuous evolution of base editors with expanded target compatibility and improved activity. *Nature Biotechnology*, *37*(9), 1070–1079. https://doi.org/10.1038/s41587-019-0193-0

Vals, M., Morava, E., Teeäär, K., Zordania, R., Pajusalu, S., Lefeber, D. J., & Õunap, K. (2017). Three families with mild PMM2-CDG and normal cognitive development. *American Journal of Medical Genetics Part A*, *173*(6), 1620–1624. https://doi.org/10.1002/ajmg.a.38235

Vals, M.-A., Pajusalu, S., Kals, M., Mägi, R., & Õunap, K. (2017). *The Prevalence of PMM2-CDG in Estonia Based on Population Carrier Frequencies and Diagnosed Patients* (pp. 13–17). https://doi.org/10.1007/8904_2017_41

van Scherpenzeel, M., Steenbergen, G., Morava, E., Wevers, R. A., & Lefeber, D. J. (2015). High-resolution mass spectrometry glycoprofiling of intact transferrin for diagnosis and subtype identification in the congenital disorders of glycosylation. *Translational Research : The Journal of Laboratory and Clinical Medicine*, *166*(6), 639-649.e1. https://doi.org/10.1016/j.trsl.2015.07.005

Varki, A. (1993). Biological roles of oligosaccharides: all of the theories are correct. *Glycobiology*, *3*(2), 97–130. https://doi.org/10.1093/glycob/3.2.97

Varki, A., Cummings, R. D., Esko, J. D., Freeze, H. H., Stanley, P., Marth, J. D., Bertozzi, C. R., Hart, G. W., & Etzler, M. E. (2009). Symbol nomenclature for glycan representation. *PROTEOMICS*, *9*(24), 5398–5399. https://doi.org/10.1002/pmic.200900708

Varki, A., Cummings, R., Esko, J., & et al. (2022). *Essentials of Glycobiology, 4th edition*. https://doi.org/10.1101/9781621824213

Vilas, A., Briso-Montiano, Á., Segovia-Falquina, C., Martín-Martínez, A., Soriano-Sexto, A., Gallego, D., Ruiz-Montés, V., Gámez, A., & Pérez, B. (2024). HepG2 PMM2-CDG knockout model: A versatile platform for variant and therapeutic evaluation. *Molecular Genetics and Metabolism*, *143*(1–2), 108538. https://doi.org/10.1016/J.YMGME.2024.108538

Vilas, A., Yuste-Checa, P., Gallego, D., Desviat, L. R., Ugarte, M., Pérez-Cerda, C., Gámez, A., & Pérez, B. (2020). Proteostasis regulators as potential rescuers of PMM2 activity. *Biochimica et Biophysica Acta (BBA) - Molecular Basis of Disease*, *1866*(7), 165777. https://doi.org/10.1016/j.bbadis.2020.165777

Vilella, A. J., Severin, J., Ureta-Vidal, A., Heng, L., Durbin, R., & Birney, E. (2009). EnsemblCompara GeneTrees: Complete, duplication-aware phylogenetic trees in vertebrates. *Genome Research*, *19*(2), 327–335. https://doi.org/10.1101/gr.073585.107

Vleugels, W., Haeuptle, M. A., Ng, B. G., Michalski, J.-C., Battini, R., Dionisi-Vici, C., Ludman, M. D., Jaeken, J., Foulquier, F., Freeze, H. H., Matthijs, G., & Hennet, T. (2009). RFT1 deficiency in three novel CDG patients. *Human Mutation*, *30*(10), 1428–1434. https://doi.org/10.1002/humu.21085

Walker, M., & Kimmel, C. (2007). A two-color acid-free cartilage and bone stain for zebrafish larvae. *Biotechnic & Histochemistry*, *82*(1), 23–28. https://doi.org/10.1080/10520290701333558

Walton, R. T., Christie, K. A., Whittaker, M. N., & Kleinstiver, B. P. (2020). Unconstrained genome targeting with near-PAMless engineered CRISPR-Cas9 variants. *Science*, *368*(6488), 290–296. https://doi.org/10.1126/science.aba8853

Weixel, T., Wolfe, L., & Macnamara, E. F. (2024). Genetic counseling for congenital disorders of glycosylation (CDG). *Journal of Genetic Counseling*, *33*(6), 1358–1364. https://doi.org/10.1002/jgc4.1856

Westphal, V., Peterson, S., Patterson, M., Tournay, A., Blumenthal, A., Treacy, E. P., & Freeze, H. H. (2001a). Functional significance of PMM2 mutations in mildly affected patients with congenital disorders of glycosylation Ia. *Genetics in Medicine*, *3*(6), 393–398. https://doi.org/10.1097/00125817-200111000-00003

Westphal, V., Peterson, S., Patterson, M., Tournay, A., Blumenthal, A., Treacy, E. P., & Freeze, H. H. (2001b). Functional significance of PMM2 mutations in mildly affected patients with congenital disorders of glycosylation Ia. *Genetics in Medicine*, *3*(6), 393–398. https://doi.org/10.1097/00125817-200111000-00003

Wickham, H. (2016). *ggplot2*. Springer International Publishing. https://doi.org/10.1007/978-3-319-24277-4

Wittbrodt, J., Shima, A., & Schartl, M. (2002). Medaka — a model organism from the far east. *Nature Reviews Genetics*, *3*(1), 53–64. https://doi.org/10.1038/nrg704

Witters, P., Edmondson, A. C., Lam, C., Johnsen, C., Patterson, M. C., Raymond, K. M., He, M., Freeze, H. H., & Morava, E. (2021). Spontaneous improvement of carbohydrate-deficient transferrin in PMM2-CDG without mannose observed in CDG natural history study. *Orphanet Journal of Rare Diseases*, *16*(1), 102. https://doi.org/10.1186/s13023-021-01751-2

Wong, S. Y.-W., Gadomski, T., van Scherpenzeel, M., Honzik, T., Hansikova, H., Holmefjord, K. S. B., Mork, M., Bowling, F., Sykut-Cegielska, J., Koch, D., Hertecant, J., Preston, G., Jaeken, J., Peeters, N., Perez, S., Nguyen, D. Do, Crivelly, K., Emmerzaal, T., Gibson, K. M., … Morava, E. (2017). Oral D-galactose supplementation in PGM1-CDG. *Genetics in Medicine*, *19*(11), 1226–1235. https://doi.org/10.1038/gim.2017.41

Xue, C., & Greene, E. C. (2021). DNA Repair Pathway Choices in CRISPR-Cas9-Mediated Genome Editing. *Trends in Genetics : TIG*, *37*(7), 639–656. https://doi.org/10.1016/j.tig.2021.02.008

Yesbolatova, A., Saito, Y., Kitamoto, N., Makino-Itou, H., Ajima, R., Nakano, R., Nakaoka, H., Fukui, K., Gamo, K., Tominari, Y., Takeuchi, H., Saga, Y., Hayashi, K., & Kanemaki, M. T. (2020). The auxin-inducible degron 2 technology provides sharp degradation control in yeast, mammalian cells, and mice. *Nature Communications*, *11*(1), 5701. https://doi.org/10.1038/s41467-020-19532-z

Yu, F., Lin, L., Sun, J., Pan, J., Liao, Y., Pan, Y., Bai, G., Ma, L., Mao, J., & Hu, L. (2023). Cysteine Pathogenic Variants of PMM2 Are Sensitive to Environmental Stress with Loss of Structural Stability. *Oxidative Medicine and Cellular Longevity*, *2023*, 1–17. https://doi.org/10.1155/2023/5964723

Yuste-Checa, P., Brasil, S., Gámez, A., Underhaug, J., Desviat, L. R., Ugarte, M., Pérez-Cerdá, C., Martinez, A., & Pérez, B. (2017). Pharmacological Chaperoning: A Potential Treatment for PMM2-CDG. *Human Mutation*, *38*(2), 160–168. https://doi.org/10.1002/humu.23138

Yuste-Checa, P., Gámez, A., Brasil, S., Desviat, L. R., Ugarte, M., Pérez-Cerdá, C., & Pérez, B. (2015). The Effects of PMM2-CDG-Causing Mutations on the Folding, Activity, and Stability of the PMM2 Protein. *Human Mutation*, *36*(9), 851–860. https://doi.org/10.1002/humu.22817

Zdrazilova, L., Rakosnikova, T., Himmelreich, N., Ondruskova, N., Pasak, M., Vanisova, M., Volfova, N., Honzik, T., Thiel, C., & Hansikova, H. (2023). Metabolic adaptation of human skin fibroblasts to ER stress caused by glycosylation defect in PMM2-CDG. *Molecular Genetics and Metabolism*, *139*(4), 107629. https://doi.org/10.1016/j.ymgme.2023.107629

Zielinska, D. F., Gnad, F., Wiśniewski, J. R., & Mann, M. (2010). Precision Mapping of an In Vivo N-Glycoproteome Reveals Rigid Topological and Sequence Constraints. *Cell*, *141*(5), 897–907. https://doi.org/10.1016/j.cell.2010.04.012

Publications

Publications during my PhD

Philipp Pöschko, Caroline M. Berrou, Kaisa Pakari, Michael J. Ziegler, Christoph Kern, Birgit Koch, Joachim Wittbrodt, Richard Wombacher (2025). **Photoactivatable Plant Hormone-Based Chemical Inducers of Proximity for In Vivo Applications.** *ACS Chemical Biology*. DOI: 10.1021/acschembio.4c00592

Andreas Hecker & Kaisa Pakari (2023). **Mit Zellkultur und Fischmodell Glykosylierungserkrankung erforschen.** *Biospektrum – Journal Club.* DOI: 10.1007/s12268-023-2035-3

Kaisa Pakari (2023). **Drag & Drop mit CRISPR-Integrase – die Zukunft für die Behandlung von genetischen Erkrankungen?** *Biospektrum – Journal Club*. DOI: 10.1007/s12268-023-1940-9

Kaisa Pakari, Joachim Wittbrodt, Thomas Thumberger (2023). **CRISPR-Fortschritte – Schnitt für Schnitt zu neuen Möglichkeiten.** *Biospektrum.* DOI: 10.1007/s12268-023-1893-z

Kaisa Pakari, Joachim Wittbrodt, Thomas Thumberger (2023). ***De novo* PAM generation to reach initially inaccessible target sites for base editing.** *Development.* 10.1242/dev.201115

Manuscript in peer review

Kaisa Pakari, Sevinç Jakab, Encarnación Sánchez Salvador, Christian Thiel, Joachim Wittbrodt, Thomas Thumberger (2025). **Establishing an auxin-inducible GFP nanobody-based acute protein knockdown system to mimic hypomorphic mutations during early medaka embryogenesis.** *bioRxiv.* DOI: 10.1101/2025.05.23.655727

Acknowledgments

First of all, thank you Jochen! I joined your lab as a fish feeding Hiwi in Bioquant, then moved on to a rotation in the lab, continued with my master thesis and finally stayed for the PhD. Your door was always open when it mattered. You took the time to discuss, offered thoughtful advice, scientifically and personally, and reminded me that everything can be solved (especially over a good coffee). Your support, encouragement, visions and belief in me truly made a difference. Turning every bug into a feature will stick with me.
I was lucky to have two supervisors. Thank you, Thomas! Not just for never-ending jokes (some bad, some good and some running gags), but for your support, your endless creativity and your ability to balance scientific seriousness and humor. From manuscript writings and coffee meetings, to Christmas party games and amazing conference trips, it was an honor to work with you.
Thanks to both of you for your support during my bike accident and hand recovery, I never had to worry, and that meant a lot to me.

Sabine, thank you for being part of my TAC committee and your dedicated leadership of the FOR2509. The meetings and courses really pushed us young scientists and offered us to grow. Thank you, Sebastian, for your support during the TAC meetings and Lauren for being part of my defense committee.

Thank you Glyco Bay! It was a pleasure to work with all of you in our little sugar cub. It became space of shared secrets, science and support. Huge thanks to my helping-hand Hiwis: first Marlen, then Johanna - your help over nearly two years was invaluable.
Encarni, we started this PhDs together and grew so much. I'm really glad we shared this journey. Your support, kindness and scientific passion inspired me every day. Thank you for always having my back.

To the amazing 5th floor crew: you were the best colleagues I could have wished for. We laughed, drank a lot of coffee, talked about science and life. The energy and mindfulness that connects us made even the tough days a lot of fun.
Thank you: Tanja, for your thoughtfulness and expertise on everything. Beate, for smoothly keeping things running in the lab. Jana, for all the fun inside and outside the lab, looking forward to the day when people finally start to ask for our opinion and let our ideas improve the world. Christina, for sports, laughs and life advice. Bettina, for the deep talks and your multitasking mastering skills. Rashi, for our random shared (weird) connection moments

and the otters in Japan. Risa, for your inspiring endurance handling your big data and solution-oriented mind. Cassian, for the shared sympathy sour cucumber gummy bears. Laura, you just fit in like you had always been here, I truly enjoy your company. Philip, I will always remember our fun “rowing-dance” and sarcastic chats. Lucie, you’re an inspiration balancing science and motherhood. Joergen, your excitement for science made every discussion more exciting.

A special thanks to the office dream team Frederike and Eva! Your behind-the-scenes coordination, open ears and your proactive mindset were priceless.

Big thanks to the fish room team, for countless chats, your interest in our experiments and taking care of the fish.

Thanks to the members of the Centanin and Weinhardt lab for your great company.

Thank you to the Thiel Lab: Christian, Virginia and Andreas, it was a pleasure collaborating with you.

To everyone who proofread my thesis: Christina, Jana, Marco, Bettina, Toni, Tanja and Thomas, thank you for your sharp eyes and quick feedback. You helped me more than you know.

Finally, to my family and friends, near and far: thank you for your love, encouragement and belief in me. And most of all, to my partner and favorite flatmate Philipp, thank you for endless support!

Declaration

I herewith declare that I have written the PhD thesis “Modeling human PMM2-CDG in medaka to understand systemic effects of hypoglycosylation on development” on my own with no other sources and aids than quoted.

Heidelberg, 2025

List of Figures

List of Tables